

Characteristics of Active Combustion Control for Liquid-Fuel Systems with Proportional Primary Fuel Modulation

by

Anne M. Hines

Thesis submitted to the Faculty of
Virginia Polytechnic Institute and State University
in partial fulfillment of the requirements for a degree of

MASTER OF SCIENCE
in
MECHANICAL ENGINEERING

Dr. William R. Saunders, Co-Chair
Dr. William T. Baumann, Co-Chair
Dr. Uri Vandsburger

May 3, 2005
Blacksburg, Virginia

Keywords: active combustion control, atomization, proportional fuel injection, simplex
nozzle, air-assist nozzle, Phase Doppler Anemometry

Characteristics of Active Combustion Control for Liquid-Fuel Systems with Proportional Primary Fuel Modulation

Anne M. Hines

ABSTRACT

The first part of this work focuses on control experiments performed on an unstable kerosene-fueled turbulent combustor. Using a phase shift controller and primary fuel modulation stability is successfully gained for a wide band of global equivalence ratios allowing the limitations of the control scheme to be characterized. It is shown that control signal saturation can significantly impact the ability of the control scheme to stabilize the system. Three different regions of controllability are defined based on the degree of saturation. A hysteresis behavior is also found to exist for the controller settings depending on whether stability is being maintained or realized for an unstable system.

The second part of this work focuses on the impact that primary fuel modulation has on the fuel spray. Measurements for a simplex nozzle and an air-assist nozzle are taken under both static and dynamic operating conditions with a Phase Doppler Anemometry system. The dynamic modulation is found to significantly impact the spray properties of both nozzles.

Acknowledgments

Success is the ability to go from one failure to another without a loss of enthusiasm.

-Winston Churchill

I have many people to thank for helping me survive the many failures and the occasional success of the last two years and helping me complete this thesis.

To my parents, Mary Lou and Larry: none of this would have been possible without your support. Thank you for always being on my side. I am truly proud to have you as parents. Thank you also to my brothers, Chris and Joe, for their support and for setting the bar very very high.

To all of the friends I have made throughout my time in Blacksburg: your friendship has meant a lot to me over the last seven years. Very special thanks to Heather (a.k.a. Okie) and Henning for putting up with me—even when I'm crazy.

To my officemates and fellow researchers Noah, Losh, Jonathan, Adam, Chris, Wajid, Scott, Steve, David, and Joe: for all your help with this research I am forever indebted to you. Thank you also for providing both the insights and distractions without which graduate school is not complete. I would particularly like to thank Wajid and David for endless hours of help running experiments.

I would also like to thank all of my committee members. Dr. Saunders, Dr. Baumann, and Dr. Vandsburger: each of you has given me support and encouragement during different parts of this research. Thanks for the opportunity to work with you—the experience has changed me forever.

Table of Contents

Acknowledgments.....	iii
Table of Contents	iv
List of Figures and Tables.....	vi
Glossary	xiii
Chapter 1. Introduction.....	1
1.1. Background	1
1.2. Motivation.....	1
1.3. Literature Review	2
1.3.1. Active Combustion Control.....	2
1.3.2. Atomization.....	5
1.4. Thesis Overview.....	7
1.4.1. Contributions of the Thesis	7
1.4.2. Thesis Organization	8
Chapter 2. Controlling Combustion Instabilities.....	9
2.1. Combustor Specifications	9
2.1.1. Hardware and Software	9
2.1.2. Uncontrolled System Characteristics	11
2.1.3. The Effect of Filter Settings	13
2.1.4. Experimental Setup and Procedures.....	16
2.2. Controller Trends.....	17
2.3. Control Performance Near the Instability Boundary	19
2.3.1. System Characteristics.....	19
2.3.2. Hysteresis.....	20
2.4. Control Performance Further From the Instability Boundary.....	22
2.4.1. System Characteristics.....	22
2.4.2. Saturation.....	26
2.5. Control Performance Far From the Instability Boundary	32
2.5.1. System Characteristics.....	32
2.5.2. Saturation.....	33
Chapter 3. Atomization Effects	37
3.1. Introduction	37
3.2. Experimental Setup and Calculations	37
3.2.1. Experimental Setup.....	37
3.2.2. Calculations	40
3.3. Experimental Results.....	41
3.3.1. Simplex Nozzle Static Measurements.....	41
3.3.2. Simplex Nozzle Dynamic Measurements	43
3.3.3. Simplex Nozzle Measurement Summary	66
3.3.4. Air-Assist Nozzle Static Measurements	67
3.3.5. Air-Assist Nozzle Dynamic Measurements.....	72
3.3.6. Spill-Return Nozzle Operation.....	78

Chapter 4. Summary and Future Work	80
4.1. Summary.....	80
4.2. Future Work.....	81
Appendix A: Phase Shift Controller, Mean Pressure Controller, and Voltage Limiter	82
Appendix B: Sensors, Filters, and Measurement Settings	83
Appendix C: Fuel System Plumbing and Control System Wiring.....	84
Appendix D: Uncontrolled Power Spectrums for the First Uncontrolled Region of the VACCG Kerosene-Fueled Combustor.	86
Appendix E: Power Spectrums for the VACCG Kerosene-Fueled Combustor, GER=0.50, Various Controller Settings.....	97
Appendix F: Wiring Diagram for Nozzle Measurements.....	136
Appendix G: Error bar plots for Nozzle Measurements	137
Bibliography.....	158
Vita	160

List of Figures and Tables

Figure 1.3.1: Dynamically modulated spill-return nozzle, Chang et al. [4].	6
Figure 1.3.2: Laser sheet images of static and dynamically modulated spill-return spray, Chang et al. [4].	7
Figure 2.1.1: VACCG kerosene-fueled combustor [20].	9
Figure 2.1.2: Diagram of the Physical System and Control System for the VACCG kerosene-fueled combustor.	10
Figure 2.1.3: a. Photograph of the flame in the stable region ($GER < 0.48$). b. Photograph of the flame in the first unstable region ($0.48 < GER < 0.75$). c. Photograph of the flame in the second unstable region ($GER > 0.75$), [20].	11
Figure 2.1.4: Limit cycle frequency versus GER for the first unstable region of the VACCG kerosene-fueled combustor.	12
Figure 2.1.5: Second Harmonic Amplitude, SPL (dB), versus GER for the first unstable region of the VACCG kerosene-fueled combustor.	13
Table 2.1.1: Configurations of filter settings used in preliminary experiments.	14
Figure 2.1.6: Magnitude and phase characteristics of the band pass filter with 100-160 setting.	14
Figure 2.1.7: Magnitude and phase characteristics of the two low pass filter settings.	15
Figure 2.1.8: Comparison of stabilized system power spectrum fundamental peaks for GER=0.5 with and without the band pass filter, low pass filter setting of 1500 Hz. Power spectrum for configuration 2 (with bandpass) taken before bandpass filter.	15
Figure 2.1.9: Comparison of stabilized system power spectrum fundamental peaks for GER=0.5 without the band pass filter, low pass filter settings of 150 and 1500 Hz.	16
Table 2.1.2: Experimental setup for control experiments.	16
Figure 2.2.1: Ranges of controller settings used to maintain control for various GERs.	18
Figure 2.3.1: Controlled and Uncontrolled System at a GER of 0.50.	19
Figure 2.3.2: GER: 0.50.	20
Figure 2.3.3: GER: 0.50, delays 24, hysteresis.	21
Figure 2.3.4: GER: 0.50, delays 28, unstable.	22
Figure 2.4.1: GER:0.60.	23
Figure 2.4.2: GER: 0.62.	23
Figure 2.4.3: GER: 0.64.	24
Figure 2.4.4: GER: 0.58.	25
Figure 2.4.5: GER: 0.61.	25
Figure 2.4.6: Theoretical delta pressure (psi) before saturation for various mean fuel pressures.	27
Figure 2.4.7: GER=0.58.	28
Figure 2.4.8: GER=0.58, combustor pressure signal, no controller.	29
Figure 2.4.9: GER=0.58, combustor pressure signal, for controller on but uncontrolled.	29
Figure 2.4.10: GER=0.58, control signal, for controller on at original setting, uncontrolled.	30
Figure 2.4.11: GER=0.58, combustor pressure signal, shifted controller setting.	30
Figure 2.4.12: GER=0.58, control signal, shifted controller setting.	31
Figure 2.5.1: GER=0.65.	32
Figure 2.5.2: Control signal, Controlled system, Delays: 15, Gain: 3.6.	33
Figure 2.5.3: GER=0.65, various controller settings.	34

Figure 2.5.4: GER=0.65, Various controller settings, close up of instability peaks.....	34
Figure 2.5.5: GER=0.65, Combustor pressure signal, Controller on, Delays:15, Gain: 3.6...35	35
Figure 2.5.6: GER=0.65, Control signal, Controller on, Delays:15, Gain: 3.6.....	35
Figure 2.5.7: GER=0.65, Combustor pressure signal, Controller on, Delays:19, Gain: 3.6...36	36
Figure 2.5.8: GER=0.65, Control signal, Controller on, Delays:19, Gain: 3.6.....	36
Figure 3.2.1: Phase Doppler Anemometry (PDA) setup for spray measurement tests.....	38
Figure 3.2.2: Water and air system for atomization tests.....	39
Figure 3.2.3: Delavan solid-cone 60° spray angle 1.0 gph simplex nozzle [10].	39
Figure 3.2.4: Delavan 0.75 gph air-assist nozzle [10].	39
Figure 3.3.1: Measurement locations for simplex nozzle experiments.	41
Figure 3.3.2: Simplex nozzle static measurements, SMD vs. radial position for various supply pressures.....	42
Figure 3.3.3: Simplex nozzle static measurements, axial velocity vs. radial position for various supply pressures.	42
Figure 3.3.4: Phase bin calculations for dynamic phase-locked measurements.....	44
Table 3.3.1: Summary of mean SMDs and axial velocities for static and dynamic testing, Simplex nozzle, 250 psi mean pressure.....	45
Figure 3.3.5: Simplex nozzle phase-locked dynamic measurement SMD results, at centerline, 250 psi mean pressure.	46
Figure 3.3.6: Simplex nozzle phase-locked dynamic measurement SMD results, at radial 0.5 cm, 250 psi mean pressure.....	46
Figure 3.3.7: Simplex nozzle phase-locked dynamic measurement SMD results, at radial 1.0 cm, 250 psi mean pressure.....	47
Figure 3.3.8: Simplex nozzle phase-locked dynamic measurement SMD results, at radial 1.5 cm, 250 psi mean pressure.....	47
Figure 3.3.9: Simplex nozzle phase-locked dynamic measurement SMD results, ±30 psi, 250 psi mean pressure.....	48
Figure 3.3.10: Simplex nozzle phase-locked dynamic measurement SMD results, ±50 psi, 250 psi mean pressure.....	48
Figure 3.3.11: Simplex nozzle phase-locked dynamic measurement SMD results, ±75 psi, 250 psi mean pressure.....	49
Figure 3.3.12: Simplex nozzle phase-locked dynamic measurement SMD results, ±100 psi, 250 psi mean pressure.	49
Figure 3.3.13: Simplex nozzle phase-locked dynamic measurement velocity results, centerline, 250 psi mean pressure.	50
Figure 3.3.14: Simplex nozzle phase-locked dynamic measurement velocity results, radial 0.5 cm, 250 psi mean pressure.....	50
Figure 3.3.15: Simplex nozzle phase-locked dynamic measurement velocity results, radial 1.0 cm, 250 psi mean pressure.....	51
Figure 3.3.16: Simplex nozzle phase-locked dynamic measurement velocity results, radial 1.5 cm, 250 psi mean pressure.....	51
Figure 3.3.17: Simplex nozzle phase-locked dynamic measurement velocity results, ±30 psi, 250 psi mean pressure.	52
Figure 3.3.18: Simplex nozzle phase-locked dynamic measurement velocity results, ±50 psi, 250 psi mean pressure.	52
Figure 3.3.19: Simplex nozzle phase-locked dynamic measurement velocity results, ±75 psi, 250 psi mean pressure.	53

Figure 3.3.20: Simplex nozzle phase-locked dynamic measurement velocity results, ± 100 psi, 250 psi mean pressure.	53
Figure 3.3.21: Simplex nozzle phase-locked dynamic measurement count (%) results, centerline, 250 psi mean pressure.	54
Figure 3.3.22: Simplex nozzle phase-locked dynamic measurement count (%) results, radial 0.5 cm, 250 psi mean pressure.	54
Figure 3.3.23: Simplex nozzle phase-locked dynamic measurement count (%) results, radial 1.0 cm, 250 psi mean pressure.	55
Figure 3.3.24: Simplex nozzle phase-locked dynamic measurement count (%) results, radial 1.5 cm, 250 psi mean pressure.	55
Figure 3.3.25: Simplex nozzle phase-locked dynamic measurement count (%) results, ± 30 psi, 250 psi mean pressure.	56
Figure 3.3.26: Simplex nozzle phase-locked dynamic measurement count (%) results, ± 50 psi, 250 psi mean pressure.	56
Figure 3.3.27: Simplex nozzle phase-locked dynamic measurement count (%) results, ± 75 psi, 250 psi mean pressure.	57
Figure 3.3.28: Simplex nozzle phase-locked dynamic measurement count (%) results, ± 100 psi, 250 psi mean pressure.	57
Table 3.3.2: Summary of mean SMDs and axial velocities for static and dynamic testing, Simplex nozzle, 200 psi mean pressure.	58
Figure 3.3.29: Simplex nozzle phase-locked dynamic measurement SMD results, centerline, 200 psi mean pressure.	59
Figure 3.3.30: Simplex nozzle phase-locked dynamic measurement SMD results, radial 1.0 cm, 200 psi mean pressure.	59
Figure 3.3.31: Simplex nozzle phase-locked dynamic measurement velocity results, centerline, 200 psi mean pressure.	60
Figure 3.3.32: Simplex nozzle phase-locked dynamic measurement velocity results, radial 1.0 cm, 200 psi mean pressure.	60
Figure 3.3.33: Simplex nozzle phase-locked dynamic measurement count (%) results, centerline, 200 psi mean pressure.	61
Figure 3.3.34: Simplex nozzle phase-locked dynamic measurement count (%) results, radial 1.0 cm, 200 psi mean pressure.	61
Table 3.3.3: Summary of mean SMDs and axial velocities for static and dynamic testing, Simplex nozzle, 300 psi mean pressure.	62
Figure 3.3.35: Simplex nozzle phase-locked dynamic measurement SMD results, centerline, 300 psi mean pressure.	63
Figure 3.3.36: Simplex nozzle phase-locked dynamic measurement SMD results, radial 1.0 cm, 300 psi mean pressure.	63
Figure 3.3.37: Simplex nozzle phase-locked dynamic measurement axial velocity results, centerline, 300 psi mean pressure.	64
Figure 3.3.38: Simplex nozzle phase-locked dynamic measurement axial velocity results, radial 1.0 cm, 300 psi mean pressure.	64
Figure 3.3.39: Simplex nozzle phase-locked dynamic measurement count (%) results, centerline, 300 psi mean pressure.	65
Figure 3.3.40: Simplex nozzle phase-locked dynamic measurement count (%) results, radial 1.0 cm, 300 psi mean pressure.	65
Figure 3.3.41: Air-assist nozzle measurement locations.	67
Figure 3.3.42: Air-assist nozzle static measurement SMD results, axial location: 35 mm.	69

Figure 3.3.43: Air-assist nozzle static measurement axial velocity results, axial location: 35 mm.....	69
Figure 3.3.44: Air-assist nozzle static measurement SMD results, axial location: 60 mm.....	70
Figure 3.3.45: Air-assist nozzle static measurement axial velocity results, axial location: 60 mm.....	70
Figure 3.3.46: Air assist nozzle static measurement SMD results, axial location: 90 mm.....	71
Figure 3.3.47: Air-assist nozzle static measurement axial velocity results, axial location: 90 mm.....	71
Table 3.3.4: Summary of static and mean dynamic SMD and axial velocity measurements, air-assist nozzle for three axial and three radial positions. Static measurements shown for 125 psi and 150 psi cases. Radial 1 is 0.2 cm for 35 mm location, 0.3 cm for 60 mm location, and 0.5 cm for 90 mm location. Radial 2 is 0.4 cm for 35 mm location, 0.6 cm for 60 mm location, and 1.0 cm for 90 mm location.....	73
Figure 3.3.48: Air-assist nozzle phase-locked measurement SMD results, axial location: 35 mm, 135 psi mean pressure.....	74
Figure 3.3.49: Air-assist nozzle phase-locked measurement SMD results, axial location: 60 mm, 135 psi mean pressure.....	74
Figure 3.3.50: Air-assist nozzle phase-locked measurement SMD results, axial location: 90 mm, 135 psi mean pressure.....	75
Figure 3.3.51: Air-assist nozzle phase-locked measurement axial velocity results, axial location: 35 mm, 135 psi mean pressure.....	75
Figure 3.3.52: Air-assist nozzle phase-locked measurement axial velocity results, axial location: 60 mm, 135 psi mean pressure.....	76
Figure 3.3.53: Air-assist nozzle phase-locked measurement axial velocity results, axial location: 90 mm, 135 psi mean pressure.....	76
Figure 3.3.54: Air-assist nozzle phase-locked measurement count (%) results, axial location: 35 mm, 135 psi mean pressure.....	77
Figure 3.3.55: Air-assist nozzle phase-locked measurement count (%) results, axial location: 60 mm, 135 psi mean pressure.....	77
Figure 3.3.56: Air-assist nozzle phase-locked measurement count (%) results, axial location: 90 mm, 135 psi mean pressure.....	78
Figure 3.3.57: Experimental setup for spill-return nozzle.....	79
Table B.1: Transducer specifications for VACCG kerosene-fueled combustor.....	83
Table B.2: Filter Specifications for VACCG kerosene-fueled combustor.....	84
Figure C.1: Fuel system plumbing schematic for the VACCG kerosene-fueled combustor.....	84
Table C.1: Bypass valve settings for different atomizers [20].....	85
Figure C.2: Wiring schematic for the VACCG kerosene-fueled combustor control experiments.....	85
Figure D.1: Uncontrolled, GER=0.5.....	86
Figure D.2: Uncontrolled, GER=0.56.....	87
Figure D.3: Uncontrolled, GER=0.58.....	87
Figure D.4: Uncontrolled, GER=0.59.....	88
Figure D.5: Uncontrolled, GER=0.60.....	88
Figure D.6: Uncontrolled, GER=0.61.....	89
Figure D.7: Uncontrolled, GER=0.62.....	89
Figure D.8: Uncontrolled, GER=0.63.....	90
Figure D.9: Uncontrolled, GER=0.60.....	90
Figure D.10: Uncontrolled, GER=0.62.....	91

Figure D.11: Uncontrolled, GER=0.64.....	91
Figure D.12: Uncontrolled, GER=0.57.....	92
Figure D.13: Uncontrolled, GER=0.51.....	92
Figure D.14: Uncontrolled, GER=0.62.....	93
Figure D.15: Uncontrolled, GER=0.64.....	93
Figure D.16: Uncontrolled, GER=0.48.....	94
Figure D.17: Uncontrolled, GER=0.5.....	94
Figure D.18: Uncontrolled, GER=0.65.....	95
Figure D.19: Uncontrolled, GER=0.58.....	95
Figure D.20: Uncontrolled, GER=0.52.....	96
Figure E.1: GER=0.5, Controller delay=24, Gain=0.75.....	97
Figure E.2: GER=0.5, Controller delay=24, Gain=0.70.....	98
Figure E.3: GER=0.5, Controller delay=24, Gain=0.65.....	98
Figure E.4: GER=0.5, Controller delay=24, Gain=0.60.....	99
Figure E.5: GER=0.5, Controller delay=24, Gain=0.55.....	99
Figure E.6: GER=0.5, Controller delay=24, Gain=0.50.....	100
Figure E.7: GER=0.5, Controller delay=24, Gain=0.45.....	100
Figure E.8: GER=0.5, Controller delay=24, Gain=0.40.....	101
Figure E.9: GER=0.5, Controller delay=24, Gain=0.35.....	101
Figure E.10: GER=0.5, Controller delay=24, Gain=0.35.....	102
Figure E.11: GER=0.5, Controller delay=24, Gain=0.30.....	102
Figure E.12: GER=0.5, Controller delay=24, Gain=0.25.....	103
Figure E.13: GER=0.5, Controller delay=24, Gain=0.20.....	103
Figure E.14: GER=0.5, Controller delay=24, Gain=0.15.....	104
Figure E.15: GER=0.5, Controller delay=24, Gain=0.10.....	104
Figure E.16: GER=0.5, Controller delay=24, Gain=0.05.....	105
Figure E.17: GER=0.5, Uncontrolled.....	105
Figure E.18: GER=0.5, Controller delay=24, Gain=0.05.....	106
Figure E.19: GER=0.5, Controller delay=24, Gain=0.10.....	106
Figure E.20: GER=0.5, Controller delay=24, Gain=0.15.....	107
Figure E.21: GER=0.5, Controller delay=24, Gain=0.20.....	107
Figure E.22: GER=0.5, Controller delay=24, Gain=0.25.....	108
Figure E.23: GER=0.5, Controller delay=24, Gain=0.30.....	108
Figure E.24: GER=0.5, Controller delay=24, Gain=0.35.....	109
Figure E.25: GER=0.5, Controller delay=24, Gain=0.40.....	109
Figure E.26: GER=0.5, Controller delay=24, Gain=0.45.....	110
Figure E.27: GER=0.5, Controller delay=24, Gain=0.50.....	110
Figure E.28: GER=0.5, Controller delay=24, Gain=0.55.....	111
Figure E.29: GER=0.5, Controller delay=24, Gain=0.60.....	111
Figure E.30: GER=0.5, Controller delay=24, Gain=0.65.....	112
Figure E.31: GER=0.5, Controller delay=24, Gain=0.70.....	112
Figure E.32: GER=0.5, Controller delay=24, Gain=0.70.....	113
Figure E.33: GER=0.5, Controller delay=24, Gain=0.75.....	113
Figure E.34: GER=0.5, Controller delay=24, Gain=0.80.....	114
Figure E.35: GER=0.5, Controller delay=24, Gain=0.85.....	114
Figure E.36: GER=0.5, Controller delay=24, Gain=0.90.....	115
Figure E.37: GER=0.5, Controller delay=24, Gain=0.95.....	115
Figure E.38: GER=0.5, Controller delay=24, Gain=1.0.....	116

Figure E.39: GER=0.5, Controller delay=24, Gain=0.75.....	116
Figure E.40: GER=0.5, Controller delay=26, Gain=0.75.....	117
Figure E.41: GER=0.5, Controller delay=28, Gain=0.75.....	117
Figure E.42: GER=0.5, Controller delay=30, Gain=0.75.....	118
Figure E.43: GER=0.5, Controller delay=28, Gain=0.75.....	118
Figure E.44: GER=0.5, Controller delay=28, Gain=0.70.....	119
Figure E.45: GER=0.5, Controller delay=28, Gain=0.65.....	119
Figure E.46: GER=0.5, Controller delay=28, Gain=0.60.....	120
Figure E.47: GER=0.5, Controller delay=28, Gain=0.55.....	120
Figure E.48: GER=0.50, Controller delay=28, Gain=0.50.....	121
Figure E.49: GER=0.5, Controller delay=28, Gain=0.45.....	121
Figure E.50: GER=0.5, Controller delay=28, Gain=0.40.....	122
Figure E.51: GER=0.5, Controller delay=28, Gain=0.35.....	122
Figure E.52: GER=0.5, Controller delay=28, Gain=0.30.....	123
Figure E.53: GER=0.5, Controller delay=28, Gain=0.25.....	123
Figure E.54: GER=0.5, Controller delay=28, Gain=0.25.....	124
Figure E.55: GER=0.5, Controller delay=28, Gain=0.20.....	124
Figure E.56: GER=0.5, Controller delay=28, Gain=0.20.....	125
Figure E.57: GER=0.5, Controller delay=28, Gain=0.15.....	125
Figure E.58: GER=0.5, Controller delay=28, Gain=0.10.....	126
Figure E.59: GER=0.5, Controller delay=28, Gain=0.05.....	126
Figure E.60: GER=0.5, Uncontrolled.....	127
Figure E.61: GER=0.5, Controller delay=28, Gain=0.05.....	127
Figure E.62: GER=0.5, Controller delay=28, Gain=0.10.....	128
Figure E.63: GER=0.5, Controller delay=28, Gain=0.15.....	128
Figure E.64: GER=0.5, Controller delay=28, Gain=0.20.....	129
Figure E.65: GER=0.5, Controller delay=28, Gain=0.25.....	129
Figure E.66: GER=0.5, Controller delay=28, Gain=0.25.....	130
Figure E.67: GER=0.5, Controller delay=28, Gain=0.30.....	130
Figure E.68: GER=0.5, Controller delay=28, Gain=0.35.....	131
Figure E.69: GER=0.5, Controller delay=28, Gain=0.40.....	131
Figure E.70: GER=0.5, Controller delay=28, Gain=0.45.....	132
Figure E.71: GER=0.5, Controller delay=28, Gain=0.50.....	132
Figure E.72: GER=0.5, Controller delay=28, Gain=0.55.....	133
Figure E.73: GER=0.5, Controller delay=28, Gain=0.60.....	133
Figure E.74: GER=0.5, Controller delay=28, Gain=0.65.....	134
Figure E.75: GER=0.5, Controller delay=28, Gain=0.70.....	134
Figure E.76: GER=0.5, Controller delay=28, Gain=0.75.....	135
Figure E.77: GER=0.5, Controller delay=28, Gain=0.80.....	135
Figure F.1: Wiring diagram for nozzle measurements.....	136
Figure G.1: Simplex nozzle, 250 psi mean pressure ± 100 , centerline.....	137
Figure G.2: Simplex nozzle, 250 psi mean pressure ± 75 , centerline.....	138
Figure G.3: Simplex nozzle, 250 psi mean pressure ± 50 , centerline.....	138
Figure G.4: Simplex nozzle, 250 psi mean pressure ± 30 , centerline.....	139
Figure G.5: Simplex nozzle, 250 psi mean pressure ± 100 , radial 0.5 cm.....	139
Figure G.6: Simplex nozzle, 250 psi mean pressure ± 75 , radial 0.5 cm.....	140
Figure G.7: Simplex nozzle, 250 psi mean pressure ± 50 psi, radial 0.5 cm.....	140
Figure G.8: Simplex nozzle, 250 psi mean pressure ± 30 , radial 0.5 cm.....	141

Figure G.9: Simplex nozzle, 250 psi mean pressure ± 100 psi, radial 1.0 cm.	141
Figure G.10: Simplex nozzle, 250 psi mean pressure ± 75 , radial 1.0 cm.	142
Figure G.11: Simplex nozzle, 250 psi mean pressure ± 50 , radial 1.0 cm.	142
Figure G.12: Simplex nozzle, 250 psi mean pressure ± 30 , radial 1.0 cm.	143
Figure G.13: Simplex nozzle, 250 psi mean pressure ± 100 , radial 1.5 cm.	143
Figure G.14: Simplex nozzle, 250 psi mean pressure ± 75 , radial 1.5 cm.	144
Figure G.15: Simplex nozzle, 250 psi mean pressure ± 50 , radial 1.5 cm.	144
Figure G.16: Simplex nozzle, 250 psi mean pressure ± 30 , radial 1.5 cm.	145
Figure G.17: Simplex nozzle, 200 psi mean pressure ± 100 , centerline.	145
Figure G.18: Simplex nozzle, 200 psi mean pressure ± 75 , centerline.	146
Figure G.19: Simplex nozzle, 200 psi mean pressure ± 50 , centerline.	146
Figure G.20: Simplex nozzle, 200 psi mean pressure ± 30 , centerline.	147
Figure G.21: Simplex nozzle, 200 psi mean pressure ± 100 psi, radial 1.0 cm.	147
Figure G.22: Simplex nozzle, 200 psi mean pressure ± 75 , radial 1.0 cm.	148
Figure G.23: Simplex nozzle, 200 psi mean pressure ± 50 , radial 1.0 cm.	148
Figure G.24: Simplex nozzle, 200 psi mean pressure ± 30 , radial 1.0 cm.	149
Figure G.25: Simplex nozzle, 300 psi mean pressure ± 100 , centerline.	149
Figure G.26: Simplex nozzle, 300 psi mean pressure ± 75 , centerline.	150
Figure G.27: Simplex nozzle, 300 psi mean pressure ± 50 , centerline.	150
Figure G.28: Simplex nozzle, 300 psi mean pressure ± 30 , centerline.	151
Figure G.29: Simplex nozzle, 300 psi mean pressure ± 100 , radial 1.0 cm.	151
Figure G.30: Simplex nozzle, 300 psi mean pressure ± 75 , radial 1.0 cm.	152
Figure G.31: Simplex nozzle, 300 psi mean pressure ± 50 , radial 1.0 cm.	152
Figure G.32: Simplex nozzle, 300 psi mean pressure ± 30 , radial 1.0 cm.	153
Figure G.33: Air-assist nozzle, 135 psi mean pressure ± 10 , axial 35 mm, centerline.	153
Figure G.34: Air-assist nozzle, 135 psi mean pressure ± 10 , axial 35 mm, radial 0.2 cm.	154
Figure G.35: Air-assist nozzle, 135 psi mean pressure ± 10 , axial 35 mm, radial 0.4 cm.	154
Figure G.36: Air-assist nozzle, 135 psi mean pressure ± 10 , axial 60 mm, centerline.	155
Figure G.37: Air-assist nozzle, 135 psi mean pressure ± 10 , axial 60 mm, radial 0.3 cm.	155
Figure G.38: Air-assist nozzle, 135 psi mean pressure ± 10 , axial 60 mm, radial 0.6 cm.	156
Figure G.39: Air-assist nozzle, 135 psi mean pressure ± 10 , axial 90 mm, centerline.	156
Figure G.40: Air-assist nozzle, 135 psi mean pressure ± 10 , axial 90 mm, radial 0.5 cm.	157
Figure G.41: Air-assist nozzle, 135 psi mean pressure ± 10 , axial 90 mm, radial 1.0 cm.	157

Glossary

Global Equivalence Ratio (GER)—The ratio of fuel to air entering the combustor divided by the stoichiometric fuel to air ratio.

Saturation—In this thesis saturation is used to describe the characteristic of a continuous signal that extends beyond either the maximum or minimum allowable value resulting in clipping of the signal.

Sauter Mean Diameter (SMD)—A representative diameter used to characterize the fineness of a collection of droplets for combustion applications. The SMD is calculated by

$$SMD = D_{32} = \frac{\sum N_i d_i^3}{\sum N_i d_i^2}$$

where d_i is the measured droplet diameter. SMD is generally given in μm .

Chapter 1. Introduction

1.1. Background

The increase in active combustion control in recent years is a result of changes in the gas turbine industry. Due to environmental concerns about the production of nitrogen oxides (NO_x) by traditional diffusion flame combustors the gas turbine industry has moved to lean pre-mixed combustors. Although lean pre-mixed combustors are effective at reducing NO_x emissions they are also susceptible to thermo-acoustic instabilities that can cause equipment damage, reduce combustor efficiency, increase emissions, and cause flame blow out. Thermo-acoustic instabilities result from a self-excited coupling between the heat release rate of the flame and the acoustics within the combustion chamber, which converge to limit-cycle behavior.

There are two broad categories of methods to control combustion instabilities: passive and active control. Passive control techniques include changing the geometry of the combustion chamber and limiting the engine to operation conditions that avoid combustion instabilities. However, these methods are not guaranteed to be effective and may not allow emissions or power output goals to be reached. Active Combustion Control (ACC), on the other hand, allows greater flexibility for regulating instability, power level, and emissions control. Methods of ACC have primarily focused on decoupling the thermo-acoustic instability and the heat release of the flame through primary fuel modulation designed to control the heat release of the flame.

Primary fuel modulation, as it is used in this thesis, refers to modulation of the mass flow rate of the liquid fuel entering the combustor. Modulating the mass flow rate of the fuel often affects the heat release rate of the fuel nonlinearly by changing other properties of the fuel spray beyond the mass flow rate. For example, using a proportional valve to modulate the primary fuel mass flow rate also changes the fuel pressure; the spray properties of many atomizers are dependant on the fuel pressure. The three primary factors affecting the heat release rate of the flame are fuel mass flow rate, the droplet sizes within the spray, and the fuel to air ratio. This thesis focuses on the characteristics of ACC for a liquid-fuel system using a proportional primary fuel modulation system developed by Schiller [20]. Also, the effect of proportional modulation on the spray characteristics of two different atomizers is investigated.

1.2. Motivation

The Virginia Active Combustion Control Group (VACCG) has researched ACC for several years, beginning in 2000 with the work of Lagimaniere [15]. In 2003, Schiller [20] developed a new fuel modulation system and had limited success stabilizing the thermo-acoustic instabilities found in the VACCG liquid fuel rig using a simple phase shift controller. Unfortunately, stability could not be gained beyond the edge of the combustors instability region and achieving steady-state stabilization was problematic. By making changes to the control system the effectiveness of the controller was greatly increased, allowing the behavior of the controller and fuel modulation system to be characterized. Of particular interest were the limitations of primary fuel modulation and the effect that the corresponding pressure oscillations had on the fuel spray. To better understand the results of

this work, a review of other ACC systems that are developed in the literature is necessary. It is also necessary to review research on the mechanism of atomization for different fuel nozzles to understand the effect of fuel pressure oscillations on their spray properties.

1.3. Literature Review

This section is divided into two parts: Active Combustion Control and Atomization. The Active Combustion Control section presents a representative sample of active combustion control experiments, their results, and analysis of these results. The Atomization section presents an overview of the atomizers used for experiments in Chapter 2 and Chapter 3.

1.3.1. Active Combustion Control

Many different ACC systems have been developed for the purpose of suppressing thermo-acoustic instabilities in gas turbine engines. This review focuses almost exclusively on those experiments with liquid fuel combustors. Because each combustor is different the results obtained by other researchers in this field are highly dependant on the specific combustors characteristics, controller design, and control hardware that was used. Some information about the experimental setup of each case will be given to provide a context for the result, however, explicit information about each case can be found in the corresponding references.

One of the first successful liquid fuel ACC systems was designed and built by Hermann et al. [12] in 1995. In this system primary fuel modulation was used to suppress a 360 Hz oscillation in a single-nozzle diesel-fueled turbulent laboratory combustor. The primary fuel modulation system consisted of two piezoelectric driven pistons to proportionally modulate the fuel flow to the atomizer. The control system was setup so that oscillations in either the combustor pressure or the heat release (measured using a photo-multiplier) could be used as the input to the phase shift controller. Two experiments were conducted at an equivalence ratio of 0.95, one using the combustor pressure as the input to the controller and the other using the heat release measurement as the input to the controller. The amplitude of the fundamental instability frequency for the uncontrolled combustor at this equivalence ratio was 140 dB. Both experiments successfully suppressed the fundamental instability frequency by 40 dB, and the peak frequency by 15 dB. Hermann et al. [12] concluded that using the heat release measurement as the input to the controller was more effective for controlling combustion instabilities because it is more closely linked to the heat release, which is the property that is directly affected by fuel pressure oscillations.

The secondary excitations that can result by using a phase shift controller to suppress thermo-acoustic instabilities were studied by Hathout et al. [11] in 1997. A combustor model was created to simulate experiments on a propane-fueled premixed laboratory combustor. The combustor pressure was used as the input to a phase shift controller, which was used to drive a loud speaker. The phase shift controller used was an all-pass filter. This study is included here because secondary peaks in the combustor pressure power spectrum occur in experiments with both liquid-fuel and gaseous-fuel combustors and when the control system uses fuel modulation or pressure modulation (using a loudspeaker). Hathout et al. [11] concluded that secondary peaks occur the combustor pressure power spectrum when a phase shift controller is used to suppress the fundamental instability peak because the phase shift controller is not tuned for a wide range of frequencies—but rather for the single instability frequency. In other words, because the phase shift controller is tuned for only one

frequency, mechanisms in the combustion process and the control process outside of the mechanisms that create or suppress the instability interact. Specifically, the authors attribute secondary peak formation to an interaction between the controller system and the flame dynamics, the stable acoustic modes, and antiresonance in the combustor. Also, the frequencies that secondary peaks occur at are dependant on the filter settings within the control system.

In 1998, ACC experiments were performed on a Siemens Model V84.3A ring combustor with two fundamental instability frequencies (217 Hz and 433 Hz) by Sueme et al. [21]. The V84.3A combustor is a premixed gaseous combustor with pilot diffusion flames. The ACC system used the combustor pressure measurement, a phase shift controller, and a high speed direct drive MOOG valve. In this case the MOOG valve was used to control the pilot flame associated with each burner. The V84.3A combustor has 24 burners arranged in a circle, which initially required that each burner have its own control system (sensor, controller, and valve) due to the difference in pressure modes at each location. On further investigation Sueme et al. [21] found that only six different control systems were required because the pressure modes at burners located 90° apart were identical. Using this ACC system, the peak of the second instability (433 Hz) was suppressed by 17 dB. However, Sueme et al. [21] found that only one dominant frequency could be suppressed at a time. It was also found that the phase and gain settings that successfully suppressed the instability were a function of the combustor operating conditions (power level and pilot gas fraction).

Cohen et al. [5] conducted ACC experiments on a single-nozzle diesel-fueled pre-mixed flame tube combustor in 1999. The fuel nozzle consisted of six “spokes” with high pressure spray tips inside of a pre-mixing chamber. For the experiments one of the fuel spokes was separated from the main fuel supply and actuated with a high speed solenoid valve. The combustors instability ranged from 180 Hz to 220 Hz depending on the operating conditions used. Also, the magnitude of the instability grew with a decreasing equivalence ratio. Two experiments were conducted to test the control system. In the first experiment open loop forcing of the solenoid valve was used. The various control signals that were tried were Pulse Width Modulated (PWM) signals at different frequencies, all with a duty cycle of 50%. However, these experiments were unsuccessful. In the second experiment the system was set up so that specific “threshold” levels of the combustor pressure signal were used to create a PWM signal, making the frequency of the control signal self-tuning. A user controlled time delay (phase shift) was also added to the control system. A bandpass filter was used to clean the combustor pressure signal. Testing of equivalence ratios from 0.47 to 0.56 typically resulted in an instability suppression of 15 dB using this control scheme. NO_x measurements also showed that lower NO_x quantities were created when the controller was used to suppress the instability. Cohen et al. [5] concluded that the lower NO_x measurements resulted from a decrease in temporal hot spots during experiments where the instability was suppressed.

Also in 1999, Banaszuk et al. [1,2] used data collected from United Technologies Research Center (UTRC) combustors to create models of the combustors operating with an ACC system. Two combustors were considered, one a single-nozzle combustor and the other a three-nozzle sector combustor. The UTRC combustors considered had higher instability amplitudes with decreasing equivalence ratio. The control scheme for these combustors used combustor pressure as the input to the phase shift controller. Additionally, two fuel

modulation methods were used; the first was proportional fuel modulation and the second on-off control (PWM signal). When considering how to model the combustor behavior, Banaszuk et al. [1,2] found that higher equivalence ratio cases could be best modeled as a linear, stable, noise-driven system. The power spectrums from experiments and modeling efforts of the combustors with proportional fuel modulation showed peak splitting for cases where the fundamental instability was suppressed. Using the linear model with proportional fuel modulation, Banaszuk et al. [1,2] concluded that the cause of secondary resonances (peak splitting) is a large delay in the plant (combustion process) that results in positive feedback at frequencies above and below the attenuation band. Additionally, limited actuator bandwidth focused on the fundamental instability frequency contributes to the creation of secondary resonances. At low equivalence ratios, the linear plant model could not be used to fit the experimental data from the UTRC combustors. The on-off fuel modulation could also not be modeled linearly. Using random input describing function analysis, Banaszuk et al. [1,2] conclude that on-off actuation can be modeled as saturated proportional actuation, and that the causes of peak splitting in the higher equivalence ratio linear model hold for the lower equivalence ratio nonlinear system.

In 2000, Murugappan et al. [17] developed an ACC system with an automated phase shift controller designed to find the optimum phase setting based upon feedback from the combustor pressure signal. The single-nozzle ethanol-fueled swirl-stabilized laboratory combustor had an instability at 220 Hz with increasing amplitude for decreasing equivalence ratio. The system used a simplex nozzle and 45° air swirlers. The fuel was modulated by an automotive fuel injector. A bandpass filter was also used to isolate frequencies between 150 Hz and 350 Hz in the combustor pressure signal. Additionally, a perturbation signal had to be added to the combustor pressure signal for the controller to operate properly. The automated phase shift controller could successfully find the optimum phase (determined by manual testing) in a very short period of time, < 2 sec. Murugappan et al. [17] tested the stability boundaries for the controller gain, which was manually controlled, and found that stability could not be attained for gains below 1 or higher than 5 in their experiment. At the higher gains the combustor jumped between the stable and unstable modes without reaching steady-state, which Murugappan et al. [17] attributed to the introduction of large delays into the system.

An adaptive controller was also designed by Johnson et al. [14] in 2000. The n-Heptane (C_7H_{16}) fueled combustor used for the experiments showed an increase in instability amplitude as equivalence ratio was increased. The primary instability frequency was 400 Hz. The proportional fuel modulation was accomplished with an adjustable atomizer, which consisted of a magnetostrictive rod attached to a pintle located in the exit orifice of the atomizer could be actuated to change the flow rate of the fuel. Only 10% to 20% of the total fuel flow was modulated during the experiments. The adaptive phase shift controller was successful in reducing pressure oscillation amplitude by up to 50%, but controllability degraded as the equivalence ratio was raised. At an equivalence ratio of 0.75 a 50% reduction was possible, while at an equivalence ratio of 1.0 only a 25% reduction in pressure oscillation amplitude was possible. Johnson et al. [14] also noted that the phase used to suppress the instability increased with increasing equivalence ratio.

A unique ACC system was designed by Barooah et al. [3] in 2003. A spinning valve actuator was designed to proportionally modulate fuel for a laboratory combustor. Experiments were

done on a Jet A-fueled single-nozzle combustor. The primary instability of this combustor was at 280 Hz and the nozzle used was a prefilming airblast atomizer. The combustor pressure signal was used as the input to a phase shift controller. The combustor pressure signal was bandpass filtered before the phase shift controller, however. Using this setup, Barooah et al. [3] successfully suppressed the instability amplitude by a factor of ten. Peak splitting occurred, making the reduction in peak frequency only a factor of three. Additionally, problems with the actuation system caused phase drift to occur during experiments.

In 2003, Cohen et al. [6] reviewed the ACC work published in the literature and made an overview of factors affecting ACC. They grouped these factors into four areas: combustor dynamics, the actuation system, sensing, and the control algorithm. The combustor dynamics that most affect ACC include whether the system is a limit cycling or a noise driven system, how many unstable modes exist, and how the system changes as a function of combustor operating conditions. Within the control system, from sensing to actuation, the most significant ACC system limitation comes from large time delay (relative to the acoustic period). Large time delays can come from many sources, in particular: filtering of the combustor pressure signal (when it is used as the control signal), and the length of fuel lines between the actuator and the injector. Cohen et al. [6] argue that time delay is especially bad because it shrinks the frequency band of controllability. Other controllability limitations can arise from the bandwidth of the actuator, and peak splitting. Cohen et al. [6] also attribute peak splitting to time delay in the control system. High controller gain settings can accentuate peak splitting. Cohen et al. [6] also note that the quality of fuel mixing affects the success of an ACC system. Good fuel mixing resulted in better instability amplitude reduction for the experiments that they reviewed.

This literature review covered the results of experiments from many different researchers. The characteristics of their results are a good reference point for considering the results of the experiments covered in Chapter 2 of this document.

1.3.2. Atomization

The two types of atomizers measured in this thesis have different spray characteristics due to the droplet formation mechanism that occurs. The simplex nozzle will be examined first followed by the air-assist nozzle. There has been a lot of research done on both of the nozzles to determine the effect of various parameters on the resulting spray. Since the research in this thesis is concerned with the effect of dynamic modulation the background on the factors influencing atomization will be limited to those parameters relevant to the experimental variables tested in chapter 3. For further information on the many of factors affecting the static spray characteristics for both atomizers see Lefebvre [16]. A limited amount of research has been done on dynamically modulated single fluid nozzle sprays and none were found for twin fluid nozzles.

Lefebvre's comprehensive summary of atomization research in 1989 [16] is still a leading authority on atomization research today. Research on simplex nozzles has shown that the atomization process is very complex. The main factors governing the quality of atomization are the liquid supply pressure, the physical properties of the air or gas that the liquid is injected into, and the size of the nozzle that is used. However, the liquid supply pressure has

the largest effect on the spray fineness because increasing the supply pressure leads to an increase in the discharge velocity of the liquid, which in turn leads to a finer spray. The SMD of the resulting spray is related to the liquid supply pressure as shown in Equation 1.3.1.

$$SMD \propto \Delta P_L^d \quad \text{Equation 1.3.1}$$

where d is an experimentally determined exponent. Different researchers have found d to range from -0.28 to -0.44.

Chang et al. [4] dynamically modulated both a simplex nozzle and a spill-return nozzle. The simplex nozzle was actuated at frequencies greater than 10 kHz. The frequency of the modulation was found to change the mean SMD and mean velocity of the droplets. Because the spray properties of the simplex nozzle are pressure dependant, a dynamically actuated spill-return assembly was designed for testing; the assembly is shown in Figure 1.3.1.

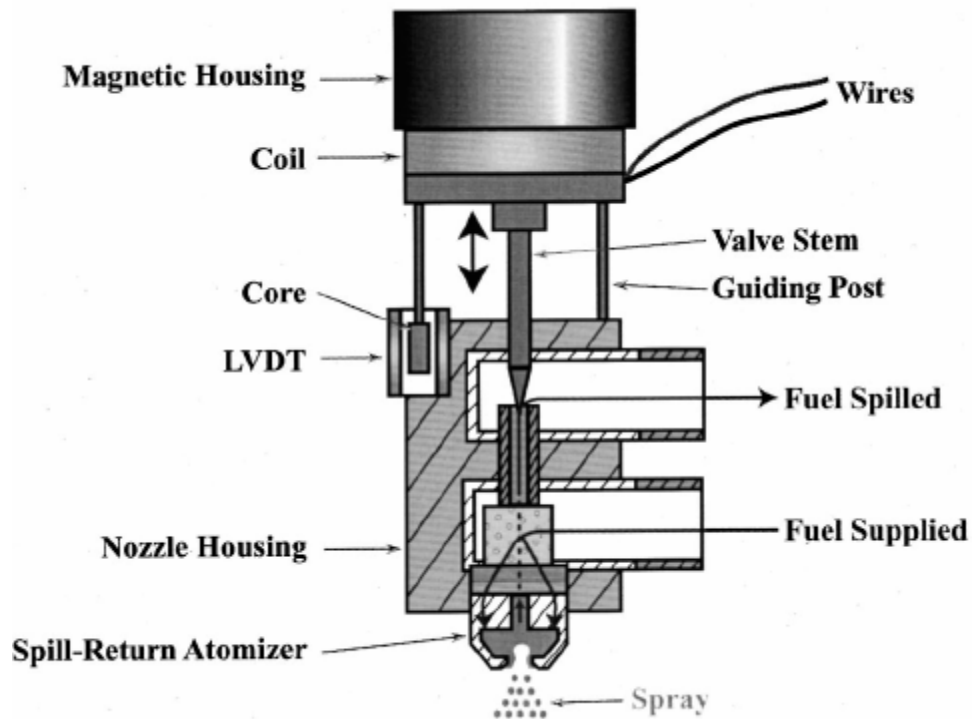


Figure 1.3.1: Dynamically modulated spill-return nozzle, Chang et al. [4].

Measurements of the dynamically modulated spill-return atomizer showed that the mean droplet sizes and velocities were not affected by the modulation. However, vortical structures developed in the spray the scale of which was frequency dependant. Laser sheet images of the internal spray patterns for static, 100 Hz, and 400 Hz modulation are shown in Figure 1.3.2. The Phase Doppler location in the image is located 19 mm from the nozzle.

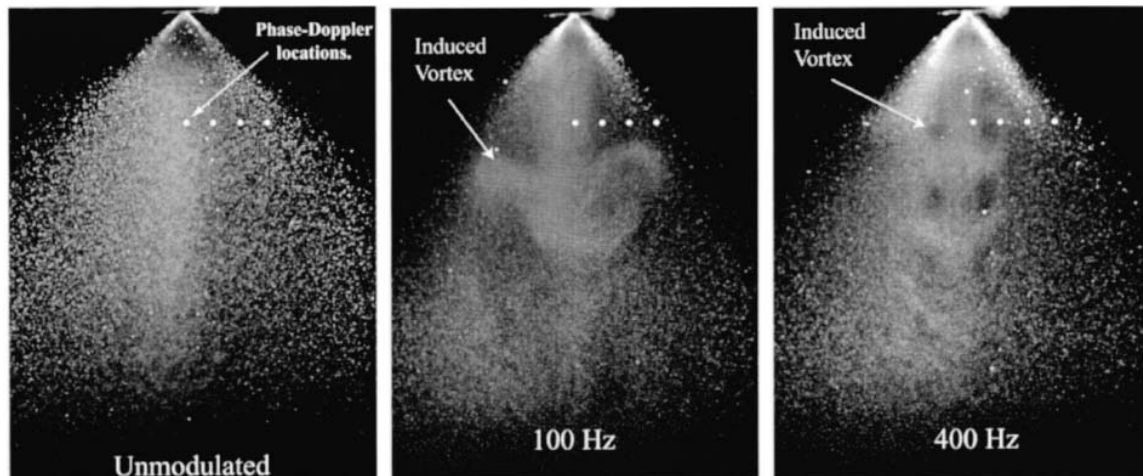


Figure 1.3.2: Laser sheet images of static and dynamically modulated spill-return spray, Chang et al. [4].

Lefebvre's [16] summary of air-assist nozzles (also called internally mixed airblast atomizers) found that for low viscosity liquids the mean drop size is inversely proportional to the relative velocity between the air and liquid. Also for low viscosity liquids, the atomizer geometry does not significantly influence the spray properties.

In 2001 Oh et al. [18] measured the spray properties of an air-assist nozzle. The cold flow measurements showed that the smallest SMD and highest axial velocity occurred at the centerline. The largest droplets and smallest mean velocities occurred at the periphery of the spray. They also found that the largest percentage of droplets occurred at the centerline. They conclude that the small droplets at the centerline more quickly reach a dynamic equilibrium with the air flow, accounting for the higher velocities.

The static measurements of the simplex nozzle and air-assist nozzle discussed in chapter 3 correspond to the results found in the literature. There is not a lot of dynamically modulated research in the literature for the simplex nozzle, and none that was found for the air-assist nozzle. In particular, no literature was found comparing different modulation amplitudes for the simplex nozzle.

1.4. Thesis Overview

1.4.1. Contributions of the Thesis

In the first half of the work control experiments are successfully carried out on a kerosene-fueled unstable combustor. The control experiments are divided into three regions that are identified by the degree of control signal saturation. Controller settings are mapped for several different global equivalence ratios and an equivalence ratio dependent trend is found. A hysteresis behavior is also shown that differentiates the controller settings that will maintain stability of the system and those that will gain stability of the unstable system. This work shows that a simple phase shift controller is flexible enough to stabilize a large range of unstable operating conditions. Control signal saturation is also uniquely identified as the reason for diminished—and ultimately lost—controllability of the unstable system. The

saturation effects and hysteresis phenomenon are important additions to the understanding of active combustion control systems.

The second half of the work focuses on the impact of proportional primary fuel modulation on the characteristics of the fuel spray. The spray characteristics of the simplex nozzle used for the first half of the work is investigated as well as an air-assist nozzle using a water spray and a Phase Doppler Anemometry measurement system. Different amplitudes of supply pressure modulation were tested to simulate different levels of gain for the active combustion control system. The dynamic measurement results for the simplex nozzle reveal that changes in gain may cause a change in phase for the fuel spray droplet sizes and axial velocities. A change in the structure of the spray is also observed for the large amplitude modulation cases. Understanding the effect of the proportional modulation on the fuel spray is as important to the understanding of active combustion control as understanding the control system behavior. This work raises more questions about the dynamic characteristics of the spray than it answers. However, these results suggest that the proportional modulation input does not result in a proportional effect on the spray characteristics.

1.4.2. Thesis Organization

The remainder of the thesis describes the active combustion control experiments carried out on the VACCG kerosene-fueled combustor with a piezoelectric actuated primary fuel modulation system and phase shift controller as well as the impact of the types of control signals used on the fuel spray. Chapter 2 presents the results of the control experiments on the combustor including limitations of the system including the effects of saturation. Chapter 3 presents the results of measurements on two different atomizers. Both static and dynamic operating conditions are presented for the simplex nozzle that was used for experiments in chapter 2 and an air-assist nozzle. Chapter 4 presents a summary of the work and also suggestions for future work.

Chapter 2. Controlling Combustion Instabilities

2.1. Combustor Specifications

2.1.1. Hardware and Software

The work in this chapter was performed on the VACCG kerosene-fueled combustor with a piezoelectric actuated primary fuel modulation system and phase shift controller. The VACCG kerosene-fueled combustor, designed by Wajid Chishti, is shown in Figure 2.1.1. The fuel modulation system and controller were designed by Noah Schiller. A block diagram of the physical hardware and control system is shown in Figure 2.1.2.



Figure 2.1.1: VACCG kerosene-fueled combustor [20].

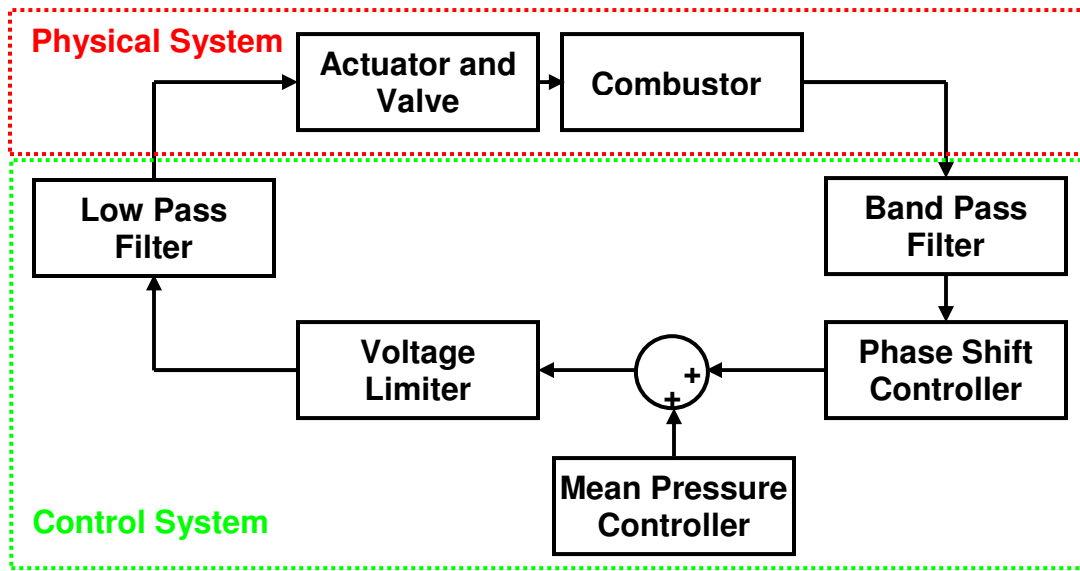


Figure 2.1.2: Diagram of the Physical System and Control System for the VACCG kerosene-fueled combustor.

The physical system shown in Figure 2.1.2 includes the combustion process, fuel and air delivery systems, and the fuel modulation system. The control system includes the phase shift controller, mean pressure controller, and all of the required signal processing associated with these controllers. The physical system will be described first, followed by the control system.

The combustor block comprises the effects of atomization, fuel and air mixing, and combustion process. The atomizer used for the experiments in this chapter was a Delavan 60° solid-cone simplex nozzle with a 1 gph flow rate [10]. The spray enters the combustor in a swirling air stream, which is created by a set of 45° swirl vanes. The 100 psi air compressor can provide up to 70 scfm. The combustor has 3 quartz windows to allow visual access to the flame. The top half of the 51 in. chimney is water cooled.

The actuator used is a 500 μm displacement piezoelectric stack manufactured by Piezomechanik GmbH [19]. The valve is a bellows sealed valve manufactured by Swagelok [22]. The actuator and valve are capable of regulating the fuel pressure into the combustor between 0 and 600 psi, the maximum fuel pump supply pressure, at the combustor instability frequency. Due to atomization effects the minimum fuel pressure used is 100 psi. The maximum fuel pressure used is 550 psi. The fuel pump is a BSM No. 10 gear pump, which is capable of providing up to 35 gph of fuel.

The band pass filter and low pass filter used were analog signal processing filters. The filter settings for both of these filters had a profound effect on the controller's ability to stabilize the thermo-acoustic instability. These effects will be discussed further in Section 2.1.3.

The phase shift controller, mean pressure controller, and voltage limiter were all included in the controller code; the relevant code is shown in Appendix A. A DSpace DAQ board (A/D

and D/A) and the associated software were used for the controller. The mean pressure controller is necessary to regulate the mean fuel pressure entering the combustor because of pressure drift in actuation system attributed to very slight movements in the actuator positioning hardware and fluctuations in the supply pressure. The mean pressure controller monitors the fuel pressure downstream of the actuated valve and adjusts the mean voltage to the actuator until the desired mean pressure and the sensed mean pressure match. The phase shift controller uses the combustor pressure signal as its input and applies a manually set delay and gain to the signal to create the phase shift controller control signal. The control signals generated by the mean pressure controller and the phase shift controller are added together to create a composite control signal. This signal passes through a voltage limiter, which prevents the controller from overdriving the actuator's amplifier. For the experiments in this thesis, the control signal voltage is limited between 0 and 3.5 V.

A list of the sensors used is shown in Appendix B. A wiring diagram is shown in Appendix C. Additional information about the fuel modulation system is provided by Schiller [20].

2.1.2. Uncontrolled System Characteristics

The uncontrolled VACCG kerosene-fueled combustor exhibited three distinct regions of operation. Photographs of the flame in these three regions are shown in Figure 2.1.3. In the stable region ($GER < 0.48$) the flame is relatively quiet, blue and compact with a peak SPL amplitude of 130 dB. In the first unstable region ($0.48 < GER < 0.75$) the flame has turbulent orange fingers extending upward from the central blue cone caused by poor mixing and has a peak SPL amplitude of 164 dB at its limit cycle frequency. The control experiments in this thesis focus on this first unstable region. In particular, a stable flame looked like Figure 2.1.3a and an unstable flame looked like Figure 2.1.3b. The flame in the second unstable region ($GER > 0.75$) was blue again and became very diffuse but still had a peak SPL amplitude near 164 dB. The flame in the second unstable region is not dealt with in this thesis.

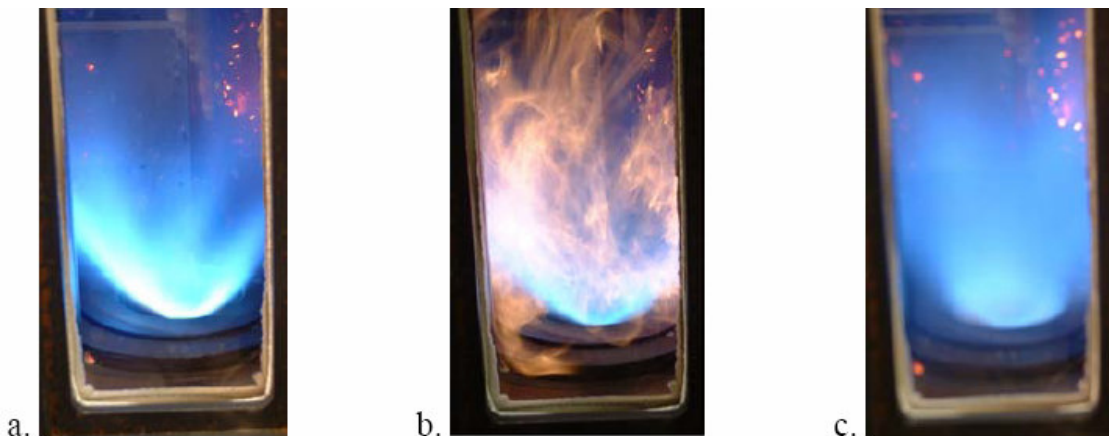


Figure 2.1.3: a. Photograph of the flame in the stable region ($GER < 0.48$). b. Photograph of the flame in the first unstable region ($0.48 < GER < 0.75$). c. Photograph of the flame in the second unstable region ($GER > 0.75$), [20].

The flame in the first unstable region had several characteristics that changed with GER. Two characteristics of particular note are the limit cycle frequency and the amplitude of the second harmonic. The limit cycle frequency versus GER is shown in Figure 2.1.4. The

frequency of the limit cycle begins at 120 Hz at a GER of 0.48 and increases by 8 Hz as the GER is raised from 0.48 to 0.65. The data points in Figure 2.1.4 were taken over the span of several months where uncontrolled experimental variables (e.g. air temperature) may affect the systems behavior. The amplitude of the second harmonic versus GER is shown in Figure 2.1.5. The variability in the data points in Figure 2.1.5 can also be accounted for by small variations in the uncontrolled operating conditions of the combustor over several months. The power spectrums for the data points in Figure 2.1.4 and Figure 2.1.5 are included in Appendix D.

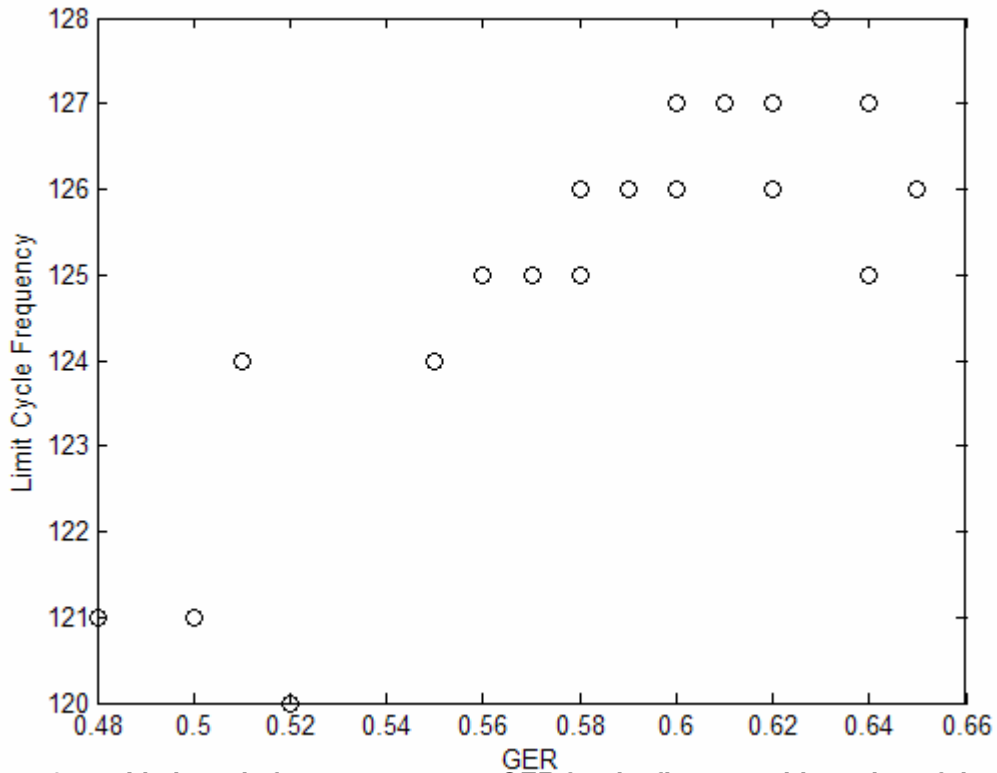


Figure 2.1.4: Limit cycle frequency versus GER for the first unstable region of the VACCG kerosene-fueled combustor.

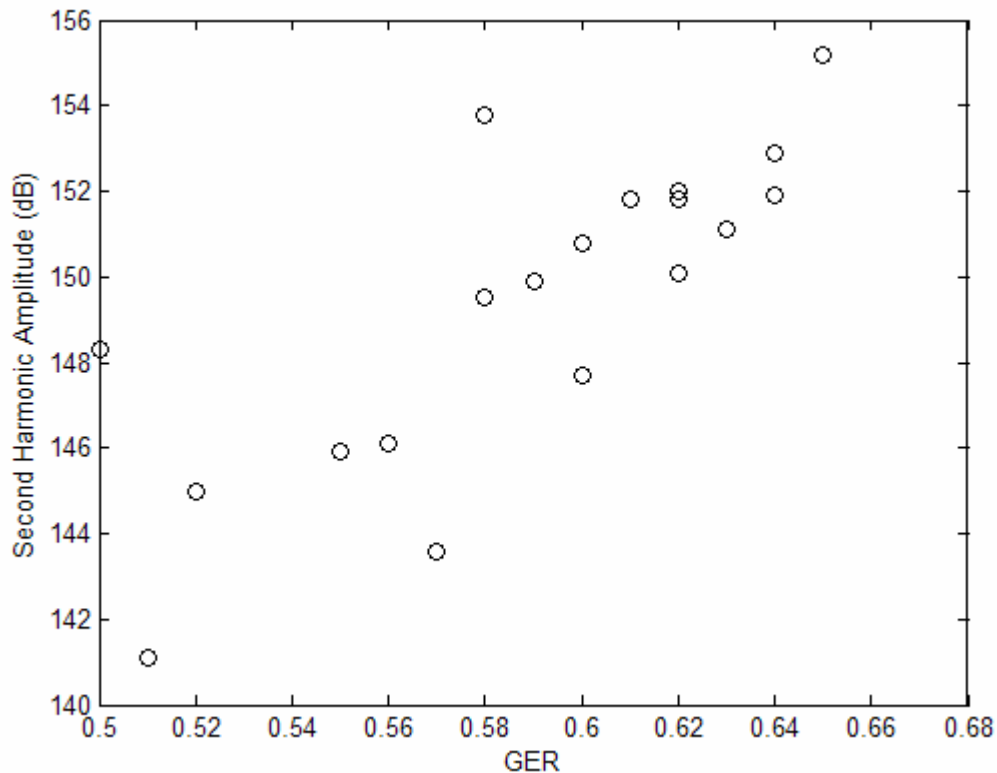


Figure 2.1.5: Second Harmonic Amplitude, SPL (dB), versus GER for the first unstable region of the VACCG kerosene-fueled combustor.

2.1.3. The Effect of Filter Settings

Four different configurations of filter settings were used in preliminary experiments. The four combinations of filter settings and the resulting authority of the controller are shown in Table 2.1.1. The band pass filter is composed of an analog low pass filter and an analog high pass filter. A band pass filter setting of ‘none’ is a system configuration without the band pass filter. The lower band pass filter setting number is the high pass filter setting and the higher number is the low pass filter setting. The magnitude and frequency characteristics for the 100-160 Hz band pass filter setting are shown in Figure 2.1.6. Two different low pass, or smoothing, filter settings were used. The magnitude and phase characteristics for both the 150 Hz and 1500 Hz filter settings are shown in Figure 2.1.7. The range of GERs that could be stabilized by the phase shift controller depended on the filter settings used; the ranges for different configurations are shown in Table 2.1.1. The largest range of stability was achieved with configuration 4. Power spectrums for the stabilized system at a GER of 0.5 for both Configuration 2 and 4 are shown in Figure 2.1.8. Power spectrums for the stabilized system at a GER of 0.5 for both Configuration 3 and 4 are shown in Figure 2.1.9. Removing the band pass filter from the system (configuration 4 versus 2) moves the primary peak of the stabilized system from the uncontrolled limit cycle frequency to a higher frequency, with a secondary peak at a lower frequency. Similarly, changing the low pass filter setting from 150 Hz to 1500 Hz (configuration 4 versus 3) also shifts the primary peak away from the uncontrolled limit cycle frequency.

Table 2.1.1: Configurations of filter settings used in preliminary experiments.

Configuration	Band Pass Filter Settings	Low Pass Filter Setting	GERs Stabilized
1	100-160 Hz	150 Hz	0.48-0.52
2	100-160 Hz	1500 Hz	0.48-0.52
3	None	150 Hz	0.48-0.55
4	None	1500 Hz	0.48-0.67

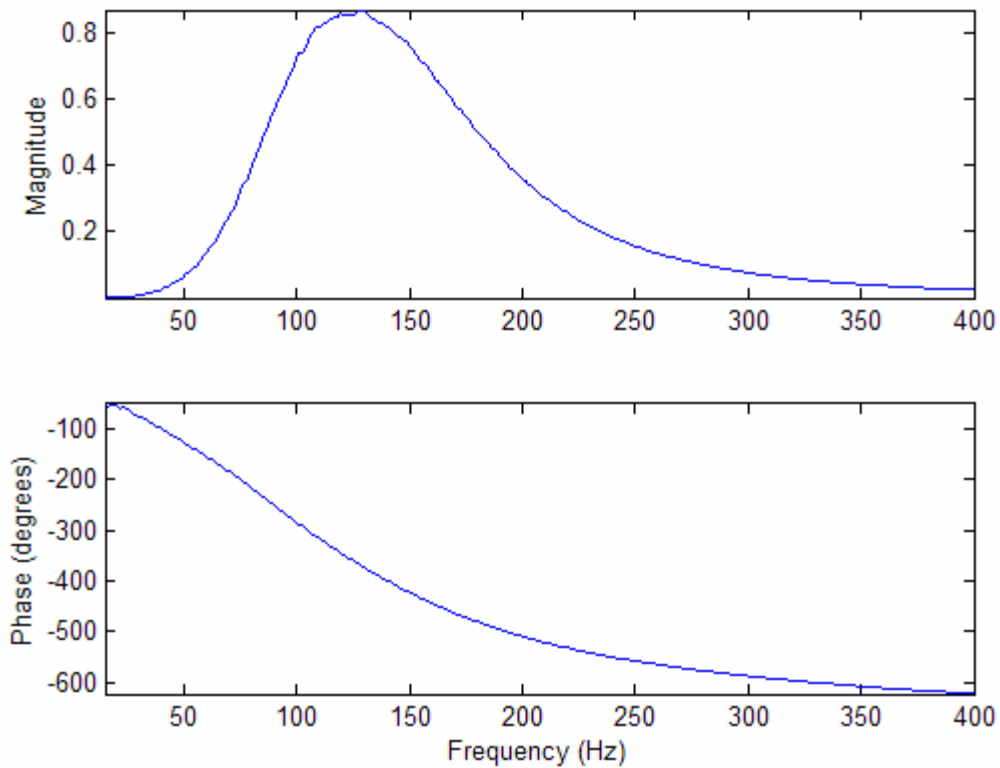


Figure 2.1.6: Magnitude and phase characteristics of the band pass filter with 100-160 setting.

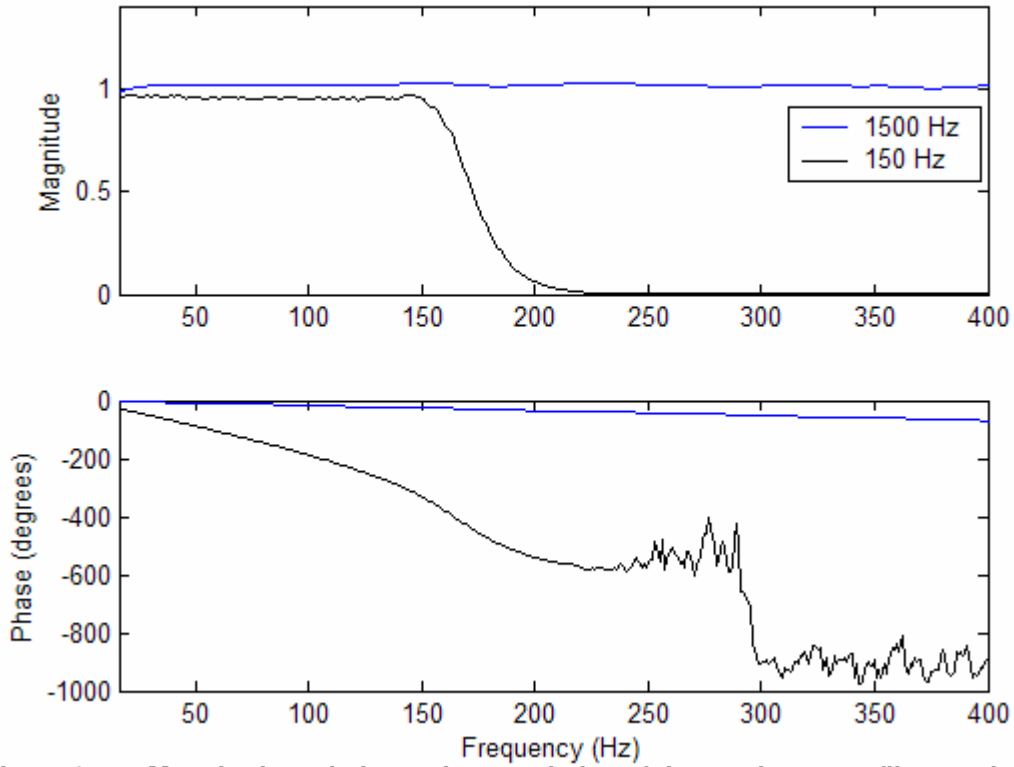


Figure 2.1.7: Magnitude and phase characteristics of the two low pass filter settings.

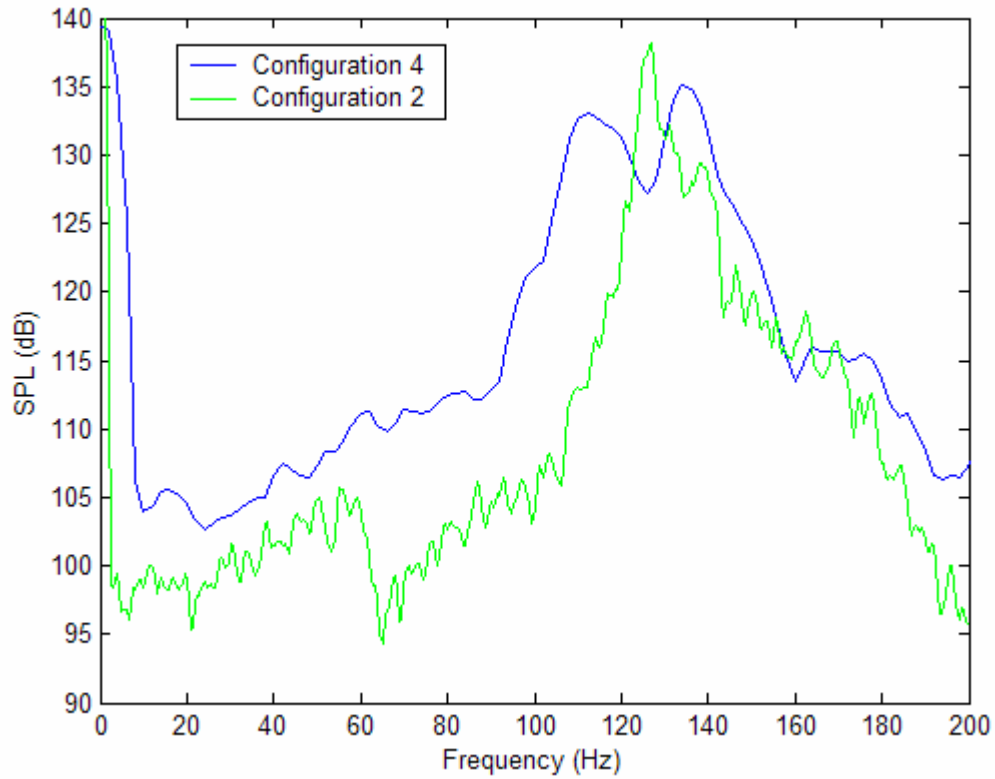


Figure 2.1.8: Comparison of stabilized system power spectrum fundamental peaks for GER=0.5 with and without the band pass filter, low pass filter setting of 1500 Hz. Power spectrum for configuration 2 (with bandpass) taken before bandpass filter.

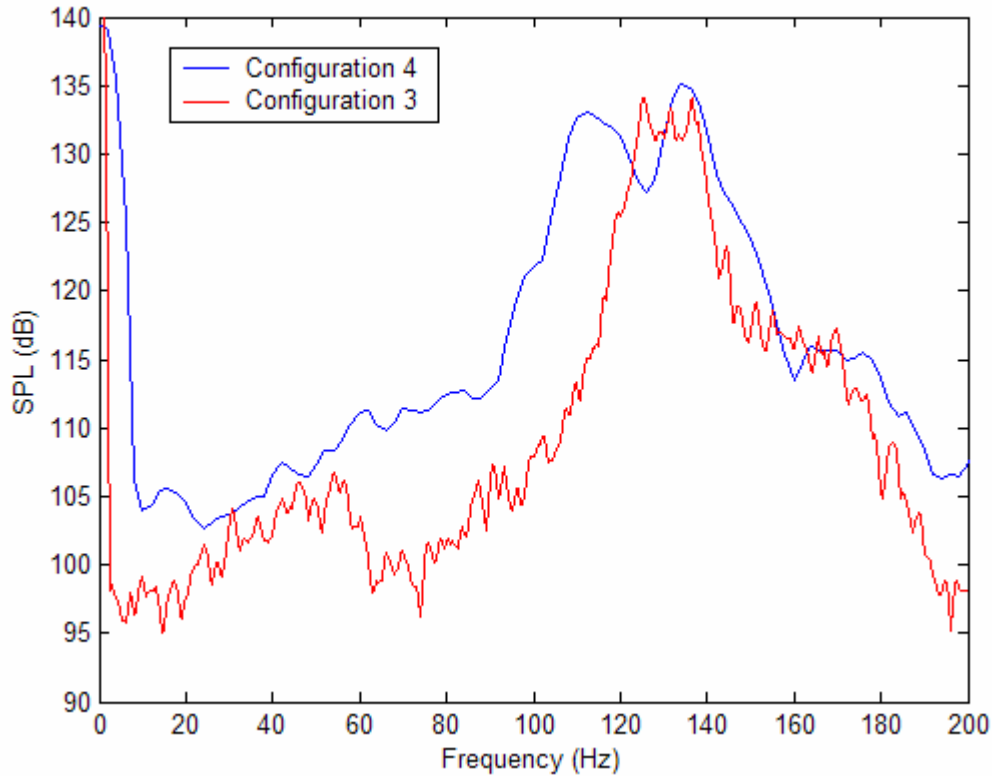


Figure 2.1.9: Comparison of stabilized system power spectrum fundamental peaks for GER=0.5 without the band pass filter, low pass filter settings of 150 and 1500 Hz.

2.1.4. Experimental Setup and Procedures

The control experiments discussed in section 2.2 through section 2.5 were performed with the settings shown in Table 2.1.2. For this work the air flow rate was kept constant and the fuel flow rate was adjusted in order to change the GER.

Table 2.1.2: Experimental setup for control experiments.

Filter Settings		Fuel and Air		Control System	
Low Pass Filter	1500 Hz	Fuel Pressure	200-400 psi	Control signal limit (upper)	3.5 V
Band Pass Filter	None	Air Flow Rate	60 scfm	Control signal limit (lower)	0 V
		Fuel Nozzle	Delavan 60° solid-cone simplex	Controller	Phase Shift

The phase shift controller settings will be denoted by a gain setting and a delay setting throughout this chapter. The delay setting can be converted to phase using Equation 2.1.1.

$$Phase(degrees) = \frac{(Freq_{sig.})(n\ delays)(360^\circ)}{sampling\ frequency} \quad \text{Equation 2.1.1}$$

where $Freq_{sig.}$, Hz, is the frequency of the signal that enters the controller, n delays is the controller delay setting, and sampling frequency, Hz, is the sampling frequency of the control computer. The sampling frequency is 6400 Hz for all experiments in this thesis.

2.2. Controller Trends

The phase shift controller settings for both the gain and the number of delays used to stabilize the system change relative to changes in the Global Equivalence Ratio (GER), which is the ratio of total fuel to air entering the combustor divided by the ratio of fuel to air in a stoichiometric mixture. In general, raising the GER of the system required the controller gain to be raised and the number of controller delays to be lowered. There is, however, significant overlap in the range of controller settings that work for each GER setting, allowing for the stabilized system to be maintained as the system was transitioned to higher GERs by minimally adjusting the controller settings. This was particularly important for the highest GERs because physical limits in the system did not allow stabilization of the uncontrolled system. Therefore, to stabilize the highest GERs the system had to be stabilized at a lower GER and then transitioned to a higher GER as a stable system. In our controller tests we were able to stabilize the system from a GER of 0.48, where the system transitioned to unstable, up to a GER of 0.67. Figure 2.2.1 shows the range of controller settings that can be used to maintain a stabilized system at three different GERs. In particular, the overlap between the different GERs and the trends of controller delay and gain settings should be noted.

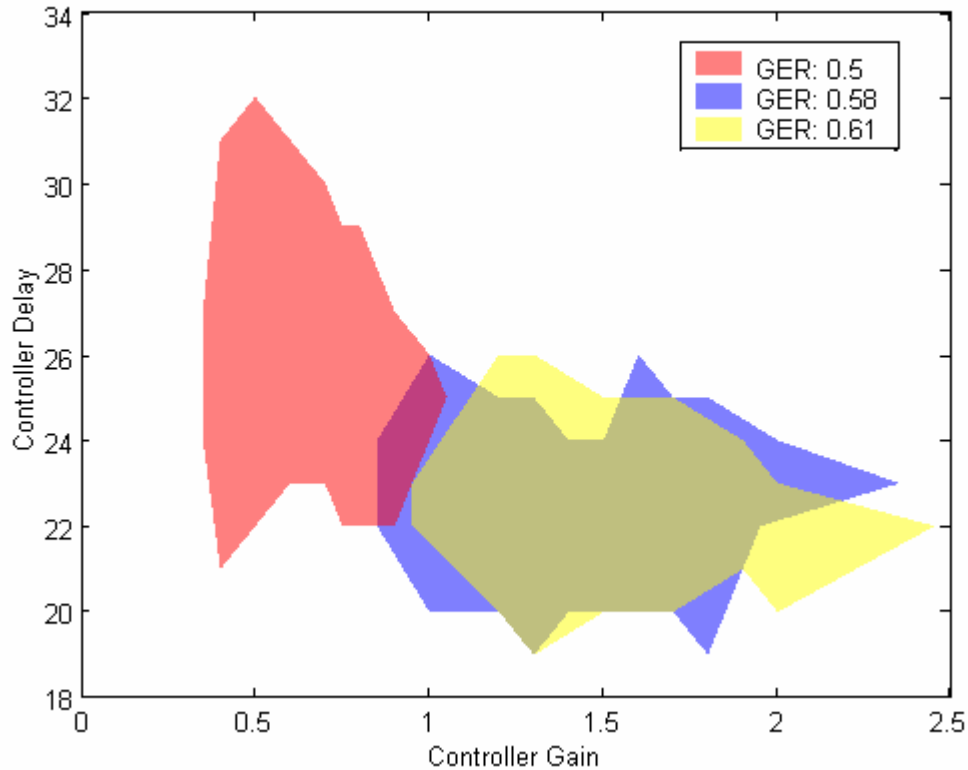


Figure 2.2.1: Ranges of controller settings used to maintain control for various GERs.

There are three distinct regions of controllability for the control system. The first region exists from 0.48, where the combustor transitions to unstable, until a GER of 0.55. In this region on-off control is possible, which means that an unstable system can be stabilized by turning the controller on at the correct setting. The second region exists from a GER of 0.56 to a GER of 0.64. In this region on-off control is not possible, however, the system can be stabilized by turning the controller on at the correct setting and then shifting the controller delay to an intermediate setting. The intermediate setting will not achieve steady-state stability, but does periodically lower the instability amplitude as the system oscillates between stable and unstable. Typically the oscillations are of a very low frequency (minutes). This allows the controller to be shifted back to the original setting while the amplitude is suppressed, thereby regaining steady-state stability. This behavior occurs because the controller gain required at these GERs result in saturation of the actuation system, a problem that becomes more acute as the GER is raised. The third region exists at a GER of 0.65 and above. In this region the controller is not gain limited as long as it remains stable. Once stability is lost, however, the system must be taken to a lower GER to regain stability. Unlike the second region, stability in this region can not be regained by shifting the controller delay setting because the actuation system is severely saturated due to the higher gain settings required for stability.

2.3. Control Performance Near the Instability Boundary

2.3.1. System Characteristics

Between the instability boundary at a GER of 0.48 and a GER of 0.55 controller settings exist where stability can be achieved simply by turning the controller on. Figure 2.3.1 shows the power spectrums of the controlled and uncontrolled system at a GER of 0.5. The amplitude is shown in Sound Pressure Level (SPL), which is calculated using Equation 2.3.1. The specific equation used with the pressure sensor used for experiments is given in Appendix B.

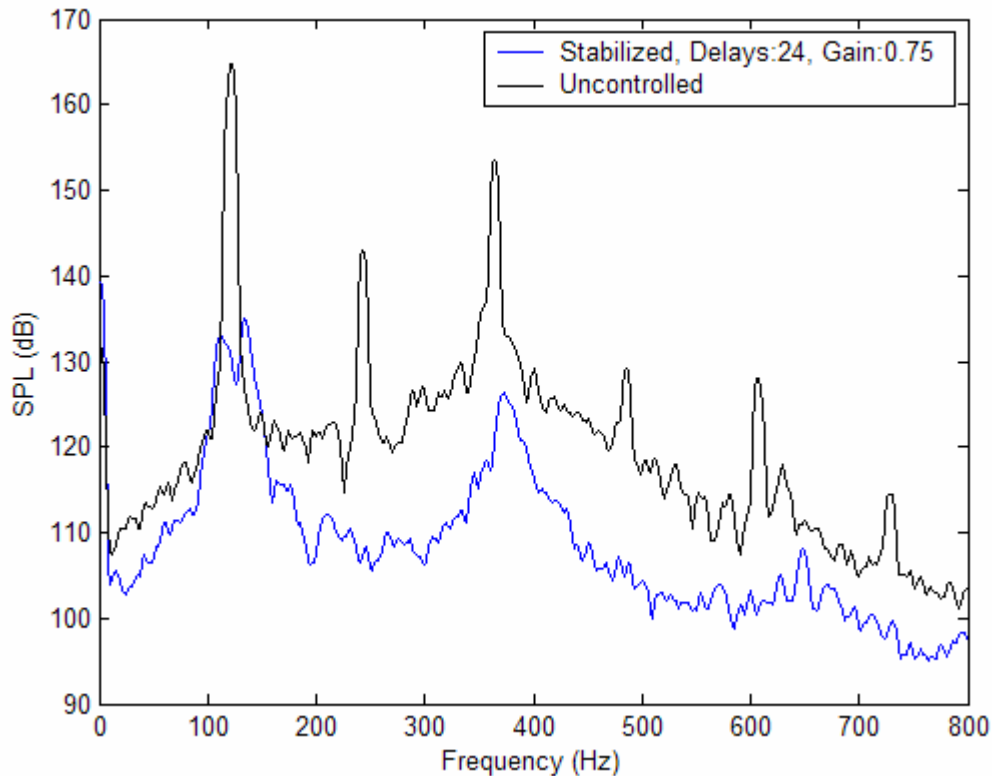


Figure 2.3.1: Controlled and Uncontrolled System at a GER of 0.50.

$$SPL = 10 \log_{10} \left(\frac{P_{rms}^2}{P_{ref}^2} \right), \text{ where } P_{ref} = 20 \mu\text{Pa}. \quad \text{Equation 2.3.1}$$

The magnitude of the peak frequency is decreased from 164 dB for the uncontrolled case to 135 dB for the stabilized case, a reduction of 29 dB. Many different control settings can be used to gain stability, and once the system is stabilized an even larger range of controllers can be used to maintain stability. Figure 2.3.2 shows a stability map for various controller settings, the circles represent the stability limits of the controller, and the triangles indicate limits where actuator saturation occurred when the system became unstable. Saturation occurs when the control signal voltage reaches either the upper or lower voltage limit, causing the desired control signal to be clipped. However, saturation in this range of GERs

is not severe enough to inhibit control. The implications of saturation will be discussed further for the next control region.

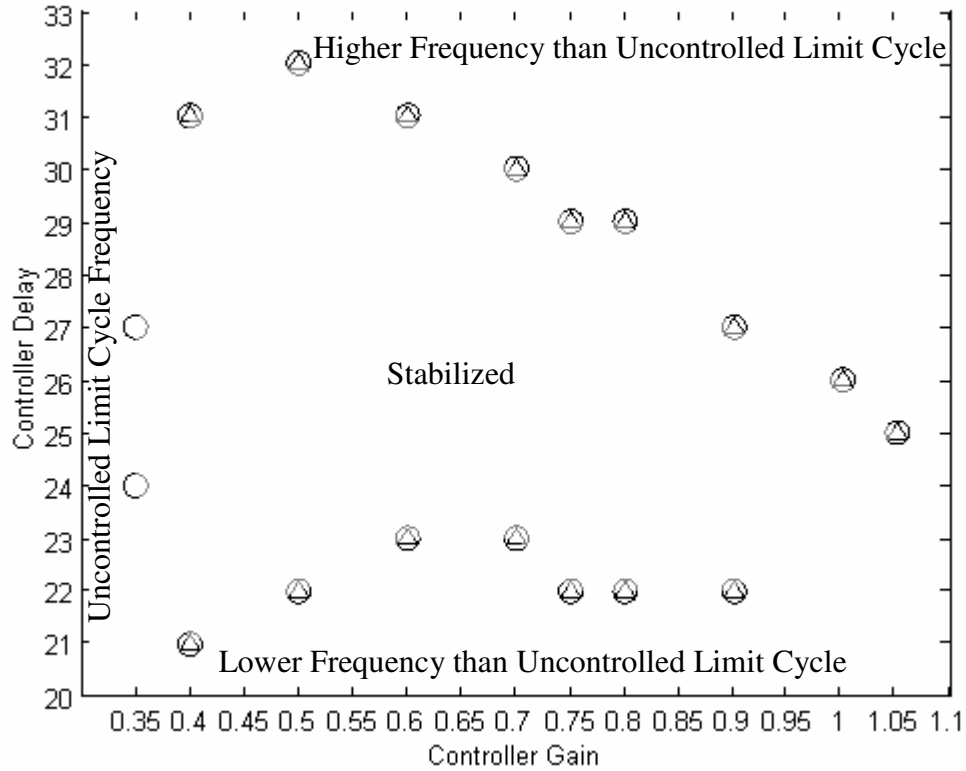


Figure 2.3.2: GER: 0.50

The uncontrolled limit cycle frequency is the dominant frequency of the unstable system when the controller is turned off, this frequency is used as a reference point for comparing the effect of different controller settings. The limit cycle frequency is different from the uncontrolled limit cycle frequency for many cases where the controller is on but the system is unstable, as indicated in Figure 2.3.2. The amplitude of the peak frequency also changes as controller settings are changed.

2.3.2. Hysteresis

Figure 2.3.3 shows the amplitude of the highest peak in the power spectrum for various gain settings at a GER of 0.5, and a controller delay setting of 24. The black circles indicate data points taken starting at a gain of 0.75 and then decreasing gain. The red circles indicate data points taken starting at a gain of 0 with increasing gain. Note that a 0 gain controller setting is the same as the controller being turned off. The amplitude of the highest peak for each controller gain is taken from an averaged power spectrum taken with that setting; these power spectrums are included in Appendix E. Two power spectrums were taken at the gain values where the system transitioned from controlled to uncontrolled and vice versa. For the black circles these are at a gain of 0.35, for the red circles these are at a gain of 0.7. Specifically points 1 and 2 are from a power spectrum taken while the system was transitioning between states. The hysteresis in Figure 2.3.3 is typical of the systems behavior,

in that fewer controller settings can be used to stabilize the system than can be used to maintain stability. Therefore, losing control the 0.3 gain stability boundary shown in Figure 2.3.2 requires the controller gain to be increased to 0.7 in order to regain stability.

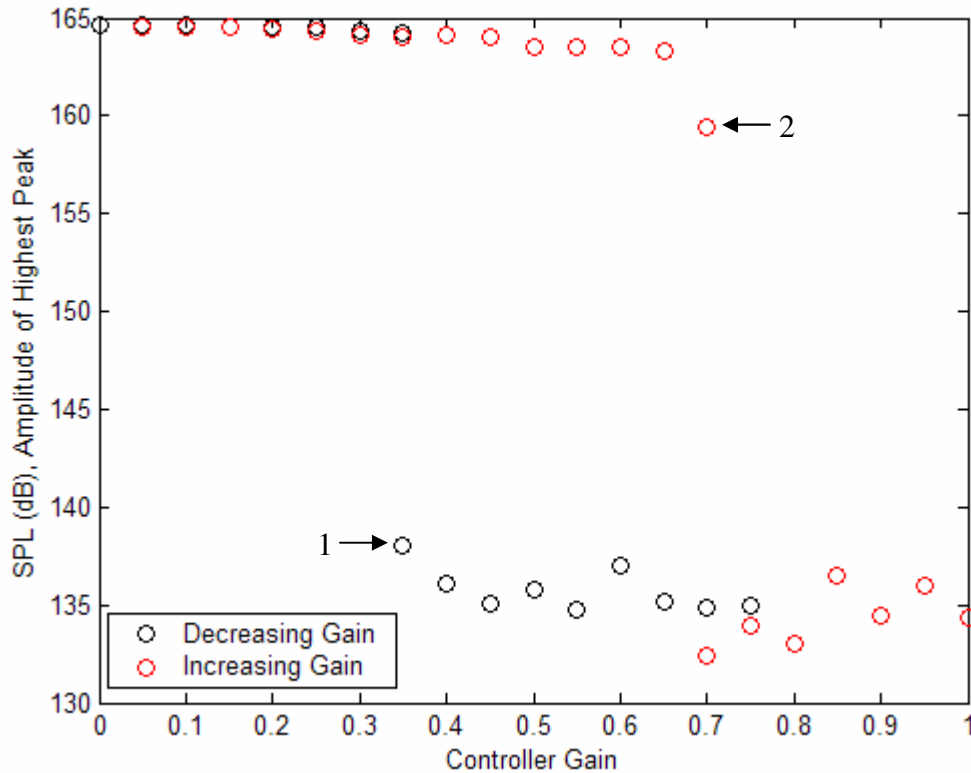


Figure 2.3.3: GER: 0.50, delays 24, hysteresis

A second set of power spectrums were taken at the same GER but with the controller delay setting shifted to 28.

Figure 2.3.4 shows the amplitude of the highest peak for this delay setting and various gains. The blue circles indicate data points taken starting at a gain of 0.75 and then decreasing gain. The green circles indicate data points taken starting at a gain of 0 with increasing gain. The relevant power spectrums for these data points are also included in Appendix E. For this controller delay setting the system was unstable for most of the settings and on the edge of stability for the gain values which suppressed the limit cycle amplitude significantly. Compared to the uniformity of peak amplitude that appears for the controlled system in Figure 2.3.3, this controller setting has much more unpredictable behavior from one gain value to the next, and even from one minute to the next. Although hysteresis is not evident here, steady-state stability also does not exist, and this is not a good controller setting.

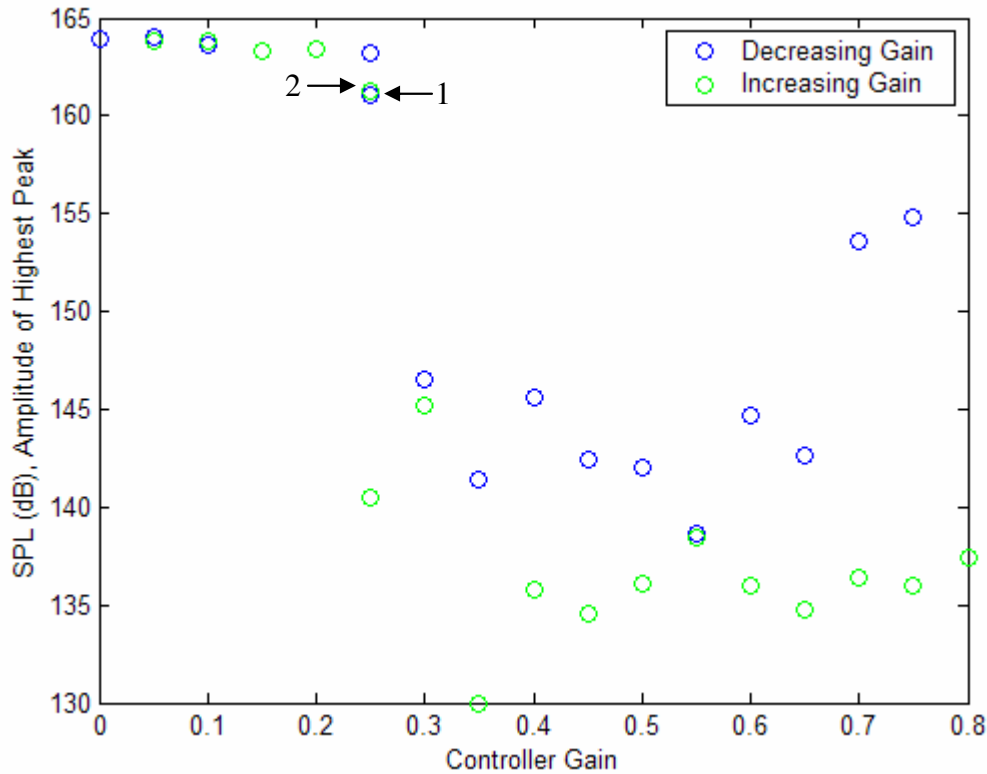


Figure 2.3.4: GER: 0.50, delays 28, unstable

2.4. Control Performance Further From the Instability Boundary

2.4.1. System Characteristics

Between a GER of 0.56 and 0.64 stability can be gained by moving from a stabilized system at a lower equivalence ratio in small increments to higher equivalence ratios while also making small adjustments to the controller. Turning the controller off and then back on with the same setting results in an unstable system, however, stability can be regained by increasing the controller delays to an intermediate setting, and then shifting back to the original controller setting. When the controller is initially turned back on, and stability is not obtained, the unstable frequency is lower than the uncontrolled limit cycle frequency, and the amplitude is about 0.5 dB higher. Shifting the controller delay setting to a higher number raises the peak frequency and reduces the amplitude. Although the amplitude is reduced at the shifted controller delay, the system will slowly oscillate in and out of stability if the controller remains at this setting, therefore the controller is shifted back to the original setting and steady-state control is regained. Figure 2.4.1, Figure 2.4.2, and Figure 2.4.3 show the stabilized system, the uncontrolled system, the unstable system when the controller is turned back on, and the system with the shifted controller setting for three different equivalence ratios in this region.

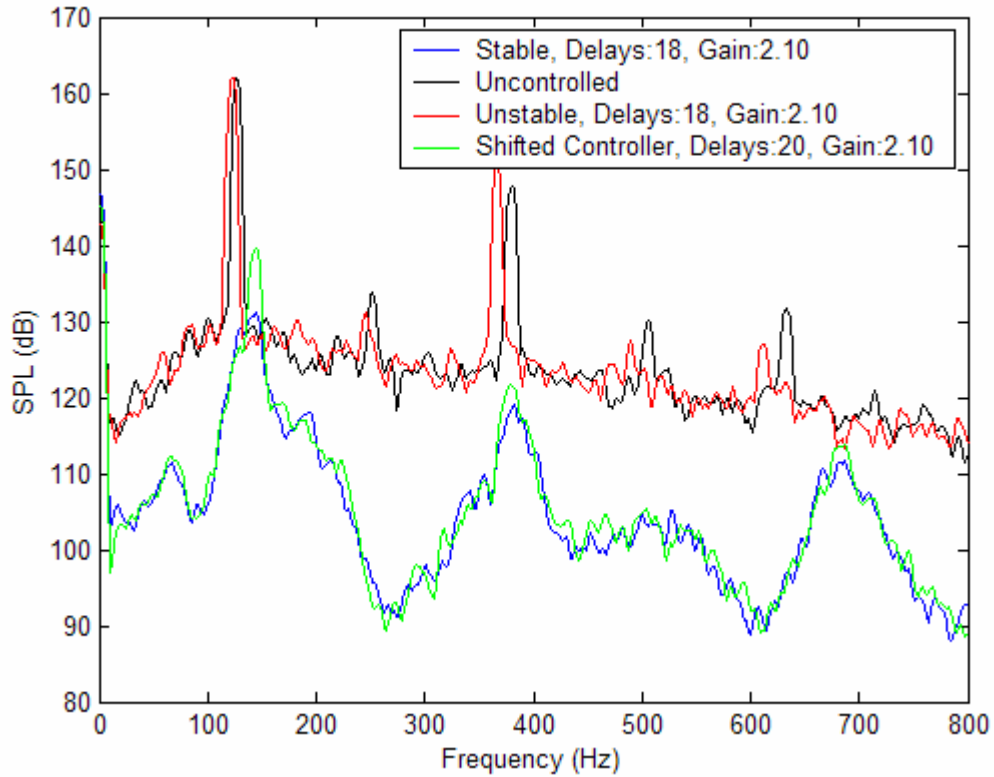


Figure 2.4.1: GER:0.60

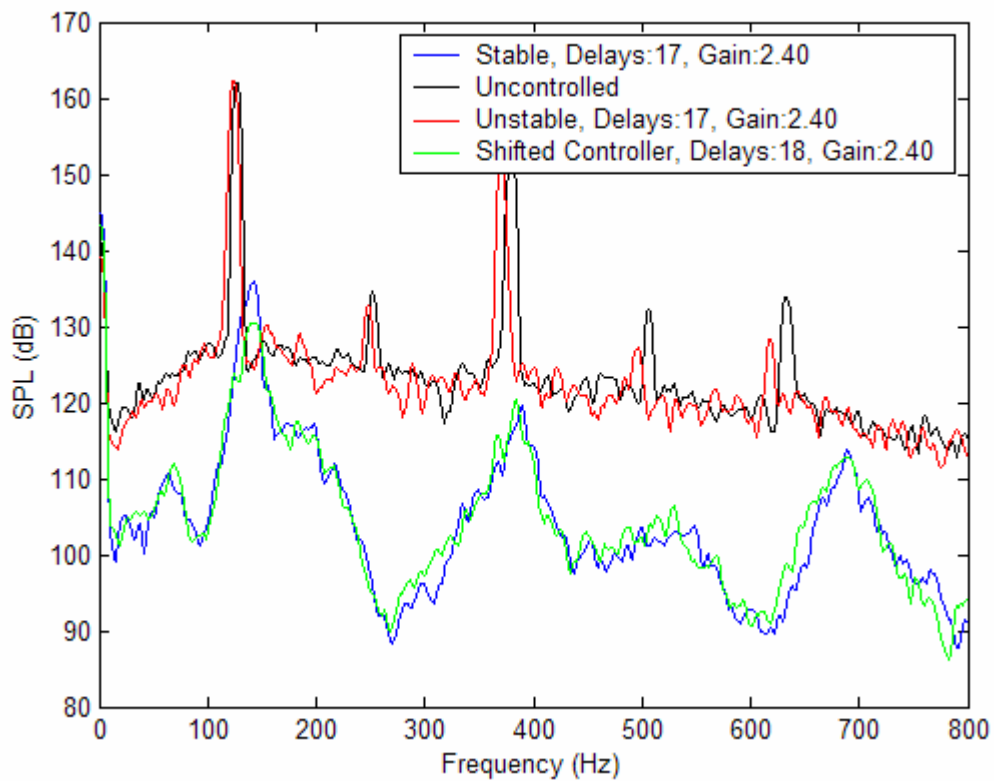


Figure 2.4.2: GER: 0.62

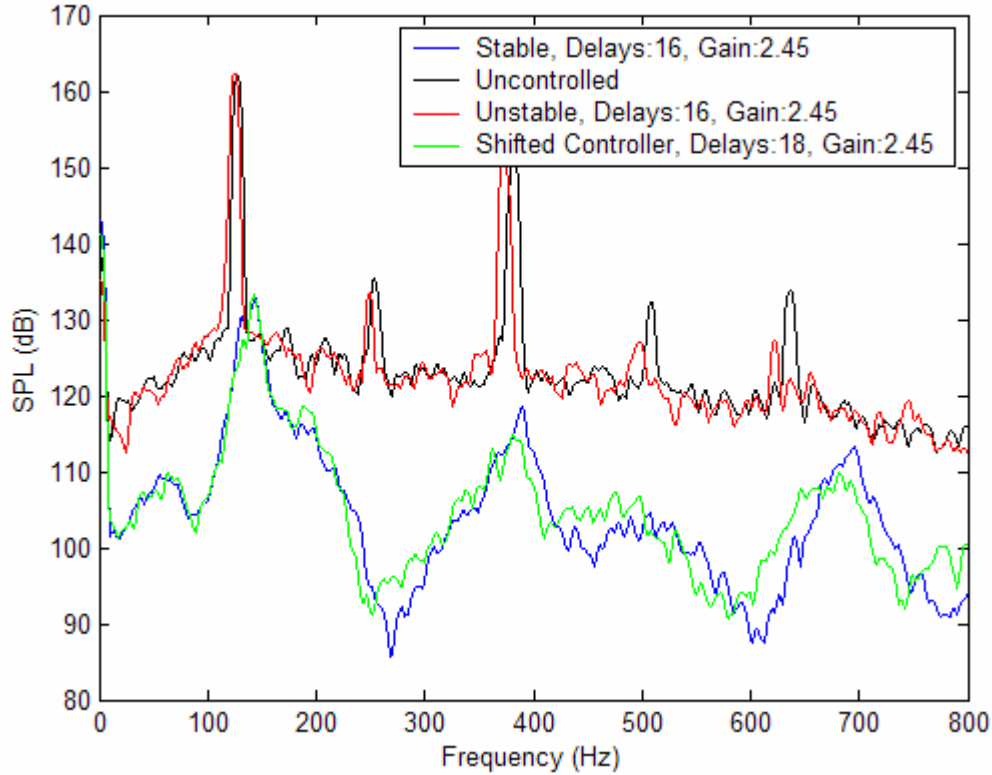


Figure 2.4.3: GER: 0.64

For the already stabilized system, the ranges of controller settings that can be used to maintain control are shown in Figure 2.4.4 and Figure 2.4.5 for two different GERs in this region. As before, the circles represent points where the system crosses from stable to unstable, while the triangles represent points where the actuator becomes saturated once the system becomes unstable. In this region, the controller gain requirements for control are such that the actuator is saturated whenever the system becomes unstable. However the degree of saturation is significant enough that changes in the controller settings, as described above, are required to regain control of the system.

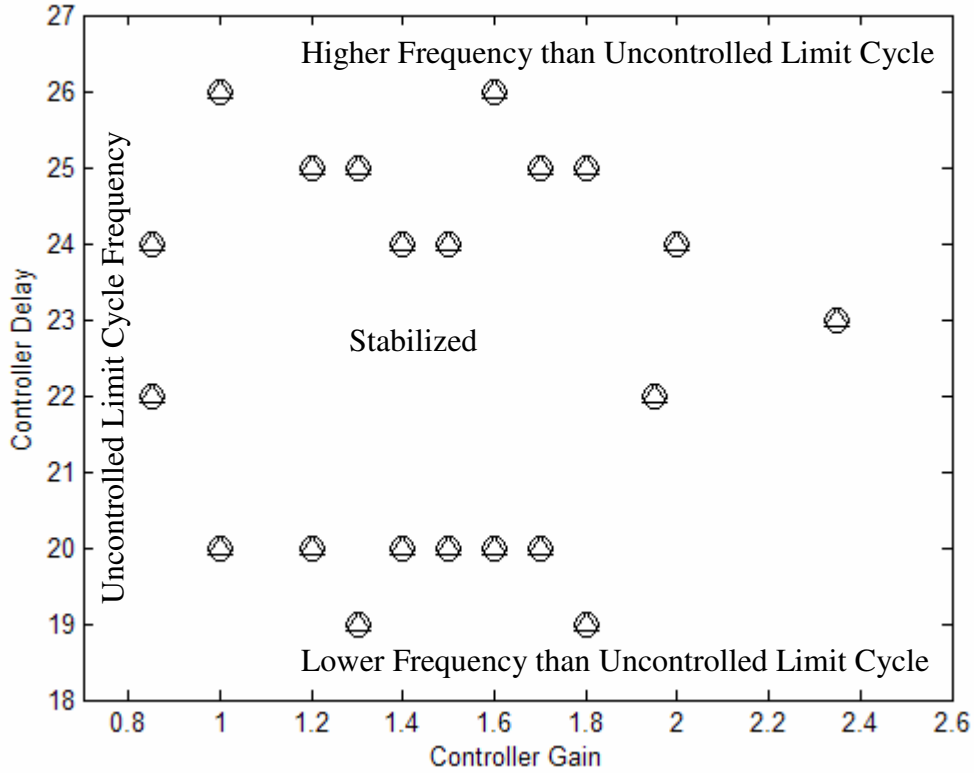


Figure 2.4.4: GER: 0.58

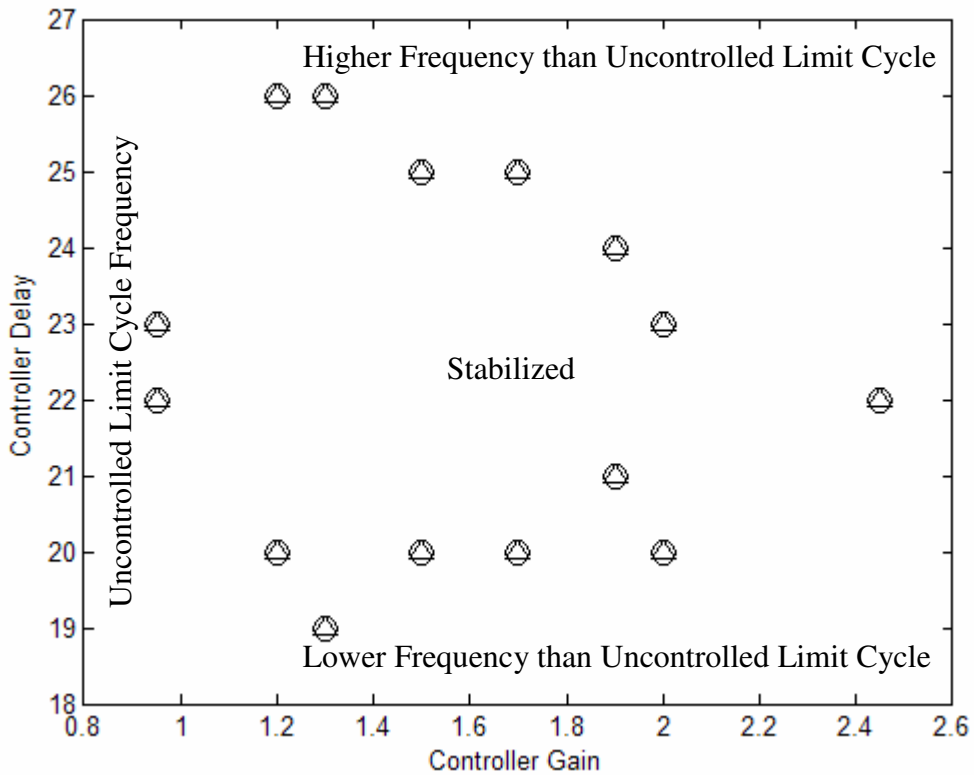


Figure 2.4.5: GER: 0.61

2.4.2. Saturation

The primary fuel modulation system for the liquid fuel combustor is set up so that a 0 V input corresponds to the maximum fuel pressure of 475 psi and the upper voltage limit of 350 V, which is set as a limit in the control software, corresponds to 50 psi. 350 V was chosen as the upper voltage limit based on the allowable driving voltages for the actuators' amplifier at the driving frequencies that are used (the primary frequencies measured in the combustor pressure signal). There is a gain of 100 between the control signal sent to the amplifier and the output of the amplifier to the actuator, therefore a control signal of 3.5 V corresponds to an actuator voltage of 350 V. For the second region, where control can be regained by shifting the controller phase setting, saturation occurs predominantly at the lower pressure limit (high voltage limit), significantly reducing the effective gain and resulting in a nonlinear control signal. At GERs in the third region, where control cannot be regained, saturation occurs at both the upper and lower pressure limits such that the control signal approximates a square wave, severely reducing the effective gain. Saturation in the third region will be discussed further in section 2.5.2.

The available pressure before saturation occurs is dependant on the mean pressure controller setting. Figure 2.4.6 shows the theoretical delta pressure available before saturation occurs for the range of mean pressures (200 psi to 375 psi) that we could typically control during control experiments. The lower end of the range, 200 psi, is the lowest pressure that was used because the atomization properties of the nozzle begin to degrade below 100 psi. The peak in Figure 2.4.6 occurs where the closest saturation point shifts from the low pressure (high voltage) limit to the high pressure (lower voltage) limit. Also, since control experiments were run such that the mean fuel pressure was increased to transition to higher GERs, the higher mean pressures correspond to higher GERs, and therefore, to generally higher gain requirements for control to be maintained. The result is that, moving to higher GERs (higher mean pressures) leads to a decrease in the available delta pressure before saturation occurs (on the right half of Figure 2.4.6) and to an increase in the controller gain requirements (see Figure 2.2.1), which causing saturation to become more severe. The three regions of controllability are also shown in Figure 2.4.6 for comparison.

In this work, saturation was only a problem for higher GER operating conditions, in part because the lowest unstable GER was 0.48 for the VACCG kerosene-fueled combustor. However, the literature shows that other combustors are unstable at leaner conditions, whereby saturation may become a problem. Since achieving stable lean combustion is the primary goal of active combustion control systems, saturation at the lower pressure limit is of particular interest because the lower pressure limit will saturate first for lower fuel pressures. However, saturation at the lower pressure limit could be addressed by using a lower flow rate nozzle. Reducing the nozzle size to a lower flow rating, but keeping constant the air entering the combustion chamber and the fuel pressure, results in a lower GER. If the correct nozzle size is chosen for the desired operating GER, the mean fuel pressure that is used can be positioned between the upper and lower fuel pressure limits so that the maximum delta pressure is available on both the upper and lower pressure sides of the mean pressure before saturation occurs. In Figure 2.4.6 the ideal mean pressure would be 285 psi. In fact, saturation at both the upper and lower fuel pressure limits could be addressed if an array of small fuel nozzles is used instead of a single fuel nozzle, provided that individual fuel nozzles could be turned on and off using a valve, to give the desired operating GER

without changing the mean fuel pressure supply to the nozzle array. This would make the maximum fuel pressure amplitude available for every GER. It should be noted that changing to an array of nozzles with an optimized mean fuel pressure does not necessarily preclude saturation from affecting the authority of the control system. However, a system with an optimized static mean fuel pressure is the best way to prevent saturation and limit its severity.

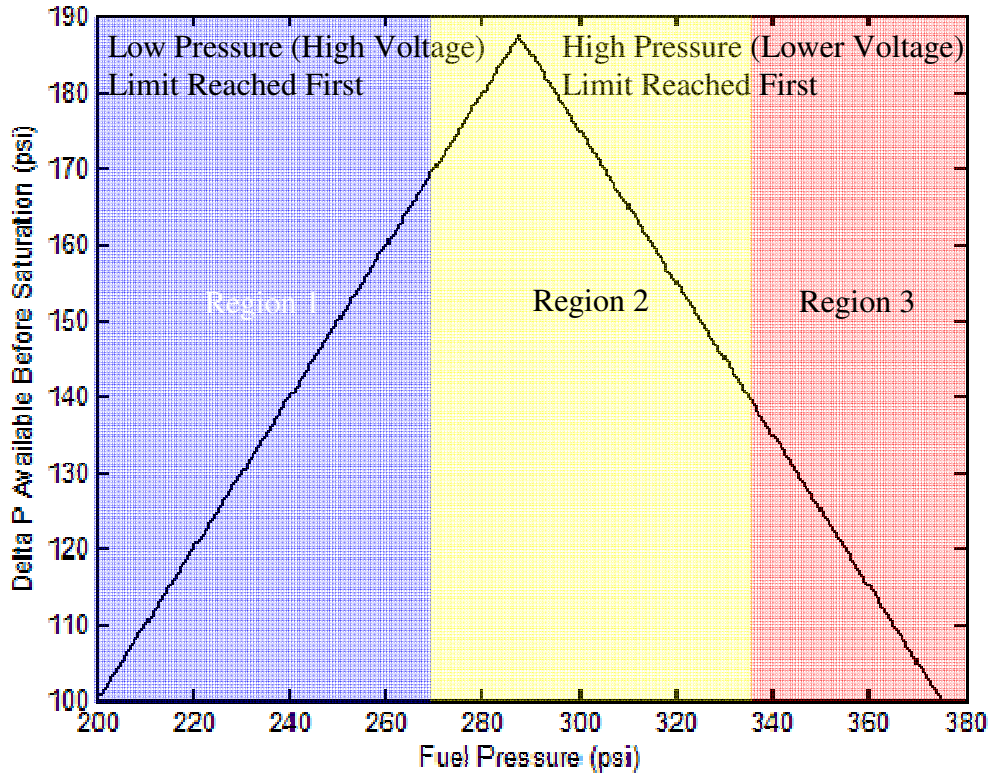


Figure 2.4.6: Theoretical delta pressure (psi) before saturation for various mean fuel pressures.

Figure 2.4.7 shows the power spectrums at a GER of 0.58 for the stabilized system, the uncontrolled system, the unstable system with the controller turned back on, and the intermediate system with a shifted controller delay setting. For this case, when the controller was turned back on the amplitude of the instability peak is 1.5 dB higher than the uncontrolled system, which is slightly higher than the difference that typically occurs in this region. Nevertheless, saturation only significantly affected the upper portion of the control signal and, by shifting the controller delay setting and then moving back to the original setting, stability was successfully regained.

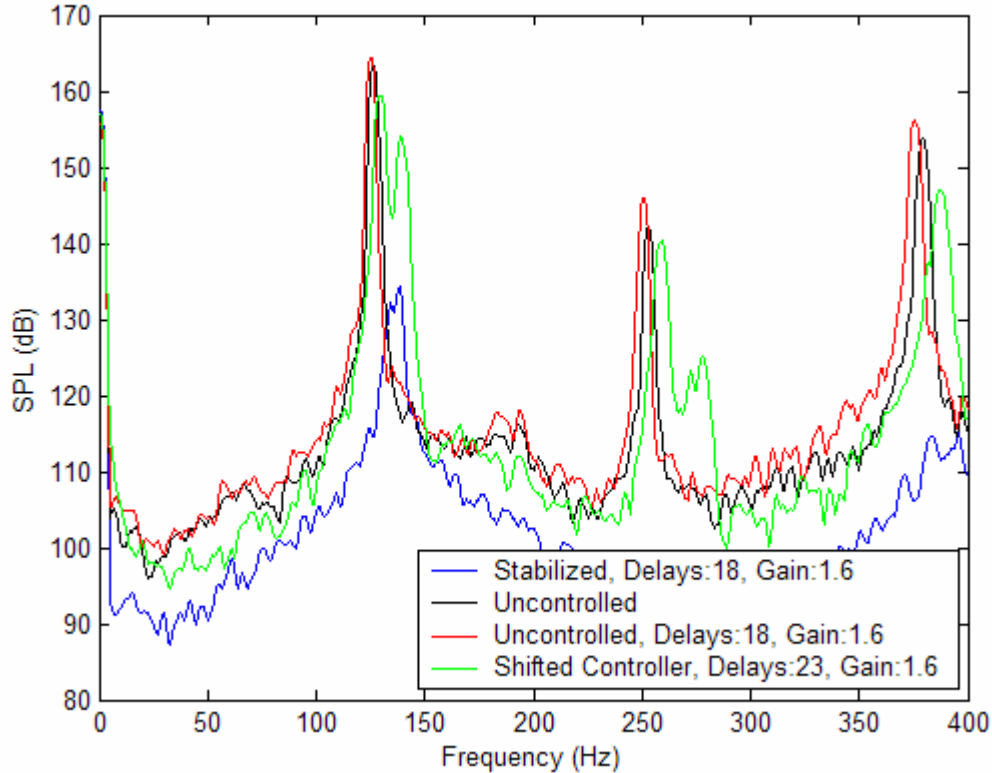


Figure 2.4.7: GER=0.58

To better understand the effect of saturation on controlling an unstable system in this region, the corresponding time traces of the combustor pressure signal and the control signal sent to the actuators' amplifier were taken for each of the power spectrums shown in Figure 2.4.7 except for the stabilized case. The time trace of the combustor pressure signal, in volts, for the uncontrolled system is shown in Figure 2.4.8. Unlike the combustor pressure signals for the first region, where only one frequency is evident in the time trace, the uncontrolled pressure signal for this case is clearly made up of more than one frequency. This change is attributed to an increase in the amplitude of the second harmonic as the GER is increased. Figure 2.4.9 and Figure 2.4.10 show the combustor pressure signal and the control signal for the unstable system with the original controller back. The control signal is the signal sent to the amplifier and is between 0 and 3.5 volts, which corresponds to an amplifier output to the actuator of 0 to 350 volts. Also, the control signal is made up of the output of the mean pressure controller, which is approximately a constant value for a given fuel pressure, added to the combustor pressure signal, shifted the set number of delays, and multiplied by the controller gain. For this example, the controller gain is 1.6 for all of the control signals shown. Figure 2.4.11 and Figure 2.4.12 show the combustor pressure signal and the control signal for the system with the shifted controller setting. The controller setting has a clear impact on the combustor pressure signal, but it does not stabilize the system.

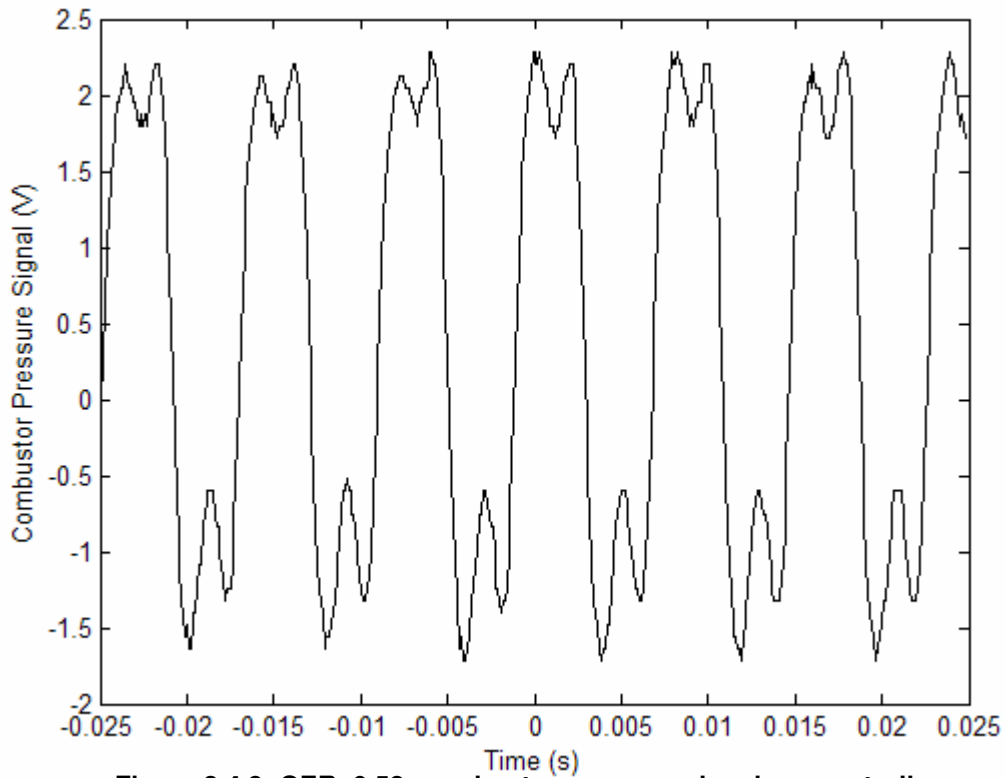


Figure 2.4.8: GER=0.58, combustor pressure signal, no controller.

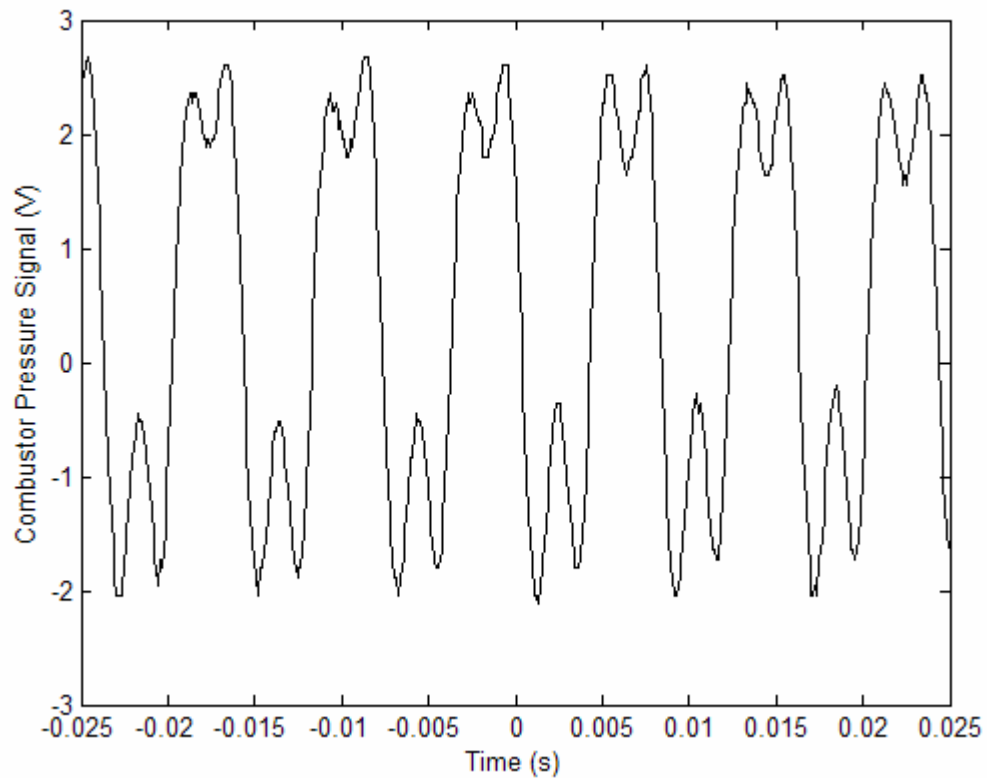


Figure 2.4.9: GER=0.58, combustor pressure signal, for controller on but uncontrolled.

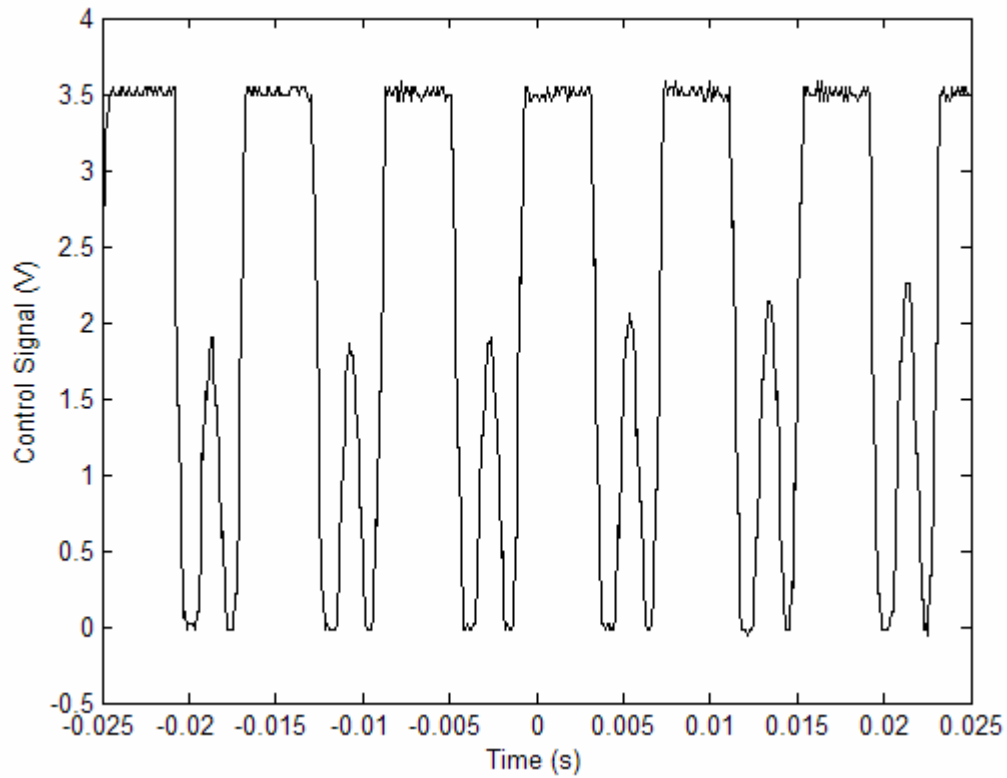


Figure 2.4.10: GER=0.58, control signal, for controller on at original setting, uncontrolled.

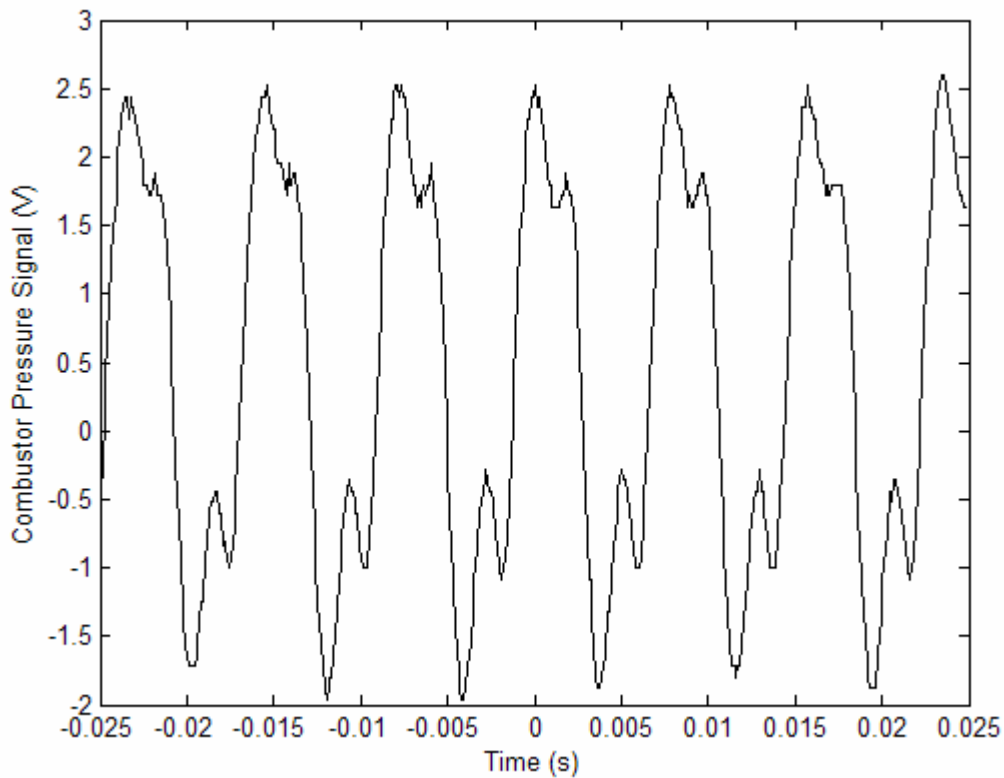


Figure 2.4.11: GER=0.58, combustor pressure signal, shifted controller setting.

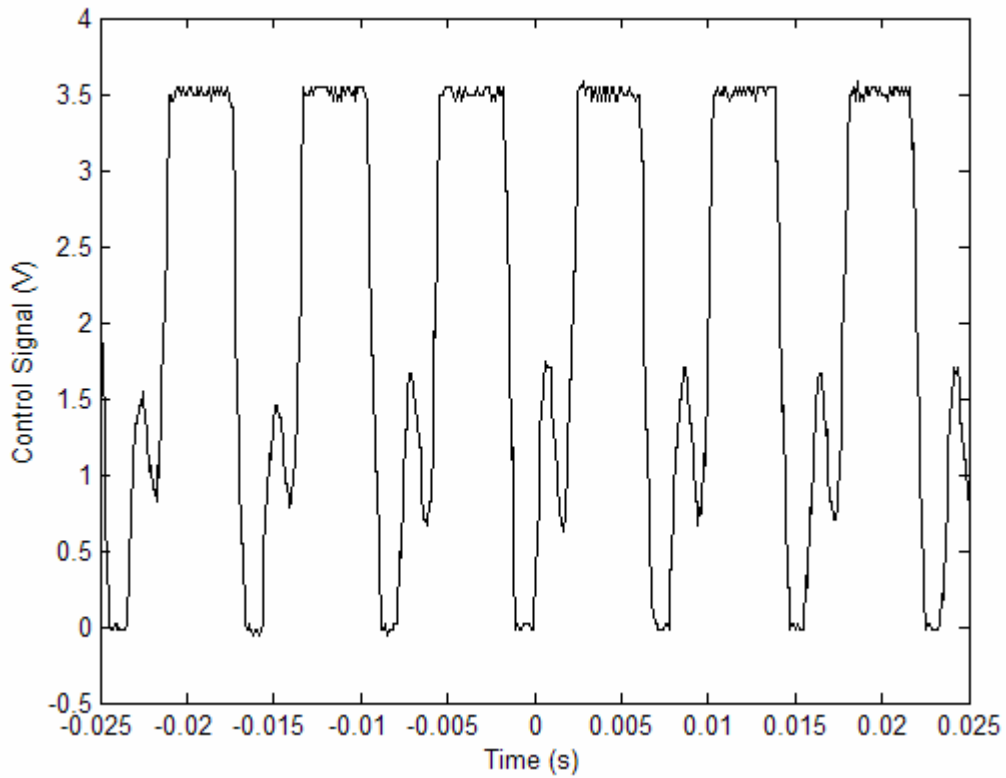


Figure 2.4.12: GER=0.58, control signal, shifted controller setting.

2.5. Control Performance Far From the Instability Boundary

2.5.1. System Characteristics

The third, and final, region where the combustor was successfully stabilized can only be reached by transitioning the stable system from a lower GER. Once stability is lost in this region, the system must be brought to a lower GER to regain stability. This region exists at a GER of 0.65 and above. Stabilized and uncontrolled power spectrums for a GER of 0.65 are shown in Figure 2.5.1. The controller can successfully lower the peak amplitude to the same level as seen in the other two regions when the system is stabilized. However, saturation of the control signal inhibits gaining control of an uncontrolled system outright in this region.

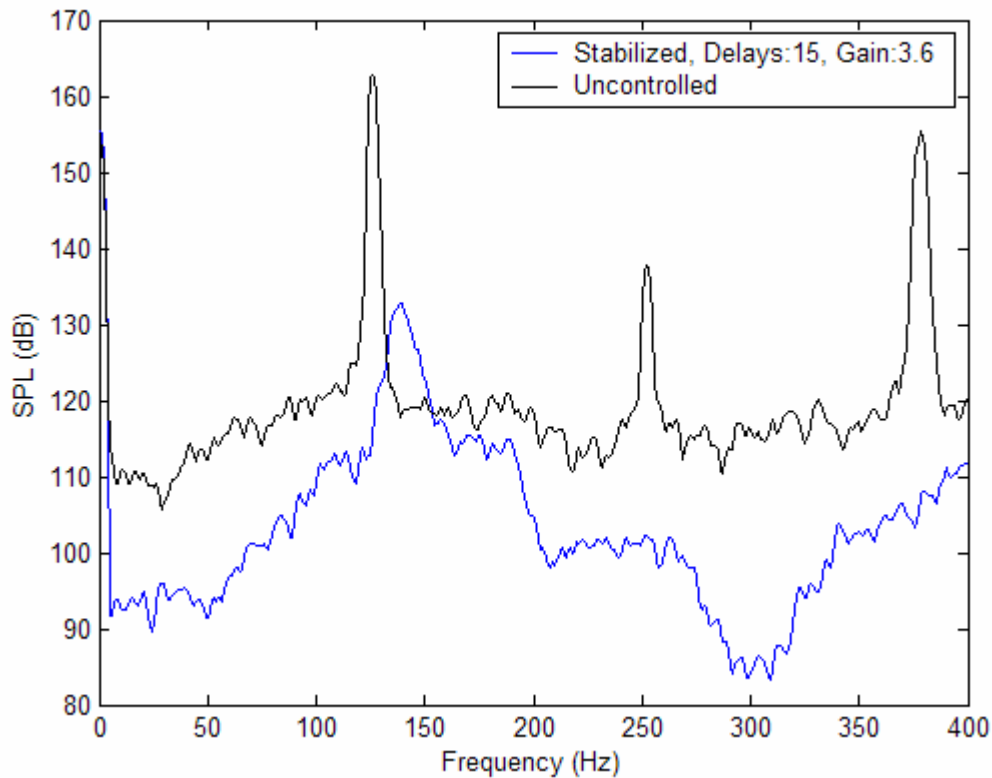


Figure 2.5.1: GER=0.65.

The control signal for the controlled case is shown in Figure 2.5.2. Note that even the control signal for the controlled system in this region has a high amplitude that will eventually approach the saturation limits if the GER is increased further.

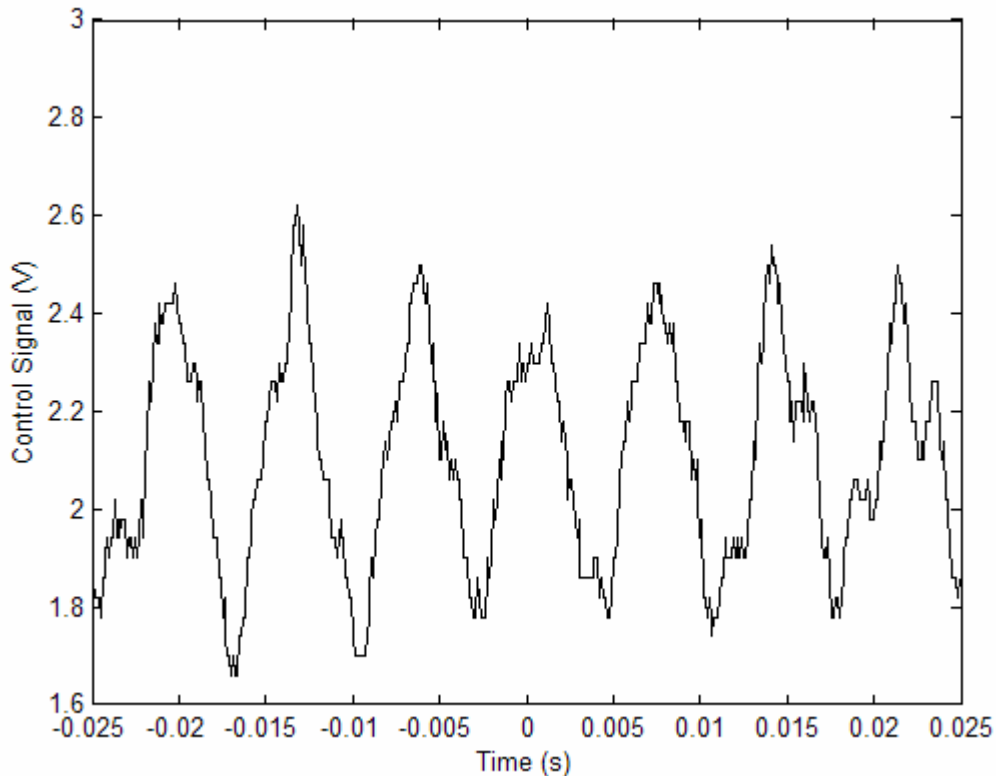


Figure 2.5.2: Control signal, Controlled system, Delays: 15, Gain: 3.6.

2.5.2. Saturation

Figure 2.5.3 shows the power spectrums for the uncontrolled system for a GER of 0.65 and then the unstable system with the controller back on and various controller delay values. All of the delay values show an increased peak amplitude compared to the uncontrolled system. Figure 2.5.4 shows a magnification of the peak amplitudes of Figure 2.5.3. Referring to the legend in Figure 2.5.3, it should be noted that increasing the controller delay setting shifts the frequency of the peak amplitude from a starting value of 125 Hz to a final value of 129 Hz, by only changing the controller delay 6 delays. This trend follows the trend observed in the first two regions (see Figure 2.3.2, Figure 2.4.4, and Figure 2.4.5). Figure 2.5.5 and Figure 2.5.6 show the combustor pressure signal and control signal for the case from Figure 2.5.3 where the controller delay setting is 15. The control signal is saturated so severely that it is a square wave. Figure 2.5.7 and Figure 2.5.8 show the combustor pressure signal and control signal for the case from Figure 2.5.3 where the controller delay setting is 19, which was the most effective of the settings tried. The control signal is still predominantly a square wave, however, the setting has some effect on the system, although minimal, which is evident in the changes to the combustor pressure signal and the control signal.

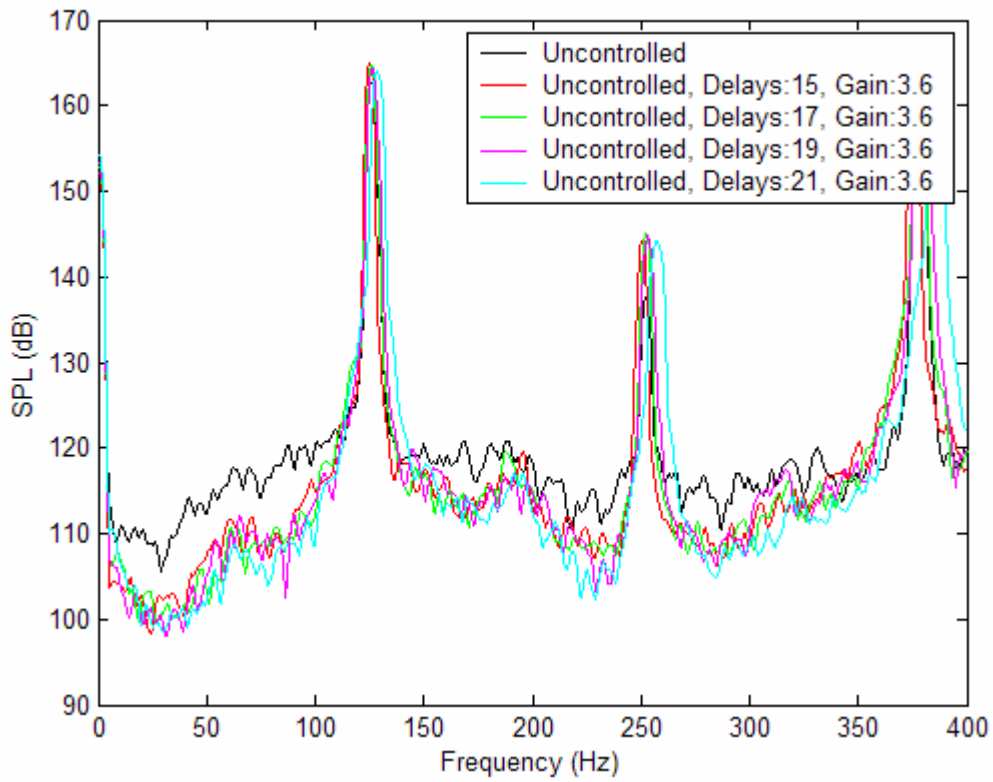


Figure 2.5.3: GER=0.65, various controller settings.

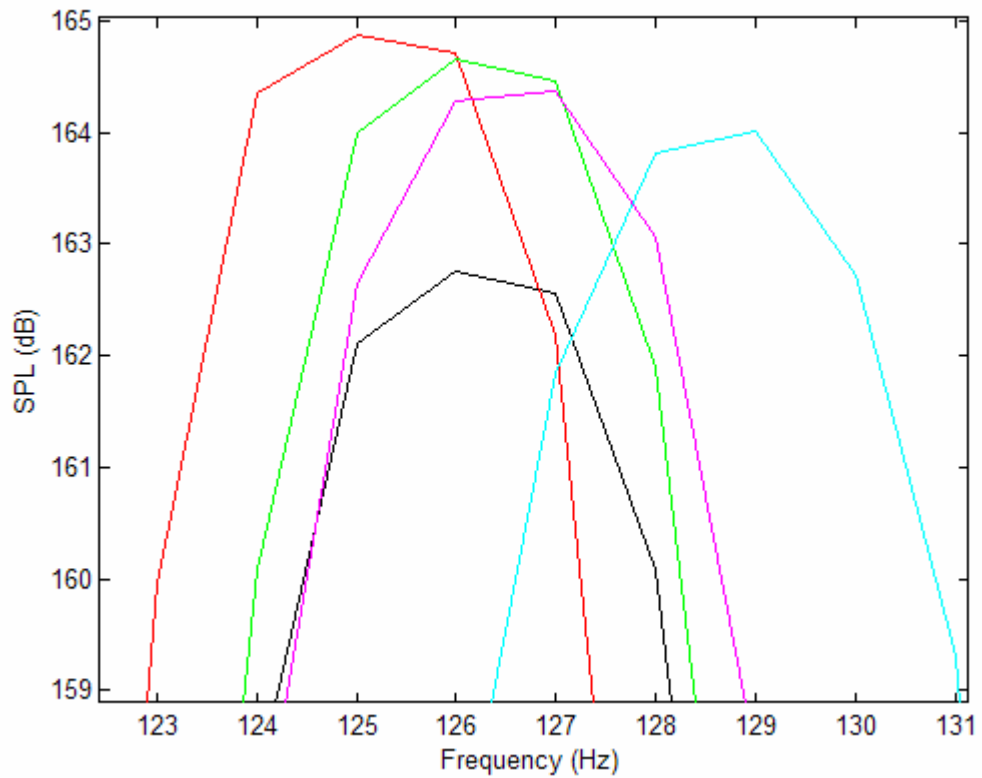


Figure 2.5.4: GER=0.65, Various controller settings, close up of instability peaks.

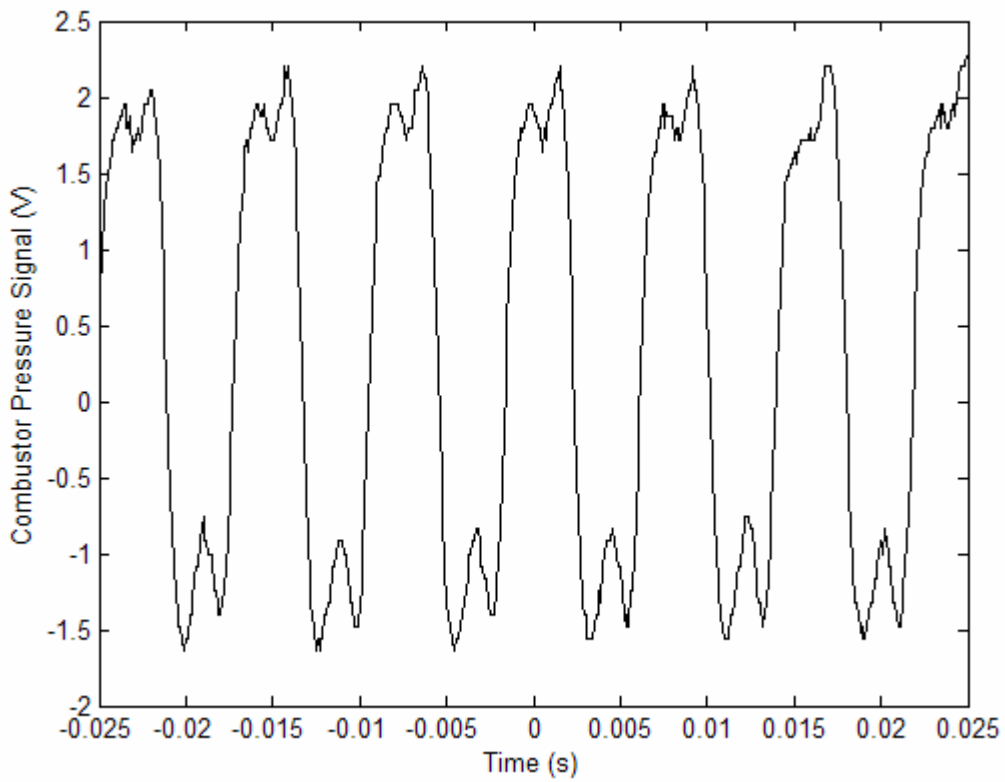


Figure 2.5.5: GER=0.65, Combustor pressure signal, Controller on, Delays:15, Gain: 3.6.

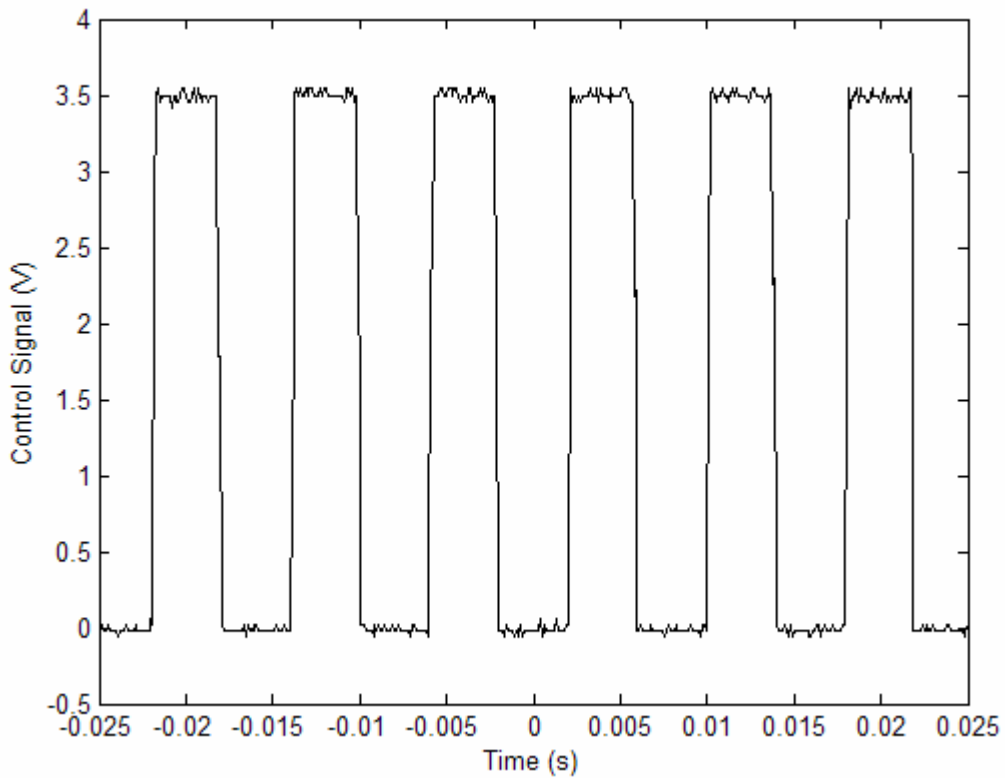


Figure 2.5.6: GER=0.65, Control signal, Controller on, Delays:15, Gain: 3.6.

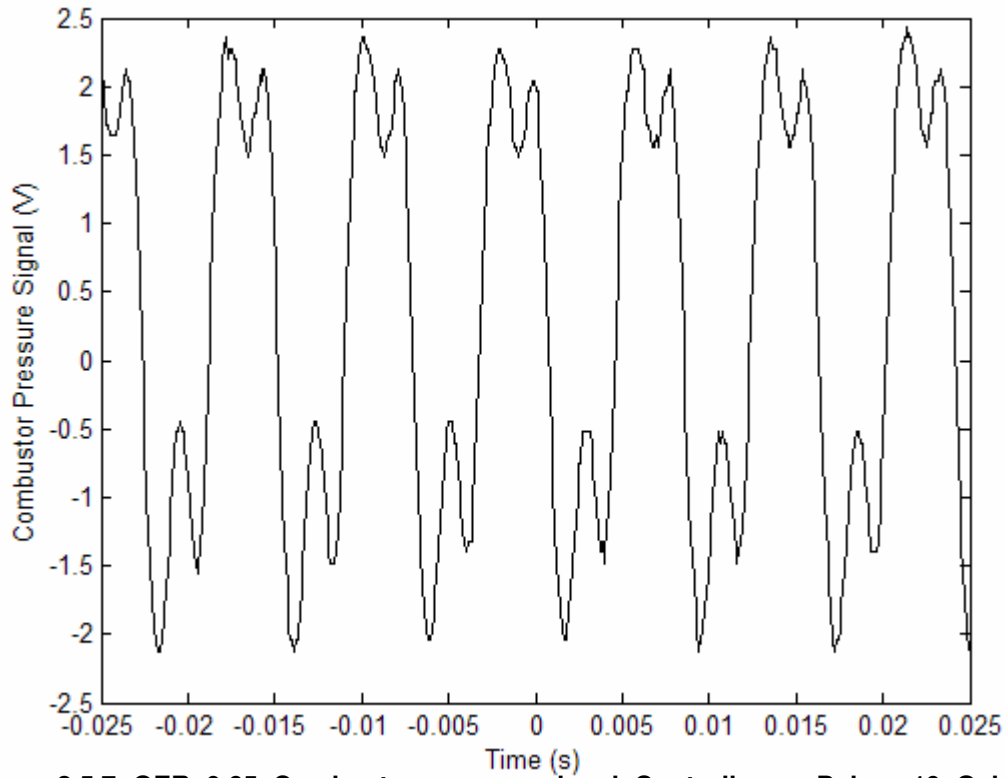


Figure 2.5.7: GER=0.65, Combustor pressure signal, Controller on, Delays:19, Gain: 3.6.

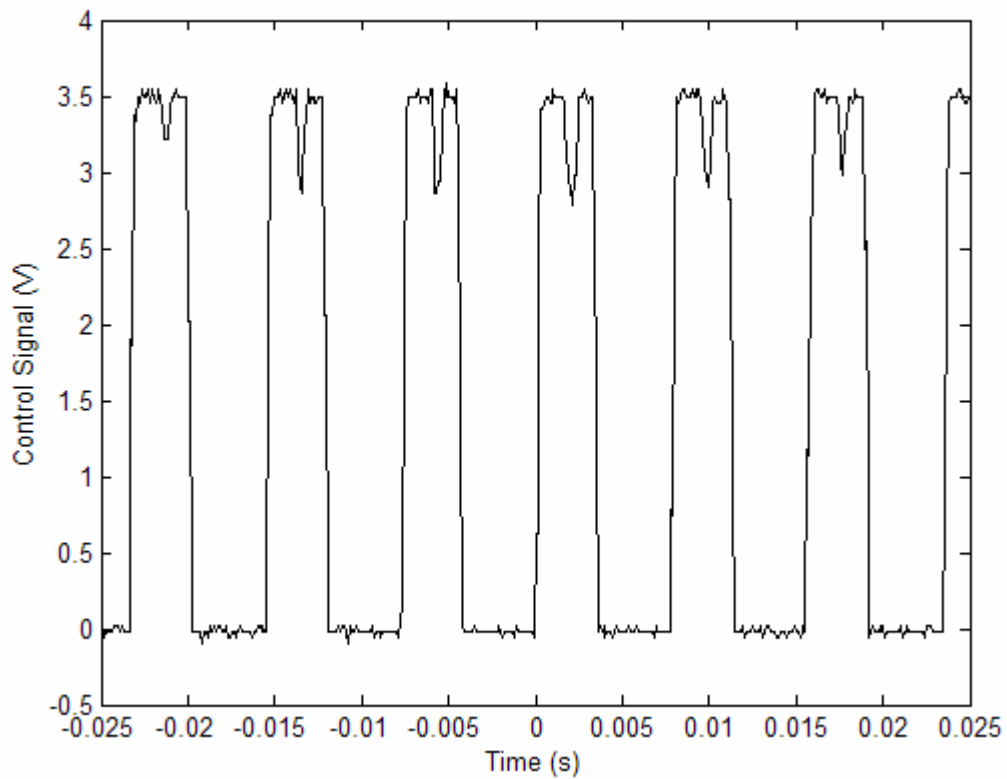


Figure 2.5.8: GER=0.65, Control signal, Controller on, Delays:19, Gain: 3.6.

Chapter 3. Atomization Effects

3.1. Introduction

To better understand the results of the control experiments in Chapter 2, the effect of proportional pressure modulation on the characteristics of the fuel spray was of direct interest. To this end, experiments were designed to measure the effect of pressure modulation on different atomizers. Measurements were taken for the Delavan simplex nozzle used for experiments in Chapter 2 and a Delavan air-assist nozzle. A DANTEC Phase Doppler Anemometry (PDA) was used for 1-D velocity and droplet size measurements at several locations within the sprays. Both static and dynamic measurements were taken for both of the atomizers.

The PDA is useful and reliable for characterizing spray droplet sizes and axial velocities, however, there are limitations to the conclusions that can be made from the one dimensional measurements taken with the PDA. The one dimensionality of the measurements means that all droplets are assumed to be spherical and only the axial velocity of the droplet can be measured. The limitations of the PDA measurements become obvious when attempting to fully understand the results of the dynamic tests in this chapter. Nevertheless, at least a cursory understanding of the spray characteristics can be made from the measurements with the PDA.

Experiments were attempted with a third type of atomizer, a Delavan Variflo™ atomizer (also called a spill-return or bypass atomizer), which was not successfully dynamically modulated for testing. A discussion of the challenges that precluded these experiments follows the discussion of the results for the simplex nozzle and the air-assist nozzle.

3.2. Experimental Setup and Calculations

3.2.1. Experimental Setup

The PDA setup for the experiments in this chapter is shown in Figure 3.2.1. PDA measurements are based upon the principle of light scattering interferometry. Measurements are taken at the point where two focused laser beams intersect, which defines the measurement volume. The intersection of the beams creates an interference fringe pattern that is composed of alternating light and dark planes. When a droplet passes through the measurement volume the light is scattered onto the three photomultipliers in the receiving optics. The signals from the photomultipliers are used to determine the diameter and axial velocity of the droplet. In Figure 3.2.1, the two laser beams are created from a single laser by the beam splitter. The laser beams then pass through the bragg cell, which shifts the phase of one of the beams; this results in the fringe pattern. The focusing and alignment optics are used to align the laser beams so that they intersect and set the position of this intersection. The HP Analyzer was used to create the modulation signal that was sent to both the angular encoder of the data processor and used as the controller input to create the pressure modulation for dynamic testing. For more information on PDA systems and operation see [8],[7].

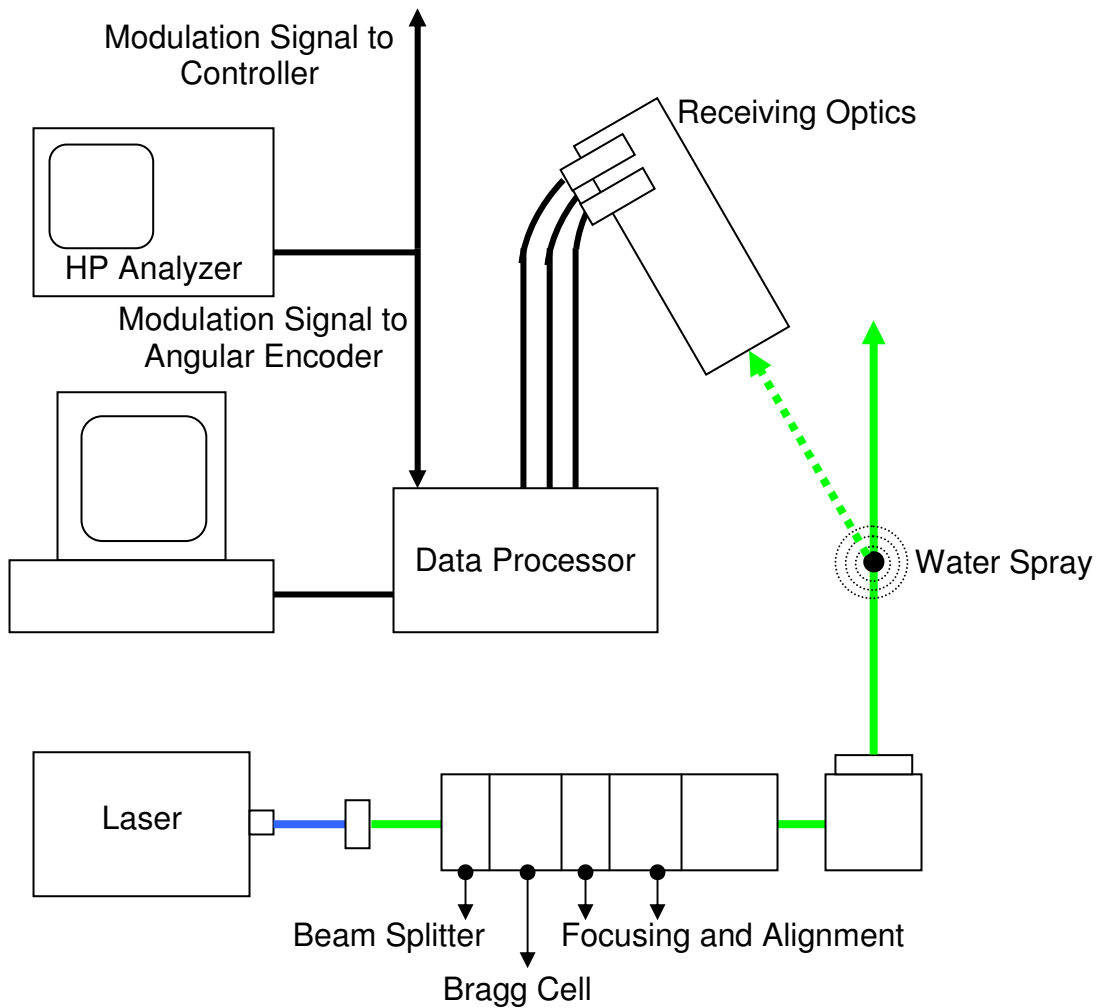


Figure 3.2.1: Phase Doppler Anemometry (PDA) setup for spray measurement tests.

The water and air system used for the simplex nozzle and air-assist nozzle tests is shown in Figure 3.2.2. The water system between the valve and the nozzle is the same as the system used between the valve and the nozzle on the VACCG kerosene-fueled combustor. Also, the actuator and valve used for these tests was the piezoelectric stack and Swagelok valve used for the control experiments in chapter 2. The bypass line is used, as in the kerosene system, to adjust the downstream impedance of the water system so that large pressure oscillations can be created in the line. The tuned water line also aids the creation of large pressure oscillations. For more information on the tuning and bypass lines see Schiller [20] and DeCastro [9]. The wiring diagram for the spray measurement tests is shown in Appendix F.

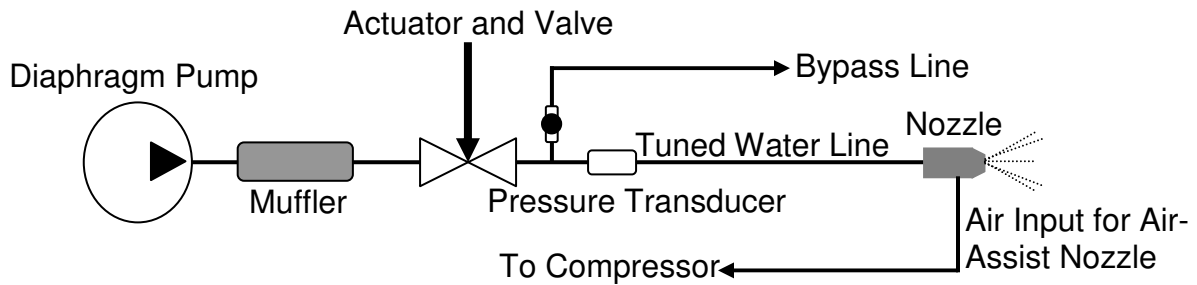


Figure 3.2.2: Water and air system for atomization tests.

The simplex nozzle and adaptor are shown in Figure 3.2.3. The air-assist nozzle and adaptor are shown in Figure 3.2.4. The nozzles are rated for the listed flow rate at a supply pressure of 100 psi. The flow rate at other supply pressures can be estimated from Equation 3.2.1, which is derived from the Bernoulli equation for incompressible flow.

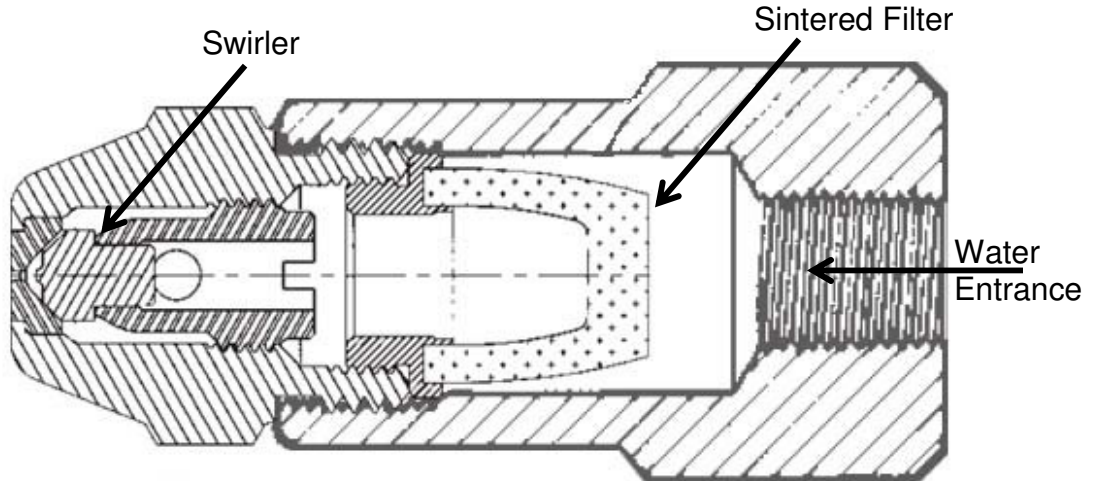


Figure 3.2.3: Delavan solid-cone 60° spray angle 1.0 gph simplex nozzle [10].

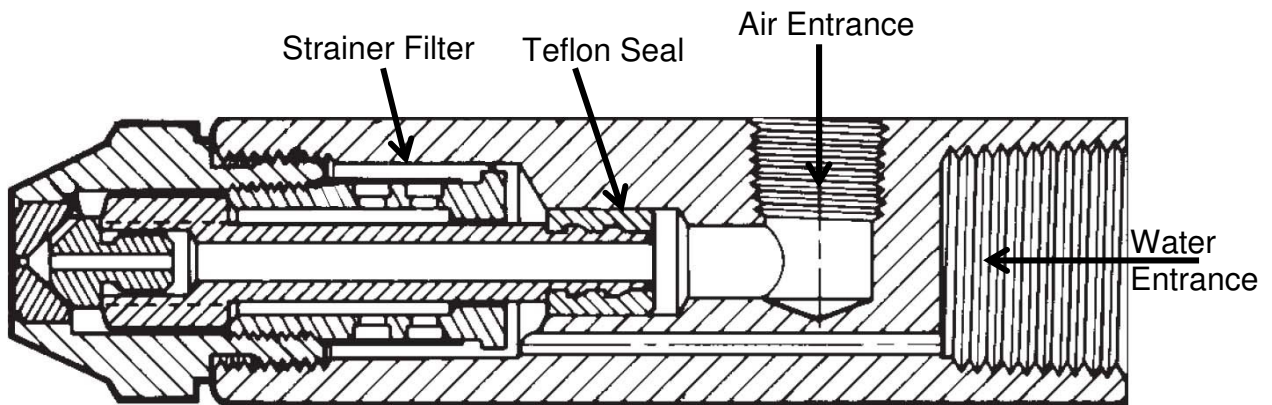


Figure 3.2.4: Delavan 0.75 gph air-assist nozzle [10].

$$Q = Q_{ref} \sqrt{\frac{P_s}{P_{ref}}} \quad \text{Equation 3.2.1}$$

3.2.2. Calculations

The Sauter Mean Diameter (SMD) is calculated from the raw droplet diameter measurements using Equation 3.2.2. The SMD is the diameter of a representative droplet that has a ratio of volume to surface area that is the same as for all of the measured droplets. SMD is typically used to represent sprays for combustion purposes because it properly indicates fineness of the spray from a combustion viewpoint [16].

$$SMD = D_{32} = \frac{\sum N_i d_i^3}{\sum N_i d_i^2} \quad \text{Equation 3.2.2}$$

where d_i is the measured droplet diameter. SMD is generally reported in μm .

The normal distribution can not be used for droplet size distributions because most droplet size distributions have a skewed distribution function with a long tail at large droplet sizes [13]. Also, droplet sizes can never be less than or equal to zero, a problem for the normal distribution which (for distributions with a large range) requires a portion of the distribution to be negative. In place of the normal distribution the lognormal distribution can be used to model the droplet size distributions found in most sprays. The standard deviation for the lognormal distribution, σ_g , is called the geometric standard deviation and is given by Equation 3.2.3 [13].

$$\sigma_g = \exp\left(\frac{\sum N_i (\ln d_i - \ln SMD)^2}{N-1}\right)^{1/2} \quad \text{Equation 3.2.3}$$

where d_i is the measured droplet diameter. The upper and lower error bar values are then calculated with Equation 3.2.4.

$$\text{error bar} = \exp(\ln SMD \pm \ln \sigma_g) \quad \text{Equation 3.2.4}$$

The error bars and corresponding data for measurements shown in this chapter are included in Appendix G. For each measurement in this chapter close to 10,000 droplets were measured with velocity and diameter validation rates greater than 90%, with most measurement validation rates at 95% and greater. The PDA has three photomultipliers; while only two are used to for a measurement. The additional photomultiplier is used to for a redundant measurement, which is compared to the first measurement. If the two measurements are close, the droplet measurement is validated. The validation rate indicates the percentage of attempted measurements that were validated. Only validated droplet measurements are saved by the software. And high validation rate means that the recorded droplet measurements are a very good representation of the spray at the location that the measurement was taken.

3.3. Experimental Results

3.3.1. Simplex Nozzle Static Measurements

The droplet diameters and axial velocities were measured for five different water pressures for the simplex nozzle. Measurements were taken at four radial positions for an axial position of 25 mm. Figure 3.3.1 shows a schematic of the measurement locations within the spray. Although the spray angle of the simplex nozzle varies slightly with supply pressure, the four locations shown in Figure 3.3.1 were used for all of the static measurements so that the results could be compared to the dynamic testing results.

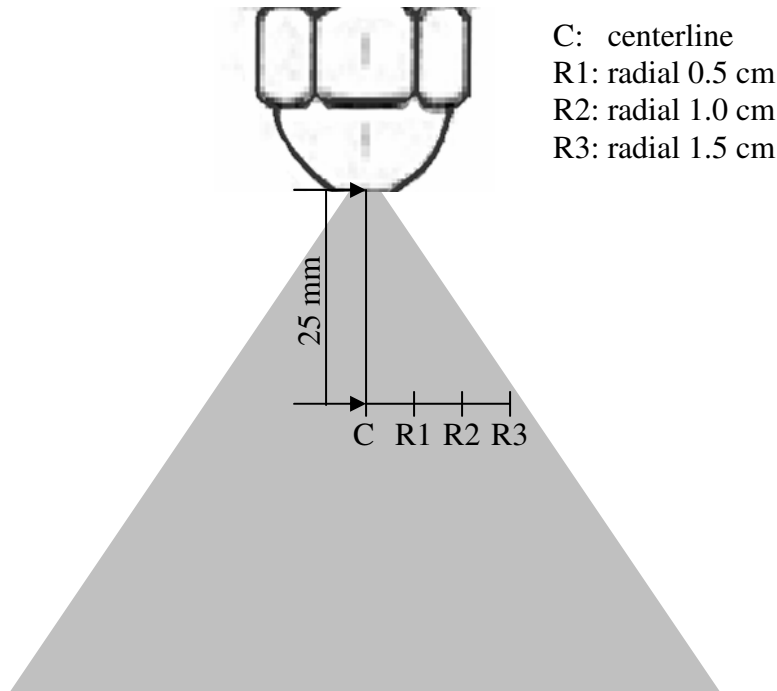


Figure 3.3.1: Measurement locations for simplex nozzle experiments.

The SMD as a function of radial position is shown for several supply pressures in Figure 3.3.2. The axial velocity as a function of radial position for several supply pressures is shown in Figure 3.3.3. Figure 3.3.2 shows that the simplex nozzle spray droplet diameters become less sensitive to increases in supply pressure as the supply pressure increases, particularly at the centerline and 0.5 cm above a supply pressure of 200 psi. The axial velocities, shown in Figure 3.3.3, also become less sensitive to changes in pressure as the supply pressure is increased. Note that the PDA takes one dimensional (axial velocity) measurements only, and for the simplex (or pressure-swirl) nozzle the radial and tangential components of velocity are also a very important component. The unmeasured radial and tangential velocity components may account for the trend in velocity at radial positions 1.0 cm and 1.5 cm.

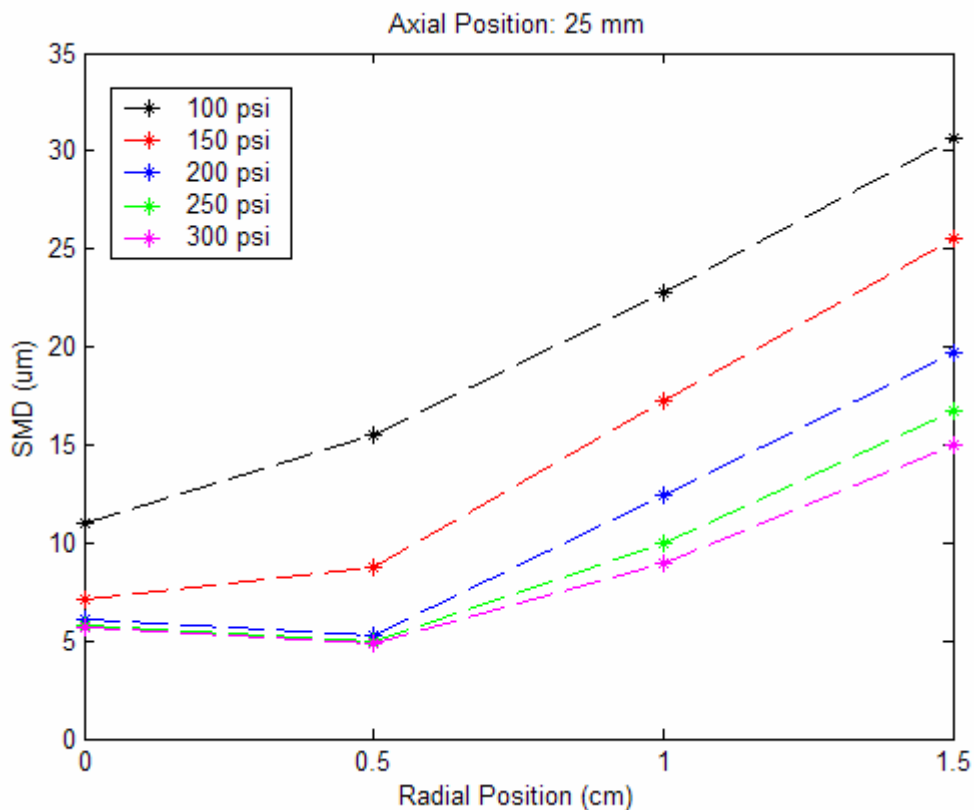


Figure 3.3.2: Simplex nozzle static measurements, SMD vs. radial position for various supply pressures.

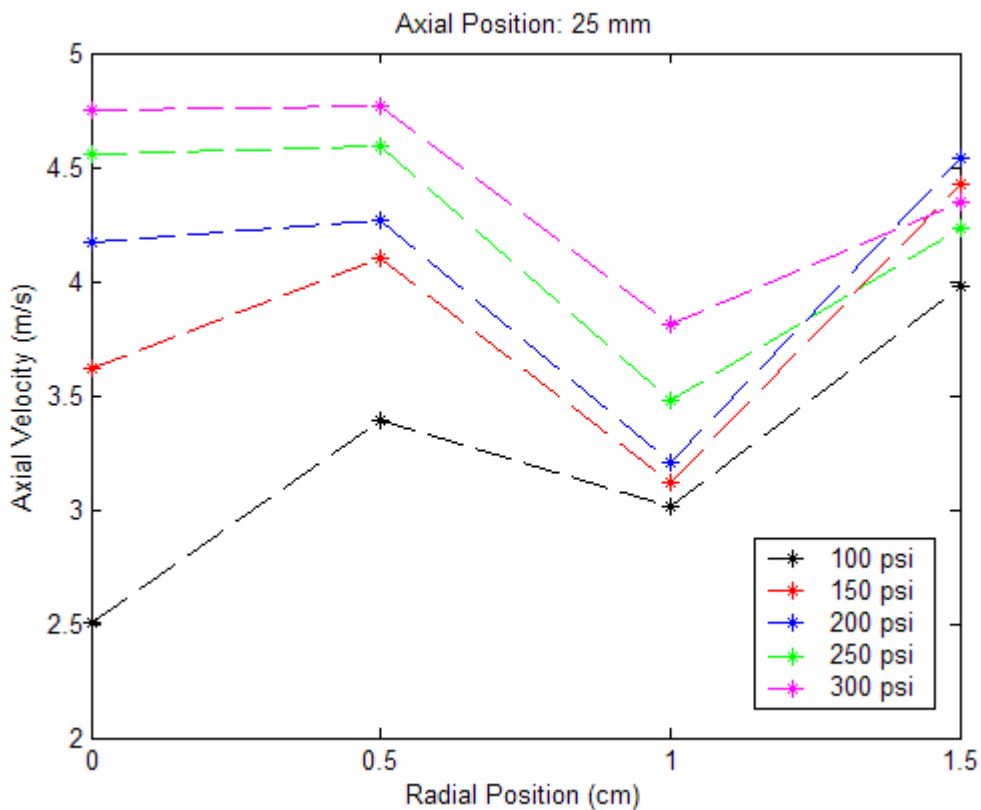


Figure 3.3.3: Simplex nozzle static measurements, axial velocity vs. radial position for various supply pressures.

3.3.2. Simplex Nozzle Dynamic Measurements

The simplex nozzle dynamic measurements used the system setup shown in Figure 3.2.1 and Figure 3.2.2. Measurements were taken for three different mean pressures (200, 250, and 300 psi) and four different sinusoidal pressure oscillation amplitudes (± 30 , ± 50 , ± 75 , and ± 100 psi). The frequency of the dynamic input was 100 Hz. Using an angular encoder attachment for the PDA, the measurements for the dynamic tests were phase-locked to the modulation signal allowing the measured droplets to be divided into separate ‘bins’ for analysis. A bin size of 2° was used to investigate the SMDs and axial velocities of droplets measured during each phase bin of the modulation signal cycle. The process of grouping droplets into phase bins and calculating the SMD, mean axial velocity, and number of droplets is illustrated in Figure 3.3.4.

The simplex atomizer under static operating conditions formed a relatively uniform density spray with some visibly larger droplets located at the outside edges of the spray. Under dynamic modulation at the highest pressure modulation amplitude (± 100 psi) the spray visibly changed structure. Instead of a uniformly dense spray, what appeared to be a very dense column of very small droplets was seen at the center of the spray. The outer edges looked similar to the outer edges of the static spray. These observations should be further investigated with high speed photography, which could also identify the formation of any vortical structures as seen by Chang et al. [4].

At a mean pressure of 250 psi measurements were taken at the four radial positions shown in Figure 3.3.1. The droplet size (in SMD) results of the four modulation amplitudes for each of the four radial positions are shown in Figure 3.3.5, Figure 3.3.6, Figure 3.3.7, and Figure 3.3.8. For comparison, the SMD results at each radial position are also shown for each of the modulation amplitudes in Figure 3.3.9, Figure 3.3.10, Figure 3.3.11, and Figure 3.3.12. There are several observations that can be made from the droplet SMD data. First, the ± 100 psi modulation data appears flat, or nearly flat, at the centerline and 0.5 cm. Second, the ± 30 psi modulation data shows the overall greatest modulation in SMD, especially at the outermost radial positions of 1.0 cm and 1.5 cm. Third, comparison of the phase that the lowest SMD occurs at for each of the pressure modulation amplitudes shows a change in phase between the different modulation amplitudes, which is most evident at 1.0 cm and 1.5 cm. Comparing the position of the lowest SMD point at each radial point for the same modulation amplitude in Figure 3.3.9, Figure 3.3.10, Figure 3.3.11, and Figure 3.3.12 shows that the phase of the lowest SMD is nearly the same across the radius for the various modulation amplitudes. The trend that was seen in the static data, where the smallest SMDs occur at the centerline and the largest at the outermost edge (1.5 cm), is also seen here.

The velocity measurements for the 250 psi mean pressure tests with the four modulation amplitudes at each of the four radial positions are shown in Figure 3.3.13, Figure 3.3.14, Figure 3.3.15, and Figure 3.3.16. For comparison, the velocity results at each radial position are also shown for each of the modulation amplitudes in Figure 3.3.17, Figure 3.3.18, Figure 3.3.19, and Figure 3.3.20. Several observations can be made from the axial velocity measurements. The largest change in axial velocity occurs at the centerline, where the smallest SMDs also occur. Phase differences between the modulation amplitudes are also evident in the axial velocity, although the phases of the peak axial velocities do not appear at the same phase across the radius of the spray when the different radial positions for the

same modulation amplitude are compared. This difference may occur because only axial velocity is measured by the PDA.

Droplets are grouped into phase bins based on the phase of their arrival time.

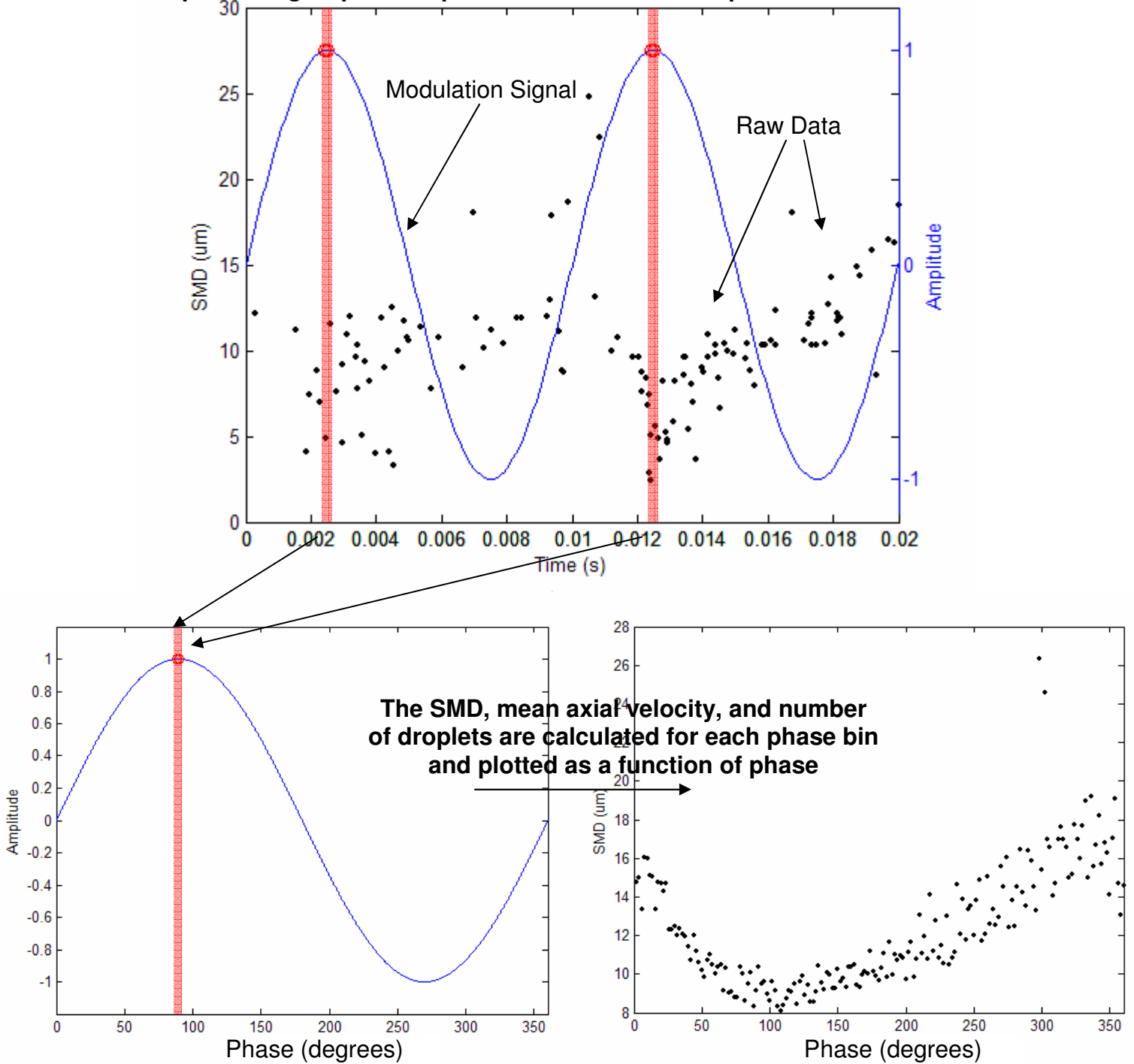


Figure 3.3.4: Phase bin calculations for dynamic phase-locked measurements.

The count (%), or number of droplets measured in each phase bin plotted as a percentage of the total number of droplets measured during each test, for the different modulation amplitudes at each radial position in Figure 3.3.21, Figure 3.3.22, Figure 3.3.23, and Figure 3.3.24. For comparison, the droplet count (%) at each radial position are also shown for each of the modulation amplitudes in Figure 3.3.25, Figure 3.3.26, Figure 3.3.27, and Figure 3.3.28. The mean value that would occur for an evenly distributed droplet count with 180 bins is 0.55. The peaks in the count that occur over the modulation cycle correspond to the minimums in the droplet SMD measurements. This is not unexpected because the larger droplets, presumably created by the lowest supply pressures, hold a larger percentage of the total volume of the spray that when coupled with the lower flow rate (lower pressure) results in the creation of fewer droplets. Since the count follows the SMD trend a phase difference between the different modulation amplitudes also appears in these plots, especially at 1.0 cm and 1.5 cm.

Table 3.3.1 shows a summary of the mean SMDs and axial velocities for the simplex nozzle with a mean pressure of 250 psi. At the centerline, the mean SMD is reduced for the modulation amplitudes of 50 psi and above and the mean axial velocity is increased for the 75 psi and 100 psi modulation cases. For the three radial positions (0.5 cm, 1.0 cm, 1.5 cm) the mean SMD increases for all of the dynamic modulation tests. In general, the mean axial velocities at 0.5 cm and 1.0 cm are reduced or remain the same. At the outermost position, 1.5 cm, the mean axial velocities for dynamic tests increase or remain the same as the static case.

Table 3.3.1: Summary of mean SMDs and axial velocities for static and dynamic testing, Simplex nozzle, 250 psi mean pressure.

Modulation (psi)	Centerline		Radial: 0.5 cm		Radial: 1.0 cm		Radial: 1.5 cm	
	SMD (μm)	V (m/s)	SMD (μm)	V (m/s)	SMD (μm)	V (m/s)	SMD (μm)	V (m/s)
0, static	6	4.6	5	4.6	9	3.5	17	4.3
±30	6.6	3.9	7.4	4.0	12.3	3.5	19.8	5.2
±50	5.8	4.3	7.6	3.8	12.0	3.5	20.5	4.9
±75	5.8	5.0	7.3	4.0	11.5	3.8	20.4	5
±100	4.5	4.8	7.1	3.8	11.9	3.5	19.7	4.3

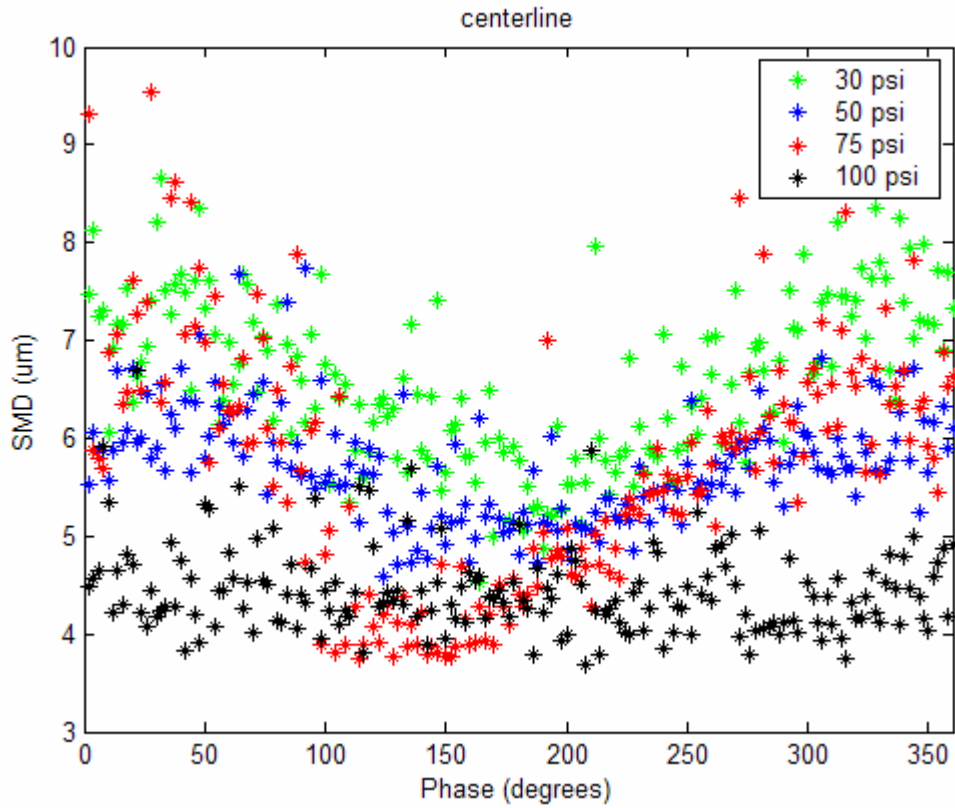


Figure 3.3.5: Simplex nozzle phase-locked dynamic measurement SMD results, at centerline, 250 psi mean pressure.

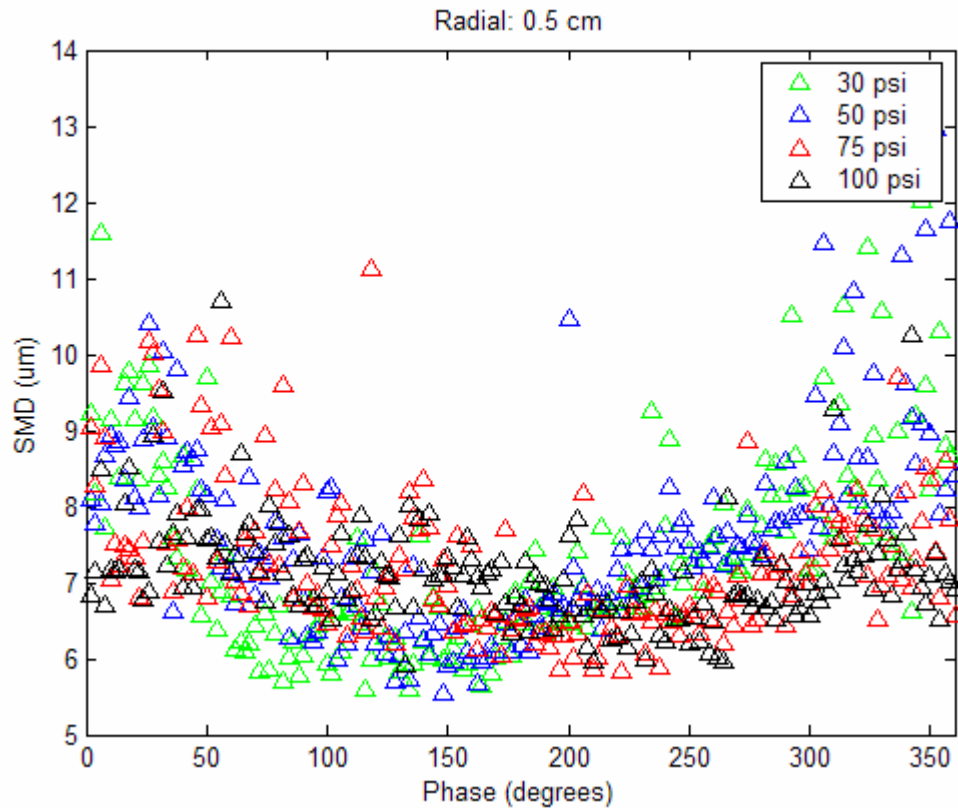


Figure 3.3.6: Simplex nozzle phase-locked dynamic measurement SMD results, at radial 0.5 cm, 250 psi mean pressure.

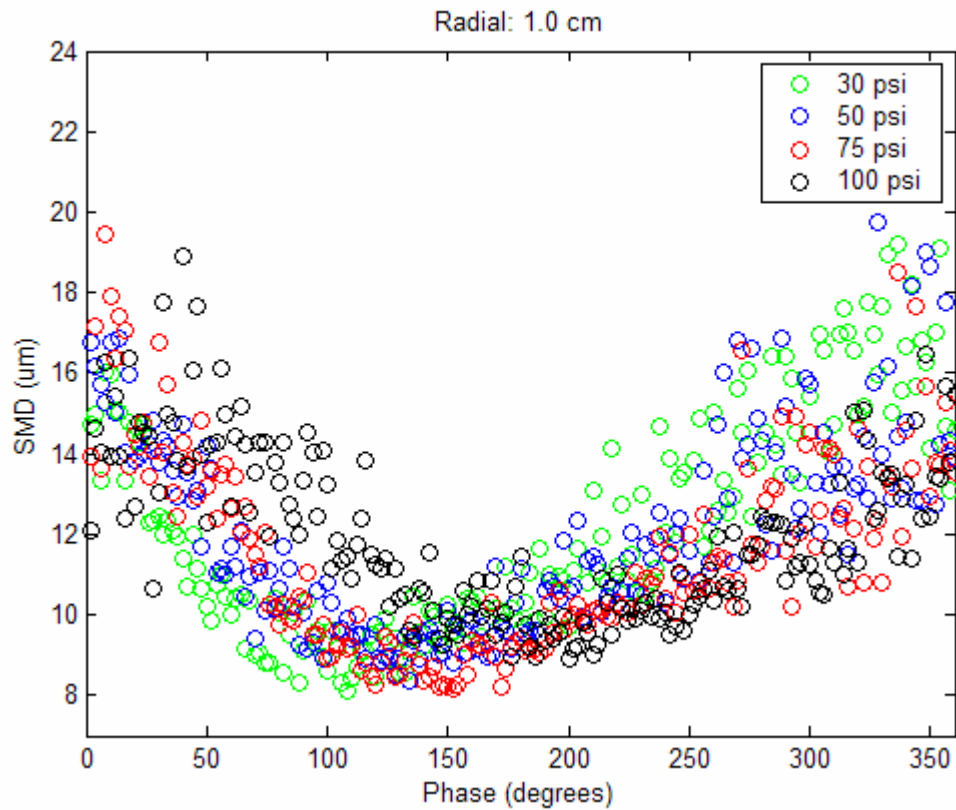


Figure 3.3.7: Simplex nozzle phase-locked dynamic measurement SMD results, at radial 1.0 cm, 250 psi mean pressure.

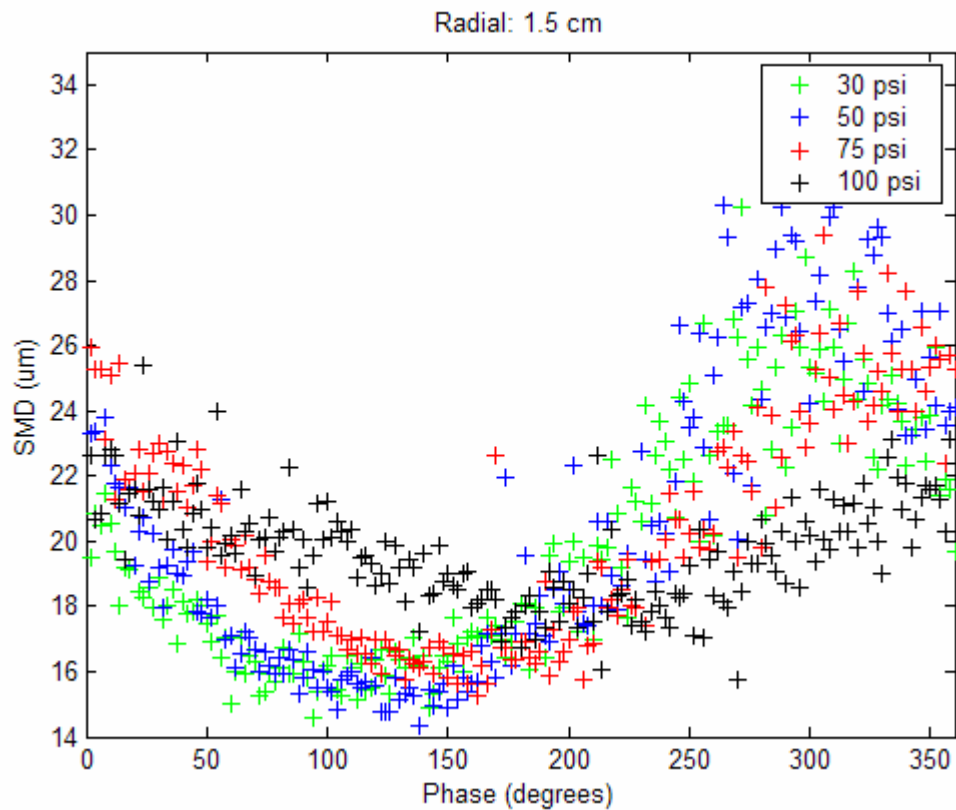


Figure 3.3.8: Simplex nozzle phase-locked dynamic measurement SMD results, at radial 1.5 cm, 250 psi mean pressure.

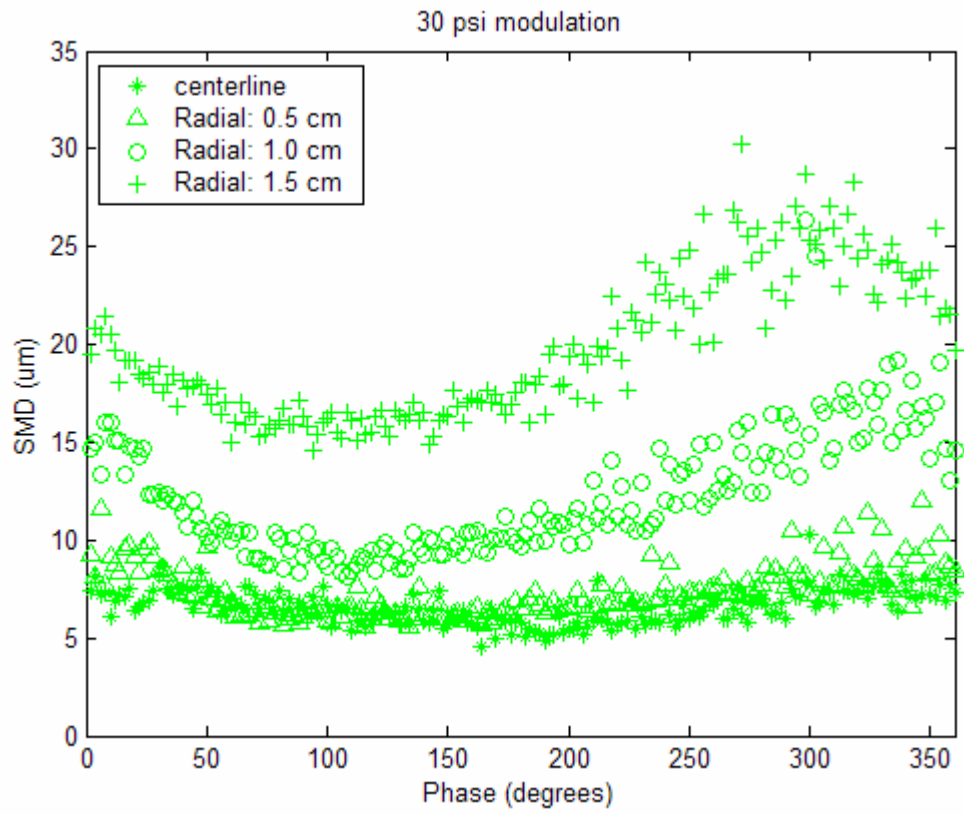


Figure 3.3.9: Simplex nozzle phase-locked dynamic measurement SMD results, ± 30 psi, 250 psi mean pressure.

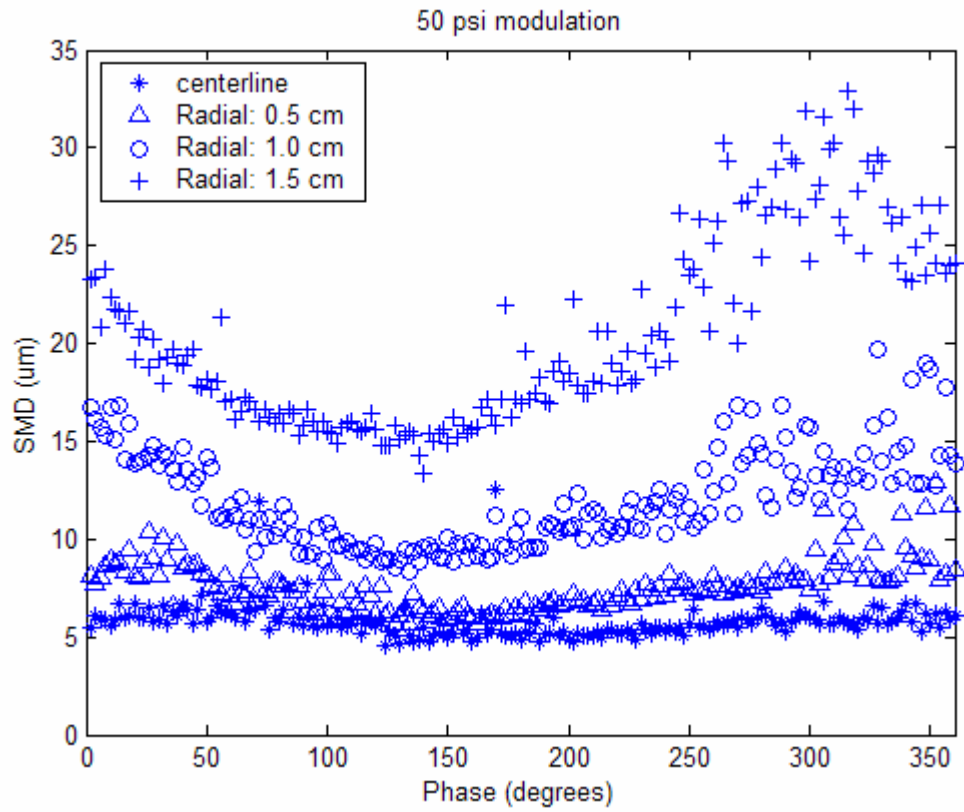


Figure 3.3.10: Simplex nozzle phase-locked dynamic measurement SMD results, ± 50 psi, 250 psi mean pressure.

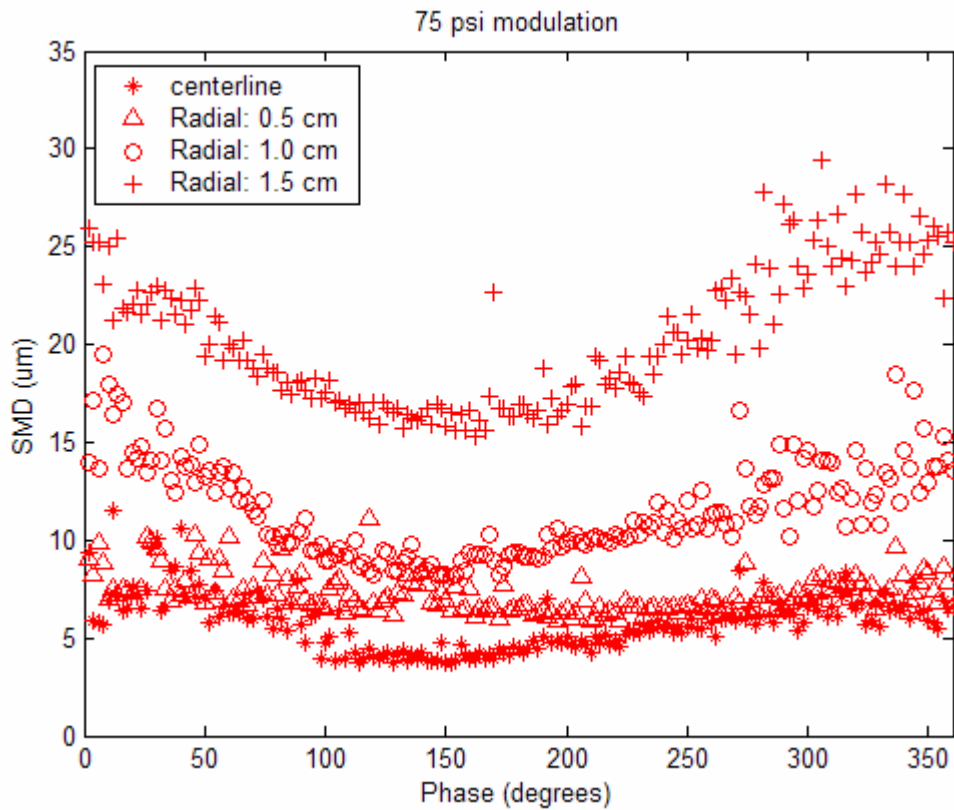


Figure 3.3.11: Simplex nozzle phase-locked dynamic measurement SMD results, ± 75 psi, 250 psi mean pressure.

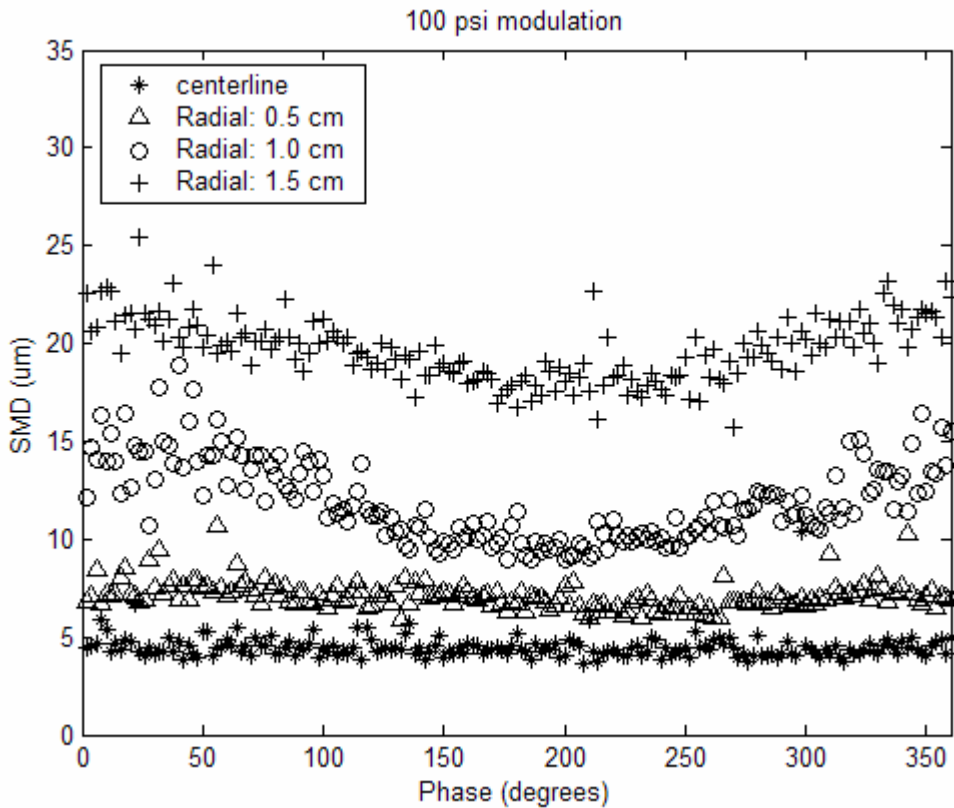


Figure 3.3.12: Simplex nozzle phase-locked dynamic measurement SMD results, ± 100 psi, 250 psi mean pressure.

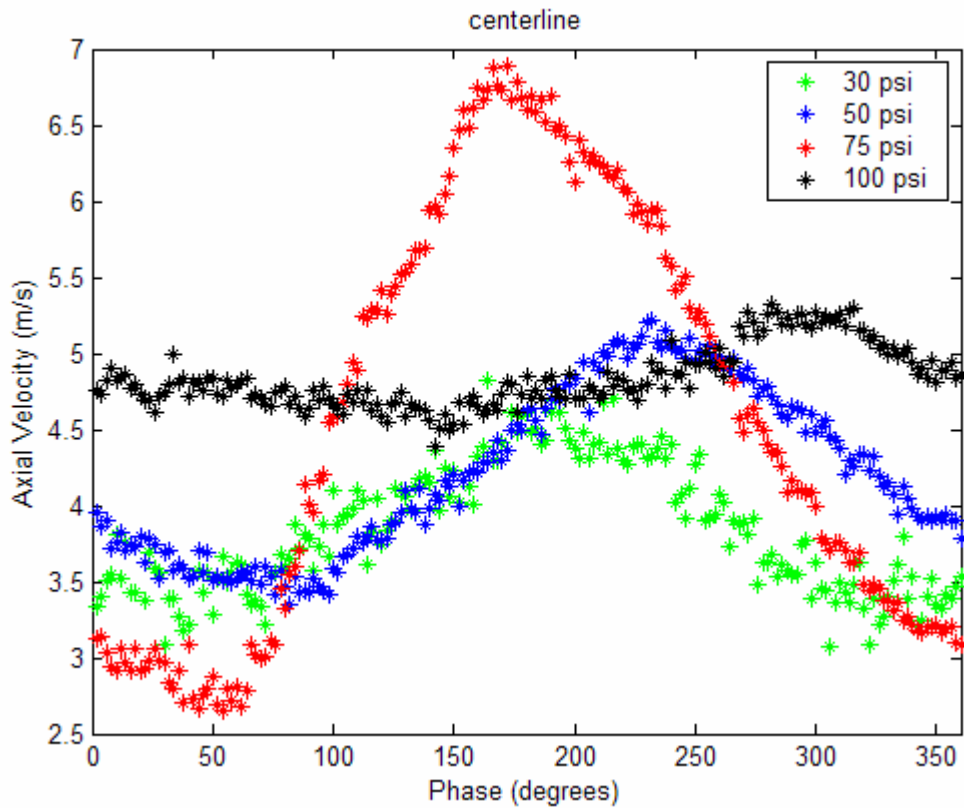


Figure 3.3.13: Simplex nozzle phase-locked dynamic measurement velocity results, centerline, 250 psi mean pressure.

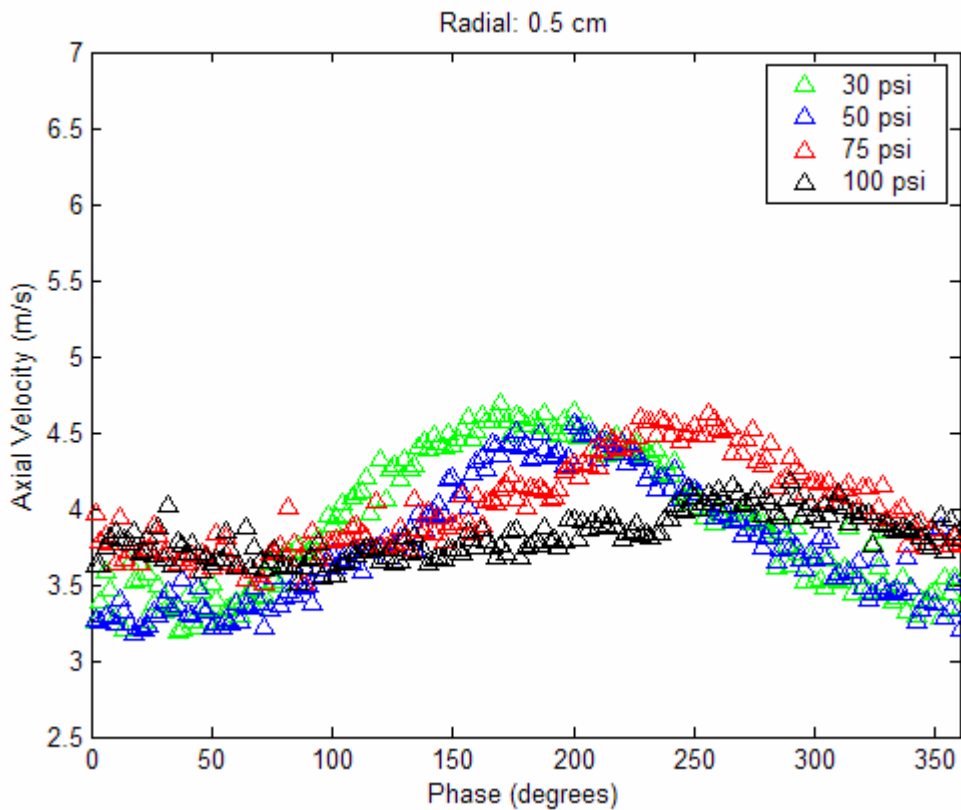


Figure 3.3.14: Simplex nozzle phase-locked dynamic measurement velocity results, radial 0.5 cm, 250 psi mean pressure.

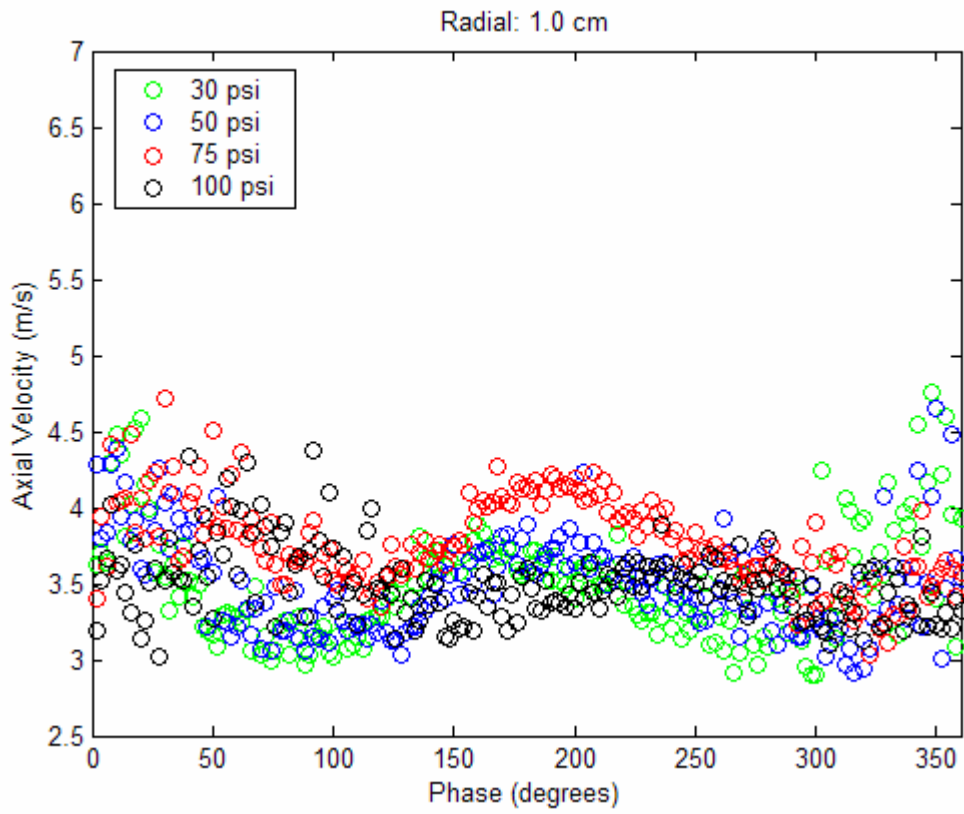


Figure 3.3.15: Simplex nozzle phase-locked dynamic measurement velocity results, radial 1.0 cm, 250 psi mean pressure.

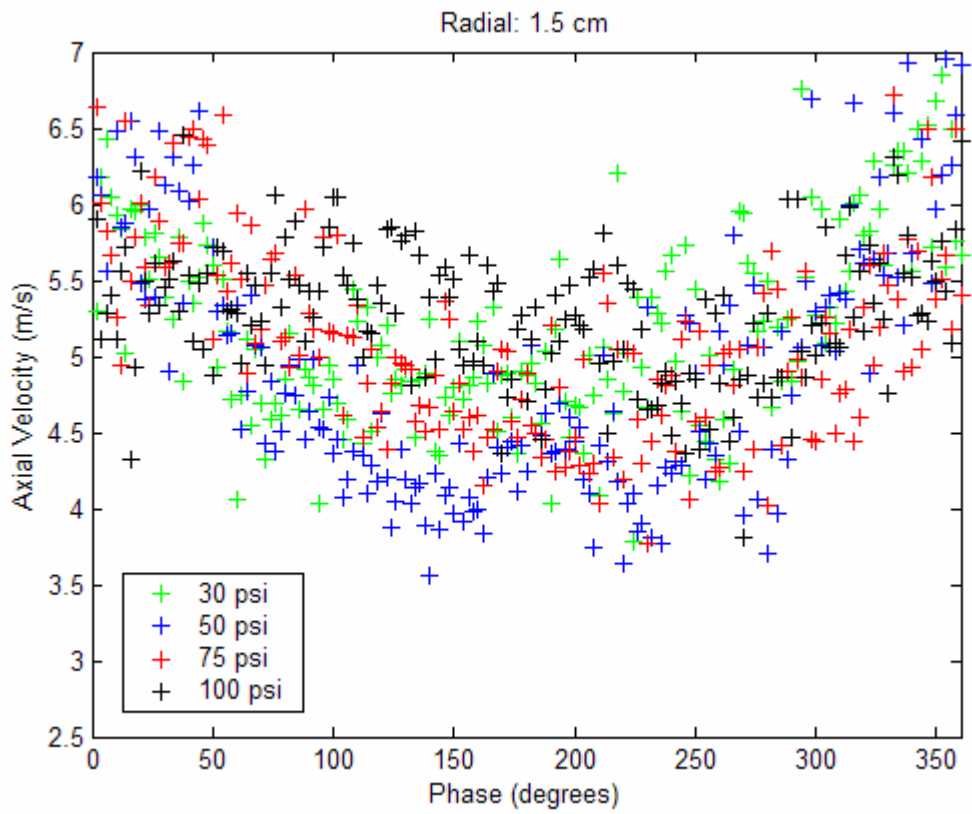


Figure 3.3.16: Simplex nozzle phase-locked dynamic measurement velocity results, radial 1.5 cm, 250 psi mean pressure.

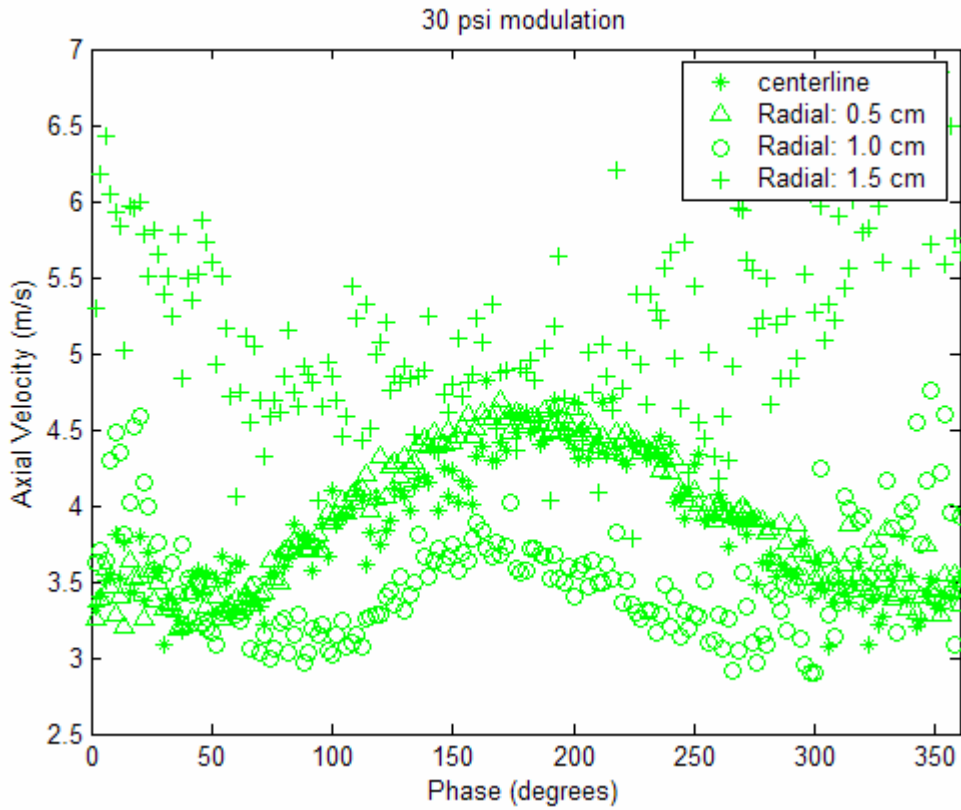


Figure 3.3.17: Simplex nozzle phase-locked dynamic measurement velocity results, ± 30 psi, 250 psi mean pressure.

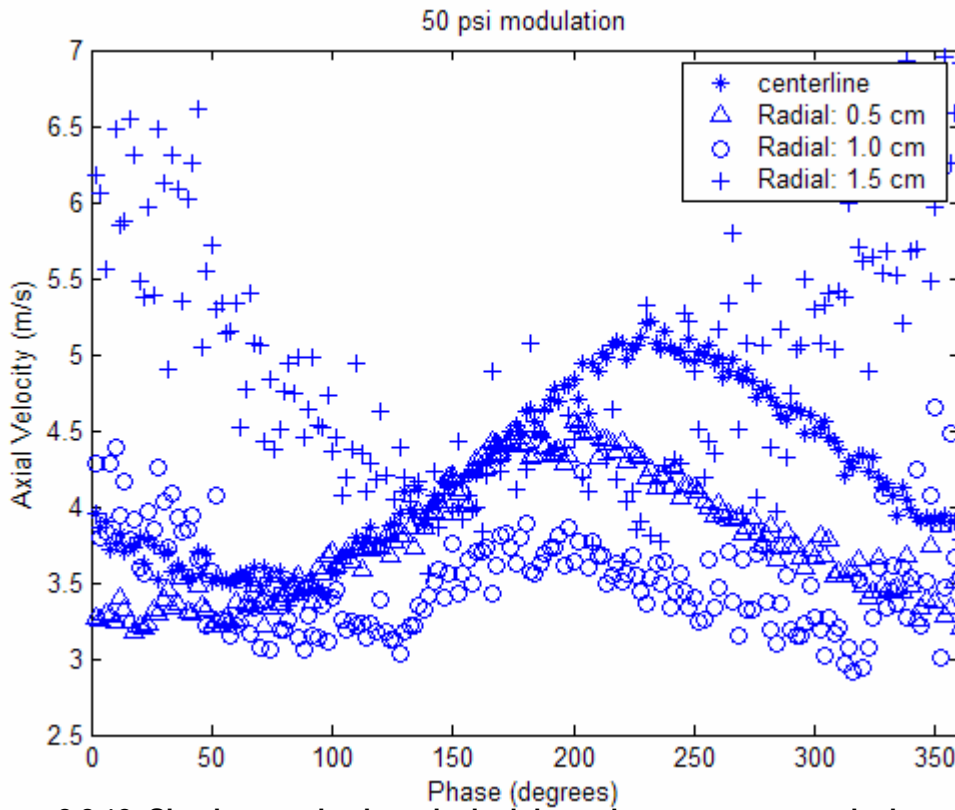


Figure 3.3.18: Simplex nozzle phase-locked dynamic measurement velocity results, ± 50 psi, 250 psi mean pressure.

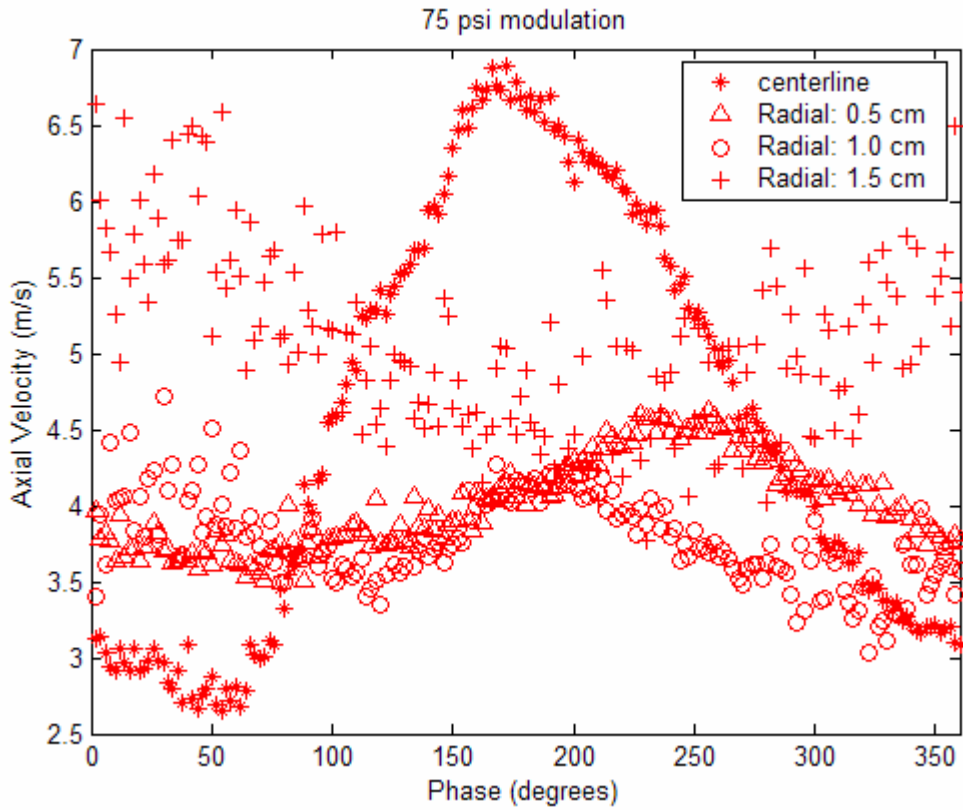


Figure 3.3.19: Simplex nozzle phase-locked dynamic measurement velocity results, ± 75 psi, 250 psi mean pressure.

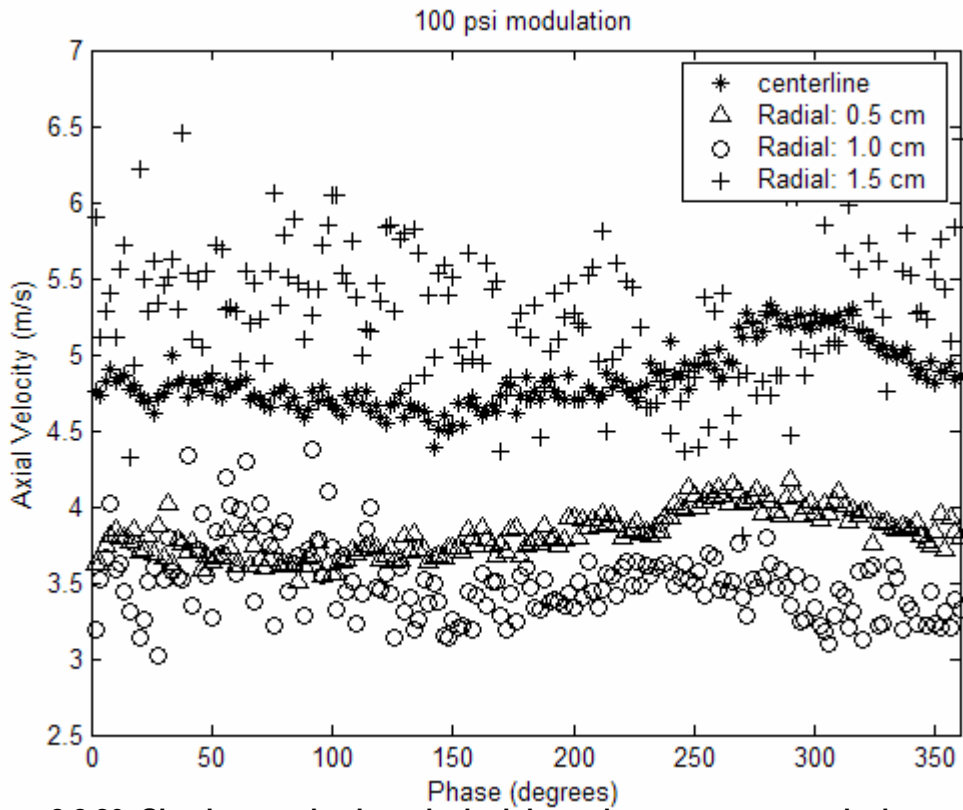


Figure 3.3.20: Simplex nozzle phase-locked dynamic measurement velocity results, ± 100 psi, 250 psi mean pressure.

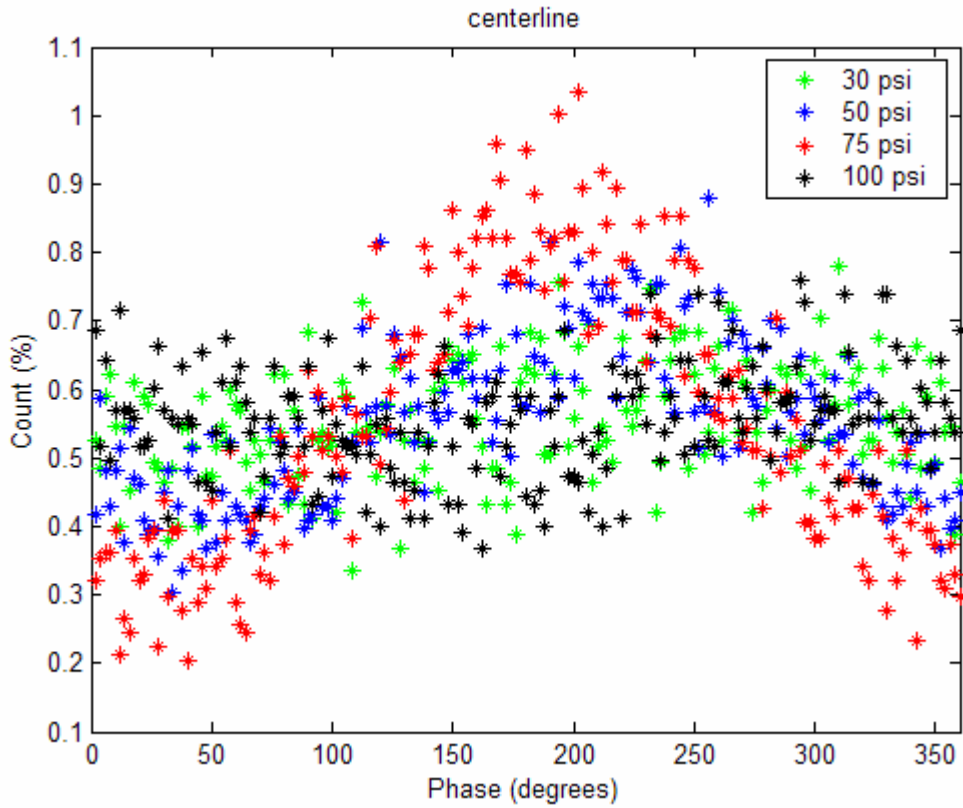


Figure 3.3.21: Simplex nozzle phase-locked dynamic measurement count (%) results, centerline, 250 psi mean pressure.

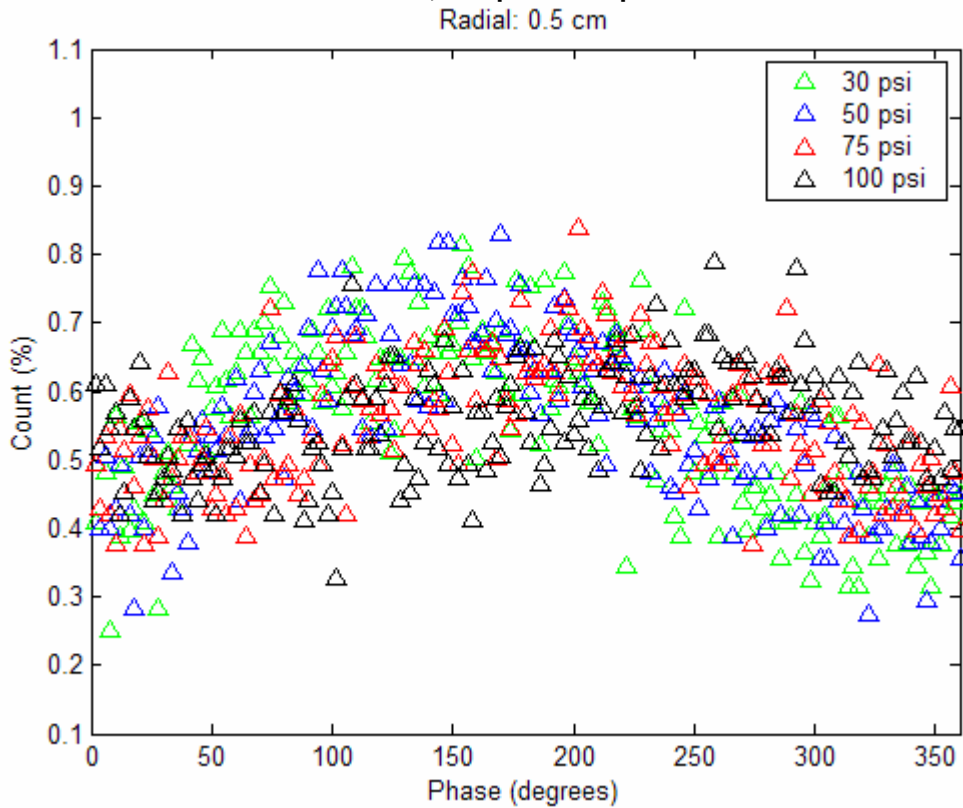


Figure 3.3.22: Simplex nozzle phase-locked dynamic measurement count (%) results, radial 0.5 cm, 250 psi mean pressure.

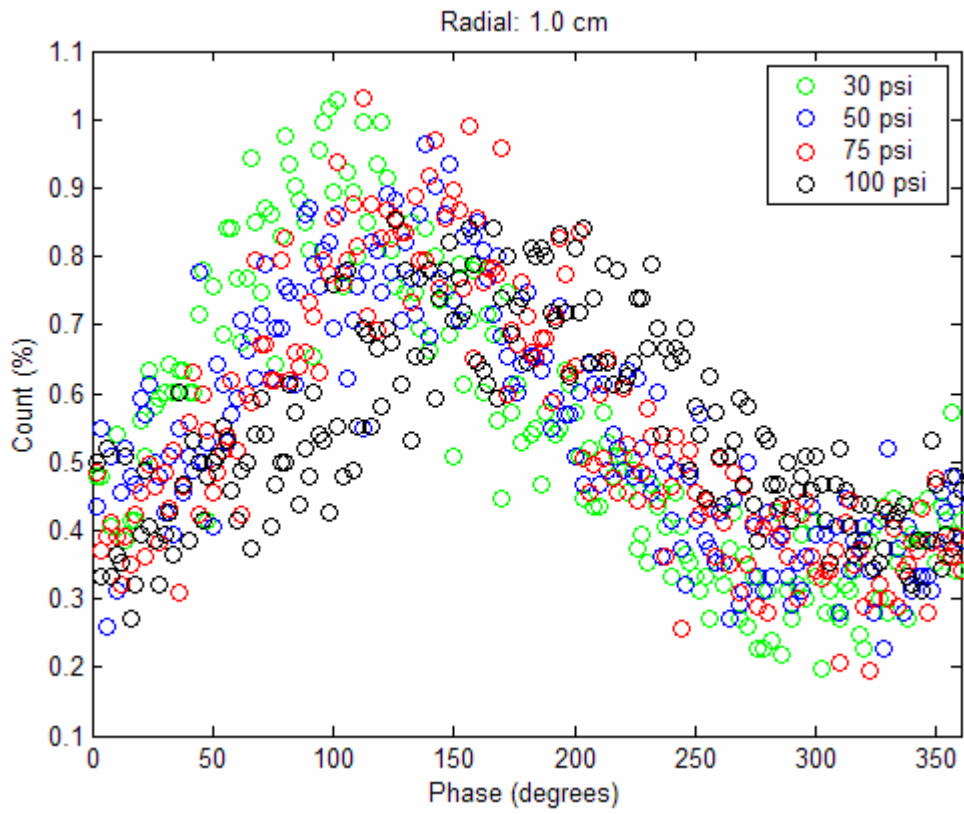


Figure 3.3.23: Simplex nozzle phase-locked dynamic measurement count (%) results, radial 1.0 cm, 250 psi mean pressure.

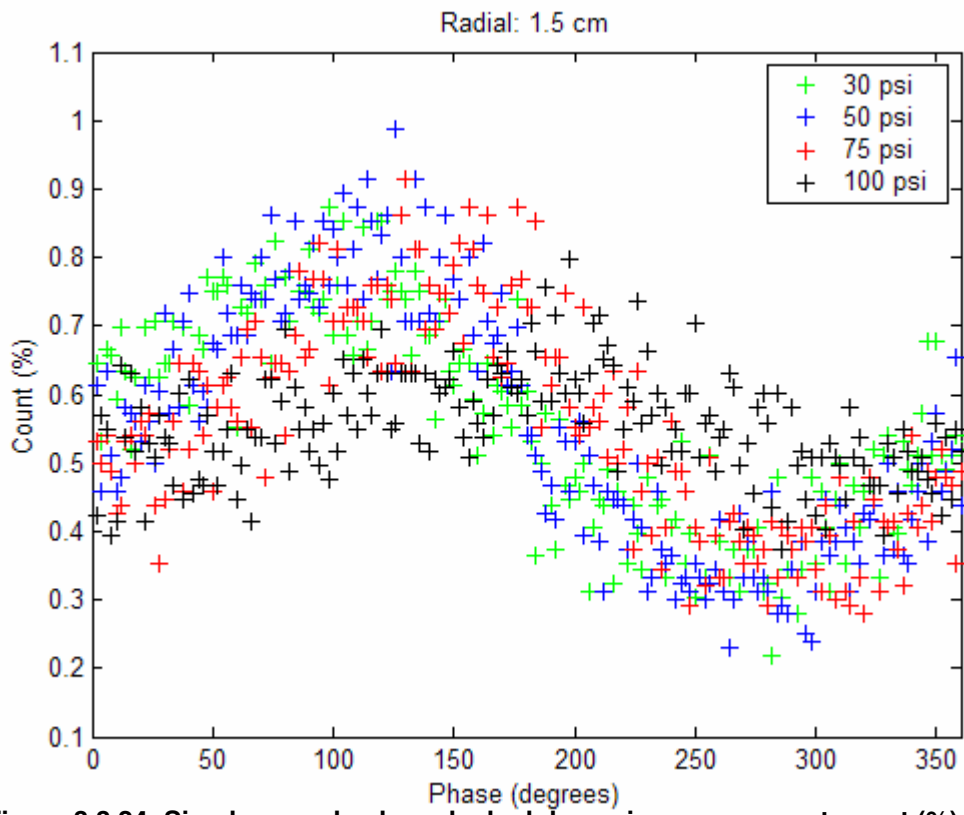


Figure 3.3.24: Simplex nozzle phase-locked dynamic measurement count (%) results, radial 1.5 cm, 250 psi mean pressure.

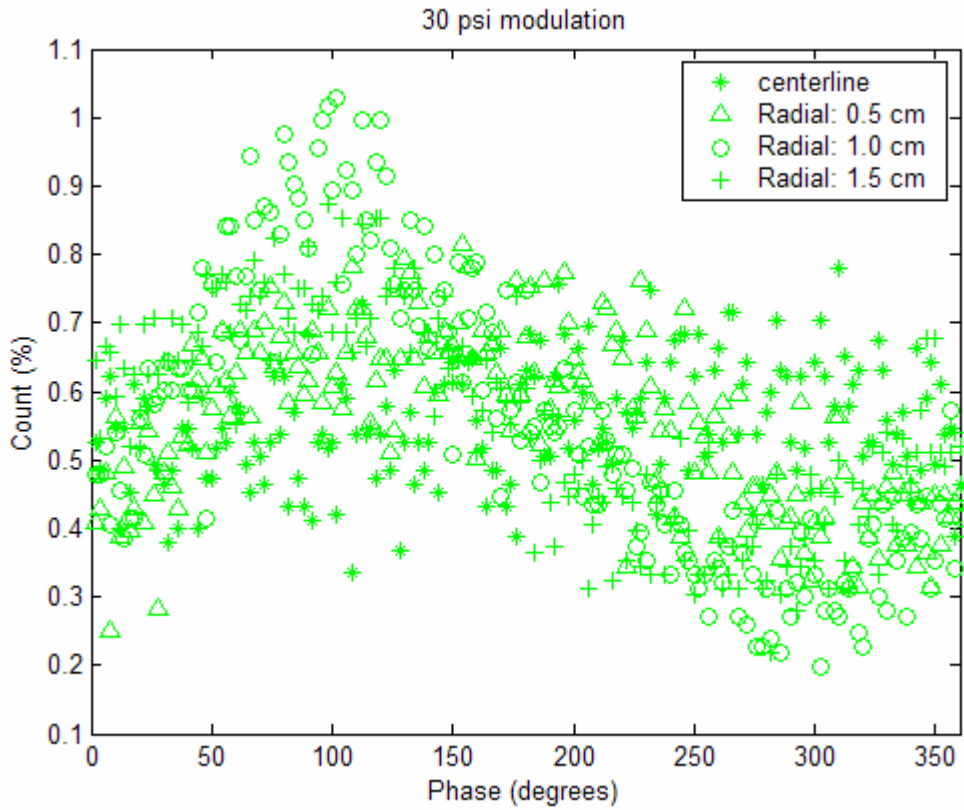


Figure 3.3.25: Simplex nozzle phase-locked dynamic measurement count (%) results, ± 30 psi, 250 psi mean pressure.

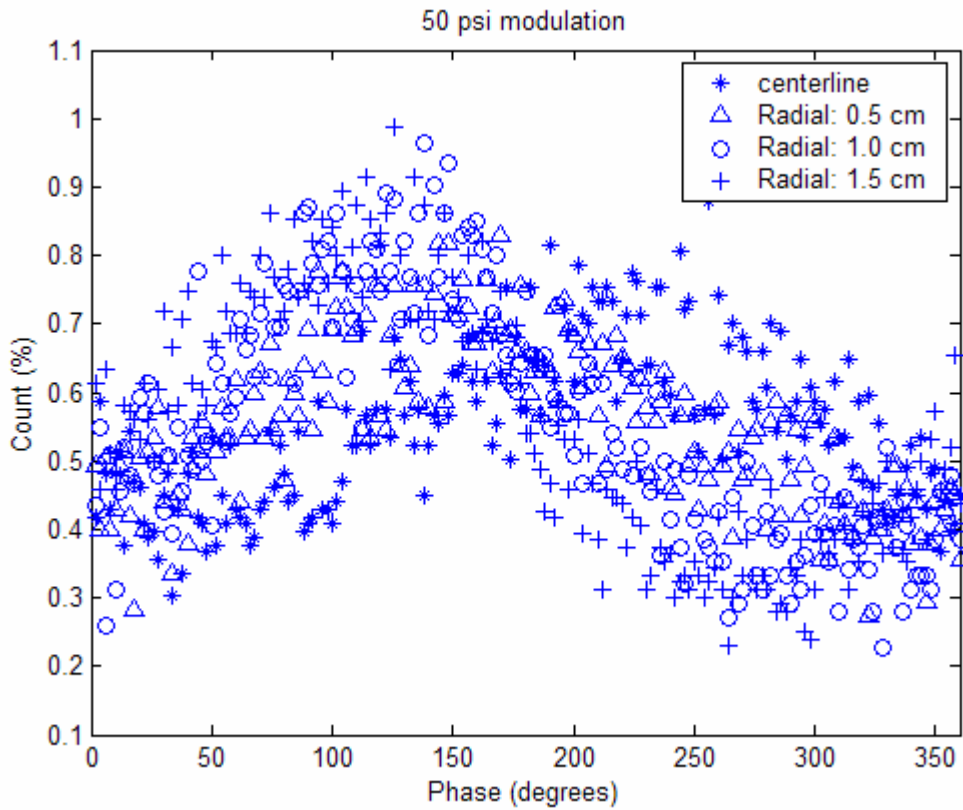


Figure 3.3.26: Simplex nozzle phase-locked dynamic measurement count (%) results, ± 50 psi, 250 psi mean pressure.

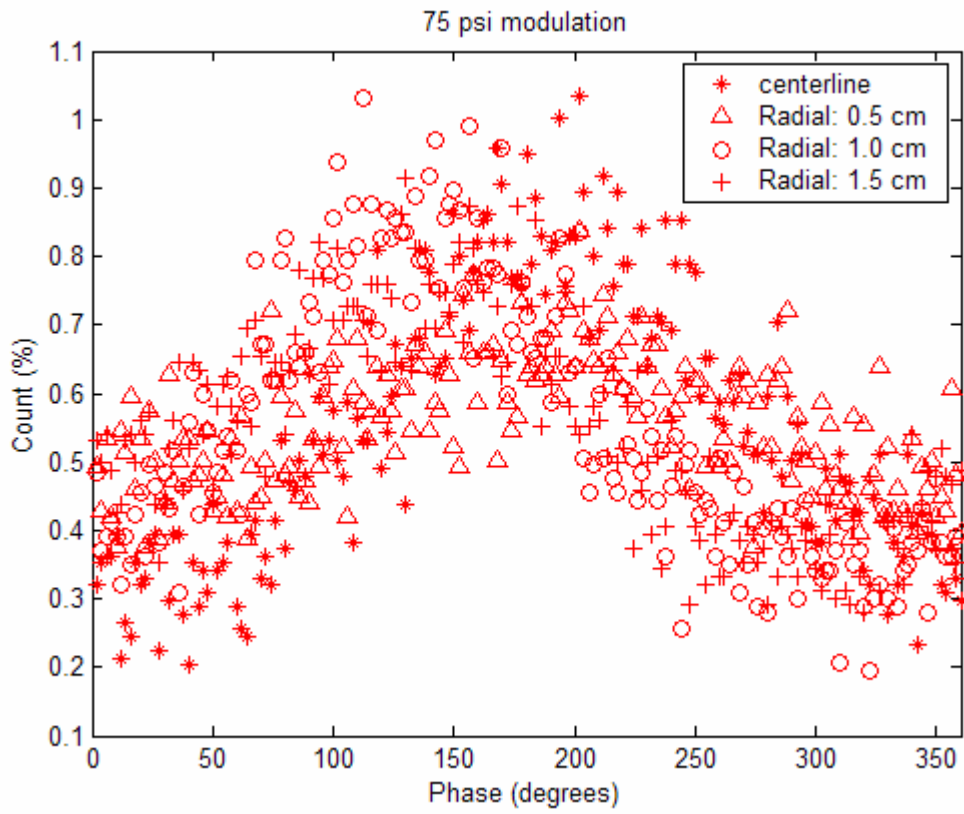


Figure 3.3.27: Simplex nozzle phase-locked dynamic measurement count (%) results, ± 75 psi, 250 psi mean pressure.

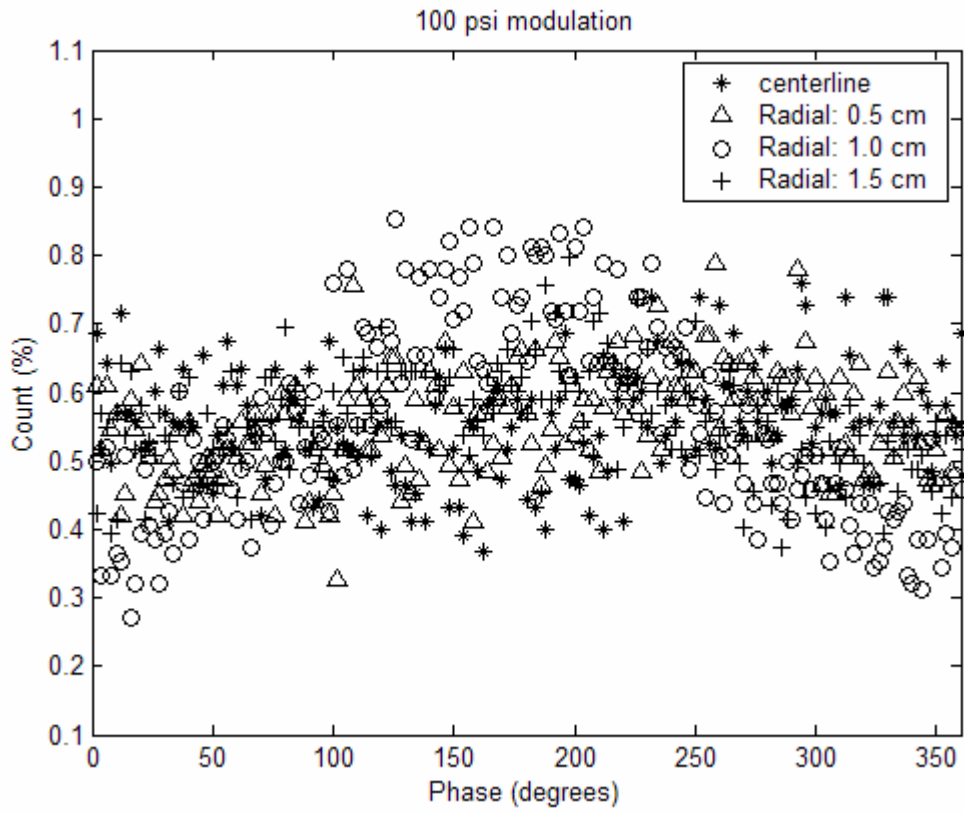


Figure 3.3.28: Simplex nozzle phase-locked dynamic measurement count (%) results, ± 100 psi, 250 psi mean pressure.

At a mean pressure of 200 psi measurements were taken at two radial positions: the centerline and 1.0 cm. The droplet size results are shown in Figure 3.3.29 and Figure 3.3.30. Again the ± 30 psi case shows the overall largest modulation in SMD. The other three modulation amplitudes also show moderate modulation. At the centerline the modulation is greater than the centerline modulation for the 250 psi mean pressure tests. Unlike the 250 psi mean pressure measurements, a phase shift between the modulation amplitude cases is not clearly distinguishable at either radial position.

The axial velocity results are shown in Figure 3.3.31 and Figure 3.3.32. At the centerline a large change in axial velocity occurs for all of the modulation amplitudes. The largest change in axial velocity occurs for ± 30 psi followed by ± 50 psi, ± 75 psi, and then ± 100 psi. For the three lowest modulation amplitudes a secondary peak occurs a little before the primary peak that does not occur in the ± 100 psi case. Also, a phase shift is evident between the different modulation amplitudes. At 1.0 cm, ± 30 psi has the largest axial velocity modulation while the three higher modulation amplitudes show a minimal amount of modulation.

The count (%) plots for the 200 psi mean pressure tests are shown in Figure 3.3.33 and Figure 3.3.34. At the centerline the modulation is evident for all of the amplitudes with ± 30 showing the largest range and ± 100 showing the least. At 1.0 cm ± 30 psi has a large range, whereas the three larger modulation amplitudes show a minimal change across the modulation cycle. Again, the peak in droplet count and axial velocity corresponds to the minimum in SMD.

Table 2.1.1 shows a summary of the mean SMDs and axial velocities for the simplex nozzle with a mean pressure of 200 psi. At the centerline the mean SMD increases for ± 30 and ± 50 psi but decreases for ± 75 and ± 100 psi as compared to the static measurement. All of the mean dynamic axial velocities increase compared to the static measurement. At 1.0 cm the mean SMD increases for the dynamic cases whereas the mean axial velocities remain very close to the static axial velocity.

Table 3.3.2: Summary of mean SMDs and axial velocities for static and dynamic testing, Simplex nozzle, 200 psi mean pressure.

Modulation (psi)	Centerline		Radial: 1.0 cm	
	SMD (μm)	V (m/s)	SMD (μm)	V (m/s)
0, static	6.0	4.1	12.4	3.2
± 30	6.3	4.5	14.7	3.2
± 50	6.4	4.4	12.9	3.4
± 75	5.5	4.4	13.0	3.2
± 100	5.2	4.3	13.6	3.1

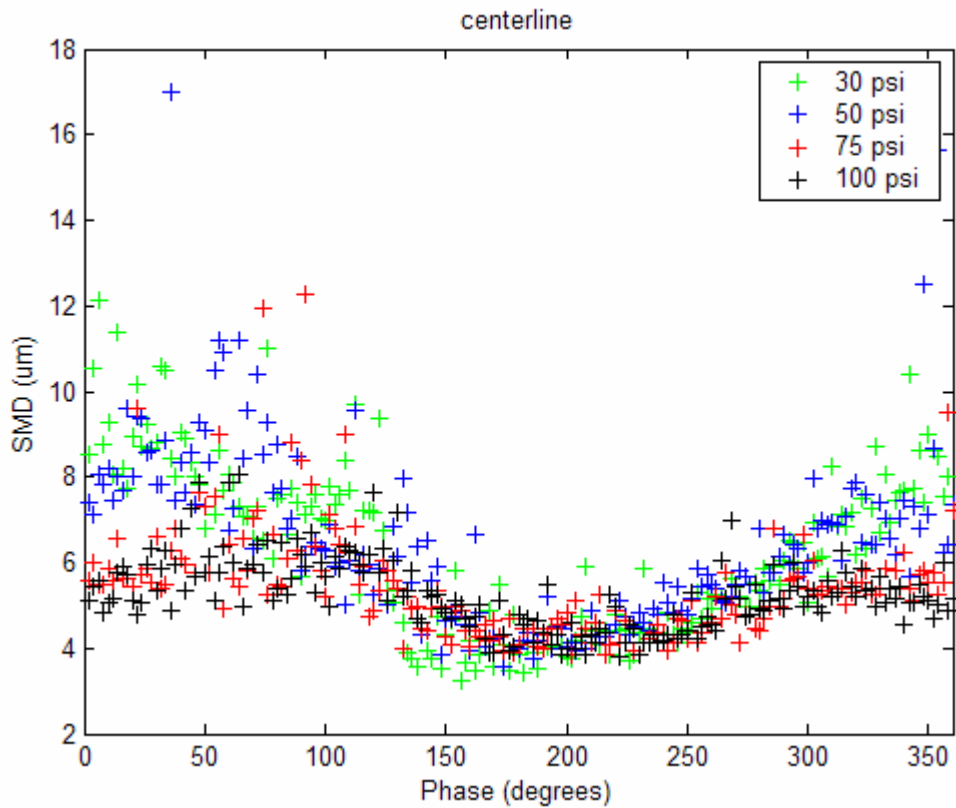


Figure 3.3.29: Simplex nozzle phase-locked dynamic measurement SMD results, centerline, 200 psi mean pressure.

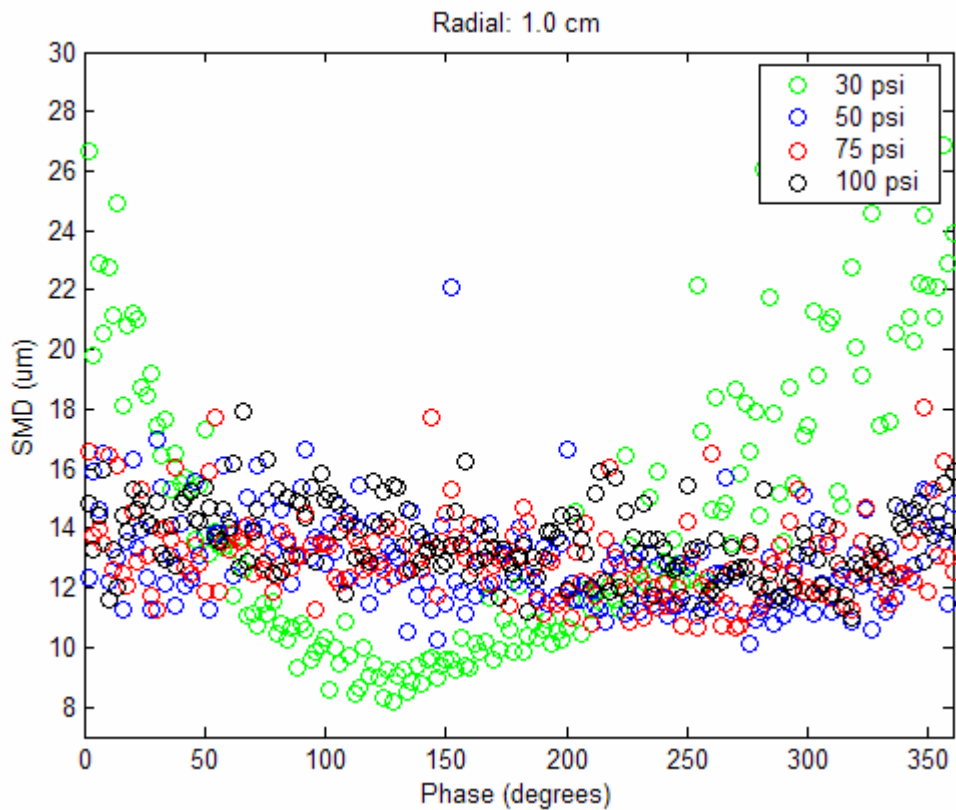


Figure 3.3.30: Simplex nozzle phase-locked dynamic measurement SMD results, radial 1.0 cm, 200 psi mean pressure.

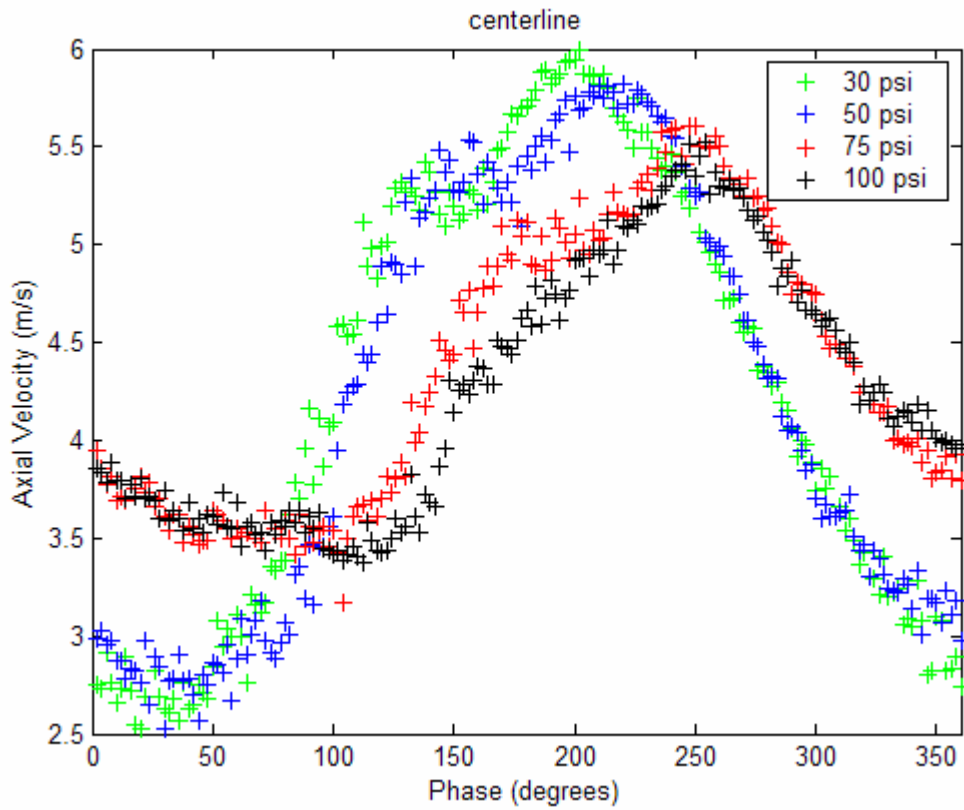


Figure 3.3.31: Simplex nozzle phase-locked dynamic measurement velocity results, centerline, 200 psi mean pressure.

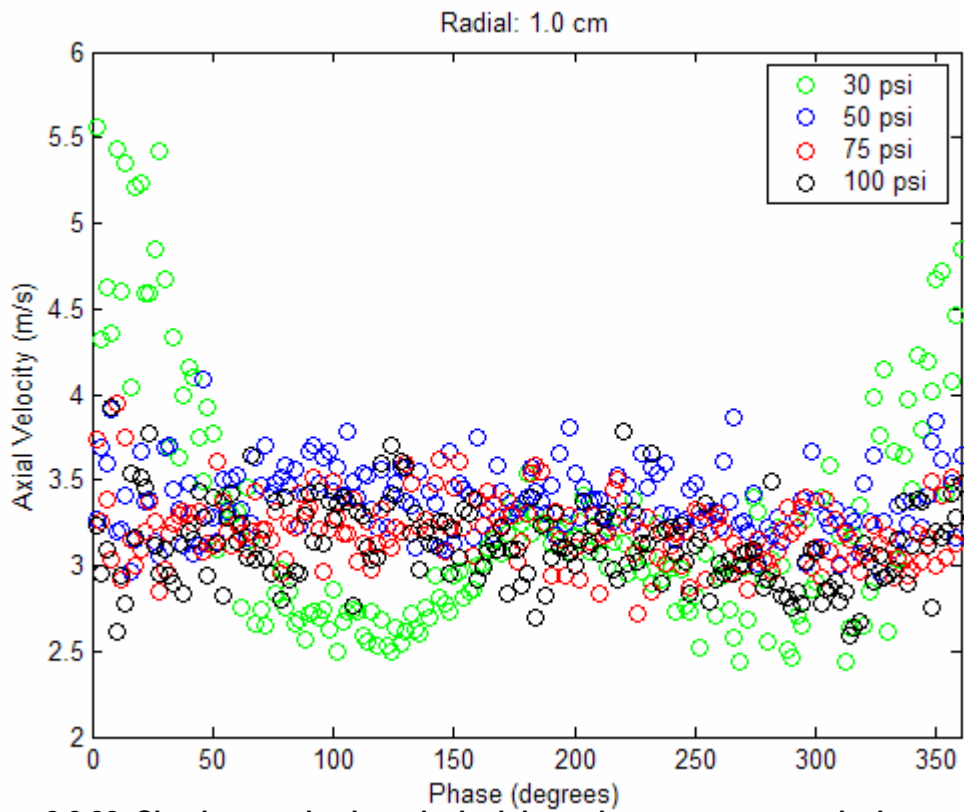


Figure 3.3.32: Simplex nozzle phase-locked dynamic measurement velocity results, radial 1.0 cm, 200 psi mean pressure.

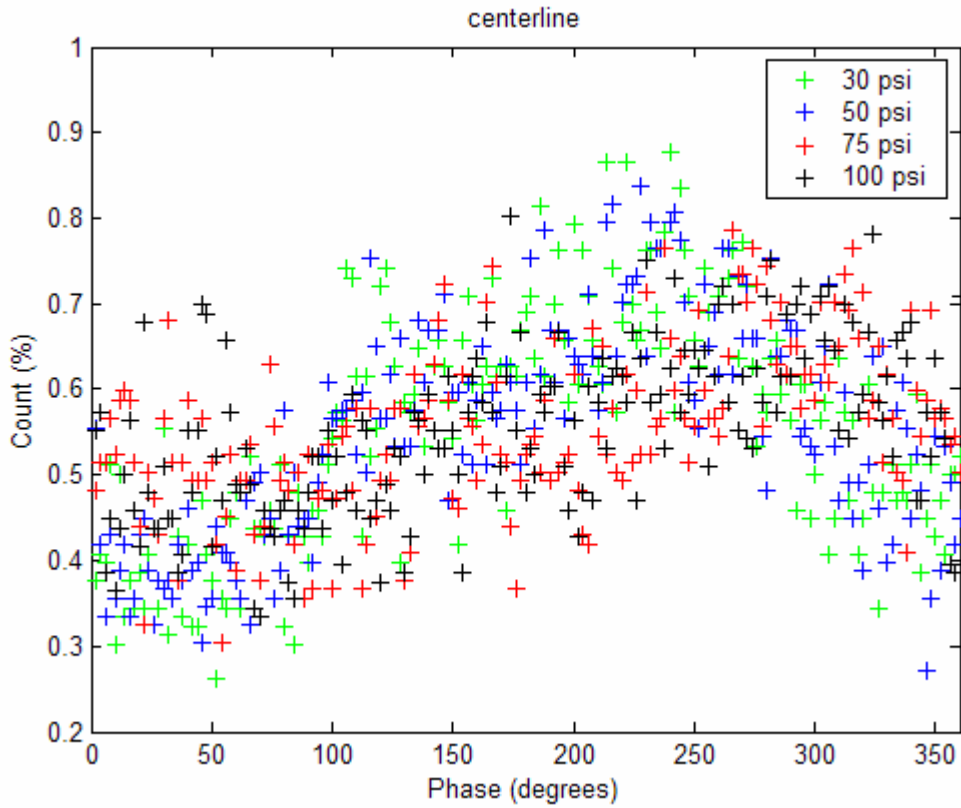


Figure 3.3.33: Simplex nozzle phase-locked dynamic measurement count (%) results, centerline, 200 psi mean pressure.

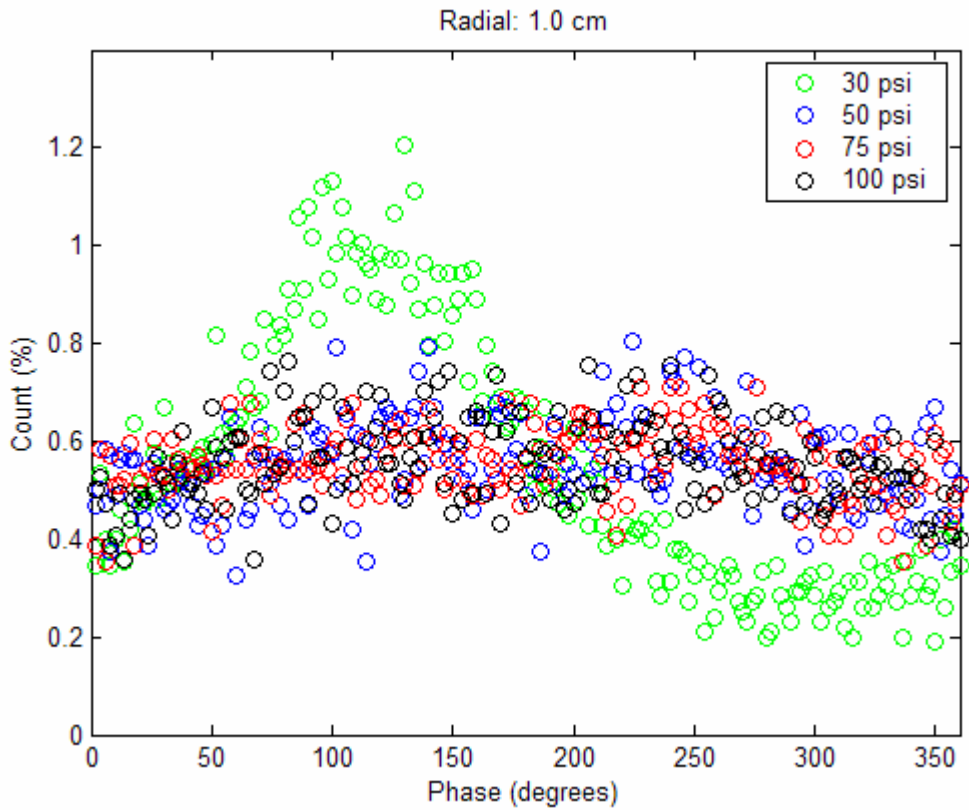


Figure 3.3.34: Simplex nozzle phase-locked dynamic measurement count (%) results, radial 1.0 cm, 200 psi mean pressure.

For a mean pressure of 300 psi measurements were taken at two radial positions: the centerline and 1.0 cm. The SMD results are shown in Figure 3.3.35 and Figure 3.3.36. Unlike the 200 psi and 250 psi mean pressure cases, ± 30 psi shows the lowest change in droplet size and ± 100 shows the largest change in droplet size. A phase difference between the low SMD point for the different modulation amplitudes is also evident at the centerline. At 1.0 cm the ± 100 psi modulation case shows slightly more modulation than the other amplitude cases. A phase difference between the different cases is not clearly defined at 1.0 cm.

The axial velocity results at a mean pressure of 300 psi are shown in Figure 3.3.37 and Figure 3.3.38. For the centerline, the ± 100 psi has shows the greatest change across the modulation cycle and the ± 30 psi case shows the least. There is no phase difference between the different modulation amplitude cases evident in the centerline axial velocities. At 1.0 cm a smaller change in axial velocity is seen for all modulation amplitudes than at the centerline. This is not surprising, since the PDA only measures axial velocity and the radial velocity would be expected to increase as the measurement locations move away from the centerline for a simplex nozzle. For both positions the phase of the higher axial velocities corresponds to the lower SMD droplets.

The count (%) for the centerline and 1.0 cm at a 300 psi mean pressure are shown in Figure 3.3.39 and Figure 3.3.40. As with the SMD and axial velocity measurement results there is a larger change across the modulation cycle at the centerline than at the 1.0 cm. Like the axial velocity measurements the phase where the higher counts occur correspond to the lower SMD values.

Table 3.3.3 is a summary of the mean SMDs and axial velocities for the 300 psi mean pressure measurements. At the centerline the ± 30 , ± 50 , and ± 75 psi modulation cases have lower mean SMDs than the static case while the ± 100 psi case is nearly the same as the static measurement. The mean axial velocities at the centerline are all higher than the static case. At 1.0 cm, the mean SMDs are all higher than the static measurement while the mean axial velocities remain nearly the same as the static case.

Table 3.3.3: Summary of mean SMDs and axial velocities for static and dynamic testing, Simplex nozzle, 300 psi mean pressure.

Modulation (psi)	Centerline		Radial: 1.0 cm	
	SMD (μm)	V (m/s)	SMD (μm)	V (m/s)
0, static	5.7	4.7	8.9	3.8
± 30	4.7	5.3	10.0	3.8
± 50	4.8	5.1	10.3	3.6
± 75	5.3	5.2	10.3	3.7
± 100	5.8	5.2	10.5	3.8

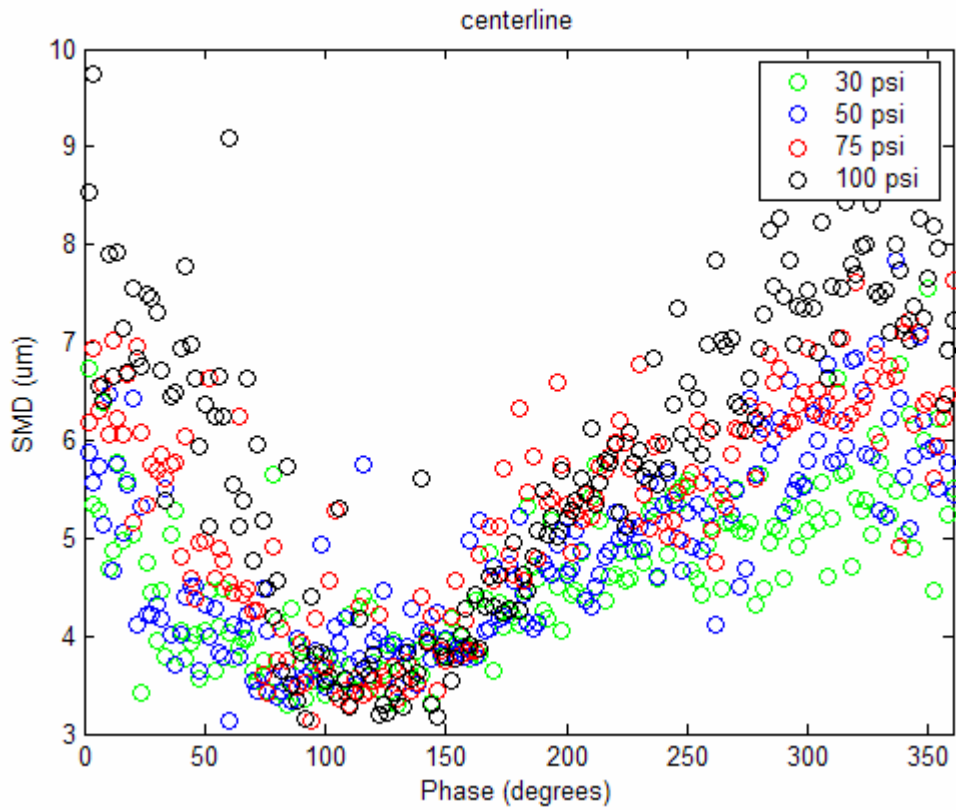


Figure 3.3.35: Simplex nozzle phase-locked dynamic measurement SMD results, centerline, 300 psi mean pressure.

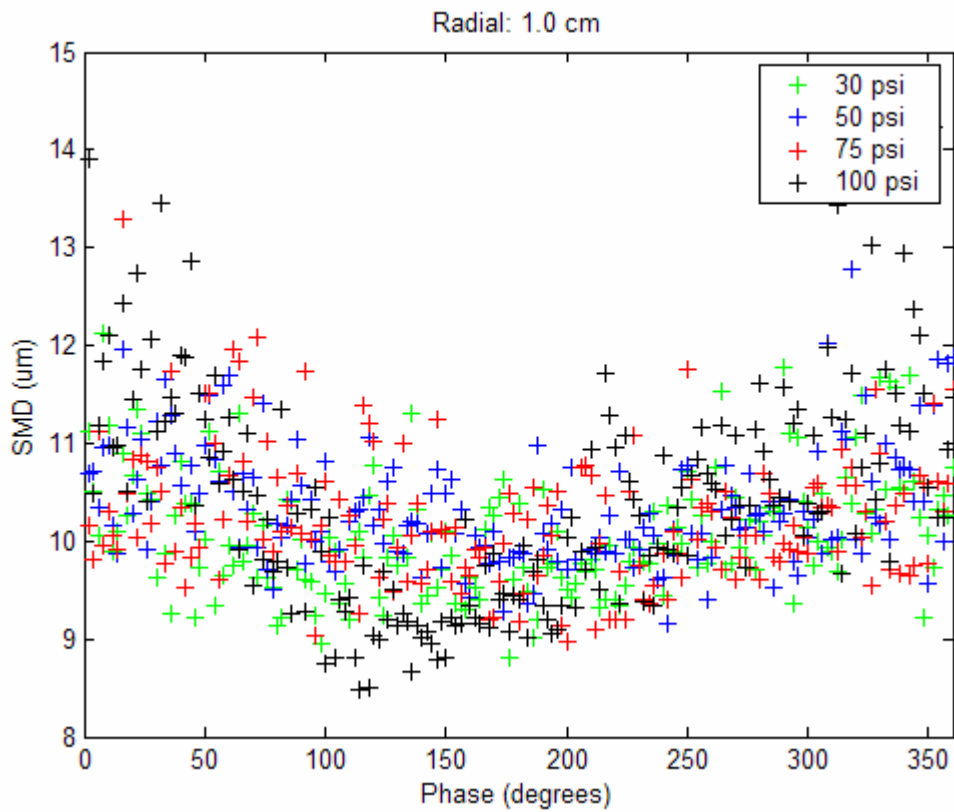


Figure 3.3.36: Simplex nozzle phase-locked dynamic measurement SMD results, radial 1.0 cm, 300 psi mean pressure.

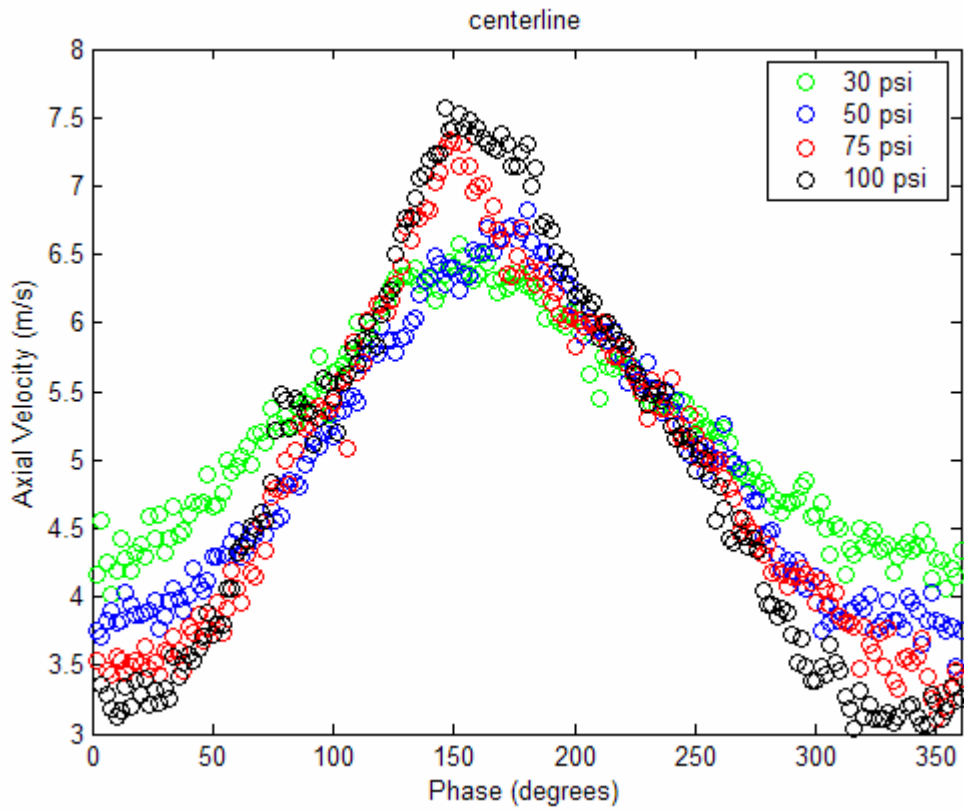


Figure 3.3.37: Simplex nozzle phase-locked dynamic measurement axial velocity results, centerline, 300 psi mean pressure.

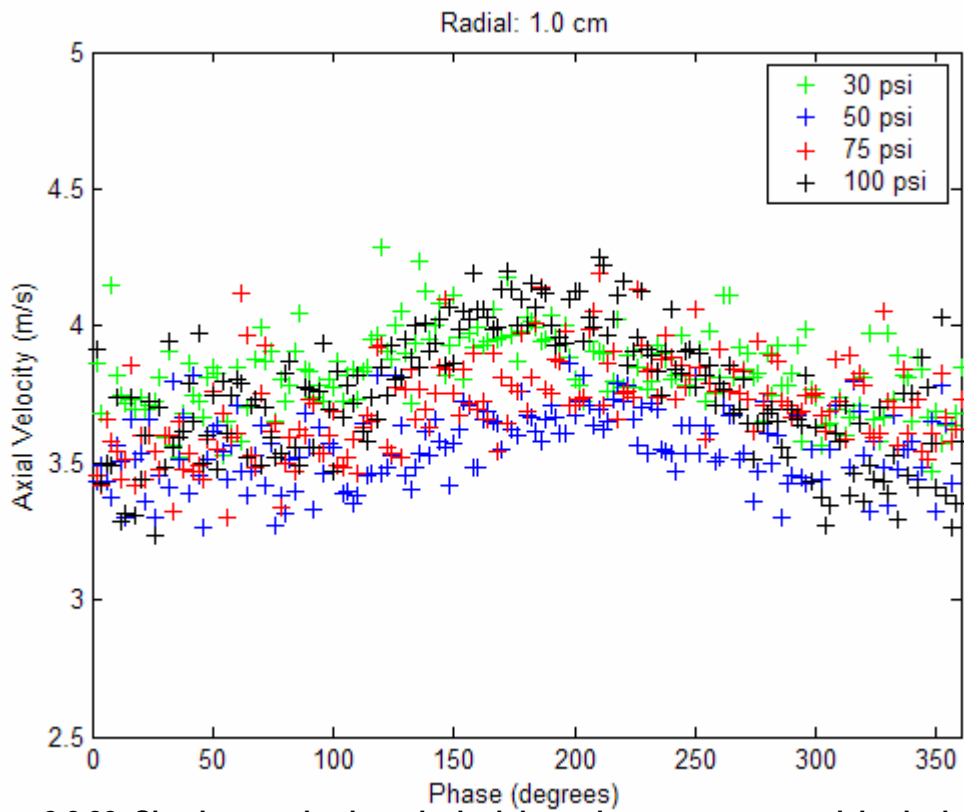


Figure 3.3.38: Simplex nozzle phase-locked dynamic measurement axial velocity results, radial 1.0 cm, 300 psi mean pressure.

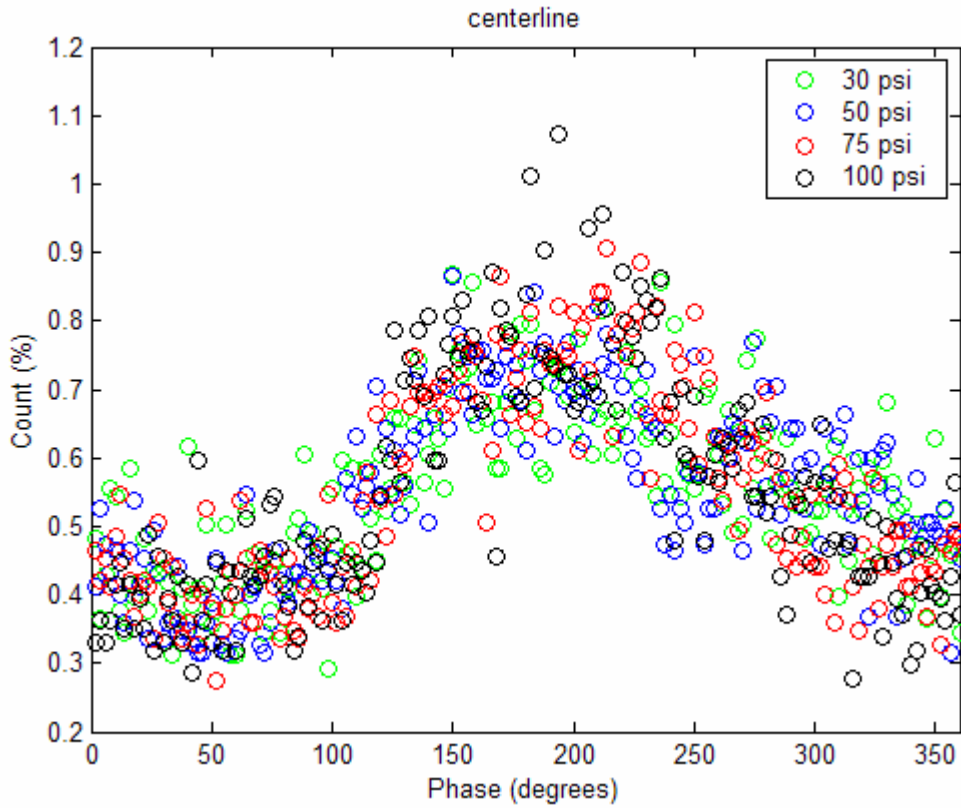


Figure 3.3.39: Simplex nozzle phase-locked dynamic measurement count (%) results, centerline, 300 psi mean pressure.

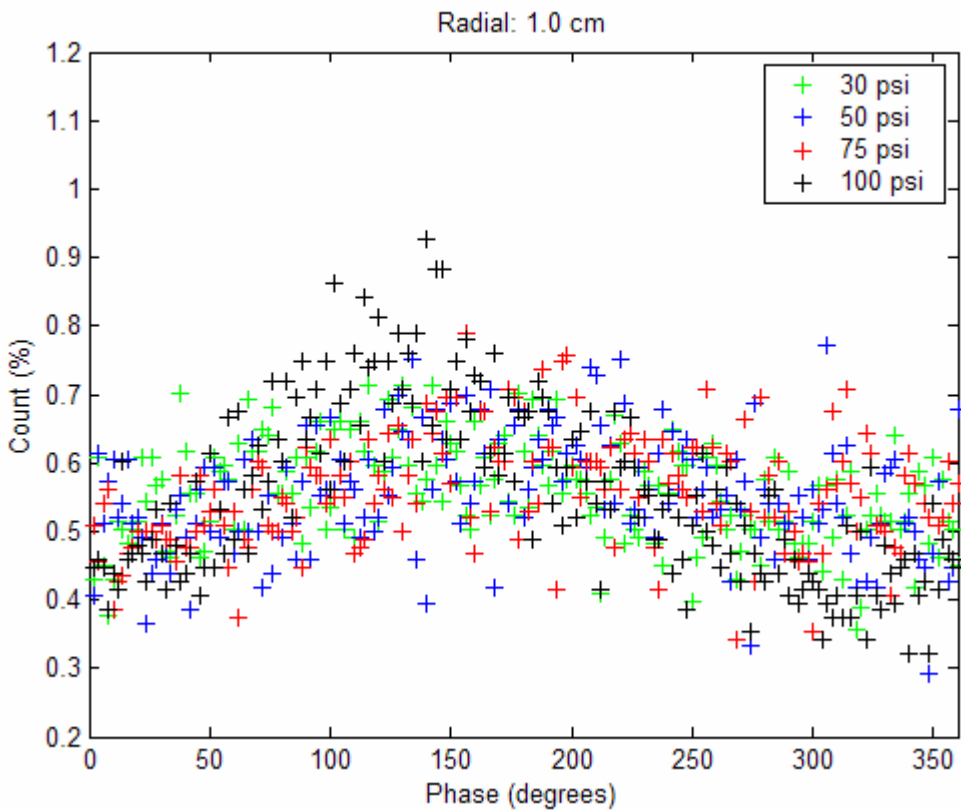


Figure 3.3.40: Simplex nozzle phase-locked dynamic measurement count (%) results, radial 1.0 cm, 300 psi mean pressure.

3.3.3. Simplex Nozzle Measurement Summary

From the dynamic measurements taken at the three mean pressures some observations can be made about the dynamic behavior of the simplex atomizer spray. However, the one dimensionality of the measurements, and because the measurements are point measurements, makes it impossible to draw broad conclusions about the nature of the spray under dynamic modulation. The measurements provide only an idea of what is happening in the spray under the tested operating conditions. Phase-locked images, such as Particle Image Velocimetry (PIV) measurements, would more fully explain the results of this research. Nevertheless, limited conclusions can be drawn from the PDA measurements.

For all of the mean pressure cases under dynamic modulation, the mean SMD of the droplets at the centerline remains the same as or is lower than the static case. But, the mean SMD of the droplets at the three radial positions (0.5, 1.0, 1.5 cm) is greater than the static case. The observation of a dense column of fine droplets occurring at the centerline for high amplitude modulation is supported by the centerline measurements for the ± 100 psi modulation cases at the 200 psi and 250 psi mean pressure settings. Also at the 200 psi and 250 psi mean pressure settings the ± 30 psi modulation amplitude shows the largest overall modulation in droplet SMDs. However at 300 psi mean pressure, ± 100 psi shows the greatest modulation and ± 30 psi shows the least. The behavior at 300 psi can be attributed to the decreasing pressure sensitivity for higher pressures, but this does not explain the behavior at the mean pressures of 200 psi and 250 psi. The presence of vortices in the spray could cause the ± 30 psi case to show higher modulation at the locations in the spray where measurements were taken; this can not be known from the PDA measurements.

The one-dimensional measurements are not as problematic for the diameter measurements as they are for velocity measurements. Because the simplex nozzle is designed to impart a radial component of velocity to the droplets it is difficult to interpret the axial velocity measurements under dynamic modulation, particularly at the locations away from the centerline. However, from the measurements it can be seen that the higher axial velocities and larger number of droplets correspond to the smaller droplet SMDs. The interpretation of this trend based on the static measurements is that the phase where the lowest SMD, highest axial velocity, and largest number of droplets occur corresponds to the highest supply pressure in the modulation cycle. Also, the difference between the phase where the lowest SMD occurs for the different modulation amplitudes suggests that changes in the modulation amplitude (gain) affect the phase of the resulting spray. This can not be conclusively shown with this research since the phase change did not exist for all of the cases.

Overall, the PDA measurements of the dynamically modulated spray raise more questions than are answered. That the modulation impacts the spray characteristics is clear however.

3.3.4. Air-Assist Nozzle Static Measurements

The droplet diameters and axial velocities were measured with one air pressure and four different water pressures for the air-assist nozzle. Measurements were taken at three radial positions for axial positions of 35 mm, 60 mm, and 90 mm. Figure 3.3.41 shows a schematic of the measurement locations within the spray. These nine locations were used for both the static and dynamic testing. The spray produced by the air-assist nozzle was longer and narrower than the spray produced by the simplex nozzle. For the air-assist nozzle the air and water supply pressures had to be close to each other to prevent the water from traveling up the air line or the air traveling up the water line; this could happen because the air and water are combined inside of the nozzle before the mixture leaves through the orifice. The maximum compressed air pressure available for testing was 100 psi, which was used for testing. The water pressures used were 100 psi, 125 psi, 150 psi, and 175 psi.

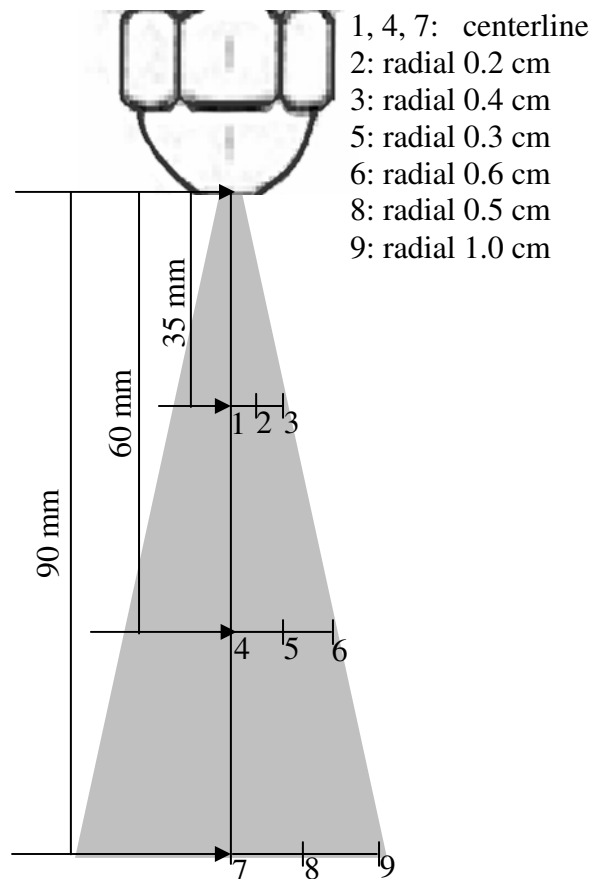


Figure 3.3.41: Air-assist nozzle measurement locations.

The radial positions shown in Figure 3.3.41 represent the centerline, outside radius of the spray, and the point halfway between the center and outside. The positions remained constant for all of the supply pressures used so that the static measurements could be compared to the dynamic measurements. The droplet SMDs and axial velocities for the four water supply pressures are shown in Figure 3.3.42 and Figure 3.3.43 for the 35 mm axial

distance. The SMD results show SMD increasing with the water pressure. This can be attributed to the static air pressure throughout the testing; as the water pressure is increased but air pressure remains static the ratio of water to air exiting the orifice of the nozzle is increasing, which results in the larger droplets. The axial velocity is also greatest for the lowest water supply pressure; this can also be attributed to the decrease in the proportion of air exiting the nozzle orifice. Similar to the simplex nozzle, the SMD is lowest at the centerline for all of the water supply pressures tested. Also, the axial velocities are highest at the centerline.

For the 60 mm axial distance the SMDs and axial velocities for the four water supply pressures are shown in Figure 3.3.44 and Figure 3.3.45 respectively. As at the 35 mm axial location, the smallest SMDs and largest axial velocities occur at the centerline.

The SMDs and axial velocities at the 90 mm axial distance are shown in Figure 3.3.46 and Figure 3.3.47 respectively. Again, the smallest SMDs and the largest axial velocities occur at the centerline.

As the droplets in the spray move downstream two distinct sets of trends appear. The first set is for the supply pressures of 100 and 125 psi. At the 60 mm axial distance the SMD of all three positions decreases and the axial velocity at the centerline and the first radial position increases. The SMD increases at the first and second radial position at 90 mm but still decreases at the centerline. The centerline axial velocity at 90 mm is maintained but the two radial positions decrease significantly. The other trend is for the supply pressures of 150 psi and 175 psi. For these supply pressures the SMD increases and the axial velocities decrease as the axial distance from the nozzle increases for the centerline and both radial positions. The difference between the two sets of water supply pressures is most likely due to the proportion of air to water that exits the nozzle orifice.

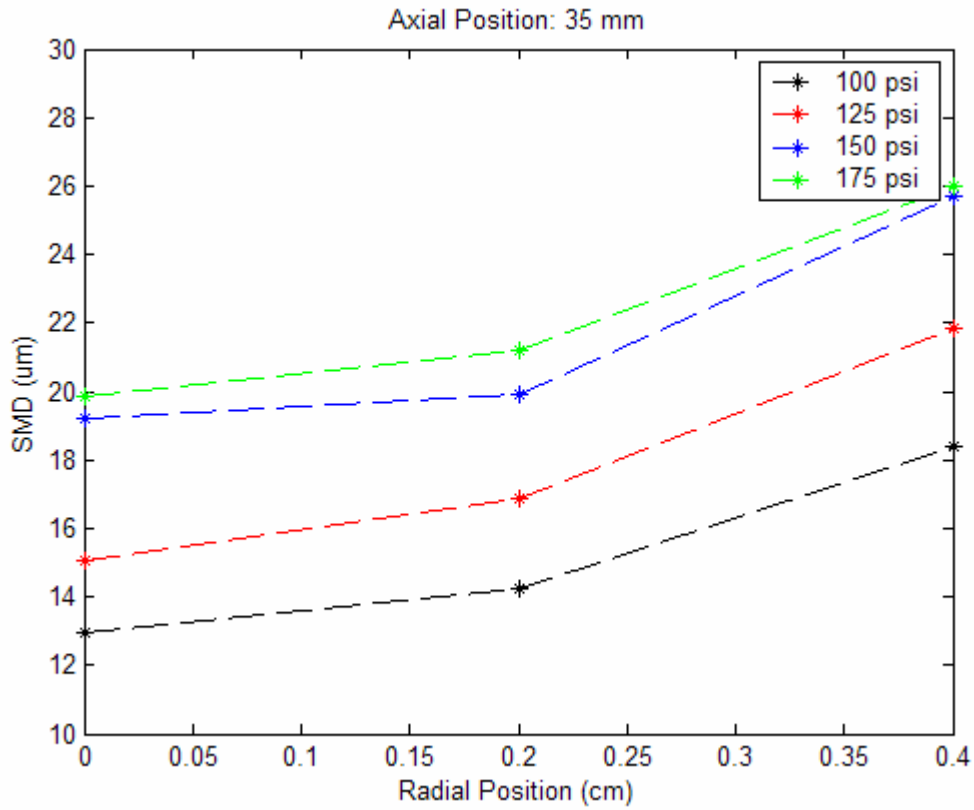


Figure 3.3.42: Air-assist nozzle static measurement SMD results, axial location: 35 mm.

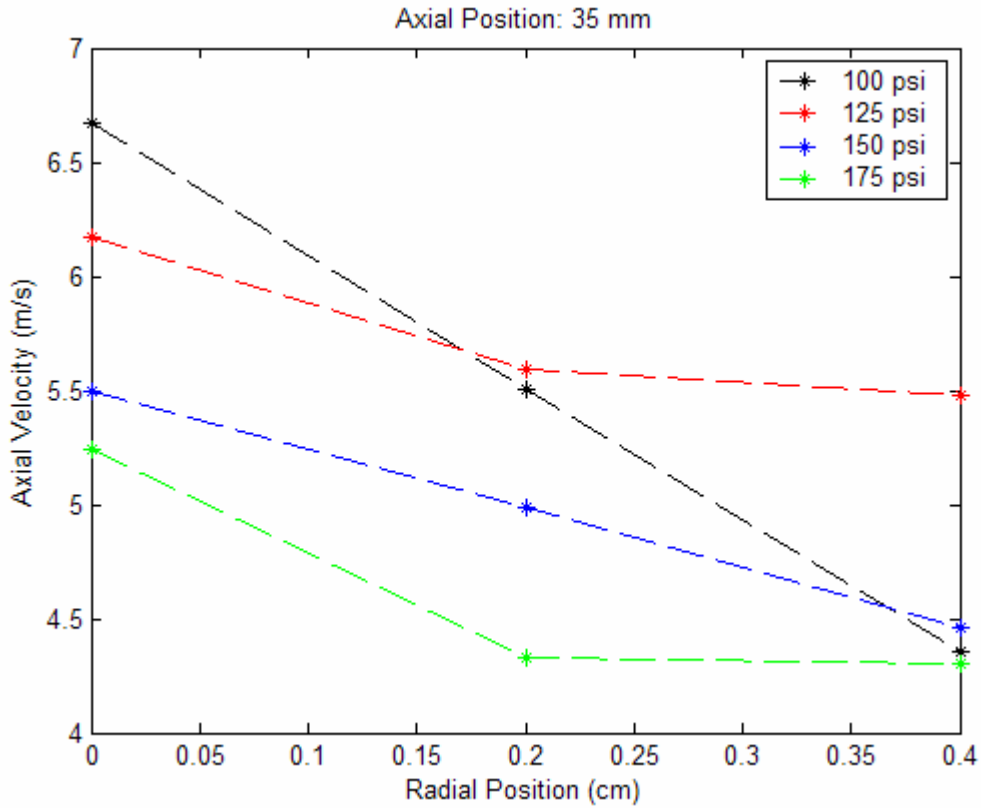


Figure 3.3.43: Air-assist nozzle static measurement axial velocity results, axial location: 35 mm.

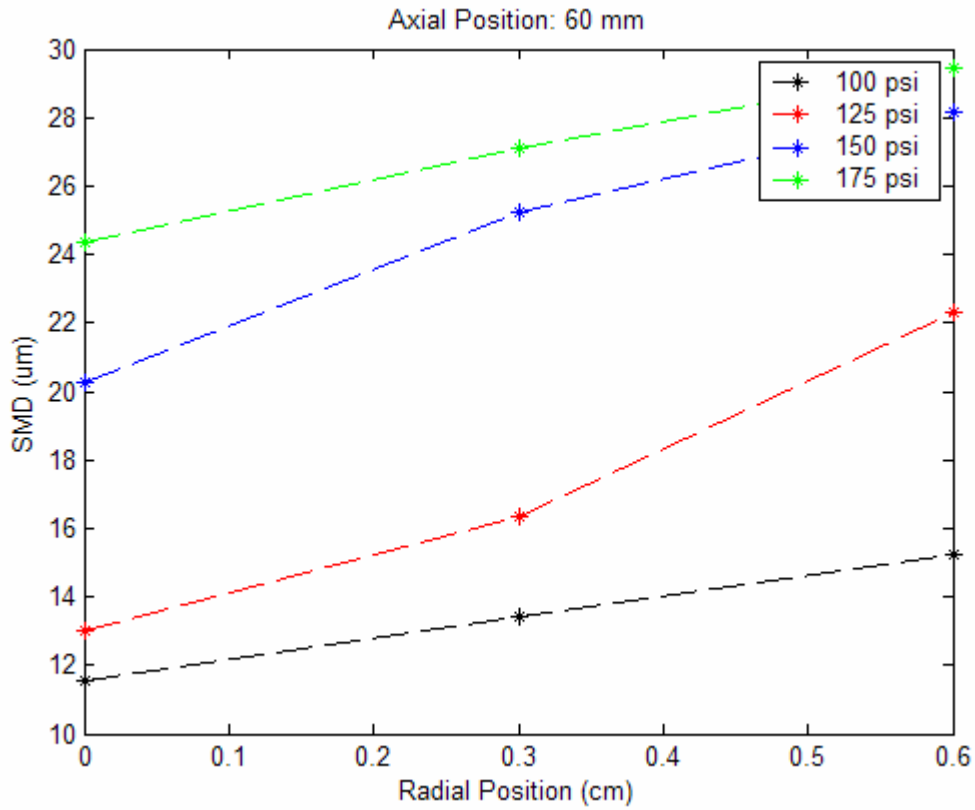


Figure 3.3.44: Air-assist nozzle static measurement SMD results, axial location: 60 mm.

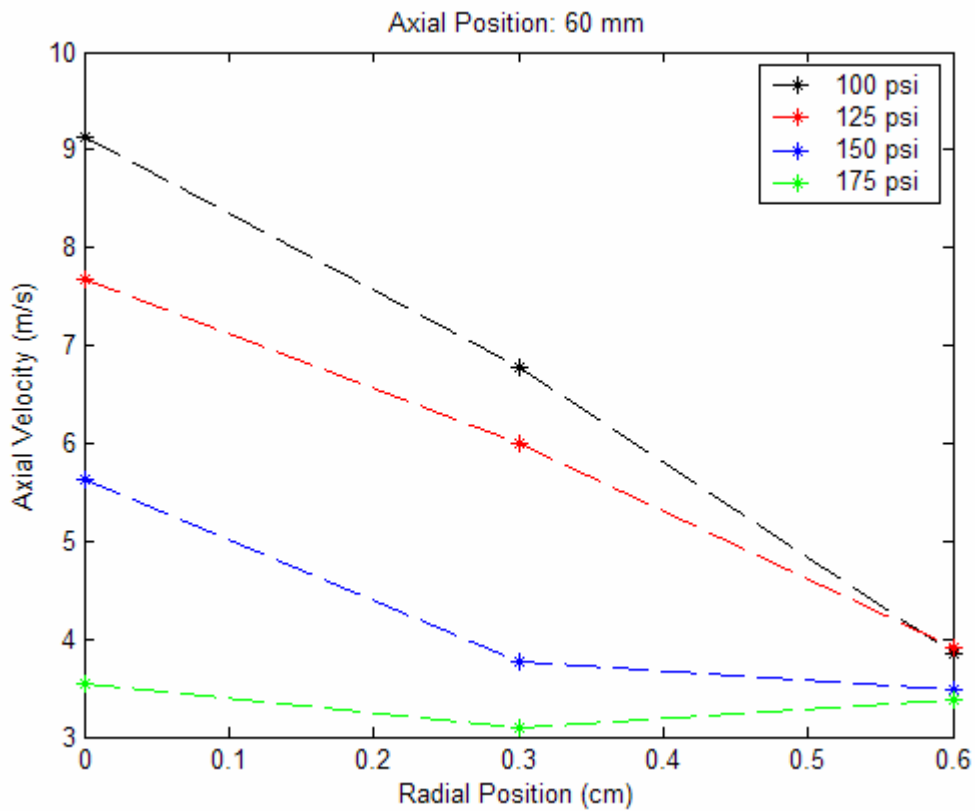


Figure 3.3.45: Air-assist nozzle static measurement axial velocity results, axial location: 60 mm.

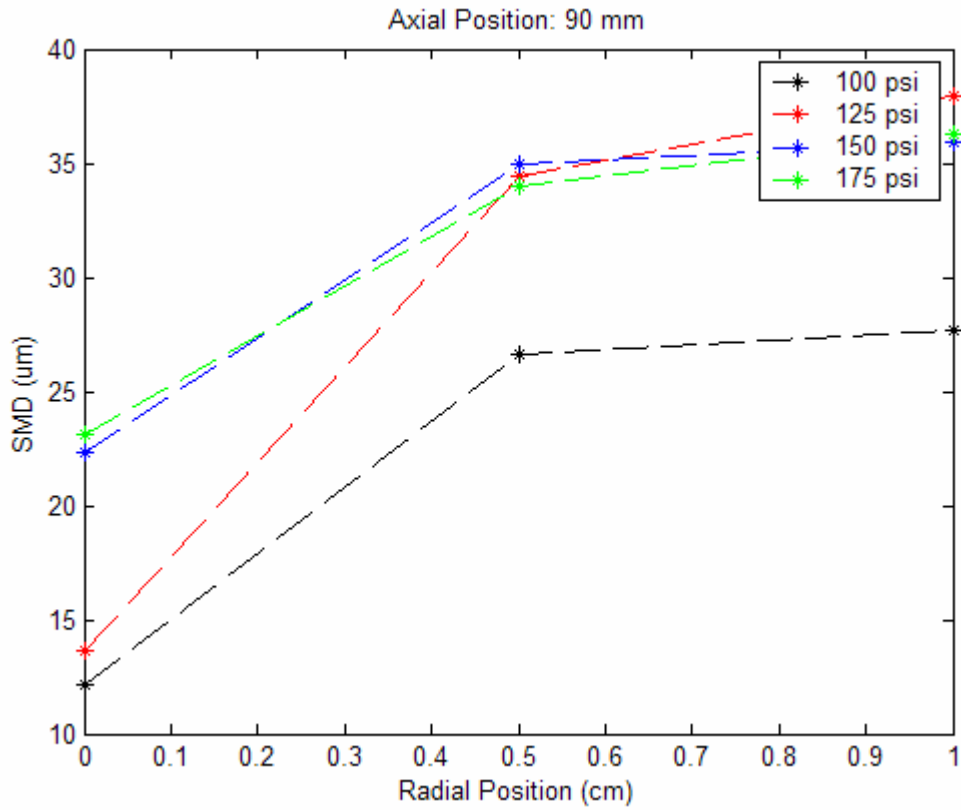


Figure 3.3.46: Air assist nozzle static measurement SMD results, axial location: 90 mm.

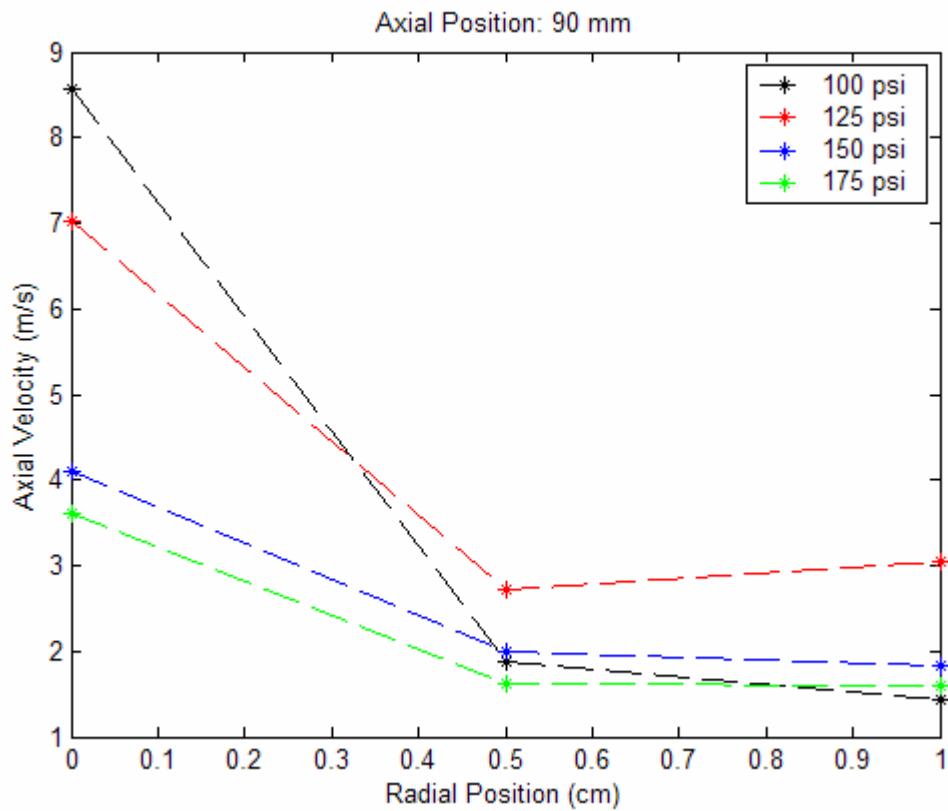


Figure 3.3.47: Air-assist nozzle static measurement axial velocity results, axial location: 90 mm.

3.3.5. Air-Assist Nozzle Dynamic Measurements

The air-assist nozzle dynamic measurements also used the system setup shown in Figure 3.2.1 and Figure 3.2.2. Measurements were taken at a mean pressure of 135 psi with sinusoidal pressure oscillation amplitude of ± 10 psi. The dynamic measurements were taken for all nine locations in the spray shown in Figure 3.3.41. The frequency of the dynamic input was 100 Hz. Using an angular encoder attachment for the PDA, the measurements for the dynamic tests were phase-locked to the modulation signal allowing the measured droplets to be divided into separate 'bins' for analysis. A bin size of 2° was used to investigate the SMDs and axial velocities of droplets measured during each phase bin of the modulation signal cycle.

The SMD results are shown in Figure 3.3.48, Figure 3.3.49, and Figure 3.3.50 for the three axial distances from the nozzle. At the 35 mm axial distance, the SMD measurements show a range of over 15 μm across the modulation cycle with all three radial positions showing the same amount of modulation and peaking at the same phase in the cycle; in addition, the three radial positions have a nearly identical SMD trace across the modulation cycle. At the 60 mm and 90 mm axial locations very little modulation appears but the SMDs at the three radial positions are separate and distinct. The effect of the modulation on the SMD for the air-assist nozzle at the 35 mm axial location is more distinct and pronounced than the effect of the dynamic modulation was on the simplex nozzle for any modulation amplitude.

The axial velocity results for all three locations are shown in Figure 3.3.51, Figure 3.3.52, and Figure 3.3.53. The axial velocity results at the 35 mm axial location show a modulation range of more than 7 m/s across the modulation cycle with all three radial positions having nearly identical velocity traces and peaking at the same cycle phase. Unlike the simplex nozzle however, the largest axial velocities correspond to the largest SMD droplets. The axial velocities at the 60 mm and 90 mm axial location show moderate modulation ranges but the three radial positions are separated and distinct.

The count (%) results for the three axial locations are shown in Figure 3.3.54, Figure 3.3.55, and Figure 3.3.56. The number of droplets occurring in each phase bin shows a lot of modulation at the 35 mm axial location, particularly at the middle radial position (0.5 cm). The largest percentage of droplets for the 35 mm location corresponds to the higher axial velocities and SMDs. The count (%) shows moderate modulation at the 60 mm and 90 mm axial locations.

At the 60 mm the modulation effects that appeared at 35 mm have disappeared. However, measurements at the 90 mm axial location show an increased modulation effect (over the 60 mm location) again. The exact cause of this unexpected behavior in the measurements is not known, but the interaction of the air and water continues to change the spray characteristics as the axial location moves further from the nozzle. And, if the effect of water pressure on the amount of air leaving the nozzle from the static measurements is accounted for, it is possible that the water pressure modulation is also in effect an air flow modulation. There may be a structural effect on the spray, like vortices, may account for the behavior at 60 mm and then at 90 mm.

The summary of mean SMD and axial velocity for the nine measurement locations in the spray is shown in Table 3.3.4. The static measurements for both 125 psi and 150 psi are given since static measurements were not taken at 135 psi. In general the dynamic modulations raised the mean SMD of the spray significantly over the static measurements at either 125 psi or 150 psi. The mean axial velocity of the dynamic measurements at the centerline is close to the static case at 125 psi for all three axial locations. The axial velocity at the 35 mm location for the radial 1 and radial 2 locations is close to the 150 psi static case. The radial 1 and radial 2 locations are closer to the static axial velocities at 125 psi.

Table 3.3.4: Summary of static and mean dynamic SMD and axial velocity measurements, air-assist nozzle for three axial and three radial positions. Static measurements shown for 125 psi and 150 psi cases. Radial 1 is 0.2 cm for 35 mm location, 0.3 cm for 60 mm location, and 0.5 cm for 90 mm location. Radial 2 is 0.4 cm for 35 mm location, 0.6 cm for 60 mm location, and 1.0 cm for 90 mm location.

Axial Location (mm), Modulation level (psi)	Centerline		Radial 1		Radial 2	
	SMD (μm)	V (m/s)	SMD (μm)	V (m/s)	SMD (μm)	V (m/s)
35, 0 (static) 125/150	15.0/19.2	6.1/5.5	16.8/19.9	5.6/4.9	21.8/25.6	5.4/4.4
35, ± 10	28.7	5.2	28.8	5.9	29.6	5.5
60, 0 (static) 125/150	13.0/20.2	7.6/5.6	16.3/25.2	6.0/3.7	22.3/28.1	3.9/3.4
60, ± 10	35.2	3.7	25.4	3.2	36.7	4.2
90, 0 (static) 125/150	13.6/22.3	7.0/4.0	34.4/34.9	2.7/2.0	37.9/35.9	3.0/1.8
90, ± 10	20.1	4.2	24.1	3.0	30.7	2.3

Probably the most valuable conclusions that can be made about the air-assist nozzle regard its use and operation requirements. The internal mixing of the air and liquid require the air pressure and fluid pressure to closely follow one another; this is required so that neither the liquid nor the air flow backwards up the others supply line. For dynamic modulation amplitudes similar to those used for the simplex atomizer measurements the air supply would also have to be modulated—and due to the compressibility of the air this would be very difficult at the frequencies used for active combustion control.

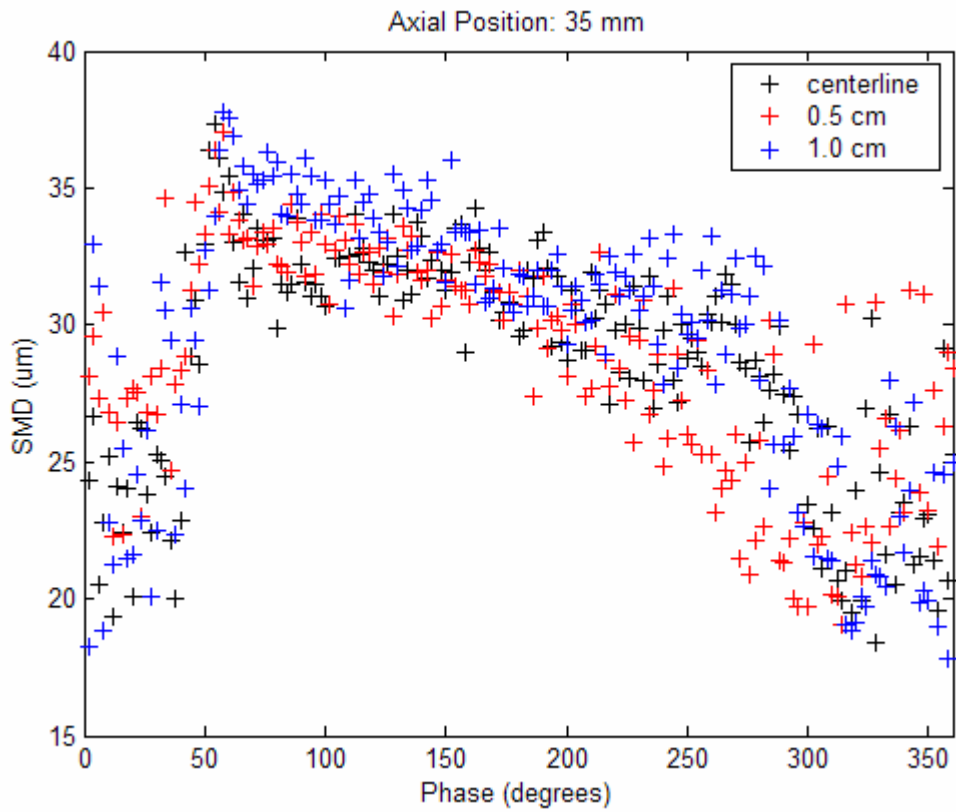


Figure 3.3.48: Air-assist nozzle phase-locked measurement SMD results, axial location: 35 mm, 135 psi mean pressure.

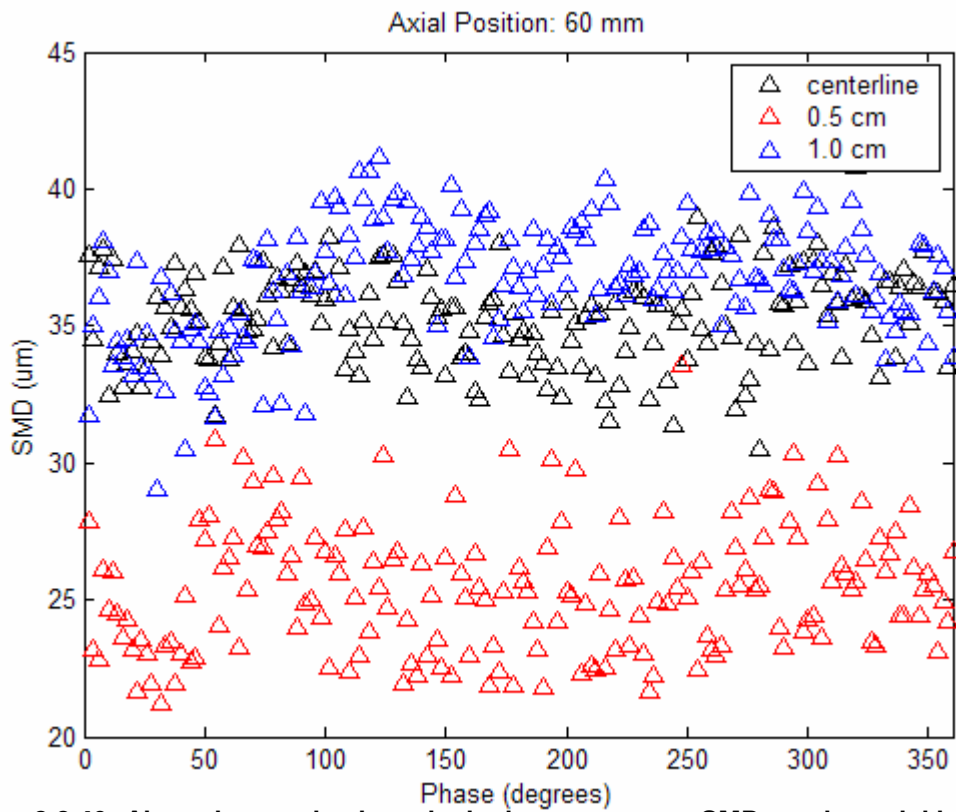


Figure 3.3.49: Air-assist nozzle phase-locked measurement SMD results, axial location: 60 mm, 135 psi mean pressure.

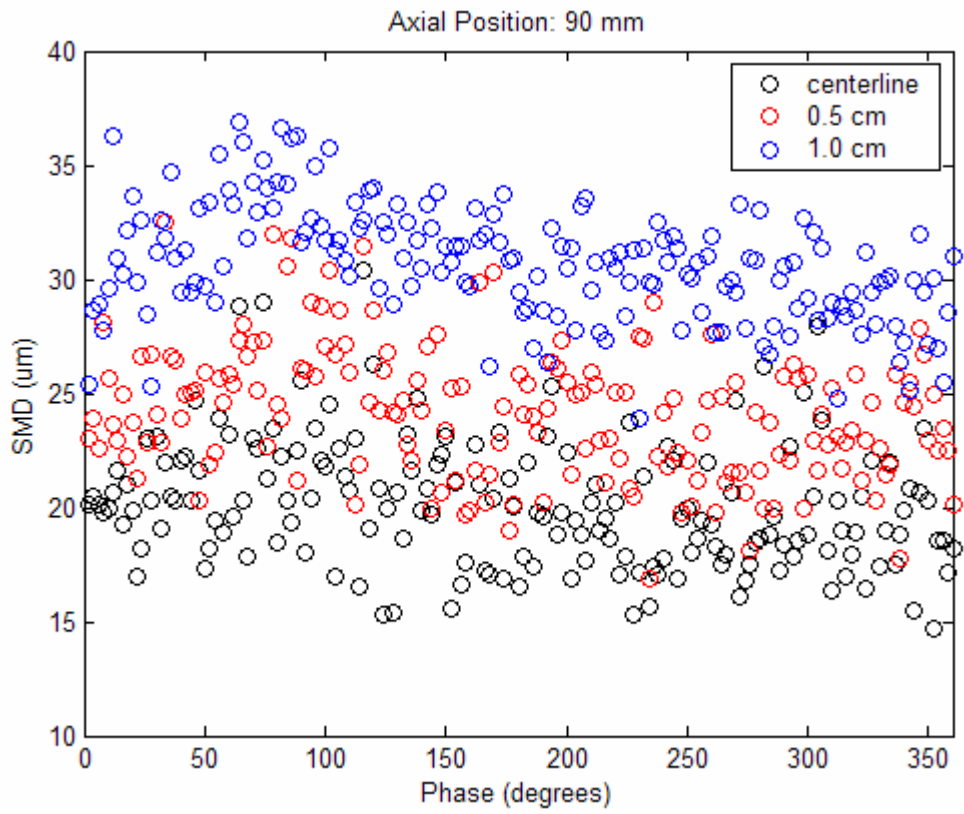


Figure 3.3.50: Air-assist nozzle phase-locked measurement SMD results, axial location: 90 mm, 135 psi mean pressure.

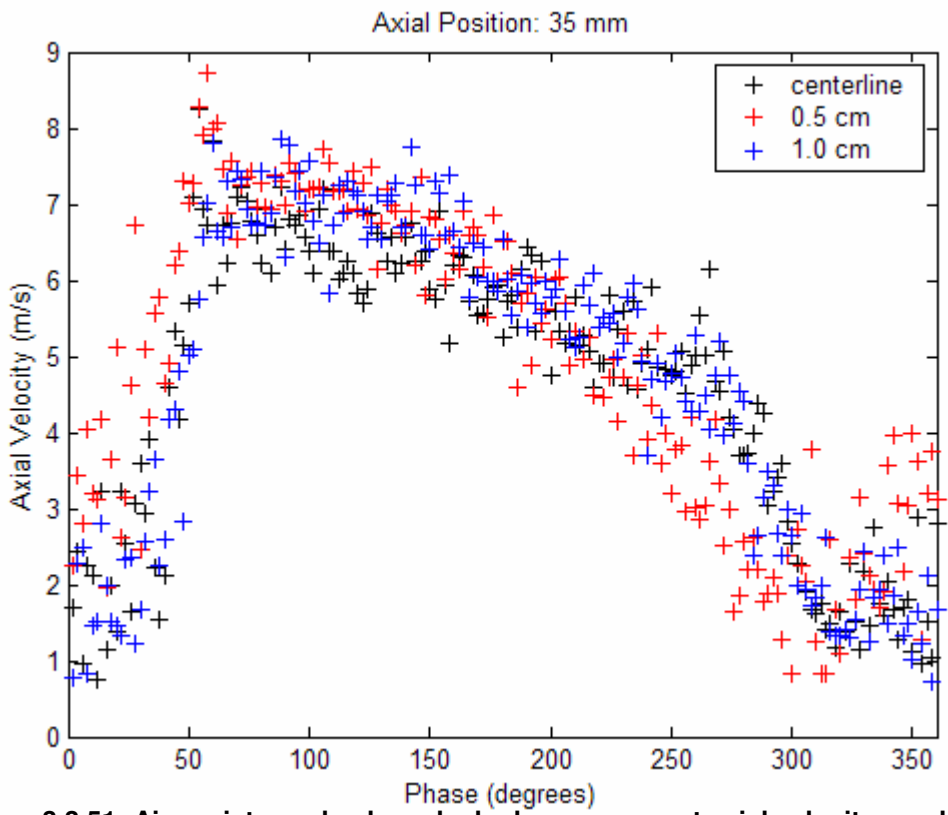


Figure 3.3.51: Air-assist nozzle phase-locked measurement axial velocity results, axial location: 35 mm, 135 psi mean pressure.

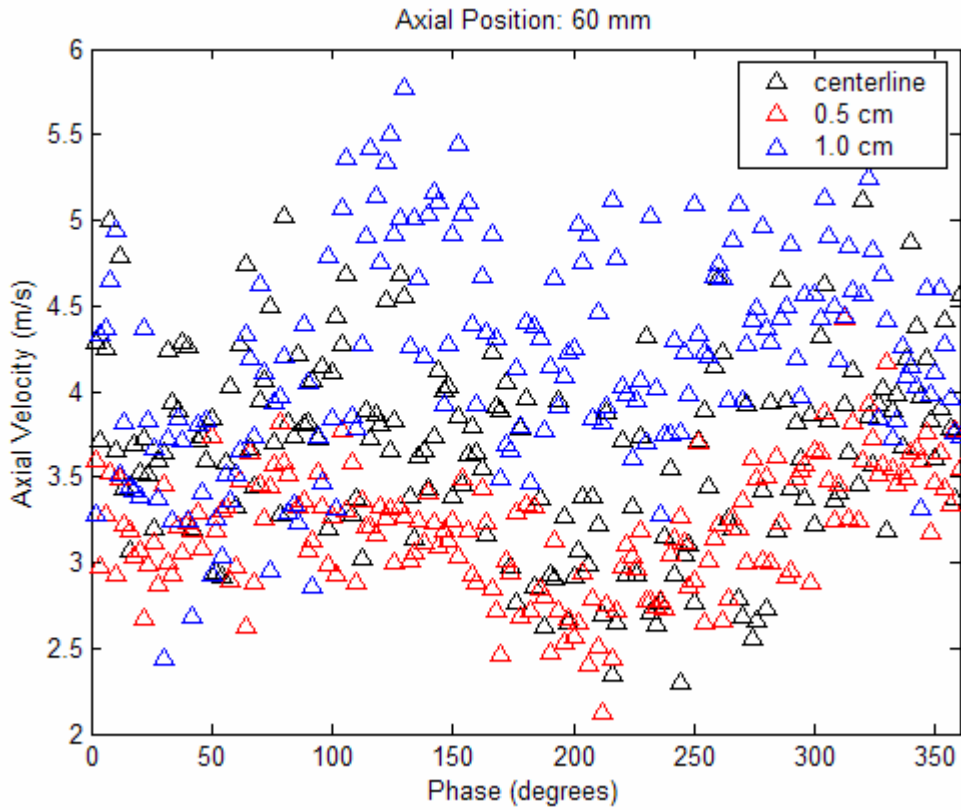


Figure 3.3.52: Air-assist nozzle phase-locked measurement axial velocity results, axial location: 60 mm, 135 psi mean pressure.

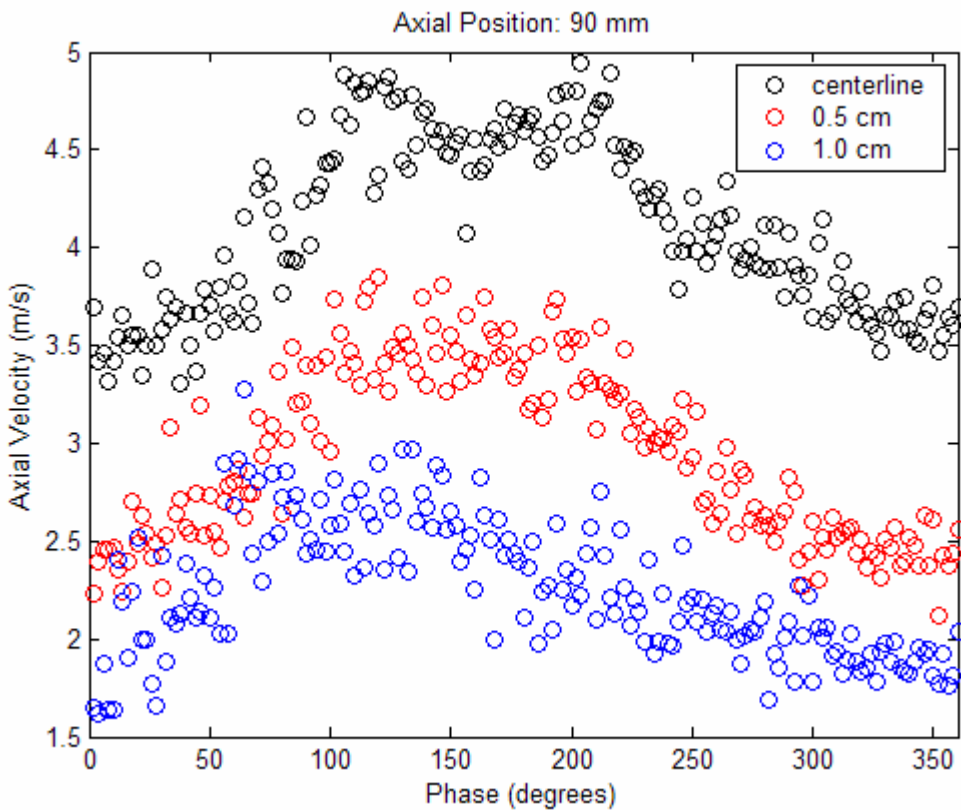


Figure 3.3.53: Air-assist nozzle phase-locked measurement axial velocity results, axial location: 90 mm, 135 psi mean pressure.

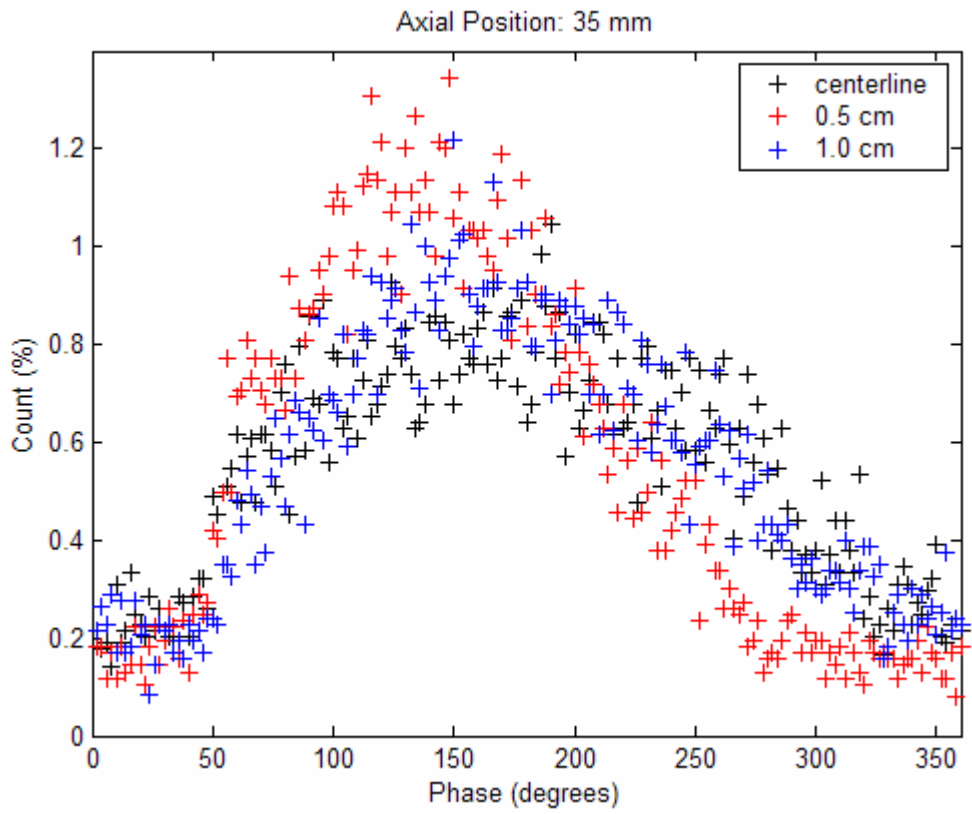


Figure 3.3.54: Air-assist nozzle phase-locked measurement count (%) results, axial location: 35 mm, 135 psi mean pressure.

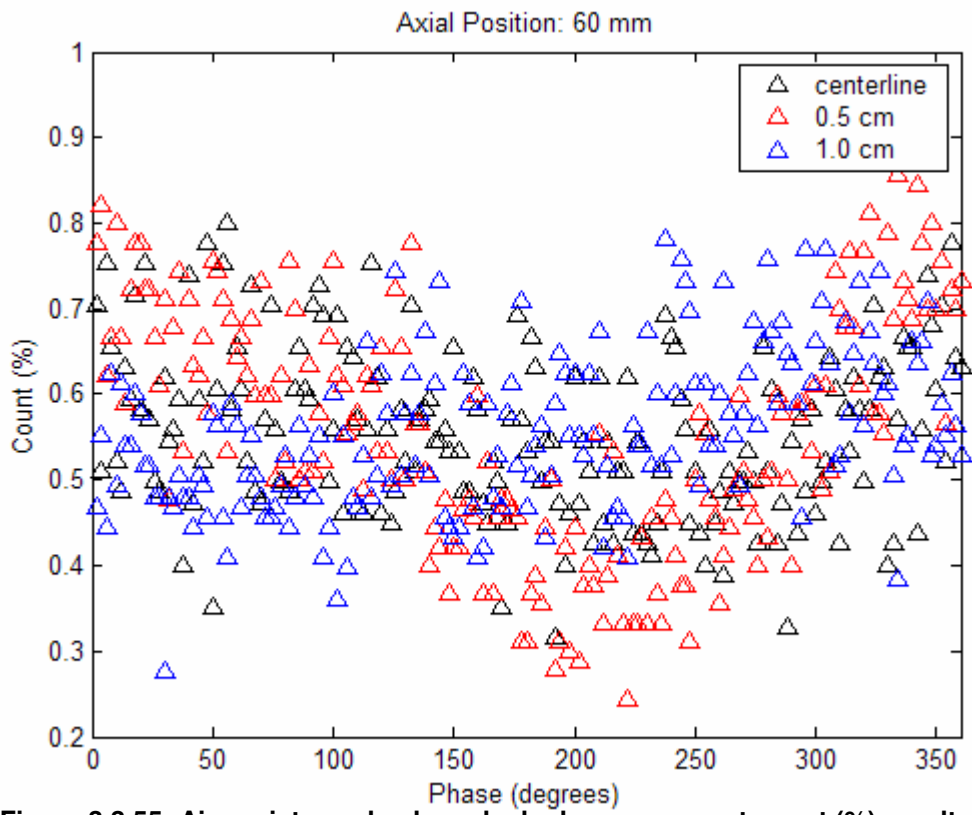


Figure 3.3.55: Air-assist nozzle phase-locked measurement count (%) results, axial location: 60 mm, 135 psi mean pressure.

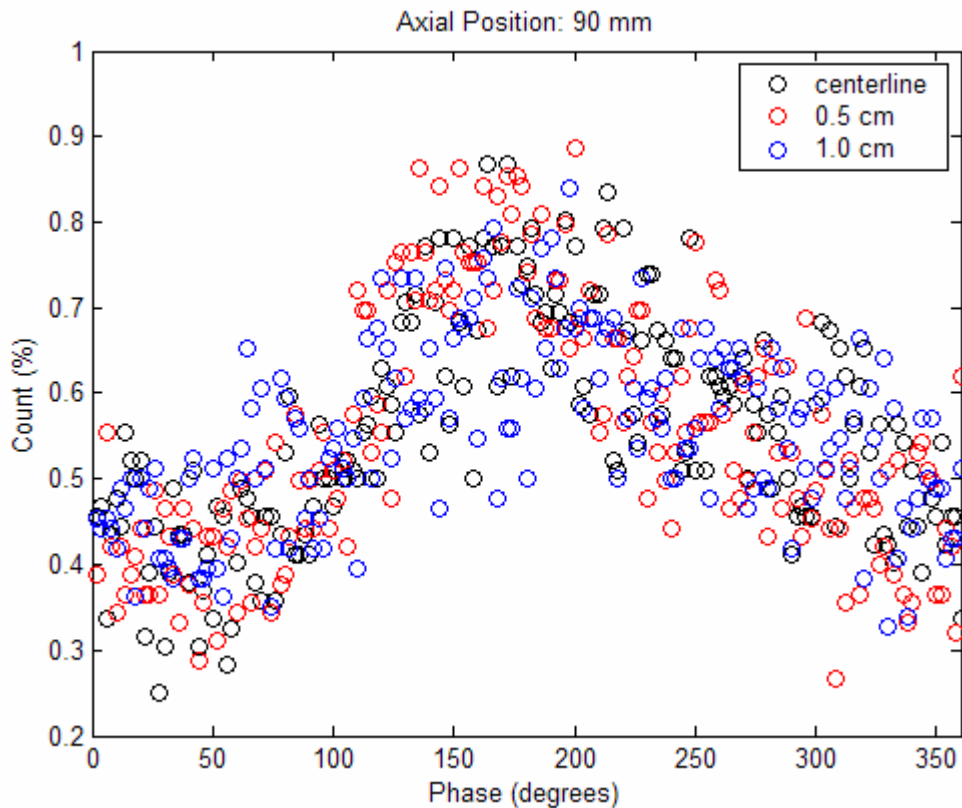


Figure 3.3.56: Air-assist nozzle phase-locked measurement count (%) results, axial location: 90 mm, 135 psi mean pressure.

3.3.6. Spill-Return Nozzle Operation

Experiments were attempted with a Delavan Variflo™ spill-return nozzle. The spill-return nozzle is a simplex nozzle with a fluid return line located in the swirl chamber. The pressure drop across the return (or bypass) line can be adjusted to change the amount of fluid that is diverted from the nozzle exit orifice. The Delavan spill-return nozzle is designed for operation with a constant pressure supply, which allows the flow rate to adjust to the requirements of the nozzle orifice and spill return line. The constant pressure supply should allow the spray to have relatively uniform characteristics for a wide range of flow rates since the spilled flow is diverted from the swirl chamber. In this way the nozzle orifice and the spill return line act as two impedances in parallel. Experiments were attempted with the setup shown in Figure 3.3.57. Using the control system used for the simplex nozzle and air-assist nozzle experiments, the static pressure drop across the actuator and valve could be controlled. However, dynamic actuation of the valve did not successfully modulate the water pressure upstream of the valve. In fact the reaction to a step response change for the mean pressure had a very slow rise time with an overshoot of 50%. Monitoring the pressure gage on the supply line during the step input response showed that the supply pressure also oscillated until the steady state pressure was reached. A similar problem was faced by DeCastro [9] during the initial design of the primary fuel modulation system. It was determined that a bypass line placed after the valve was required to adjust the impedance of the system and that a large rise time significantly limited the modulation amplitudes that could be commanded. Since the bypass line in the spill-return setup returns to the tank, the impedance that would need to be corrected is the impedance between the valve and the

nozzle. Therefore, in this case a bypass line cannot be used to correct the impedance of the system. Modulating the return line of a spill-return nozzle is possible as seen in the work by Chang et al. [4]. However, the system that they used modulated the spill return flow rate inside of the nozzle.

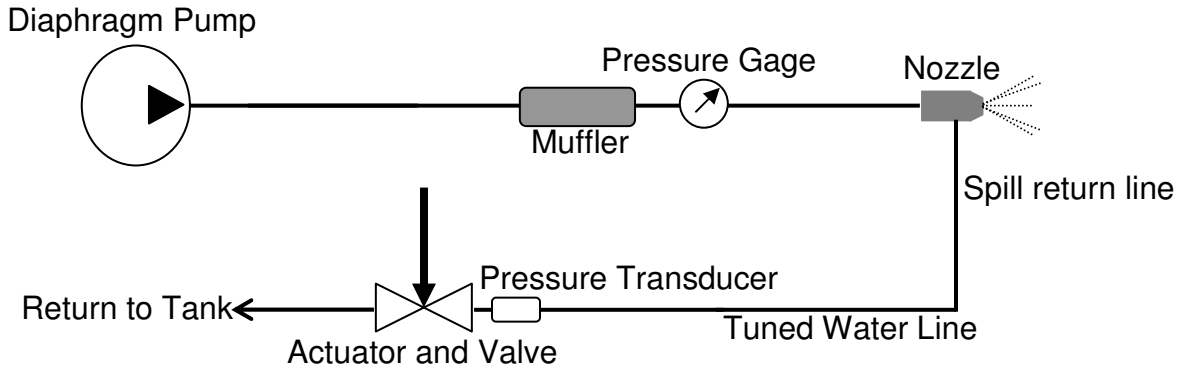


Figure 3.3.57: Experimental setup for spill-return nozzle.

Chapter 4. Summary and Future Work

4.1. Summary

In the first part of the work control experiments were performed on an unstable liquid-fueled combustor. It was found that the signal processing filter settings could significantly impact the ability of the phase shift controller to stabilize the unstable system. A filter setting configuration that significantly improved the effectiveness of the controller was found for use on the control experiments. With this filter configuration the combustor was successfully stabilized from a GER of 0.48, the instability boundary, up to a GER of 0.67. Subsequently, a series of control experiments were run that allowed the controller behavior to be characterized. Three distinct regions of controllability were found for different ranges of the GER. The regions were found to correspond to differences in the degree of control signal saturation that occurred. Increasing the fuel pressure to raise the GER moved the system closer to the saturation limits; this, coupled with the requirement of higher controller gains at higher GERs, resulted in increased saturation severity with increasing GER. The saturation was so severe at the highest GERs successfully stabilized that the stability of an unstable system could not be gained; in this case stability had to be maintained as the system was transitioned from a lower GER. Other observed controller behavior included hysteresis. Hysteresis appeared because one set of controller settings could be used to gain control of the unstable system and a larger set of controller settings could be used to maintain stability.

In the second part of this work the impact of primary fuel modulation on the fuel spray characteristics was investigated. Both static and dynamic PDA measurements were taken for the simplex nozzle used in the kerosene combustor for the control experiments and an air-assist nozzle. The dynamic pressure modulation had an impact on the spray characteristics of both atomizers. Using an angular encoder attachment for the PDA the results of the dynamic tests were phase locked allowing the spray characteristics across the modulation cycle to be measured. A 100 Hz sinusoidal signal was used for the modulation signal. For the simplex nozzle four different pressure modulation amplitudes were used for three different mean pressures. The limitations of the PDA measurements prevent broad conclusions from being drawn about the results of these tests but some general observations can be made. A change in the amplitude of the pressure modulation may change the phase of the resulting spray. Also, at the lower two mean pressures the greatest modulation in SMD was seen for the smallest modulation amplitude case; this suggests that vortices may be caused by the dynamic modulation as seen by Chang et al. [4]. As expected, the smallest droplets were the most numerous and had the largest axial velocities in both the static and dynamic measurements. Further investigation is needed to understand the impact of dynamic modulation on the simplex nozzle. Testing with the air-assist nozzle found that the internal mixing of the air and water is problematic for dynamic operation of the nozzle over a wide range of either air pressure or water pressure. The small amplitude (± 10 psi) of pressure modulation had a significant impact on the spray measurements taken nearest to the nozzle exit orifice. Unlike the simplex nozzle, though, very little difference was found across the radius of the spray for the dynamic measurements. Also, the largest droplets were the most numerous and had the highest axial velocities for the dynamic measurements.

4.2. Future Work

For the combustion experiments, the fuel supply system could be upgraded to mitigate the saturation problems experienced during experiments in this thesis. Additionally, the control system could be used with a higher power (higher fuel flow rate) combustor to find if the control system behavior, including the percentage of modulation required to gain stability, translate to the higher powered combustor. Since the actuation system was designed to be scaled to higher flow rates this would only require a larger fuel pump and welded lines for the fuel delivery system to accommodate higher pressures and flow rates. Addressing the saturation limitation reached in this work would allow control experiments at higher GERs to be carried out. The control system capabilities in the second unstable region of the current kerosene-fueled combustor could then be tested.

For the spray measurement work, the dynamic modulation cases should be measured with a phase-locked imaging system, such as a PIV system, to determine if vortices are present and to gain a more complete measurement of the spray characteristics. PIV measurements would allow more than one velocity component to be measured as well as allowing the mass flux of the spray to be measured. Also, the effect of a saturated control signal on the spray behavior could be measured. The saturated measurements could then be compared to the unsaturated spray measurements to find if differences, other than a reduced effective gain, occur in the spray. Other types of nozzles could also be tested such as an airblast nozzle. A fuel nozzle that separates the mass flow rate modulation from the resulting fuel spray characteristics would help determine whether mass flow modulation alone is enough for active combustion control. One way to do this might be to use an over pressurized simplex nozzle, or group of smaller nozzles, since the simplex nozzle becomes less sensitive to pressure change at high pressures. Using a smaller nozzle at higher pressures would allow the same fuel flow rates used in this work to be tested for comparison.

Appendix A: Phase Shift Controller, Mean Pressure Controller, and Voltage Limiter

The phase shift controller, mean pressure controller, and voltage limiter for the control system were implemented in the DSPACE Control Desk Program. The control algorithms were developed by previous researchers in the VACCG Noah Schiller, Jonathan DeCastro, and Aaron Greenwood.

```

/*****
                                PHASE SHIFT CONTROL
This algorithm shifts the input signal a variable amount of samples with an adjustable
gain
*****/
else if ((STATE == 1) && (ControlAlgorithm == PhaseShift))
{
    samp_store[input_count] = Input;
    output_count = input_count+1;
    if (output_count > delay_samples) output_count = 0;
        control_output = GainMultiplier * samp_store[output_count];
    if (array_full != 1) control_output = 0;
        input_count++;
    if (input_count > delay_samples)
    {
        input_count = 0;
        array_full = 1;
    }
}

/*****
                                MEAN PRESSURE CONTROLLER
*****/
OutputThreshold = AmplifierThreshold / 1;

if (CLControl == 1)
{
    //offset_output = Offset(Pmean,Pds[0],Pds[1],control[0]);
    offset_output = control[0] + CompGain*(Pf[0] - 0.99*Pf[1]);
}

else offset_output = amp_offset/1;
output = control_output + offset_output;
TrueOut = output;
if (output > OutputThreshold) output = OutputThreshold;
else if (output < 0) output = 0;

```

```

for(i = MaxOrder - 1; i >= 0; i--)
{
    Pds[i] = Pds[i-1];
    control[i] = control[i-1];
    Pf[i] = Pf[i-1];
    Fds1[i] = Fds1[i-1];
    Fds2[i] = Fds2[i-1];
    Fds3[i] = Fds3[i-1];
}

control[0] = offset_output;
Vout = output;
output = output/10;

```

Appendix B: Sensors, Filters, and Measurement Settings

Table B.1: Transducer specifications for VACCG kerosene-fueled combustor.

Component	Description	Bridge Excitation Voltage (V)	Strain Gage Amplifier Gain	Sensitivity (no gain)	Sensitivity (with associated gain)
Fuel Line Pressure Transducer (4" downstream of valve)	Omega PX212-1KGV pressure transducer	10	5x20	0.1 mV/psi	10 mV/psi
Combustor Pressure Transducer (6" above nozzle)	SenSym SX01D diaphragm pressure transducer	10	3.75x20	4.0 mV/V/psi	0.435 mV/Pa

Note: $SPL = 10 \log_{10} \left(\frac{P_{rms}^2}{P_{ref}^2} \right) = 20 \log_{10} \left(\frac{P_{rms}}{P_{ref}} \right)$, where $P_{ref} = 20 \mu Pa$.

Specifically, $SPL = 20 \log_{10} \left(\frac{0.707 cp \left(\frac{1}{0.000435} \right)}{20 \times 10^{-6}} \right)$, where cp is in volts.

Table B.2: Filter Specifications for VACCG kerosene-fueled combustor.

Filter	Description	Low Pass Setting (Hz)	High Pass Setting (Hz)
Frequency Devices 9002	Digital low pass filter.	1500	n/a
Bandpass	Analog high pass filter and low pass filter wired in series.	160	100

Appendix C: Fuel System Plumbing and Control System Wiring

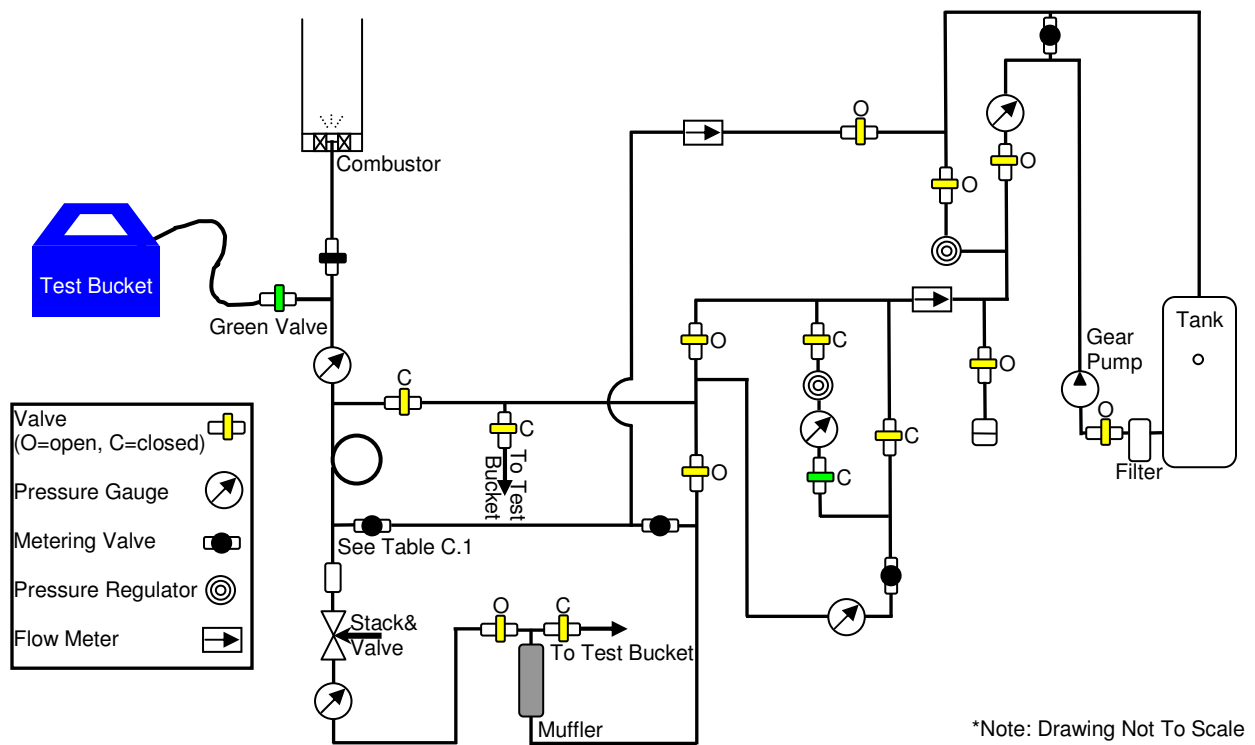


Figure C.1: Fuel system plumbing schematic for the VACCG kerosene-fueled combustor.

Table C.1: Bypass valve settings for different atomizers [20].

Atomizer Size	Bypass Setting (turns open)
Closed	5.77
0.5	5.55
0.75	5.44
1.0	5.33
1.5	5.10
2.0	4.88
2.5	4.66
3.0	4.43
4.0	3.98
5.0	3.54
6.0	3.09
8.0	2.20
10.0	1.30

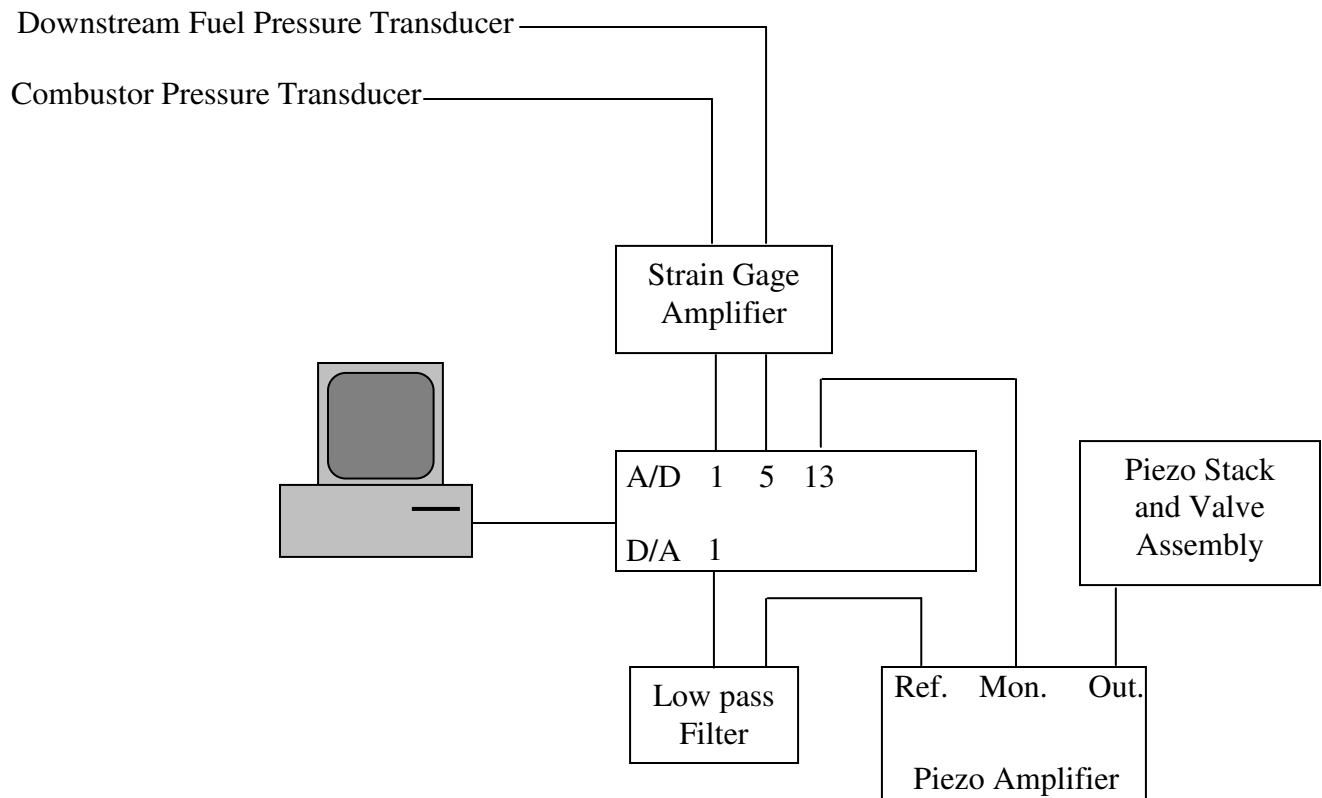


Figure C.2: Wiring schematic for the VACCG kerosene-fueled combustor control experiments.

Appendix D: Uncontrolled Power Spectrums for the First Uncontrolled Region of the VACCG Kerosene-Fueled Combustor.

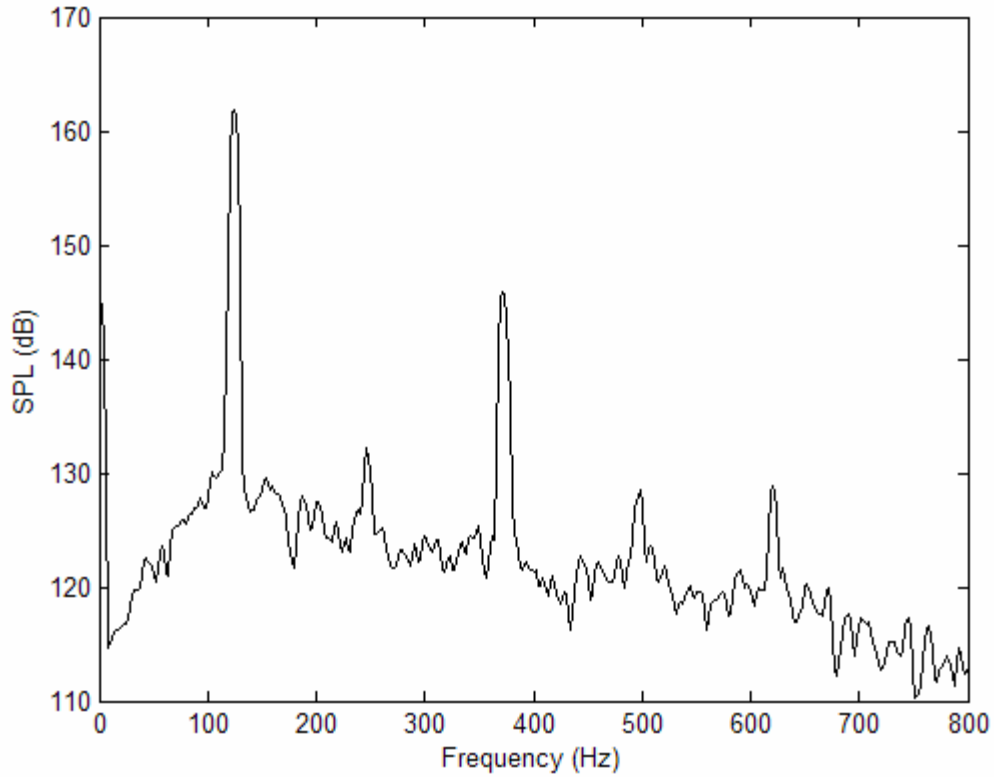


Figure D.1: Uncontrolled, GER=0.5.

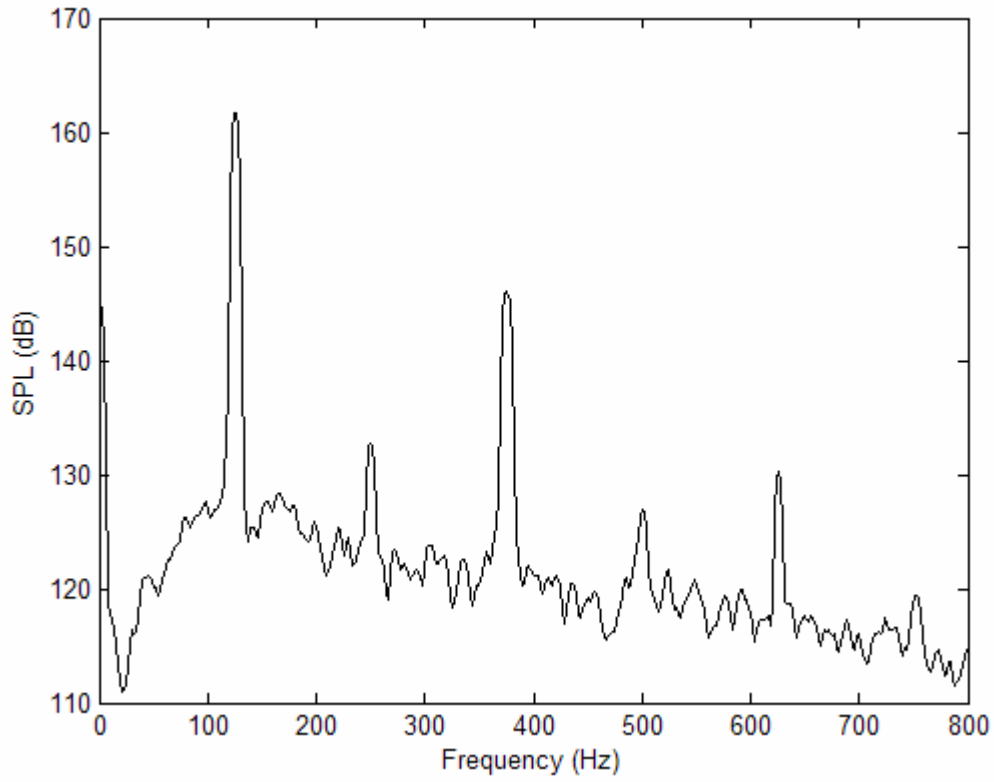


Figure D.2: Uncontrolled, GER=0.56.

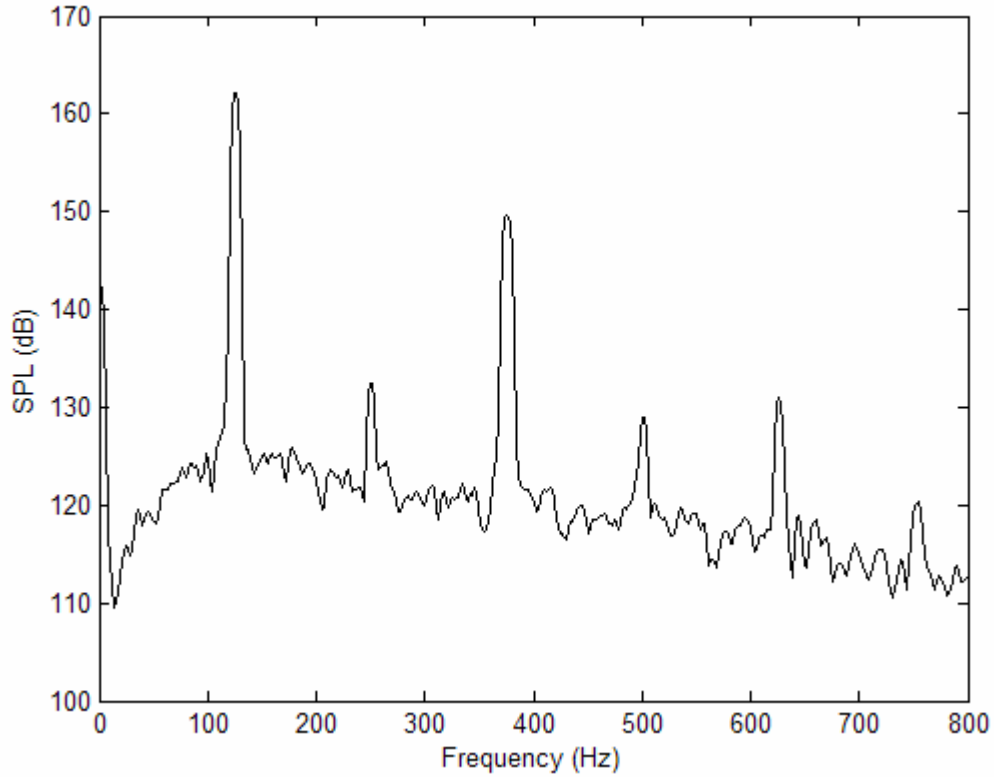


Figure D.3: Uncontrolled, GER=0.58.

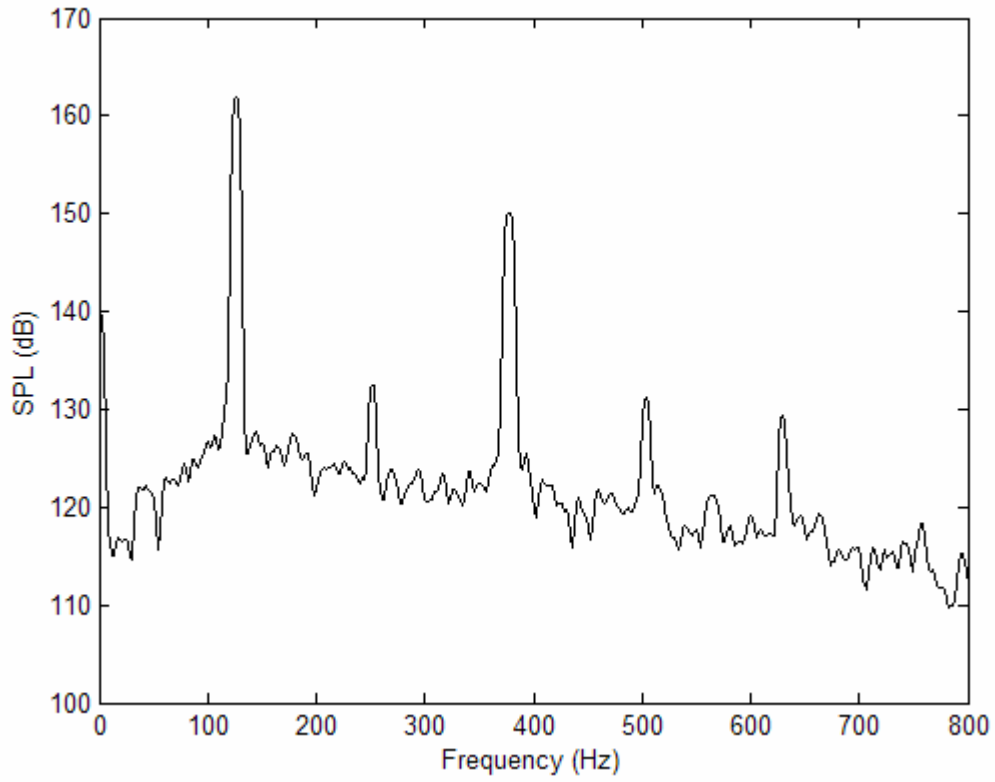


Figure D.4: Uncontrolled, GER=0.59.

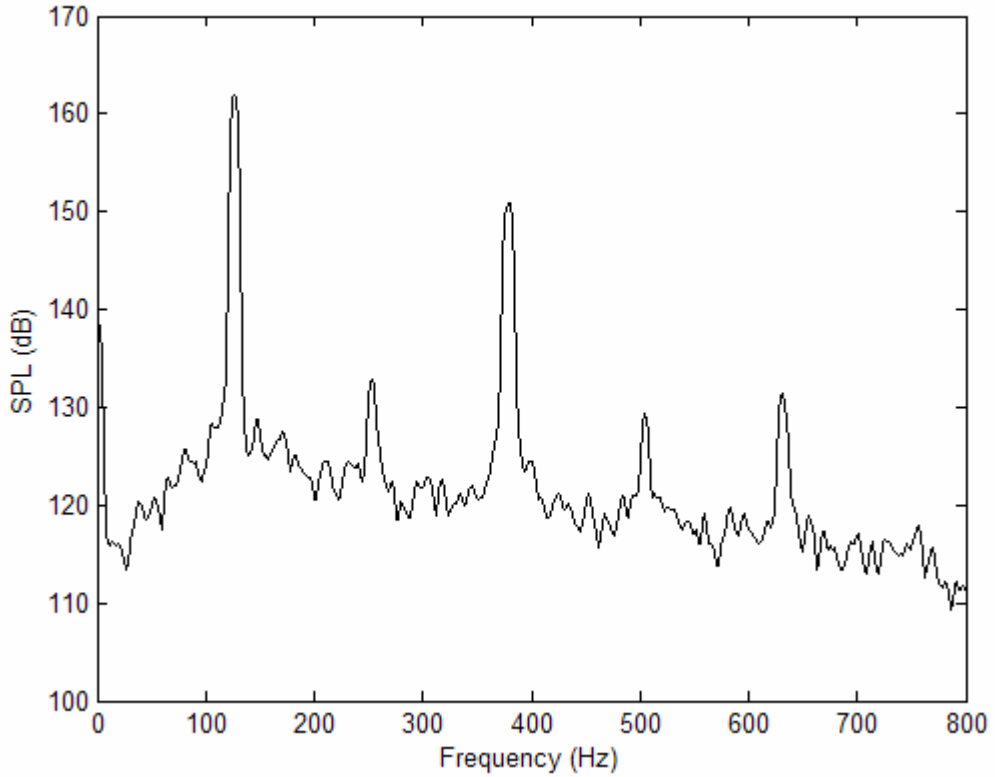


Figure D.5: Uncontrolled, GER=0.60.

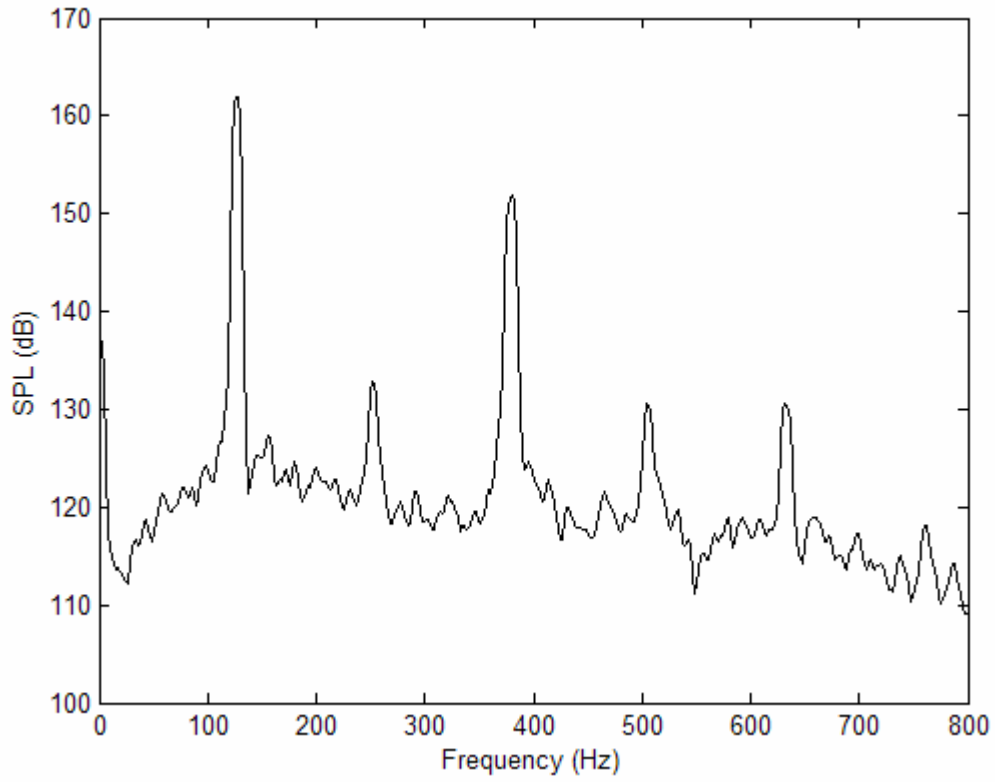


Figure D.6: Uncontrolled, GER=0.61.

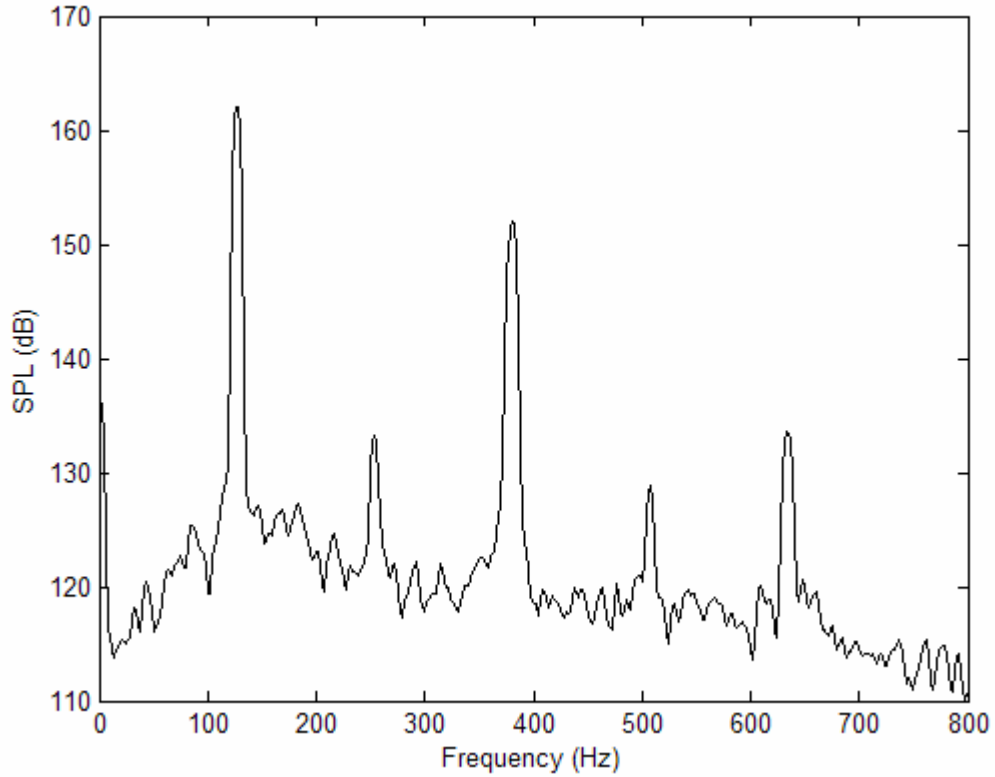


Figure D.7: Uncontrolled, GER=0.62.

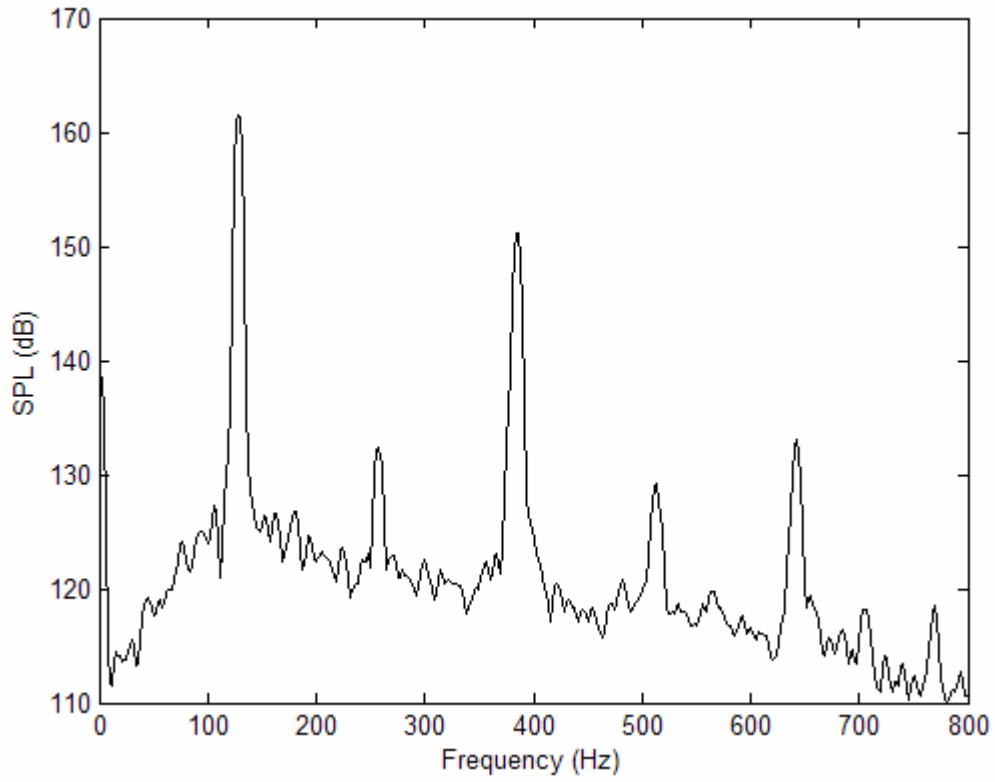


Figure D.8: Uncontrolled, GER=0.63.

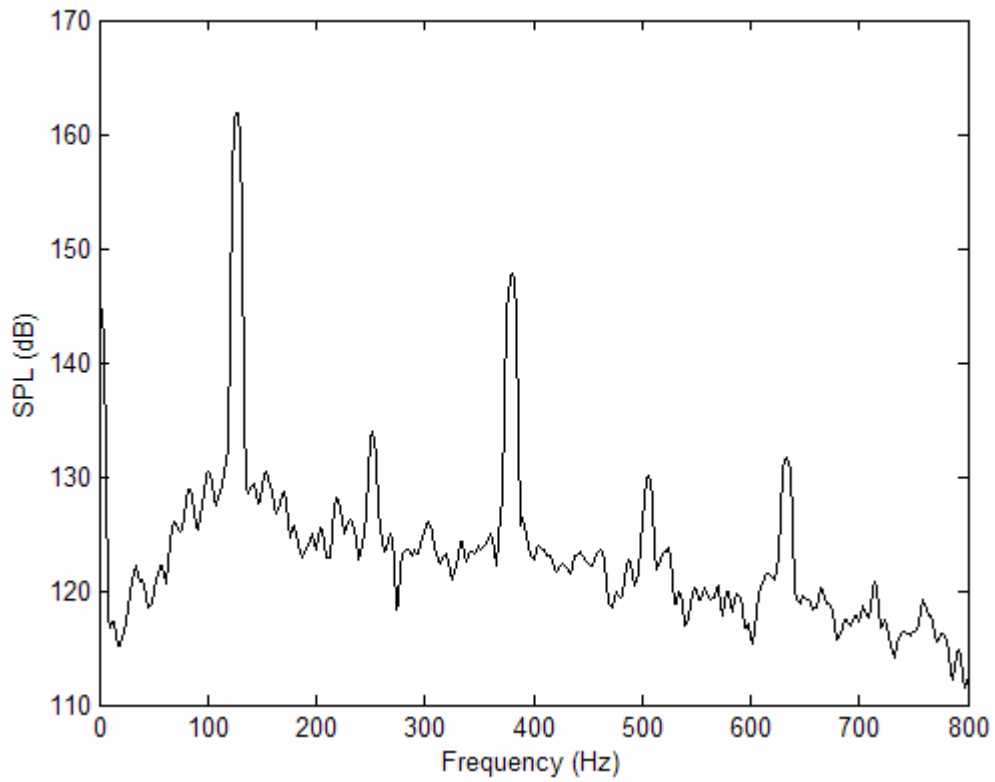


Figure D.9: Uncontrolled, GER=0.60.

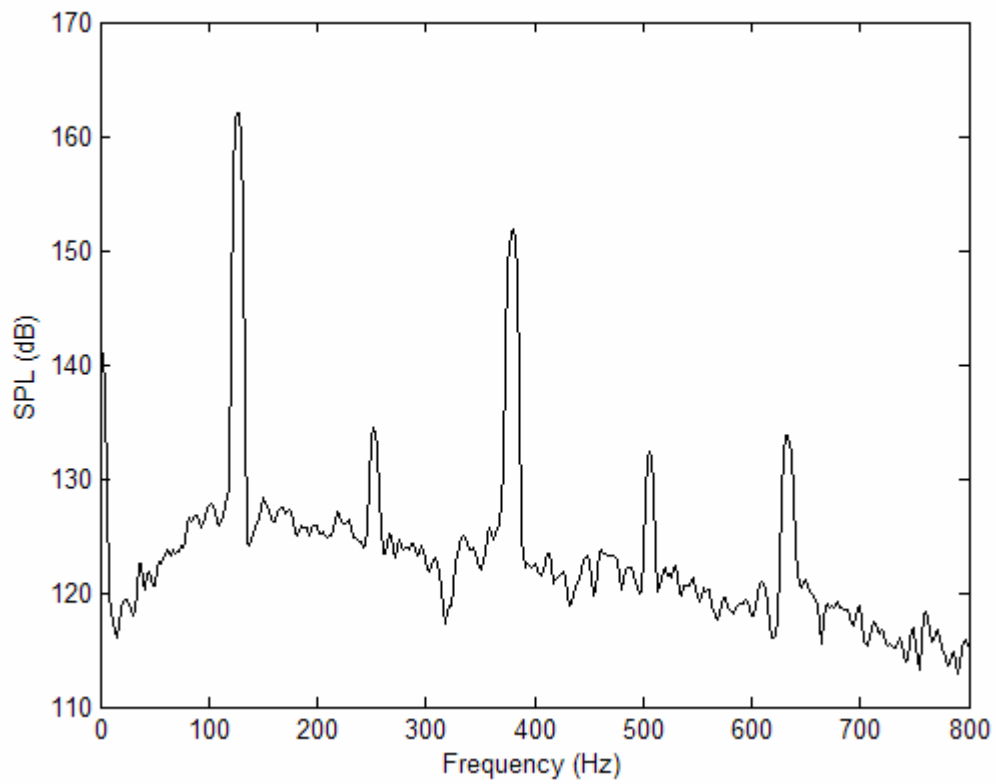


Figure D.10: Uncontrolled, GER=0.62.

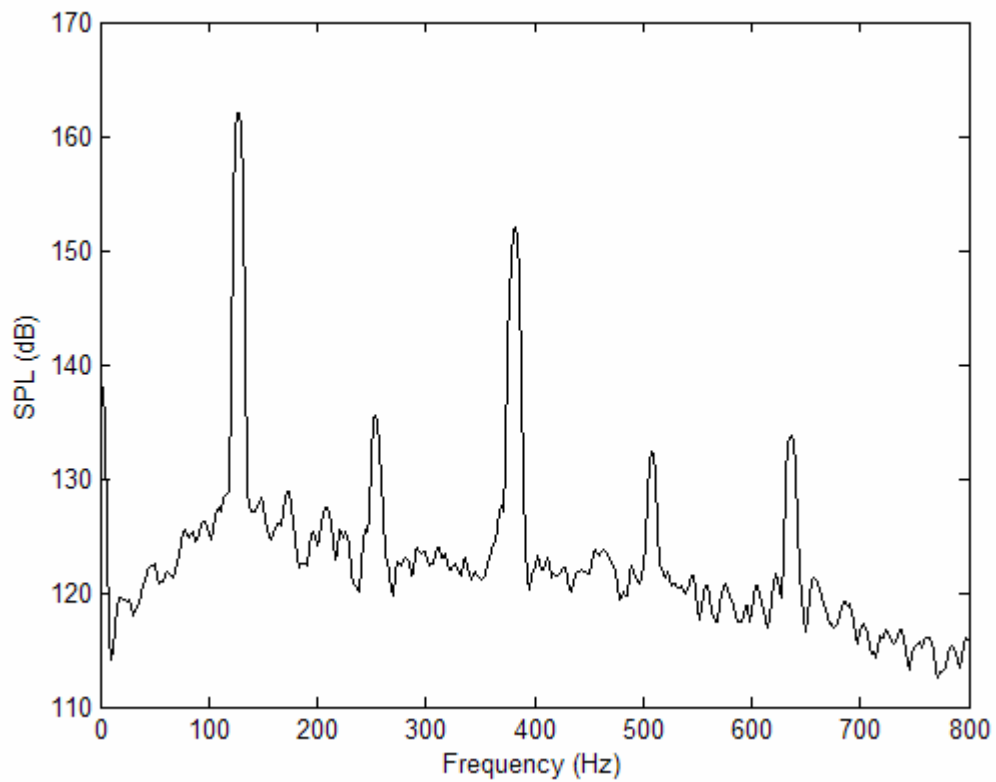


Figure D.11: Uncontrolled, GER=0.64.

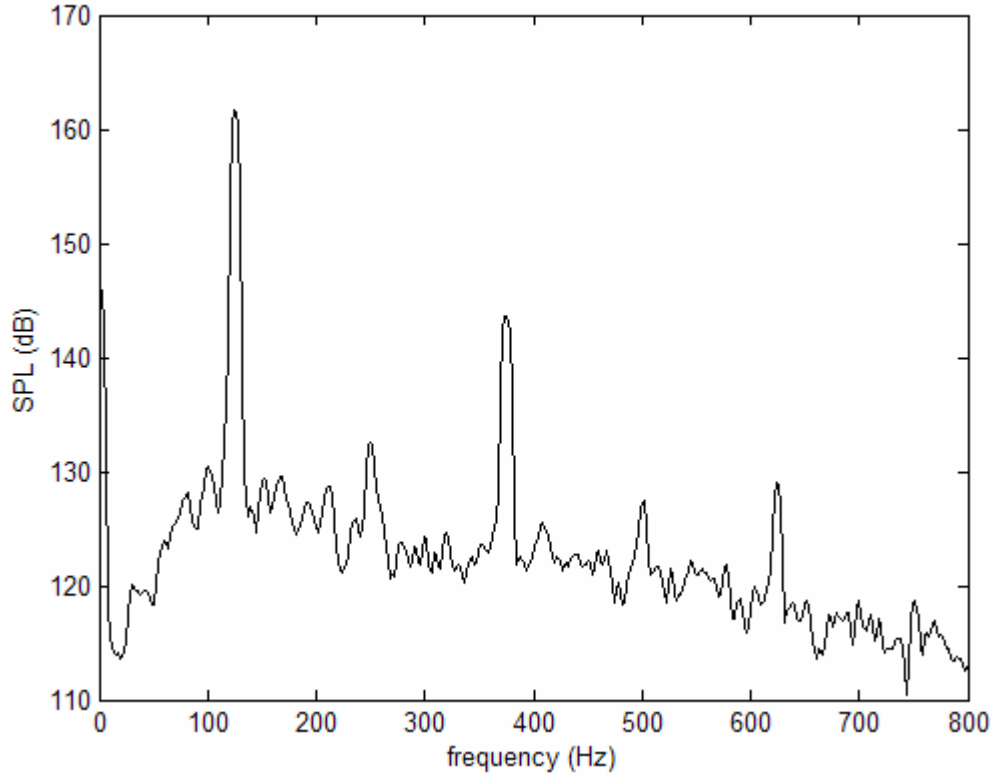


Figure D.12: Uncontrolled, GER=0.57.

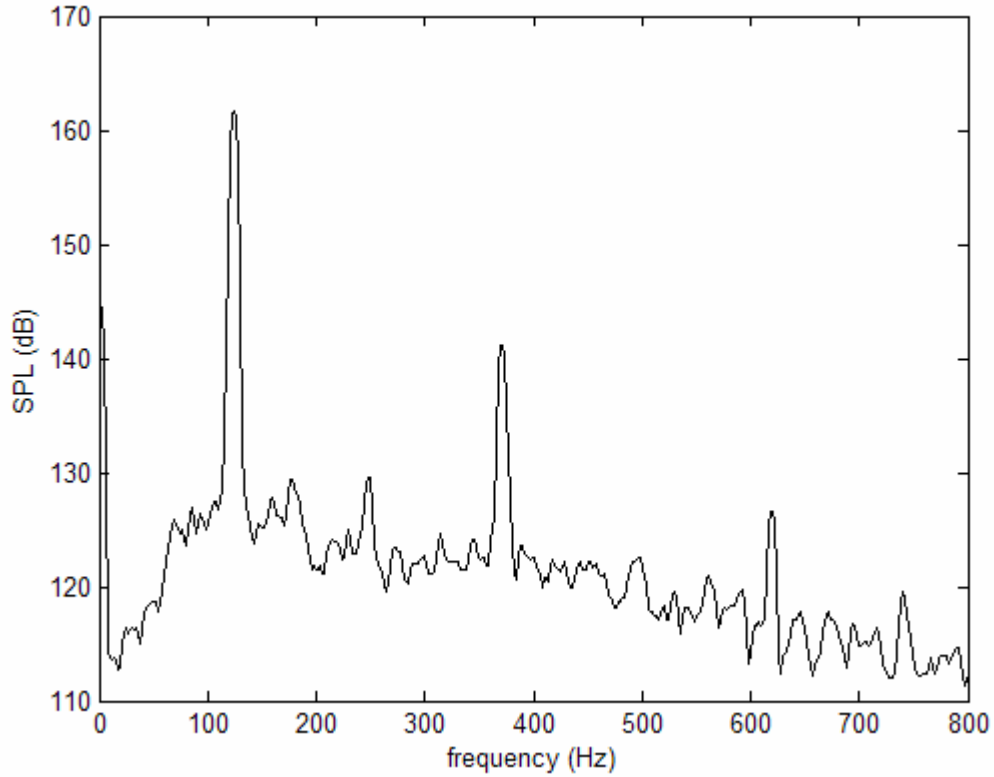


Figure D.13: Uncontrolled, GER=0.51.

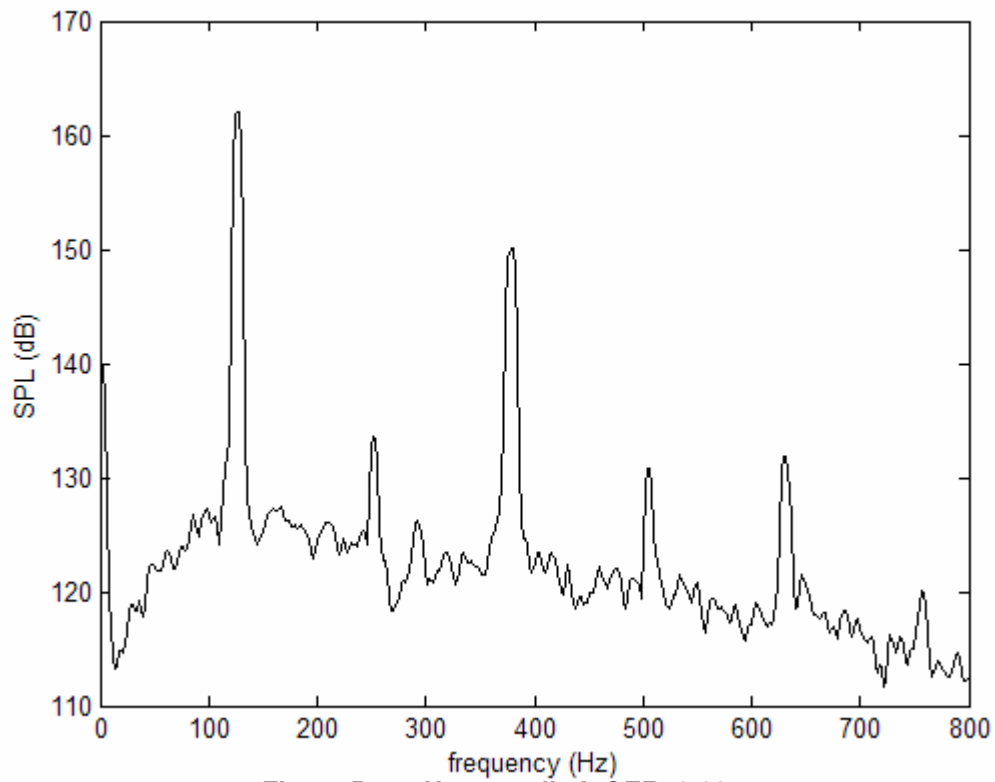


Figure D.14: Uncontrolled, GER=0.62.

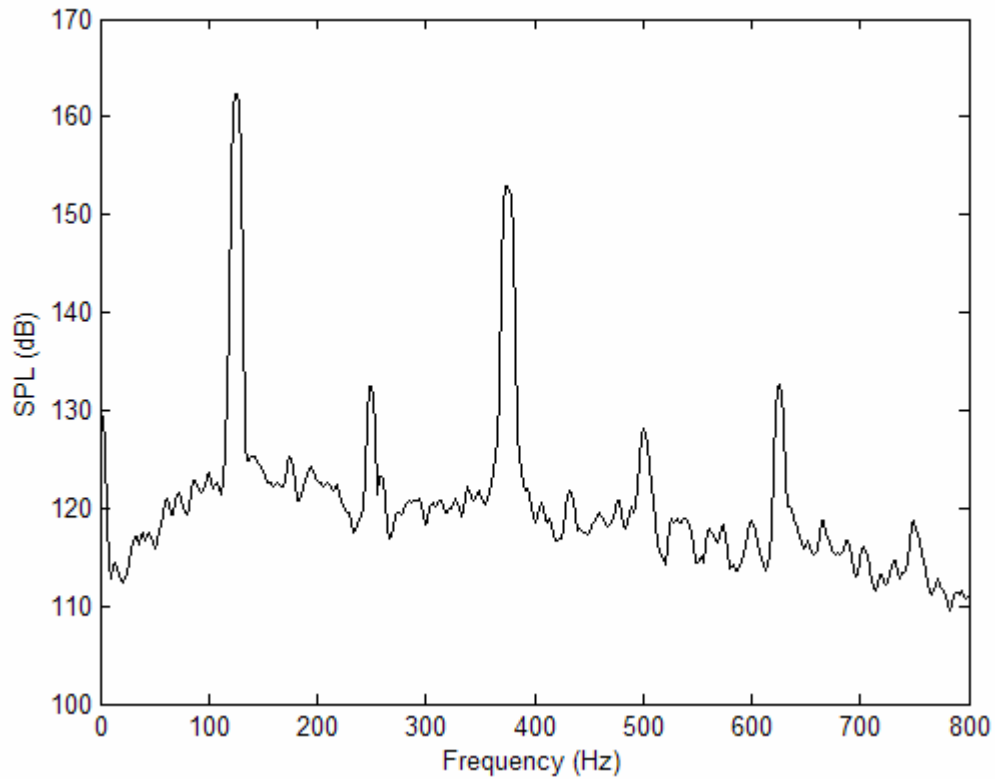


Figure D.15: Uncontrolled, GER=0.64.

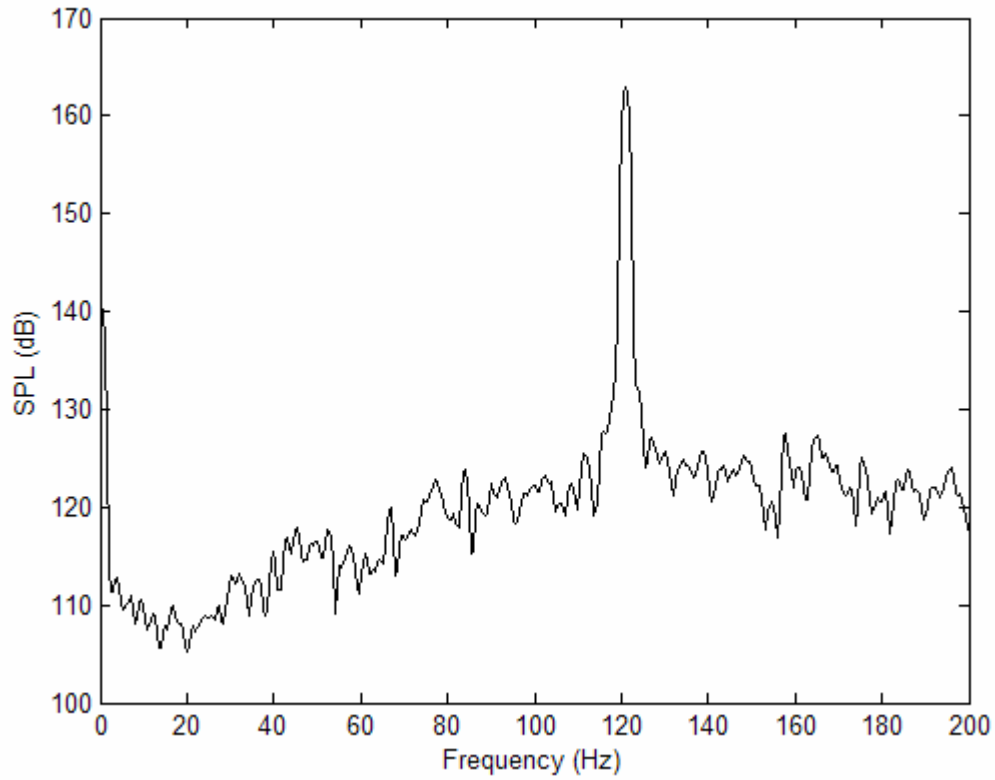


Figure D.16: Uncontrolled, GER=0.48.

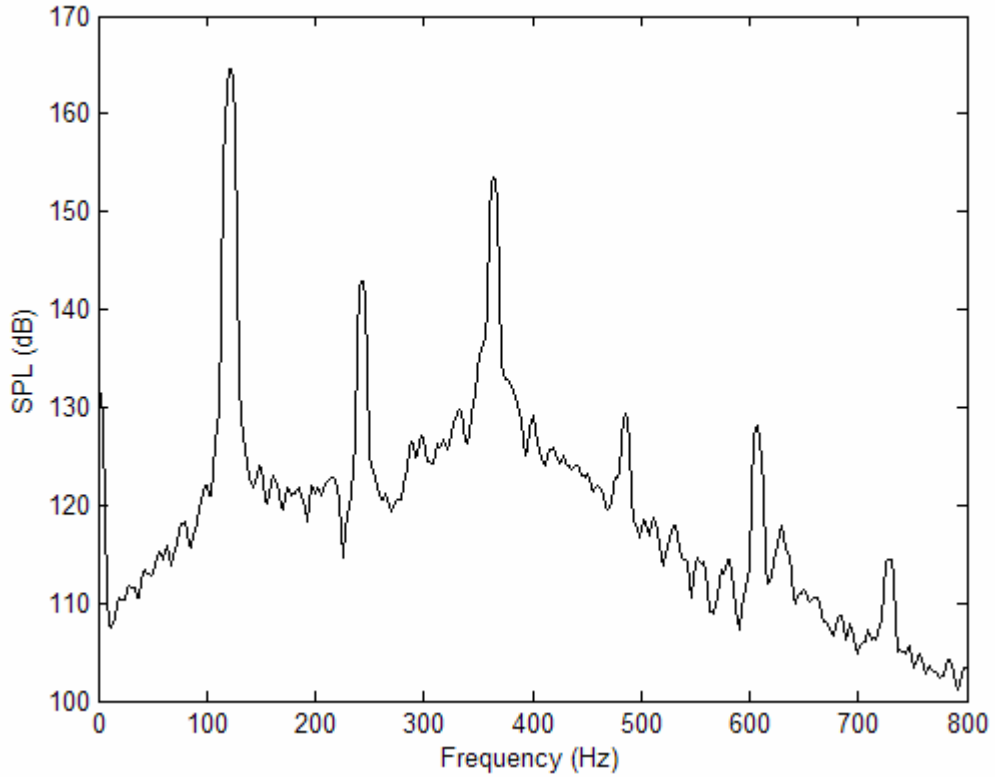


Figure D.17: Uncontrolled, GER=0.5.

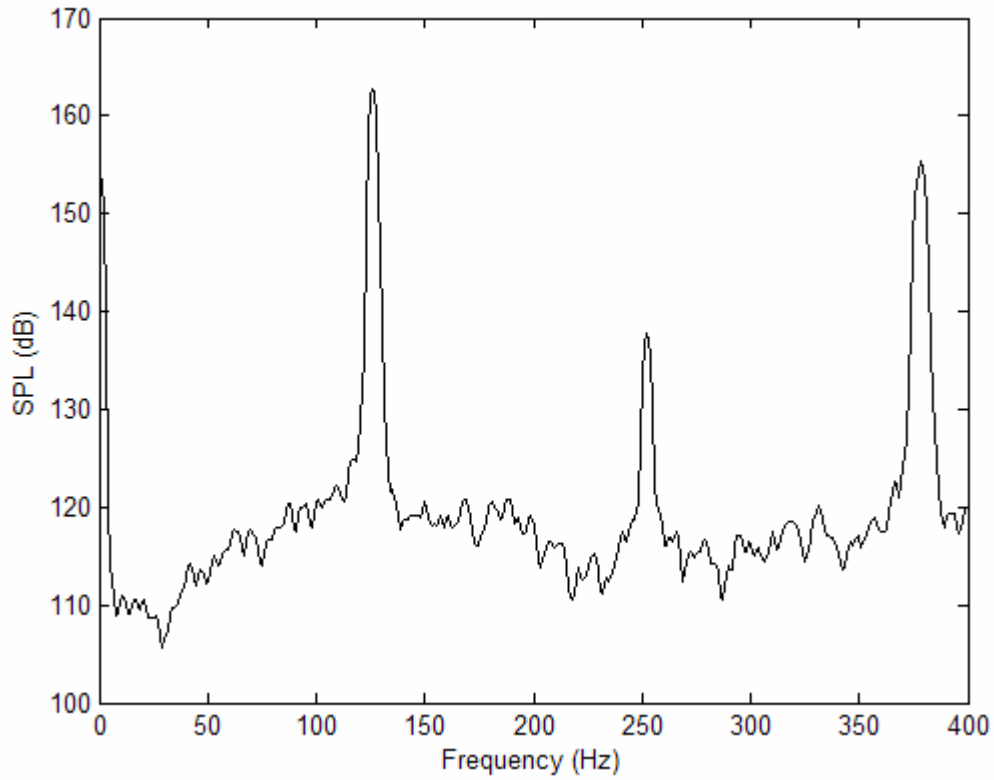


Figure D.18: Uncontrolled, GER=0.65.

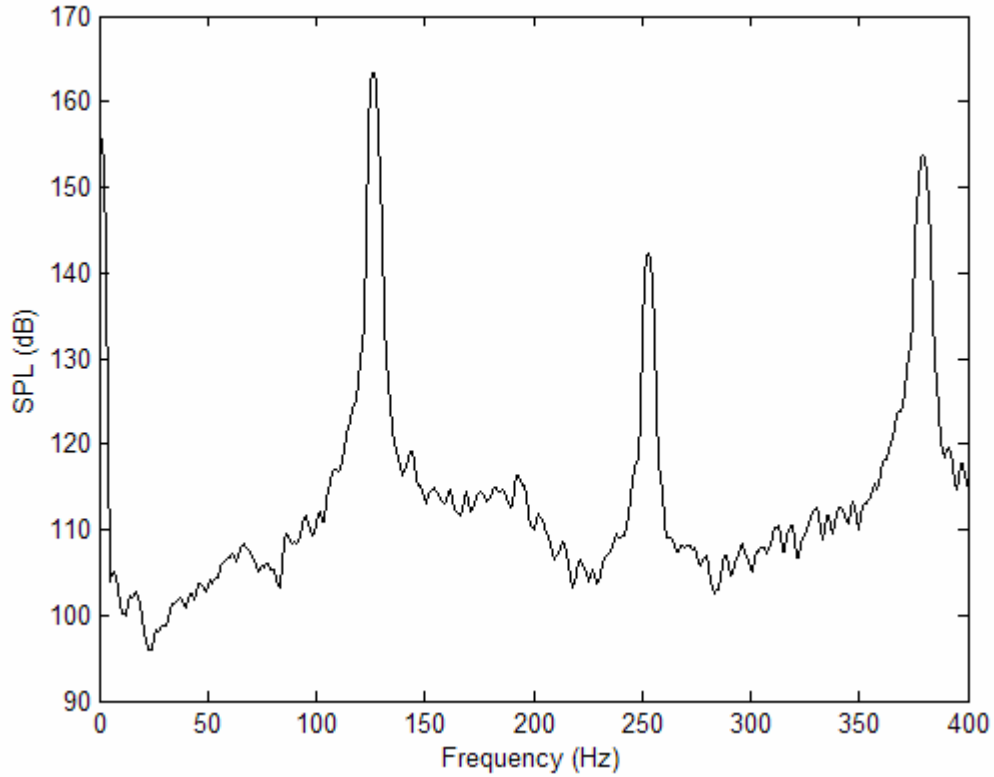


Figure D.19: Uncontrolled, GER=0.58.

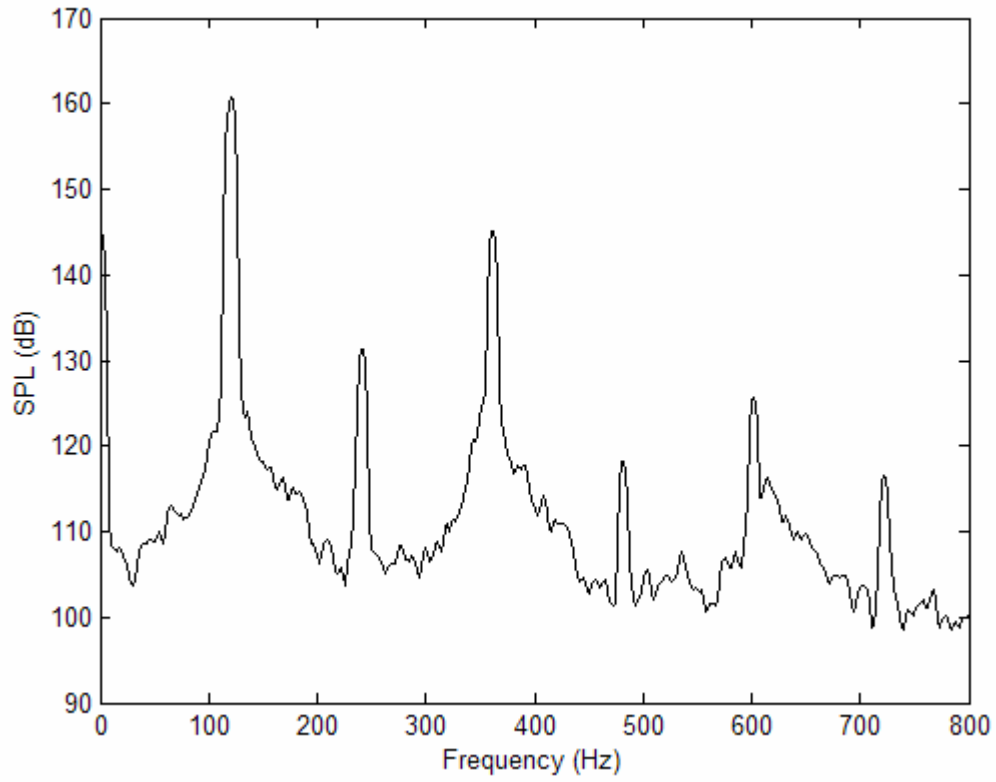


Figure D.20: Uncontrolled, GER=0.52.

Appendix E: Power Spectrums for the VACCG Kerosene-Fueled Combustor, GER=0.50, Various Controller Settings

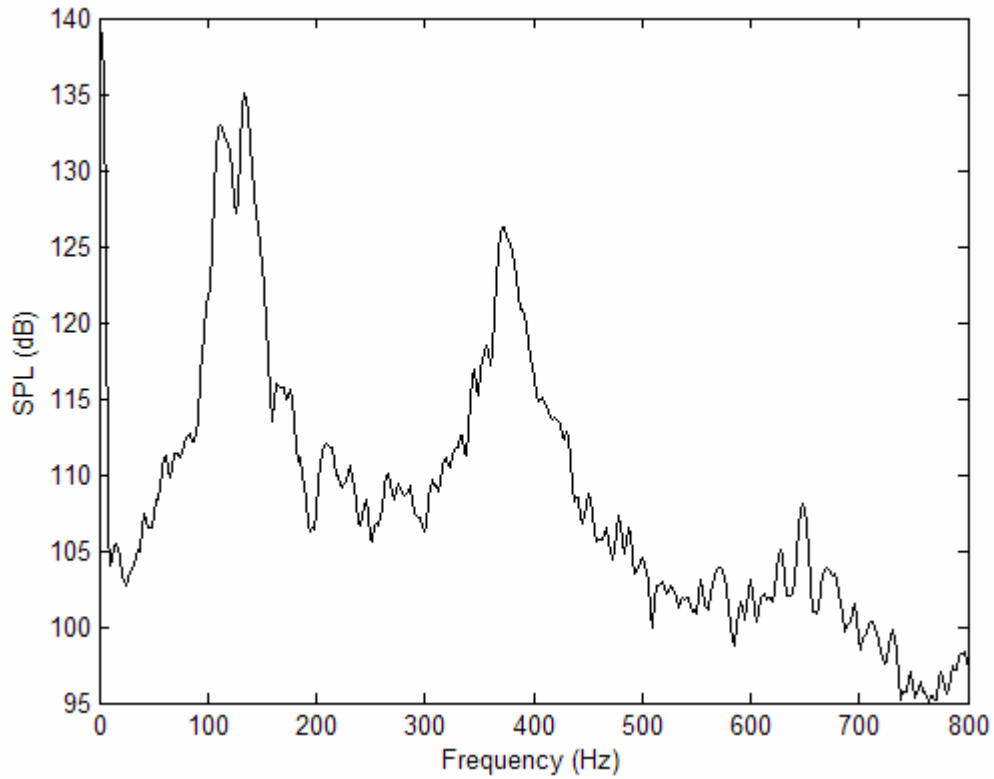


Figure E.1: GER=0.5, Controller delay=24, Gain=0.75.

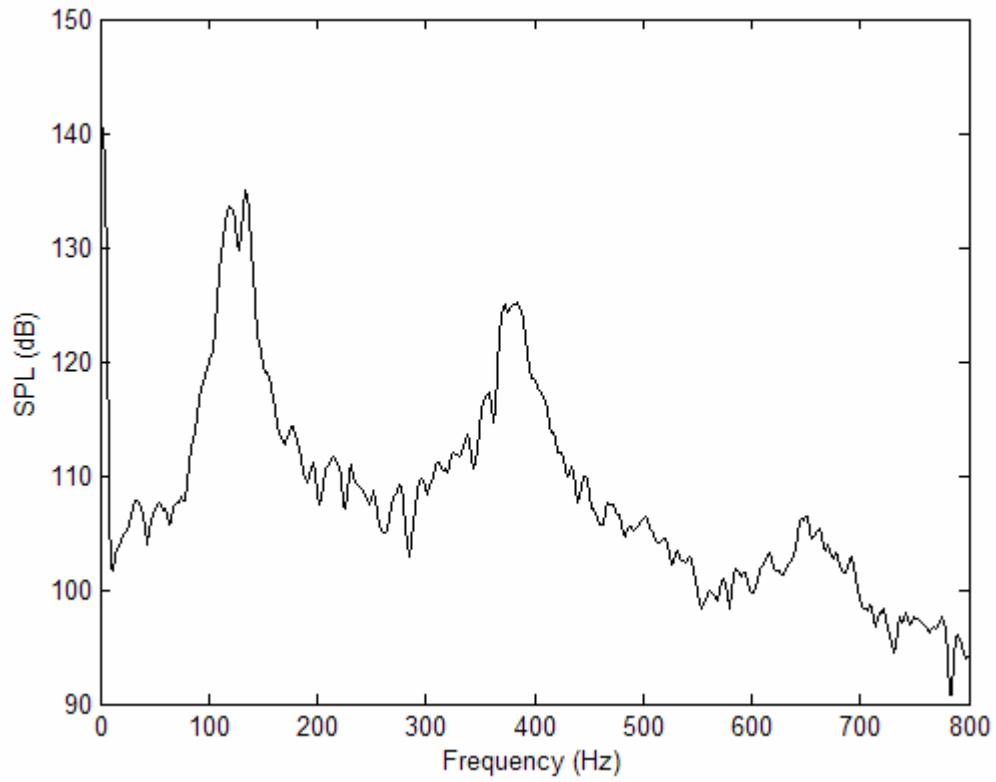


Figure E.2: GER=0.5, Controller delay=24, Gain=0.70.

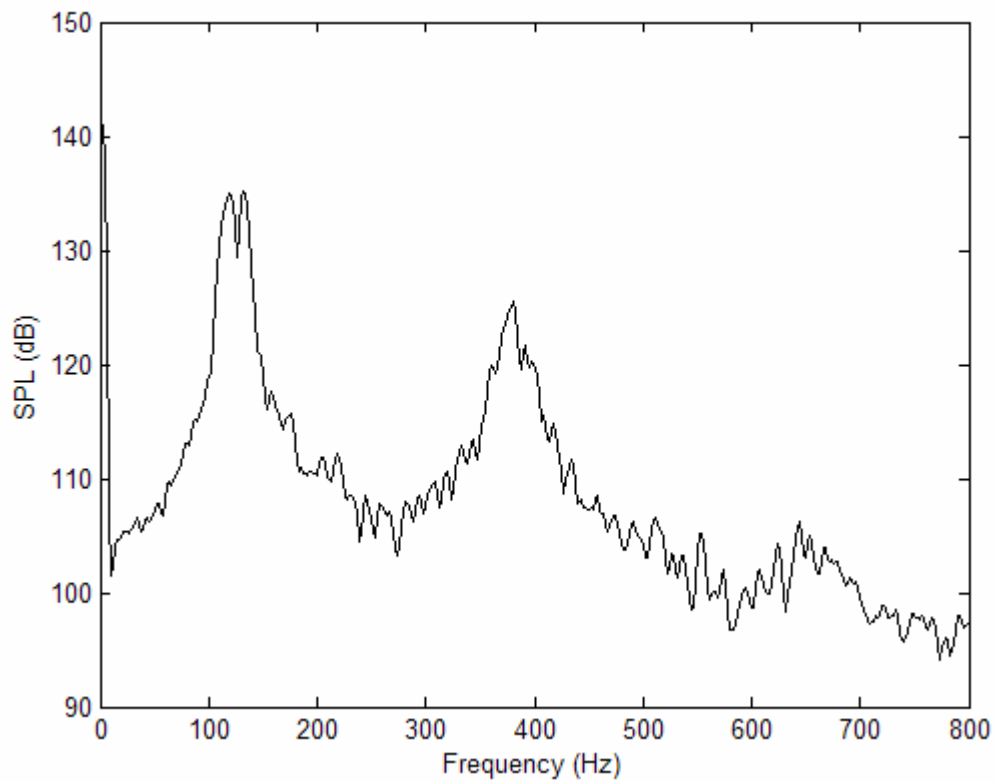


Figure E.3: GER=0.5, Controller delay=24, Gain=0.65.

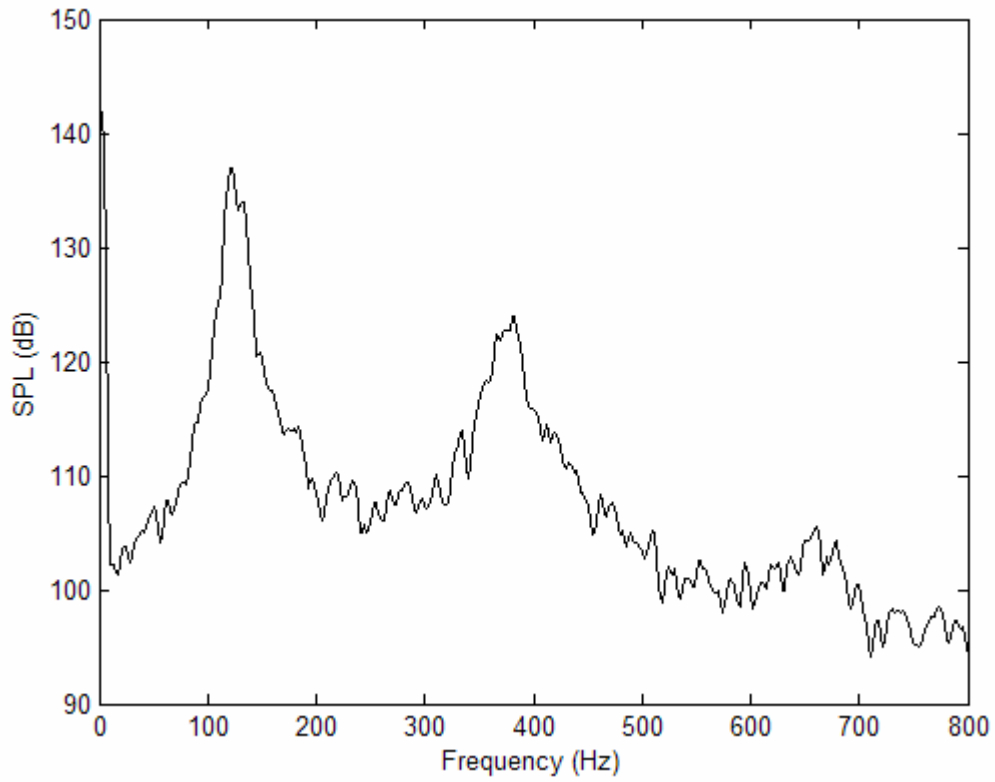


Figure E.4: GER=0.5, Controller delay=24, Gain=0.60.

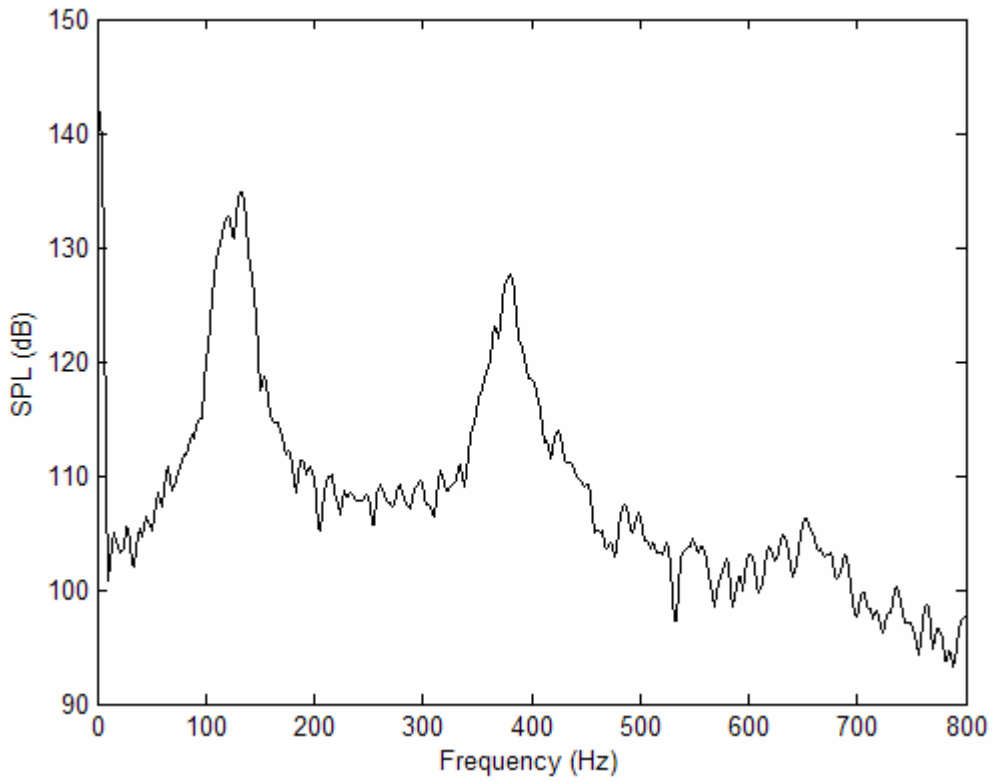


Figure E.5: GER=0.5, Controller delay=24, Gain=0.55.

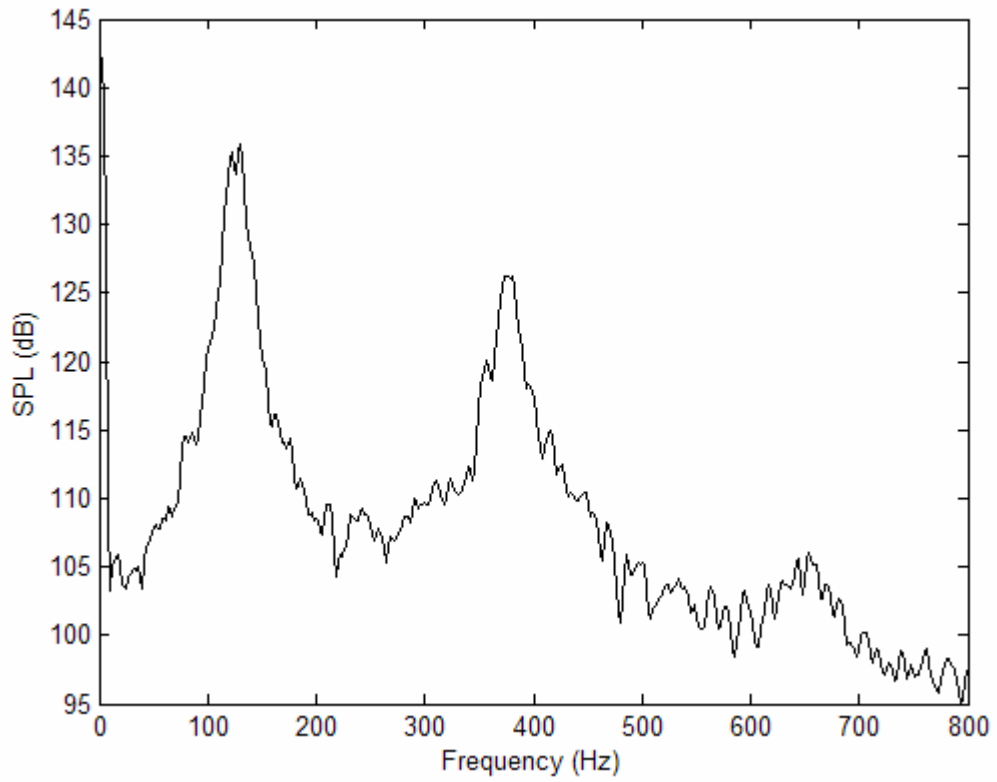


Figure E.6: GER=0.5, Controller delay=24, Gain=0.50.

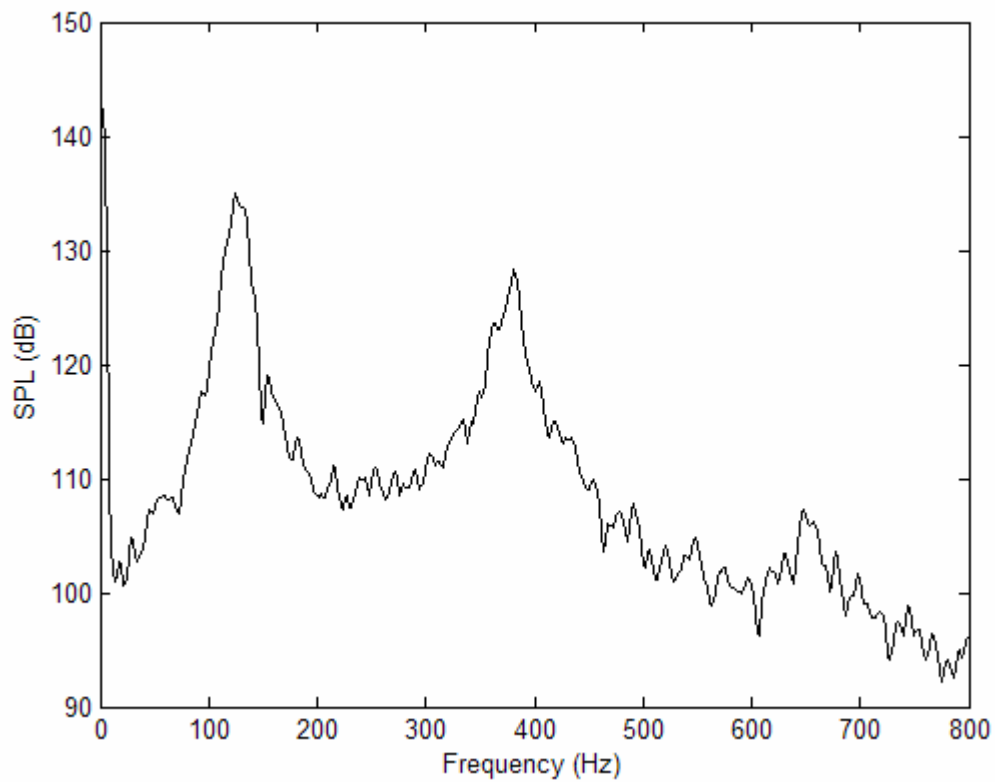


Figure E.7: GER=0.5, Controller delay=24, Gain=0.45.

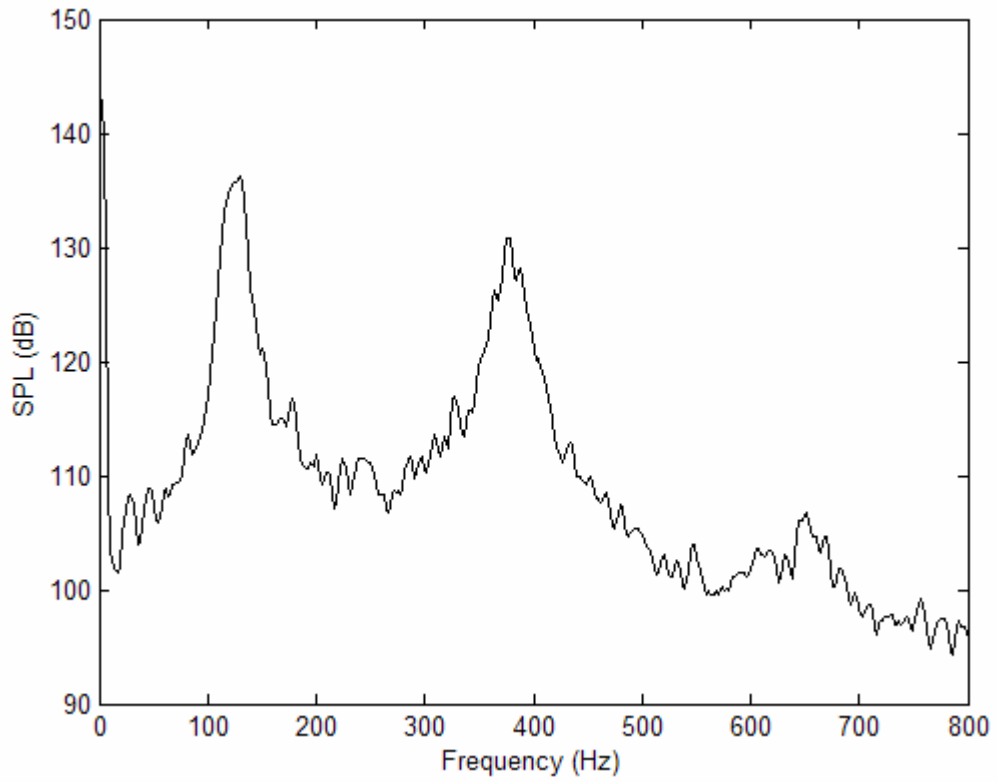


Figure E.8: GER=0.5, Controller delay=24, Gain=0.40.

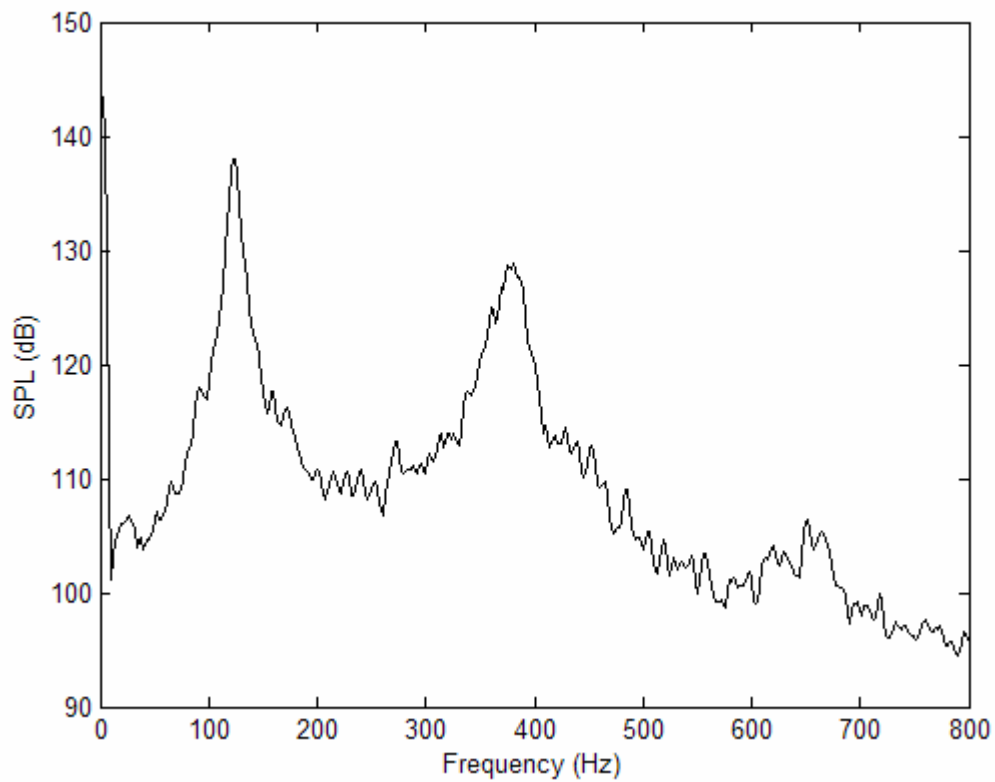


Figure E.9: GER=0.5, Controller delay=24, Gain=0.35.

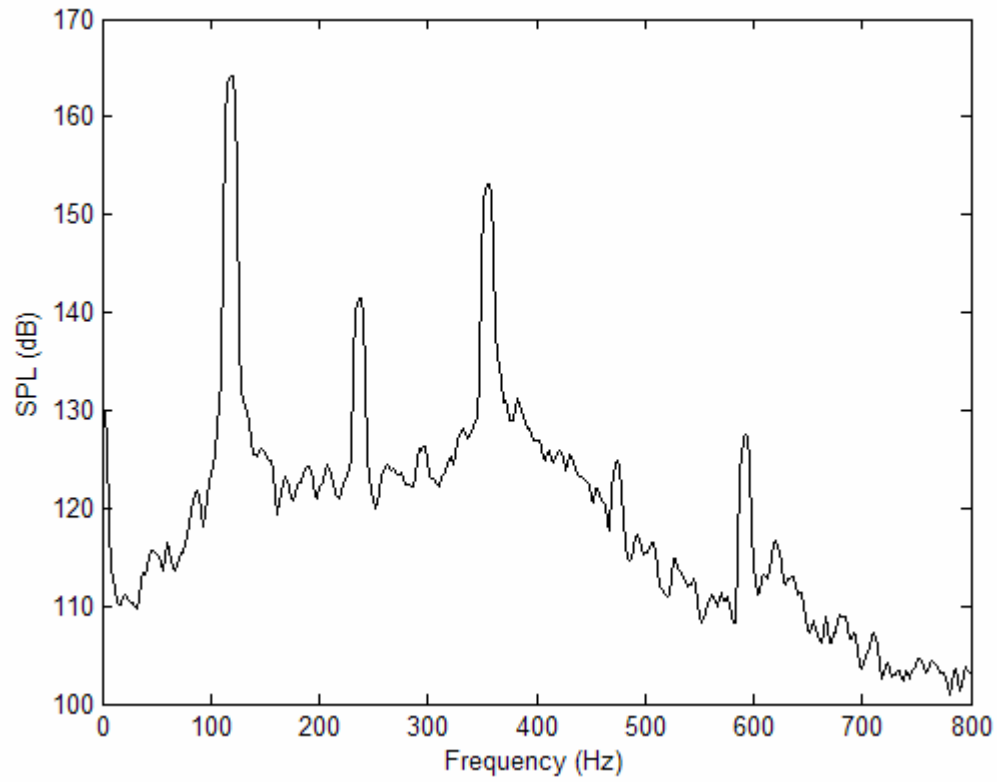


Figure E.10: GER=0.5, Controller delay=24, Gain=0.35.

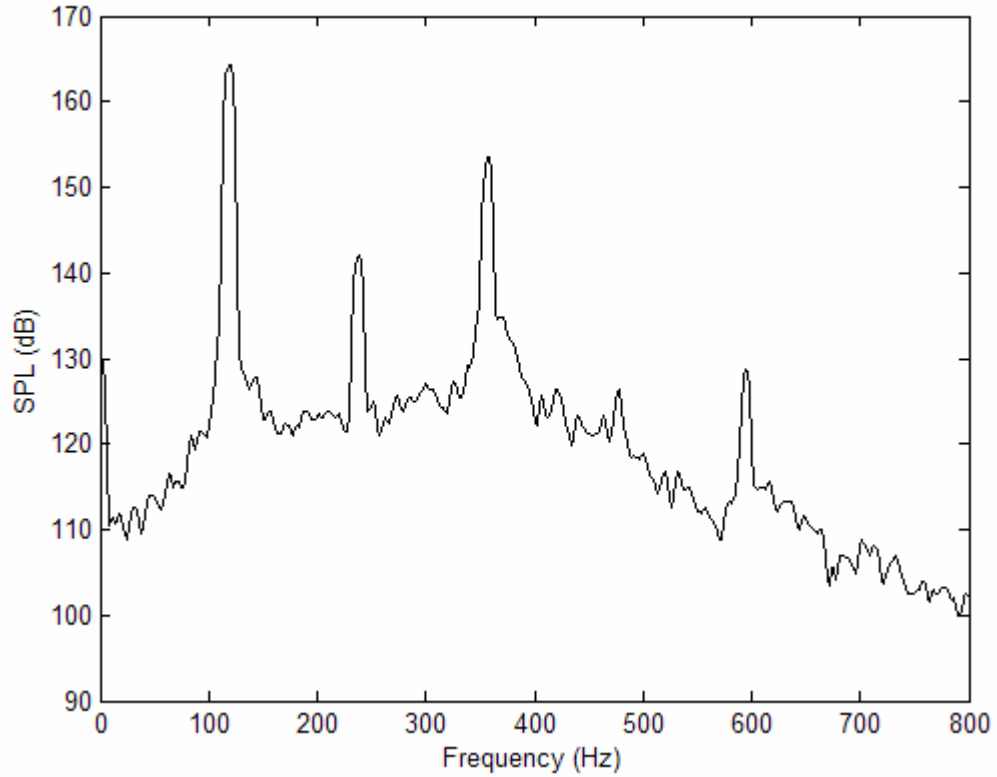


Figure E.11: GER=0.5, Controller delay=24, Gain=0.30.

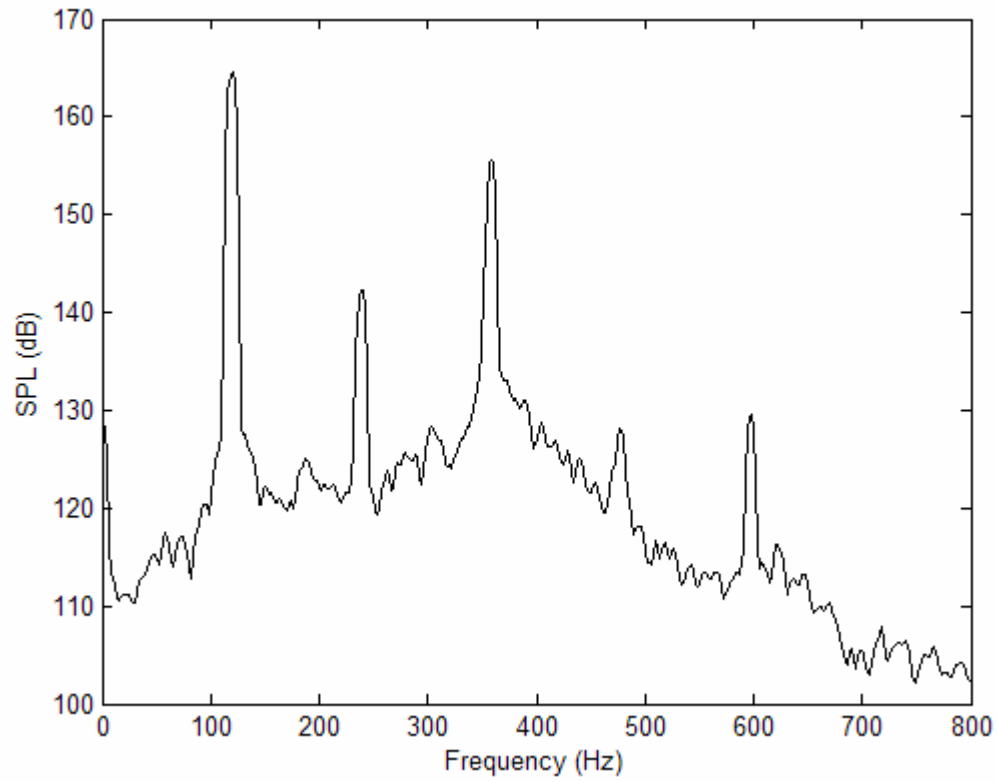


Figure E.12: GER=0.5, Controller delay=24, Gain=0.25.

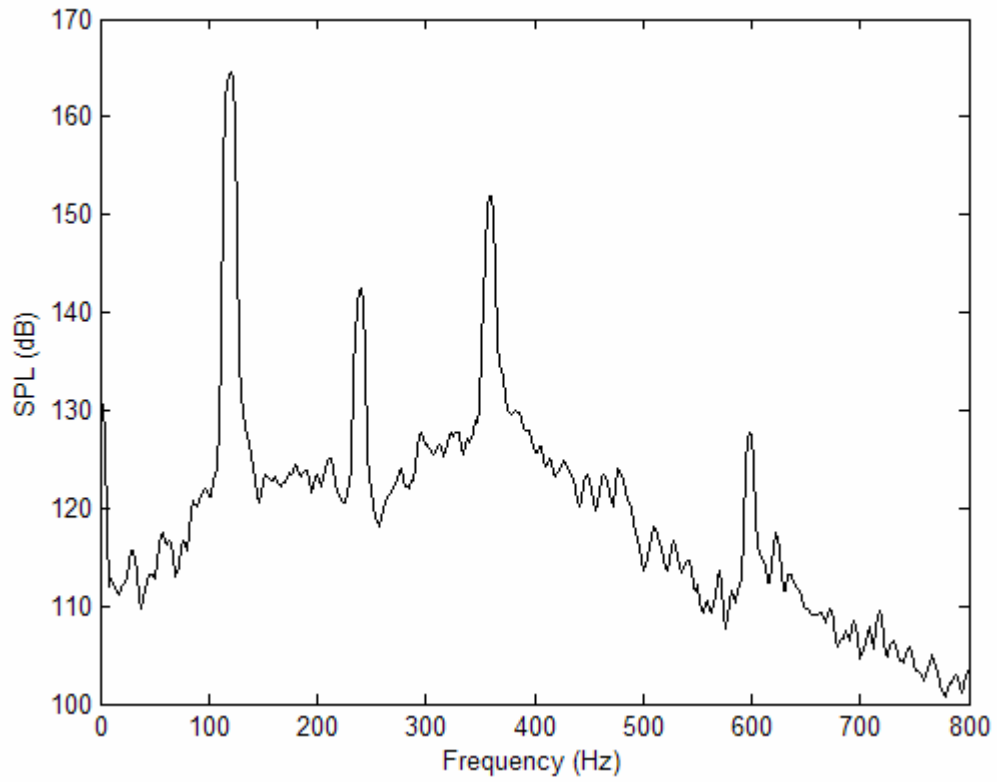


Figure E.13: GER=0.5, Controller delay=24, Gain=0.20.

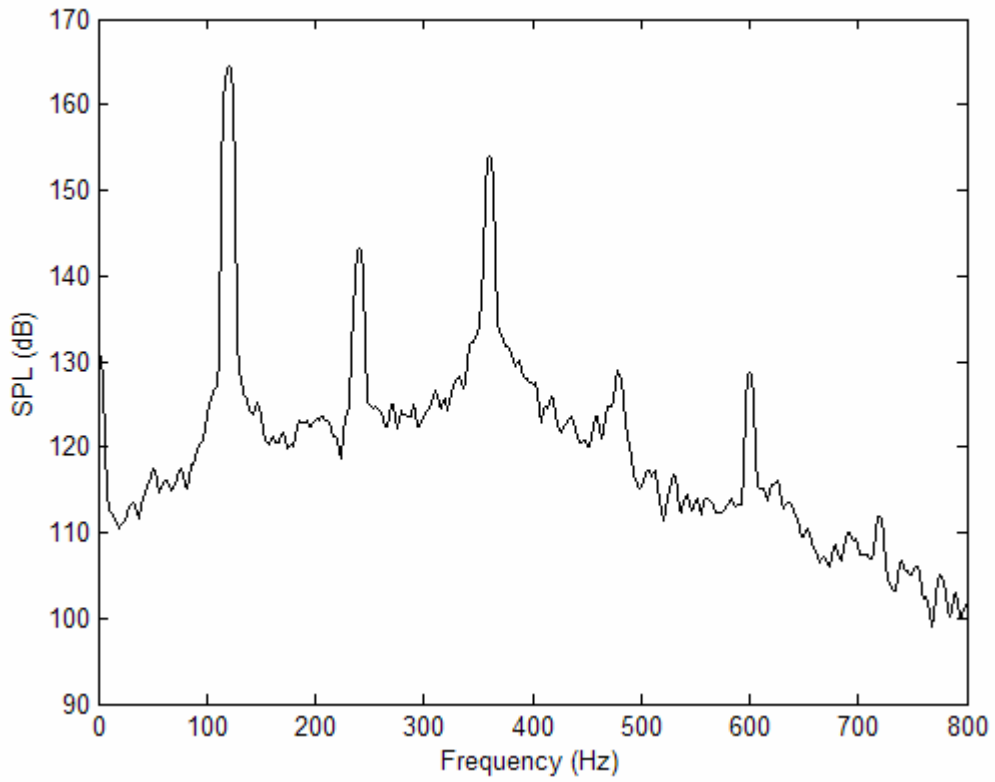


Figure E.14: GER=0.5, Controller delay=24, Gain=0.15.

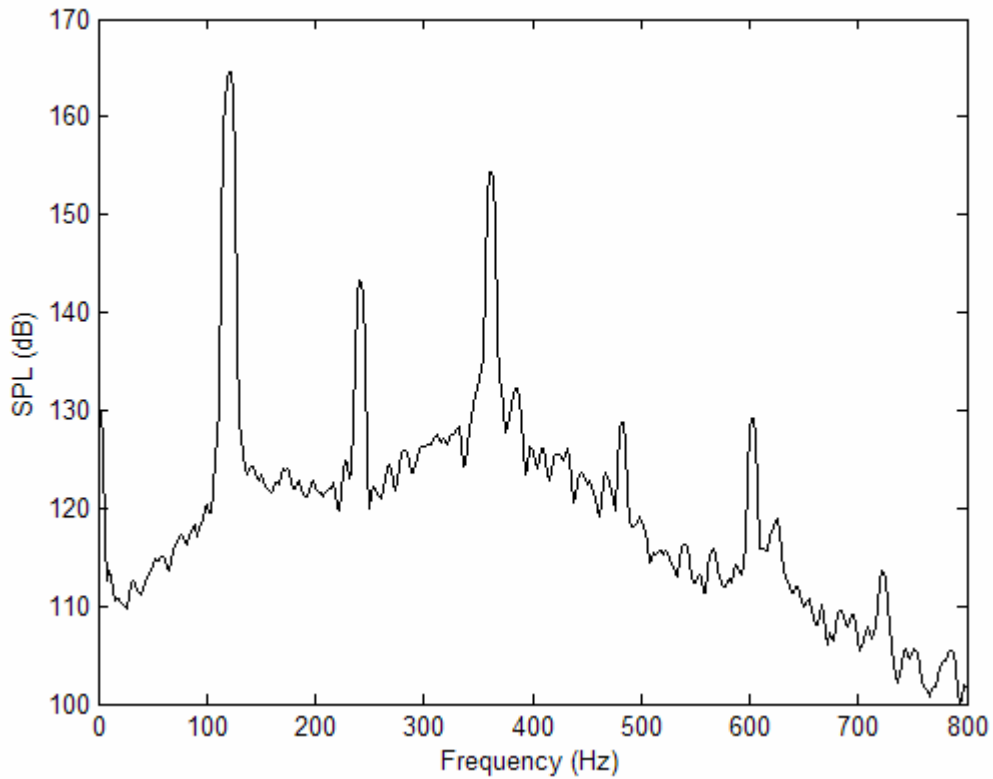
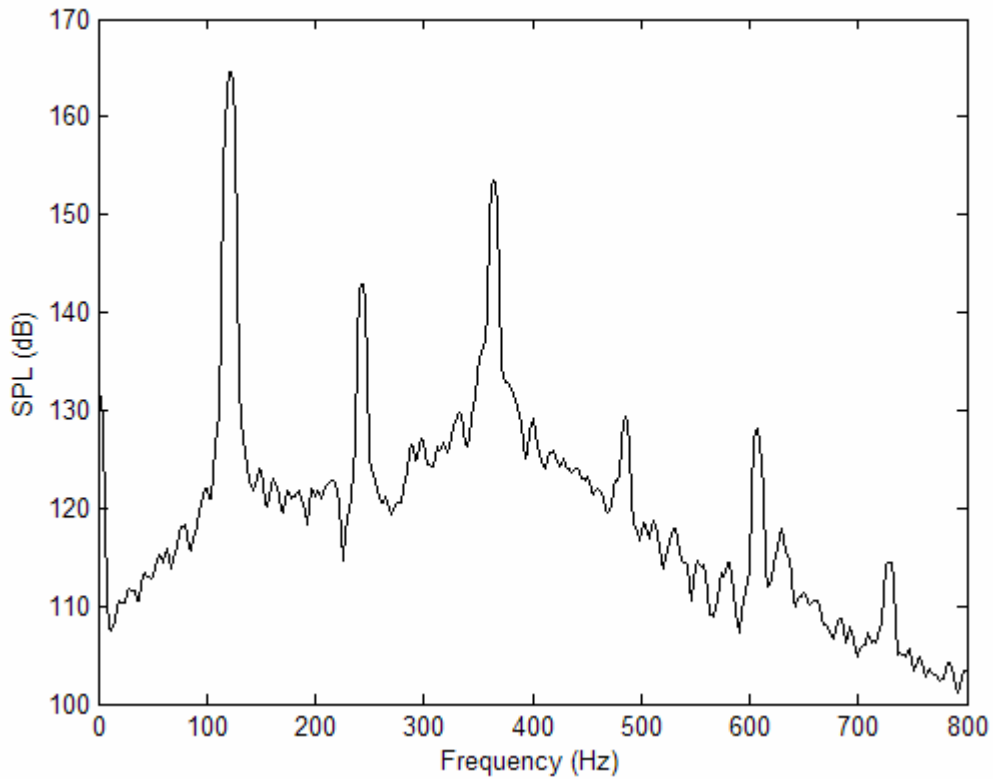
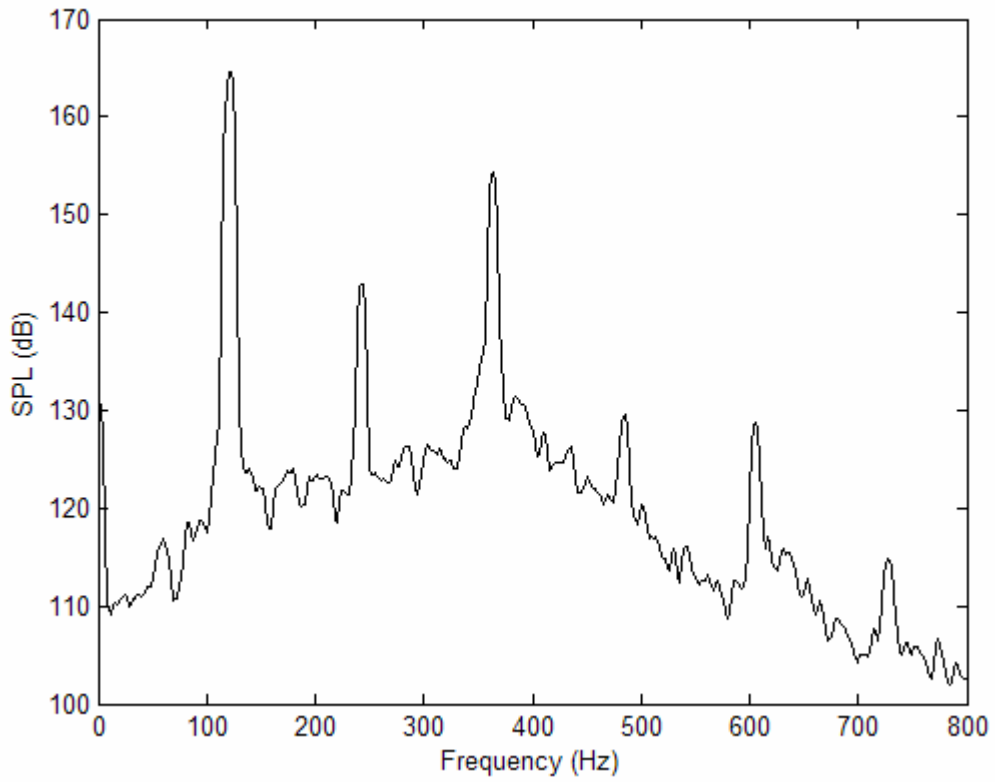


Figure E.15: GER=0.5, Controller delay=24, Gain=0.10.



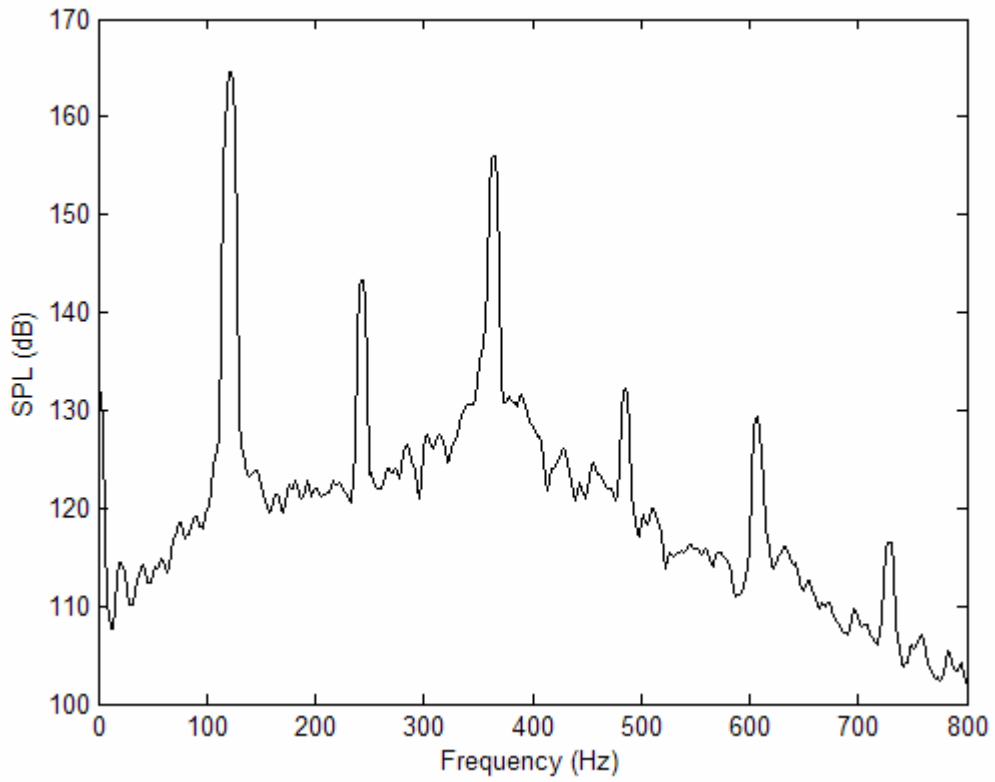


Figure E.18: GER=0.5, Controller delay=24, Gain=0.05.

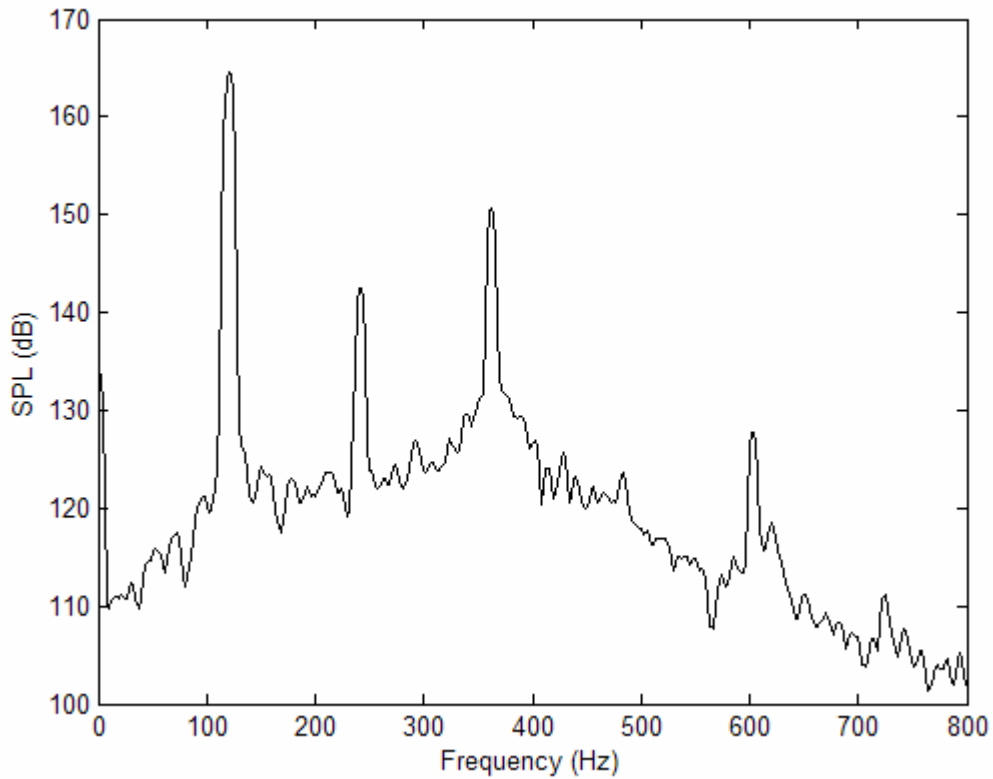


Figure E.19: GER=0.5, Controller delay=24, Gain=0.10.

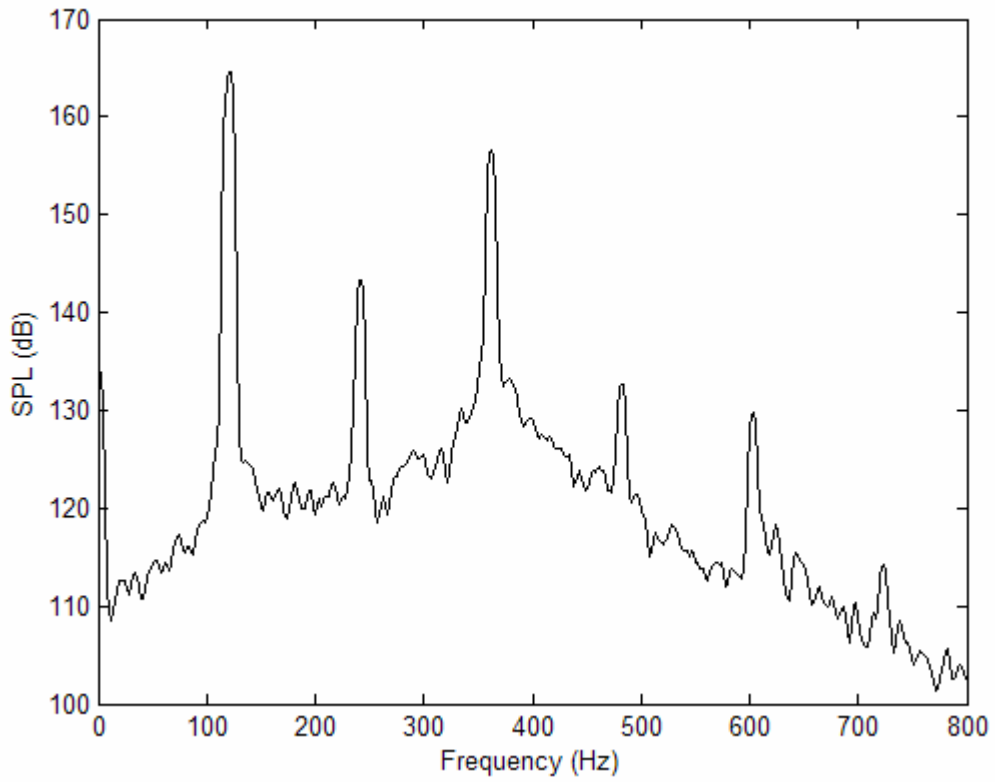


Figure E.20: GER=0.5, Controller delay=24, Gain=0.15.

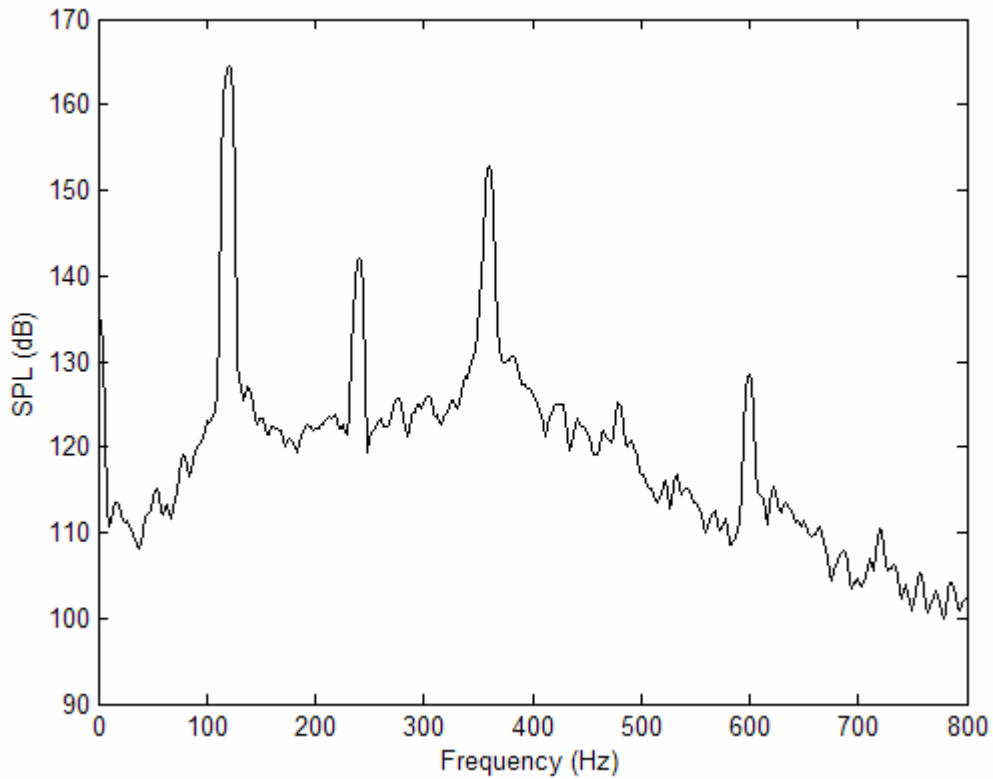


Figure E.21: GER=0.5, Controller delay=24, Gain=0.20.

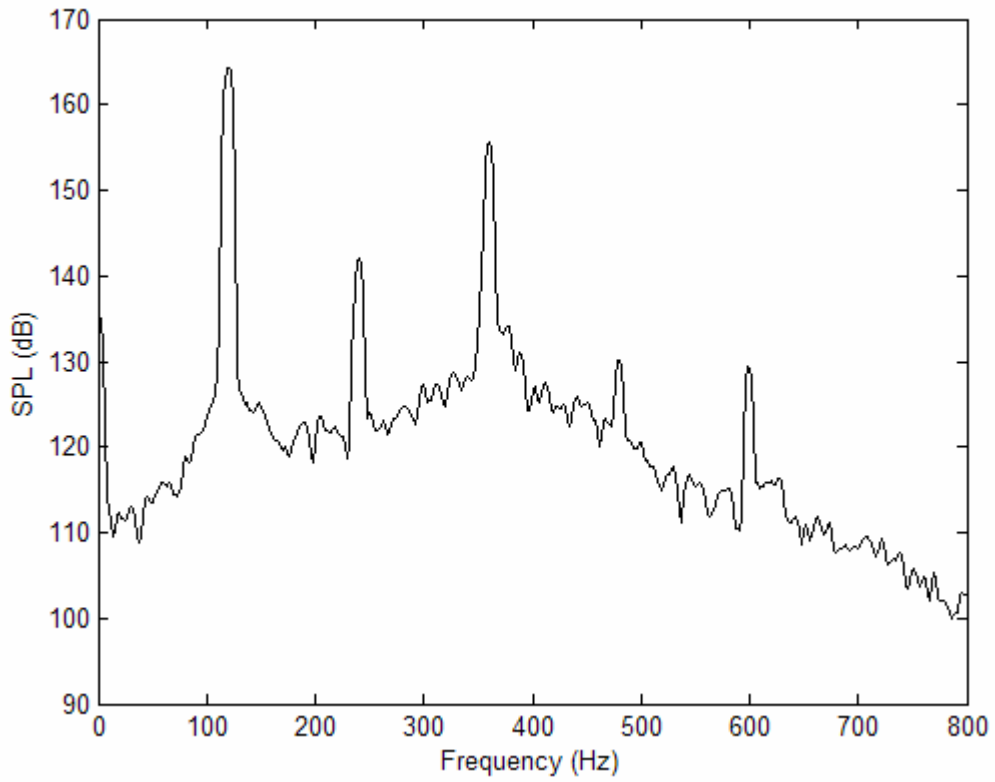


Figure E.22: GER=0.5, Controller delay=24, Gain=0.25.

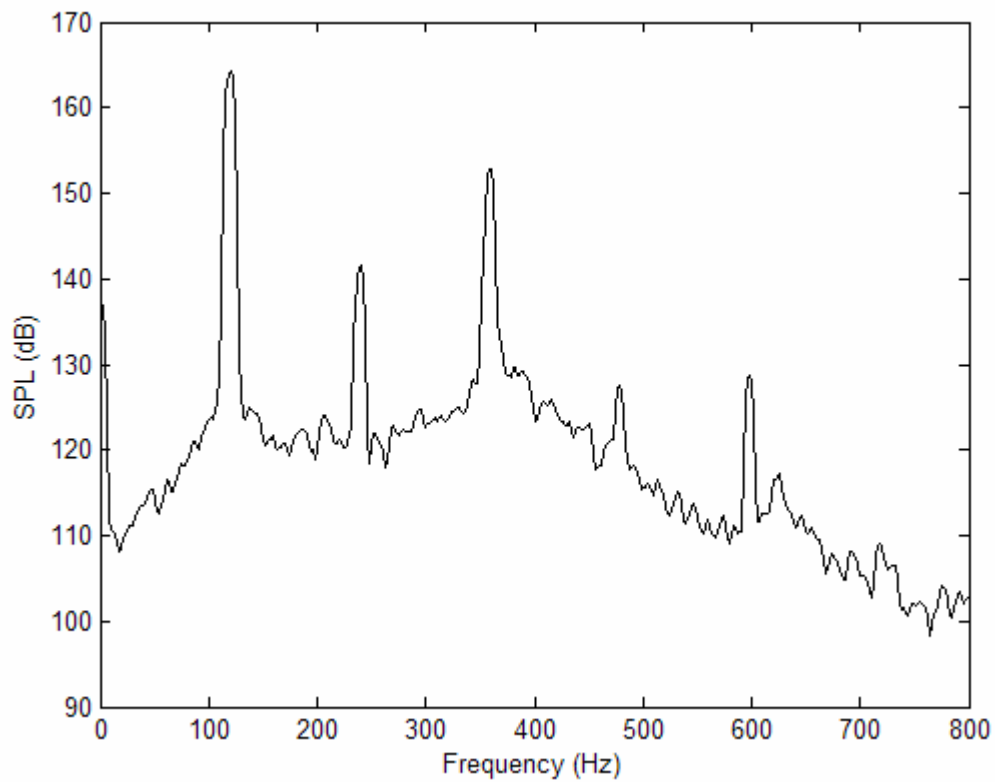


Figure E.23: GER=0.5, Controller delay=24, Gain=0.30.

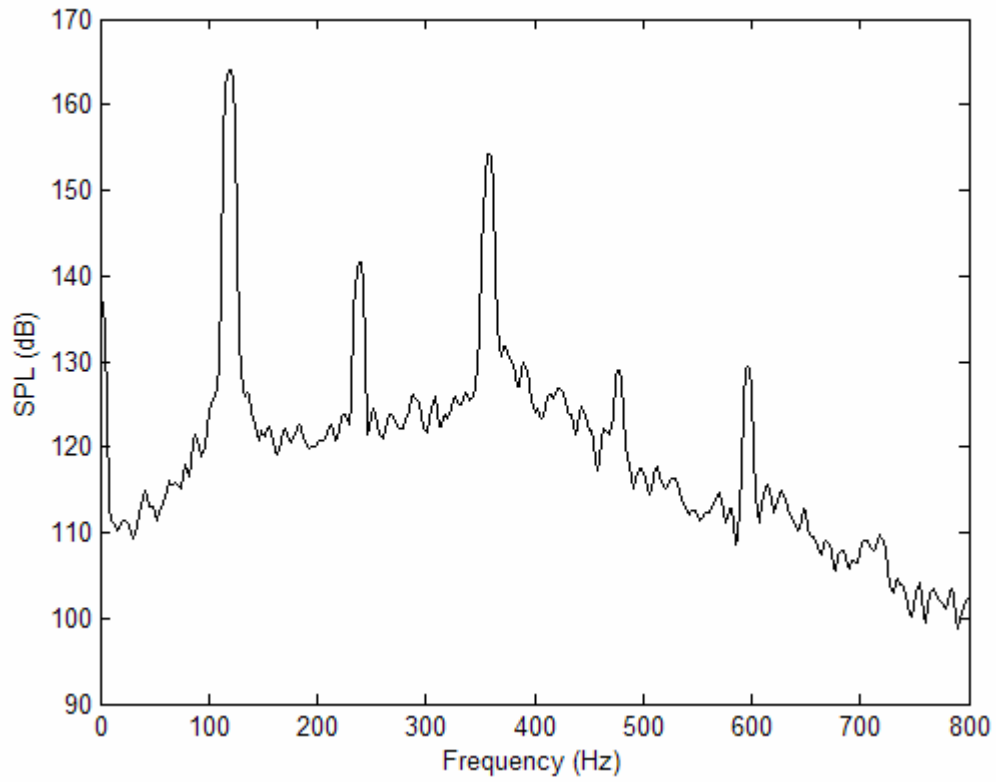


Figure E.24: GER=0.5, Controller delay=24, Gain=0.35.

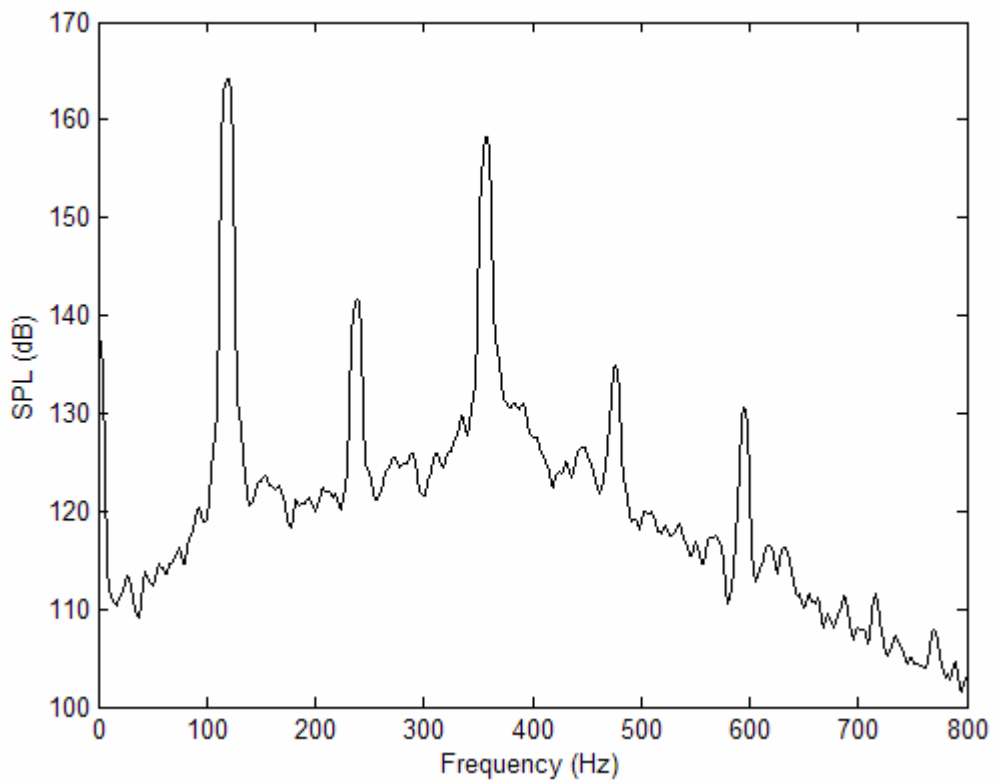


Figure E.25: GER=0.5, Controller delay=24, Gain=0.40.

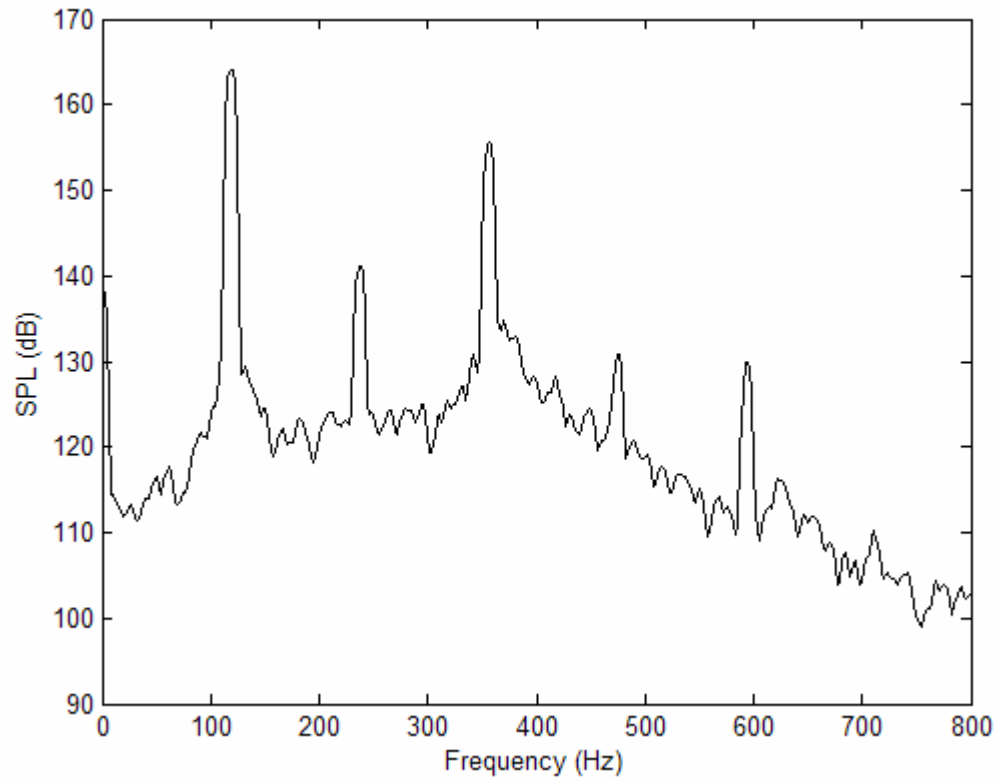


Figure E.26: GER=0.5, Controller delay=24, Gain=0.45.

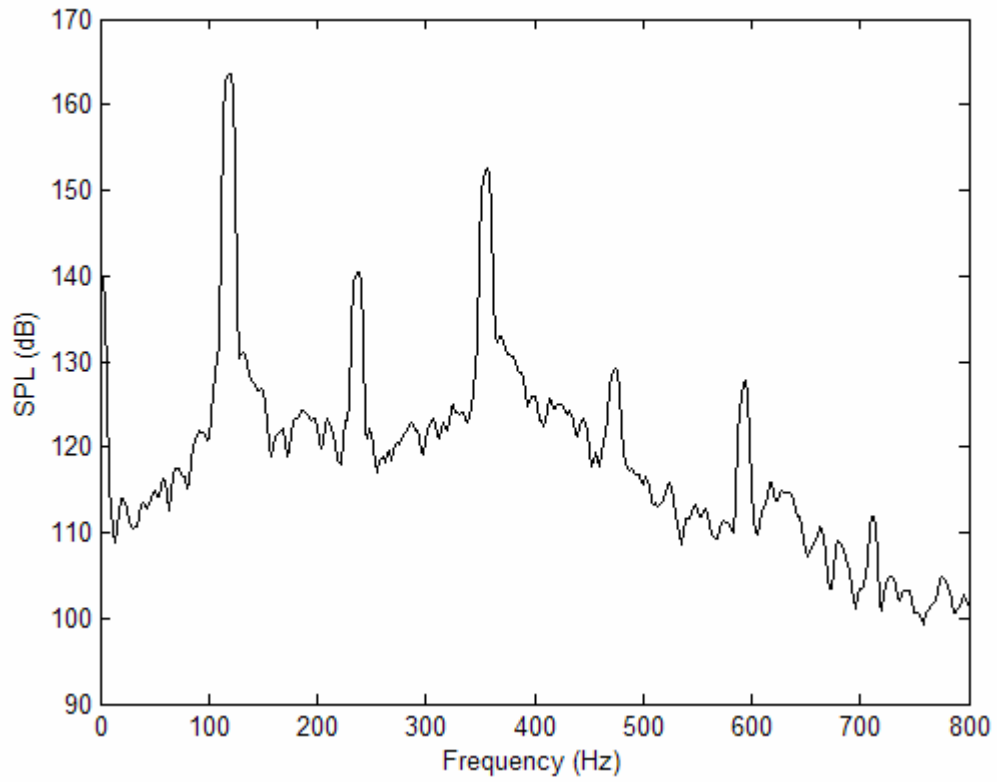


Figure E.27: GER=0.5, Controller delay=24, Gain=0.50.

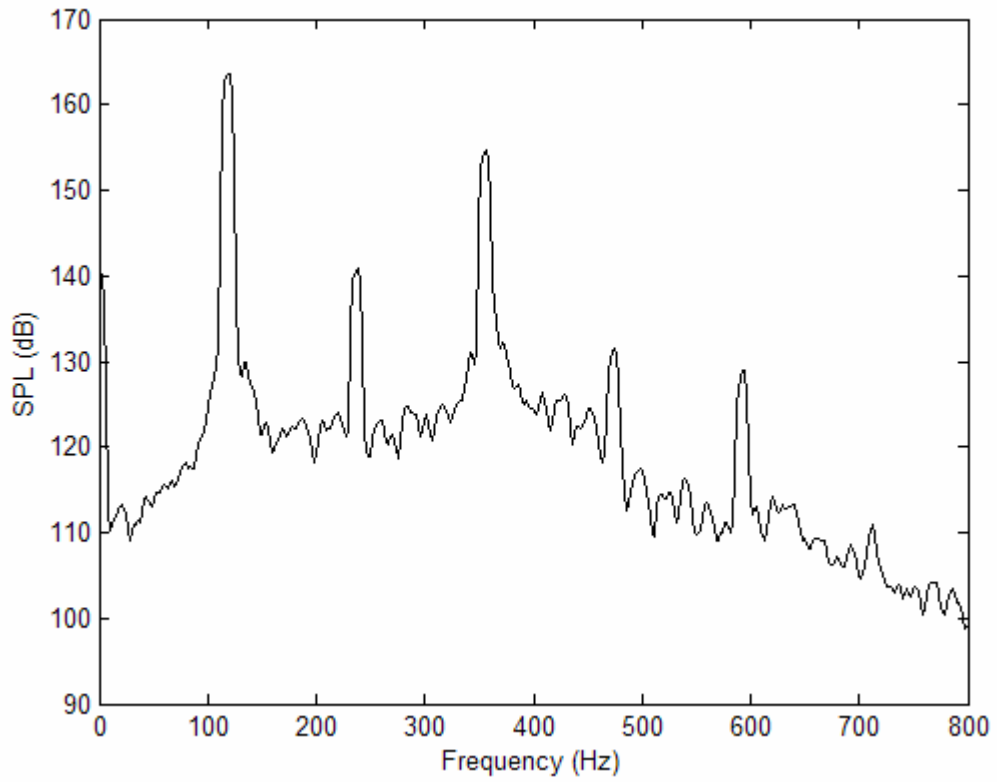


Figure E.28: GER=0.5, Controller delay=24, Gain=0.55.

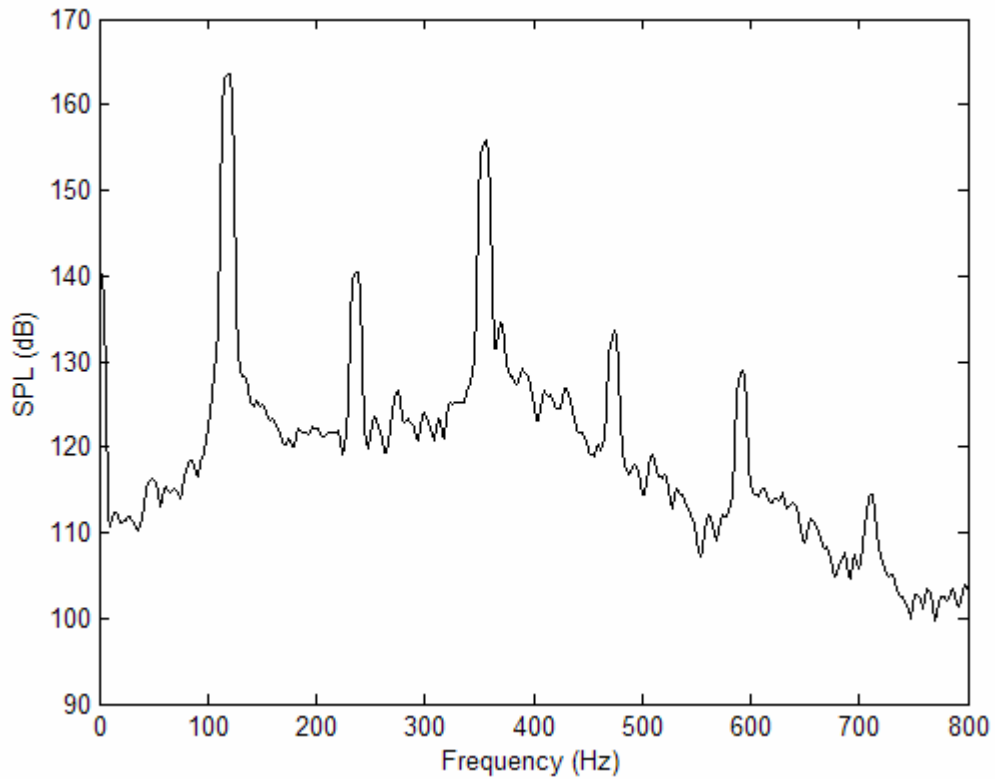


Figure E.29: GER=0.5, Controller delay=24, Gain=0.60.

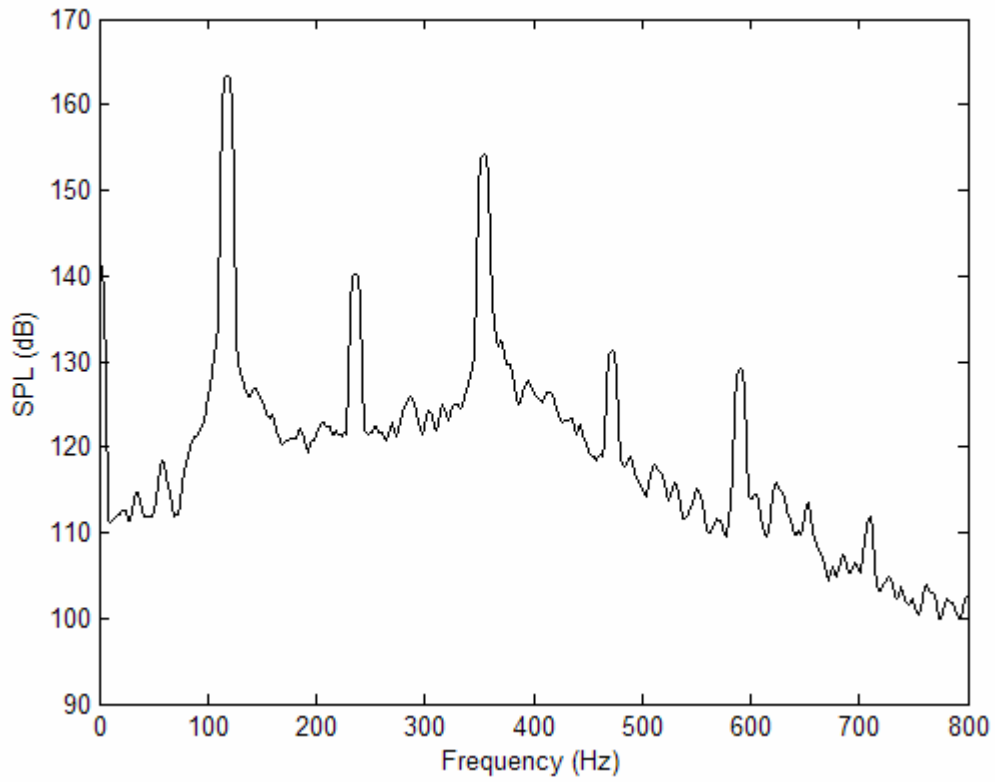


Figure E.30: GER=0.5, Controller delay=24, Gain=0.65.

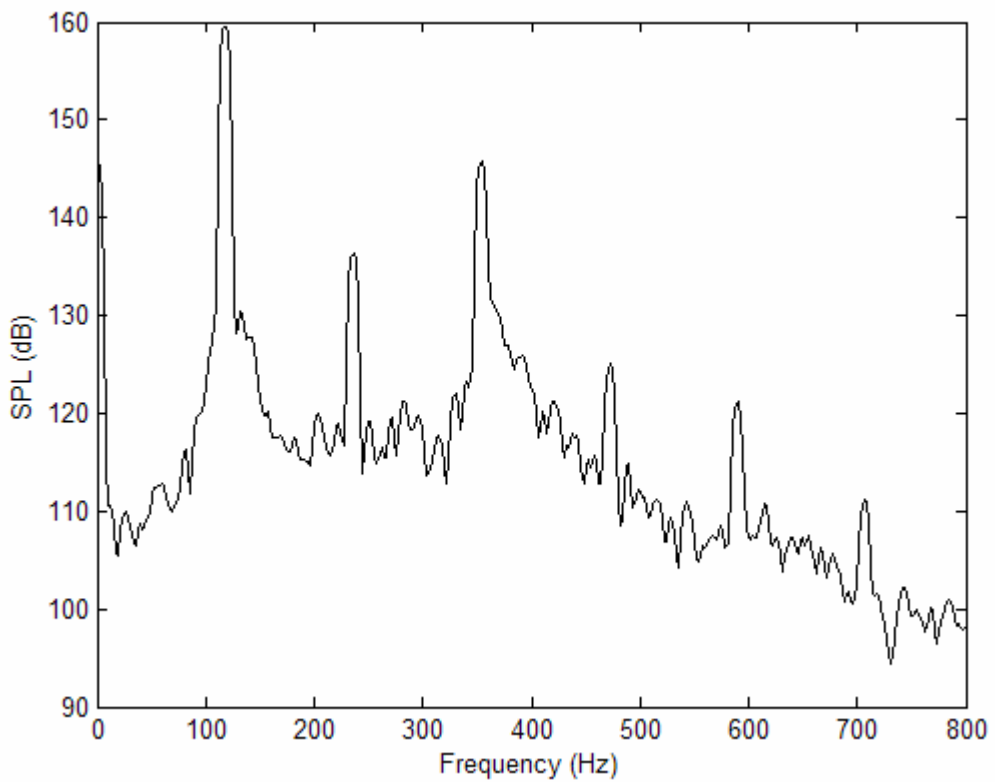


Figure E.31: GER=0.5, Controller delay=24, Gain=0.70.

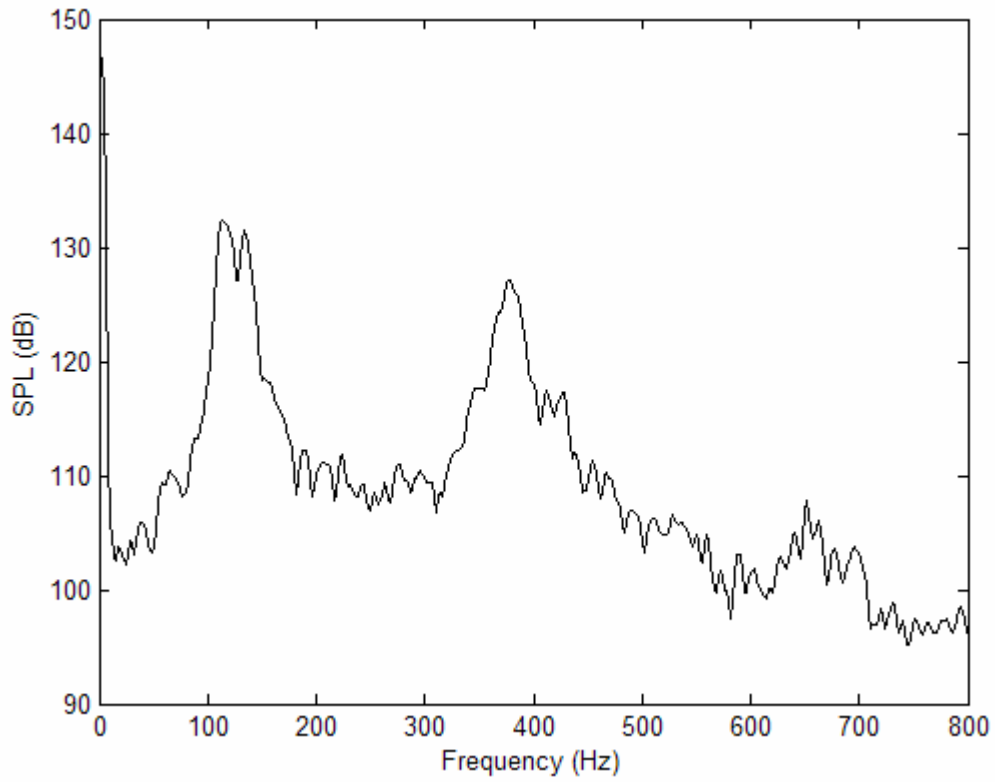


Figure E.32: GER=0.5, Controller delay=24, Gain=0.70.

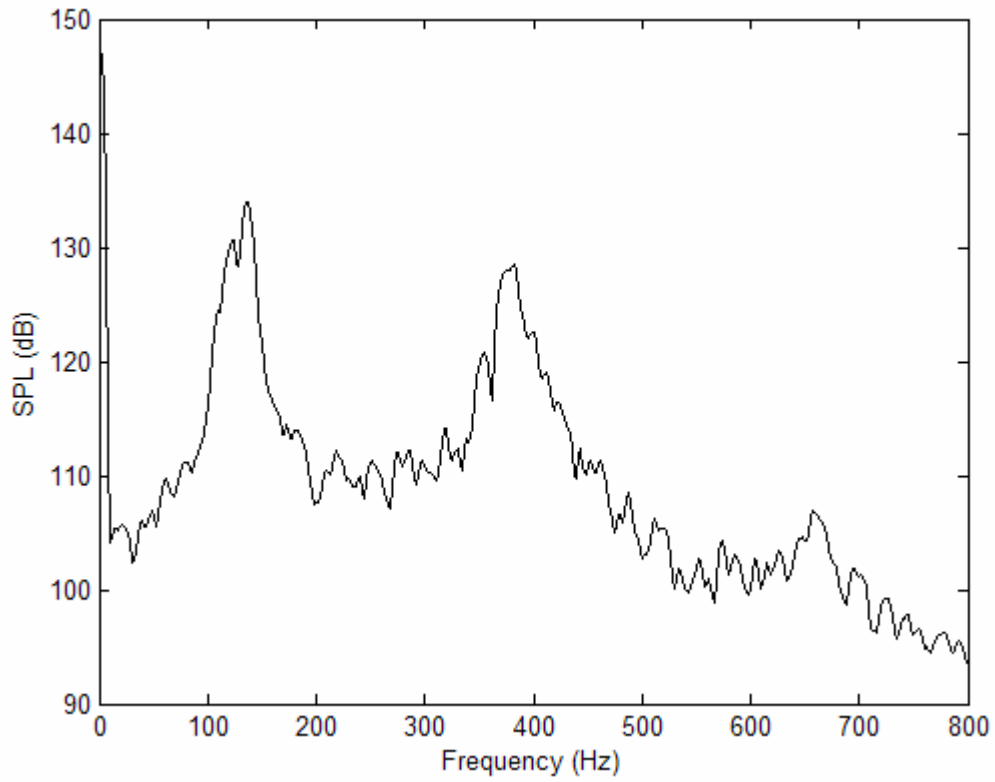


Figure E.33: GER=0.5, Controller delay=24, Gain=0.75.

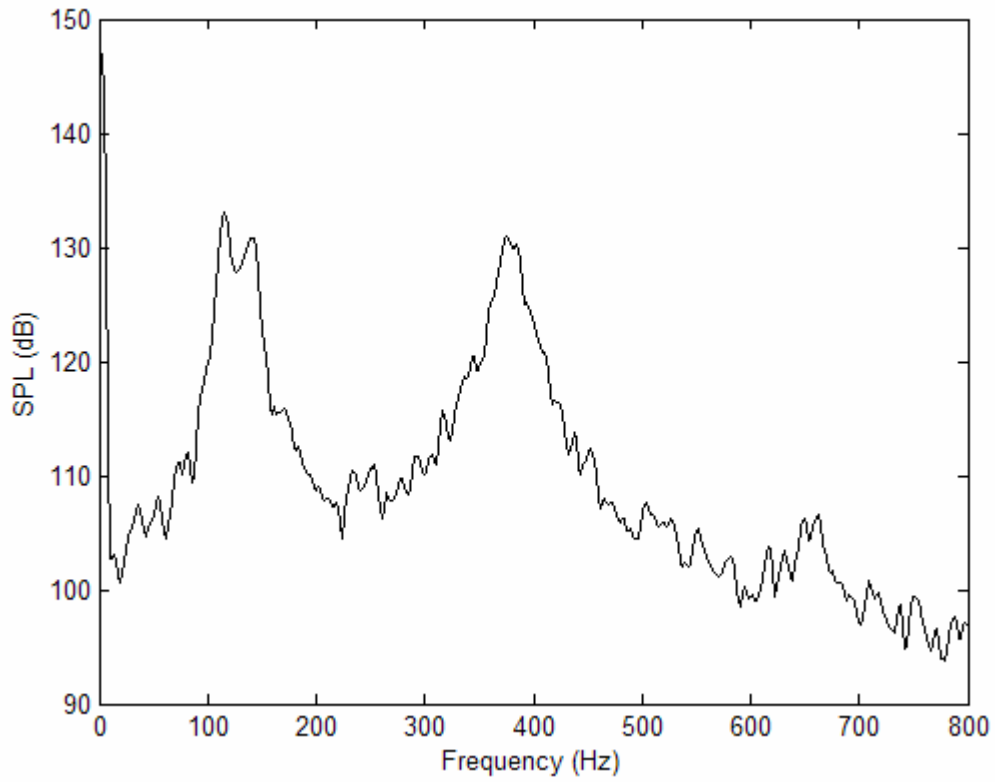


Figure E.34: GER=0.5, Controller delay=24, Gain=0.80.

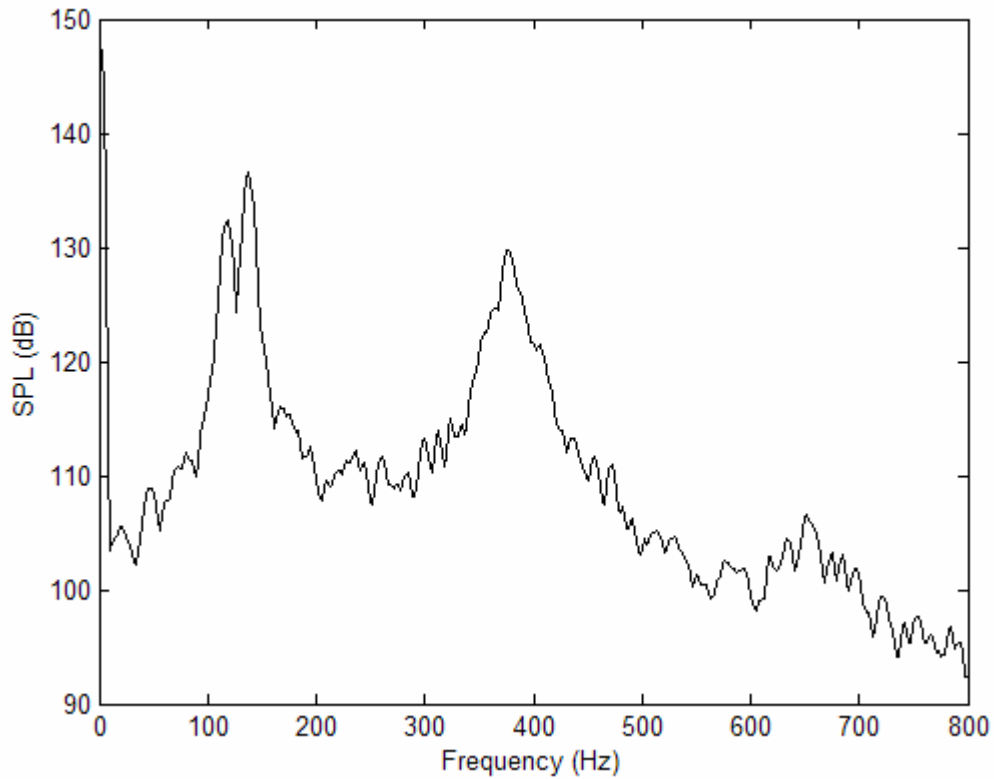


Figure E.35: GER=0.5, Controller delay=24, Gain=0.85.

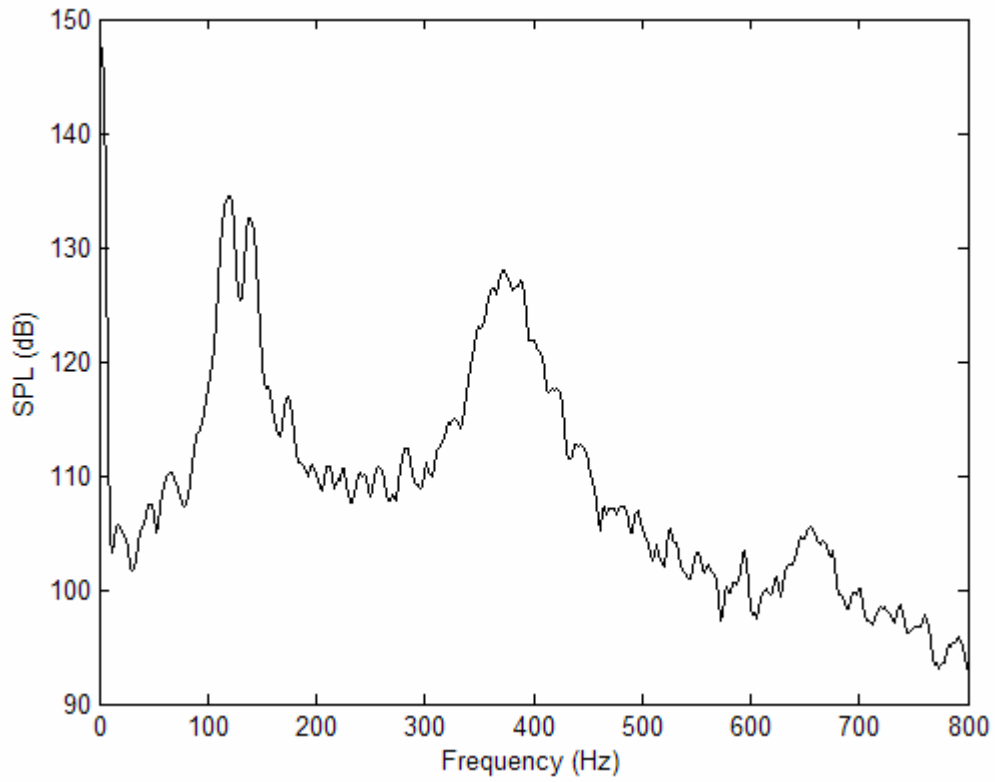


Figure E.36: GER=0.5, Controller delay=24, Gain=0.90.

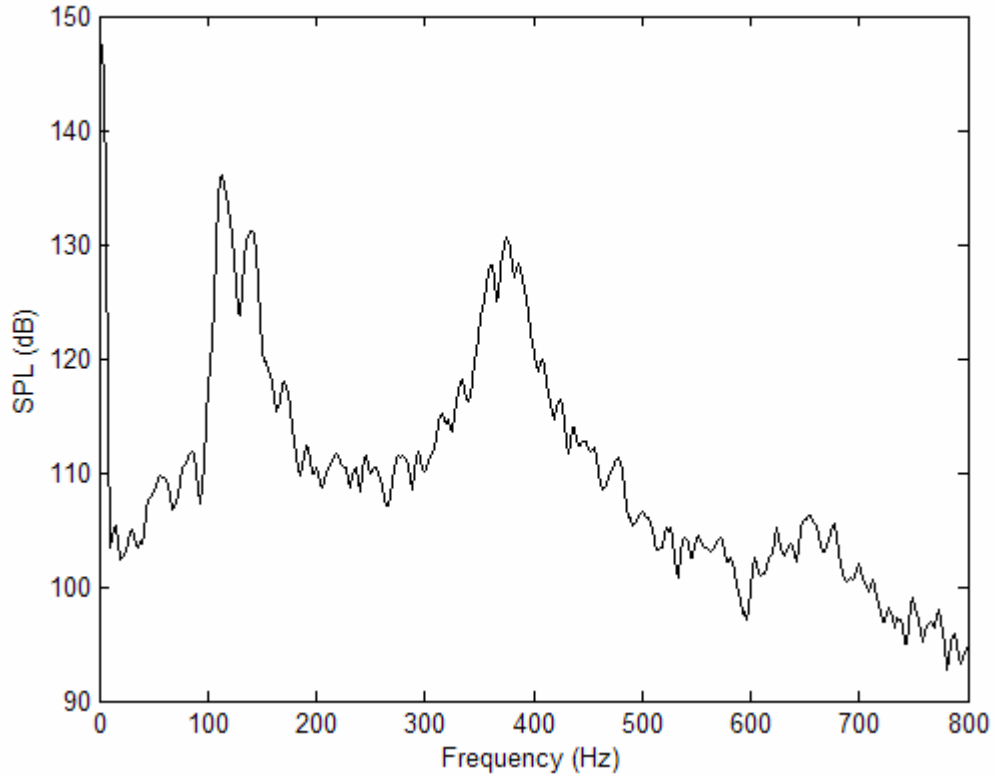


Figure E.37: GER=0.5, Controller delay=24, Gain=0.95.

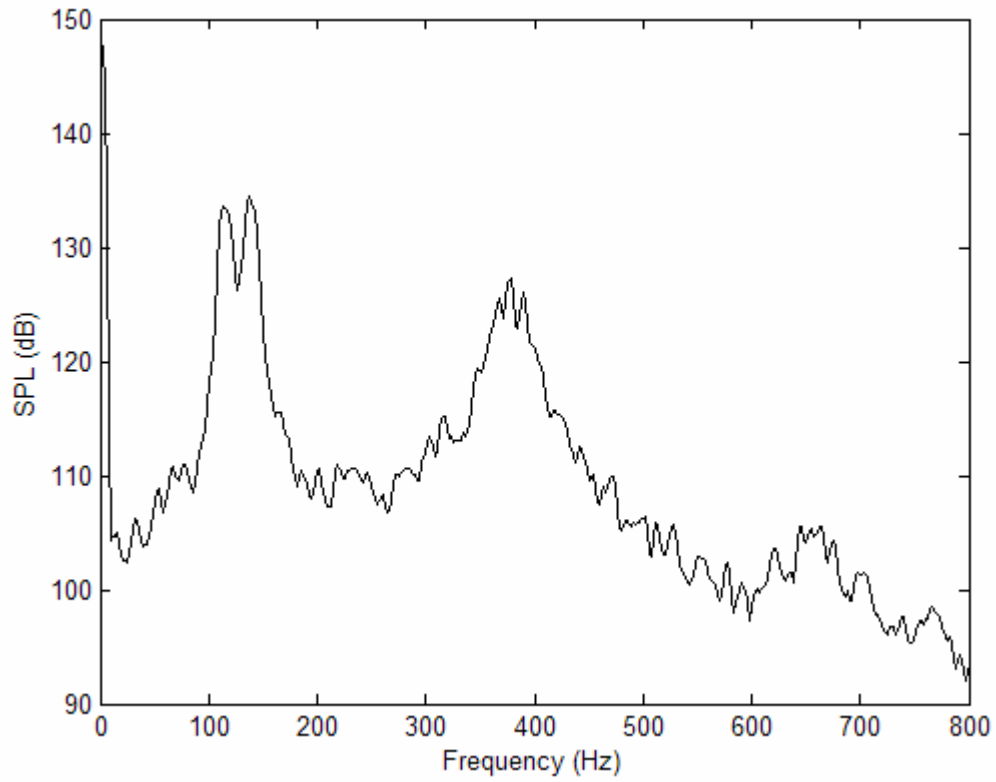


Figure E.38: GER=0.5, Controller delay=24, Gain=1.0.

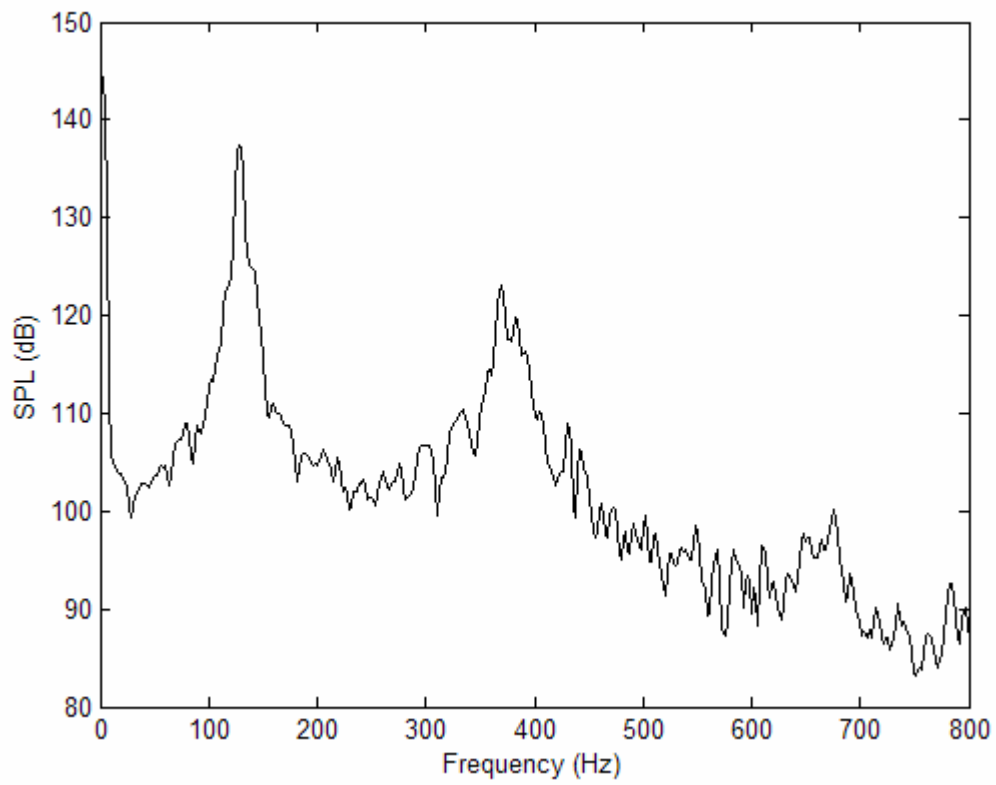


Figure E.39: GER=0.5, Controller delay=24, Gain=0.75.

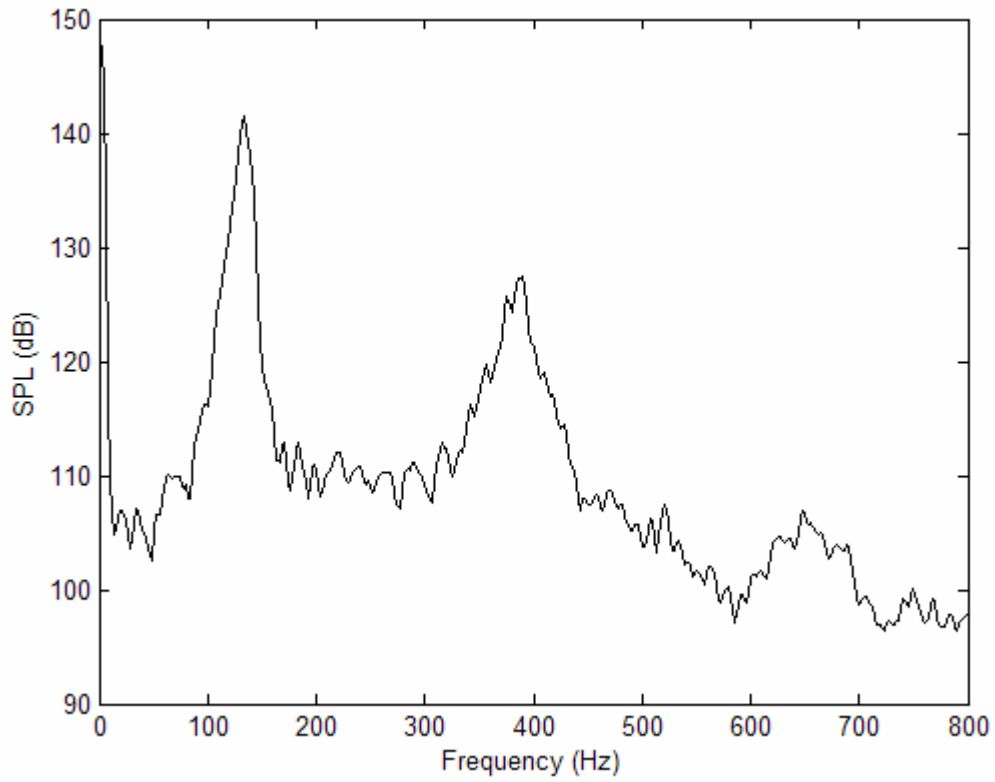


Figure E.40: GER=0.5, Controller delay=26, Gain=0.75.

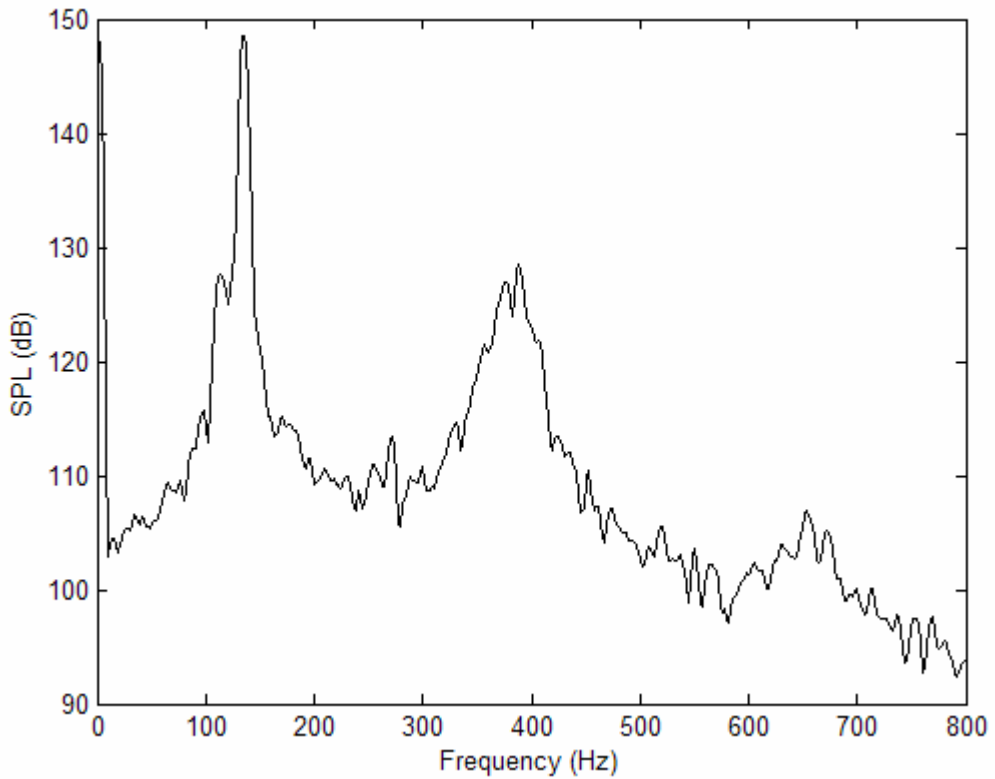


Figure E.41: GER=0.5, Controller delay=28, Gain=0.75.

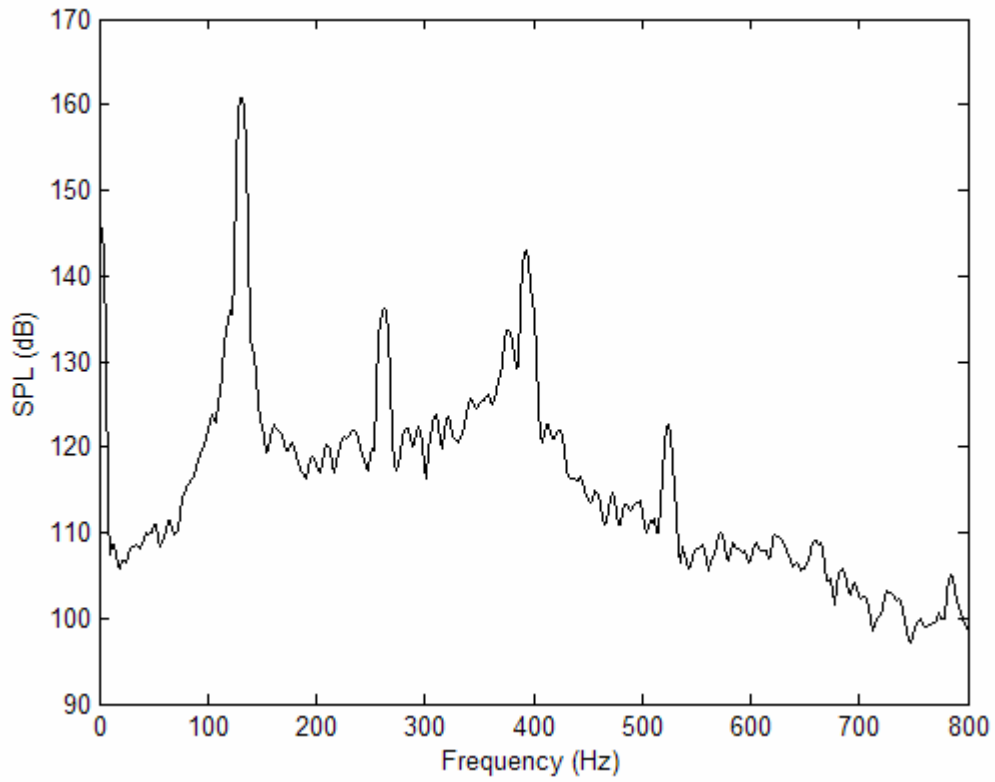


Figure E.42: GER=0.5, Controller delay=30, Gain=0.75.

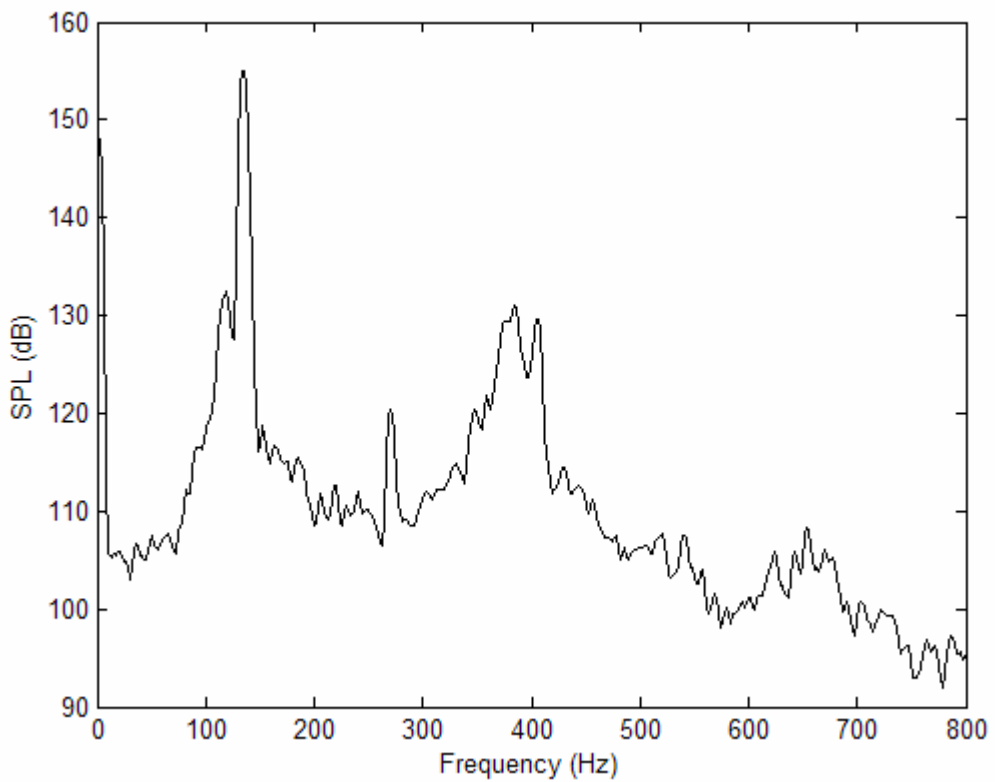


Figure E.43: GER=0.5, Controller delay=28, Gain=0.75.

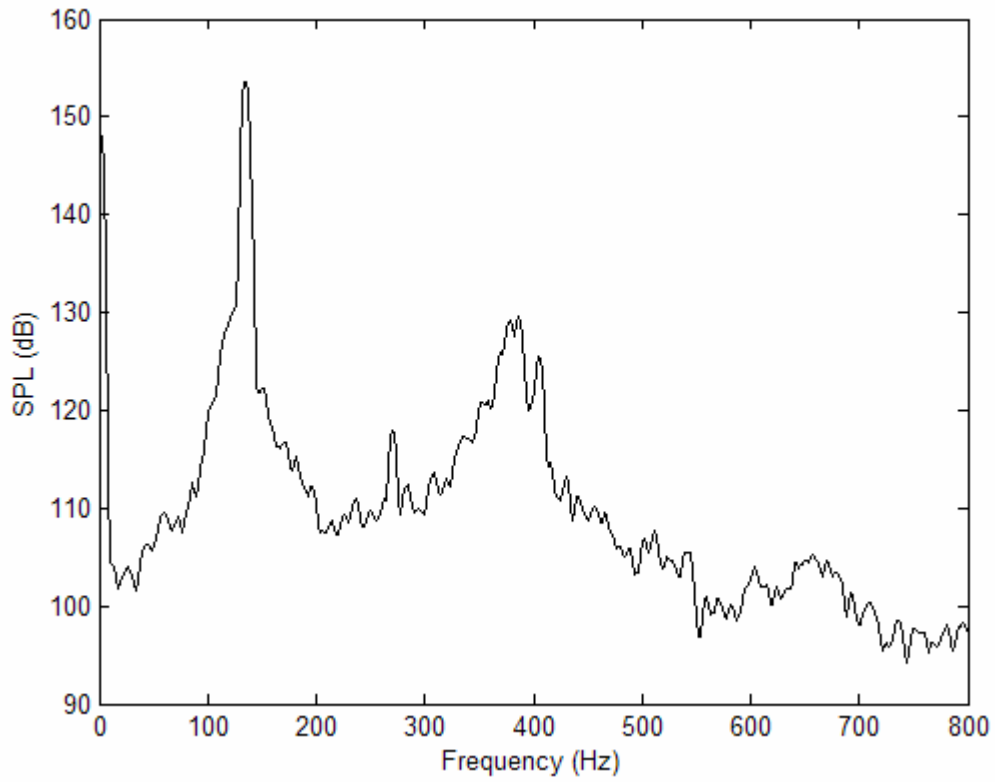


Figure E.44: GER=0.5, Controller delay=28, Gain=0.70.

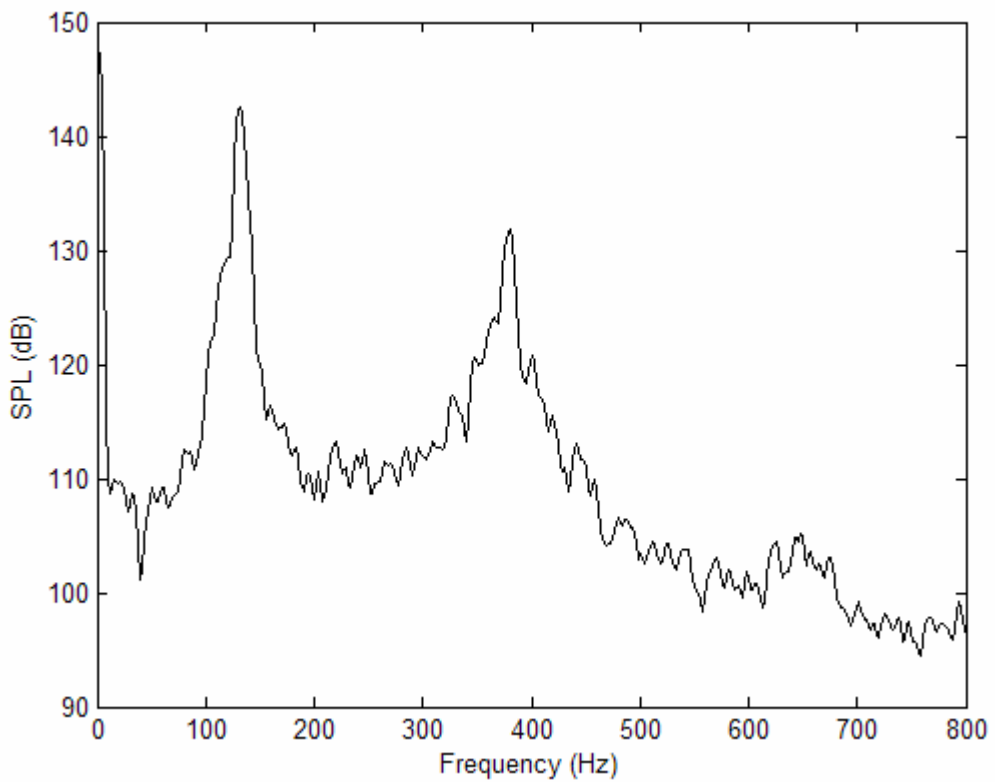


Figure E.45: GER=0.5, Controller delay=28, Gain=0.65.

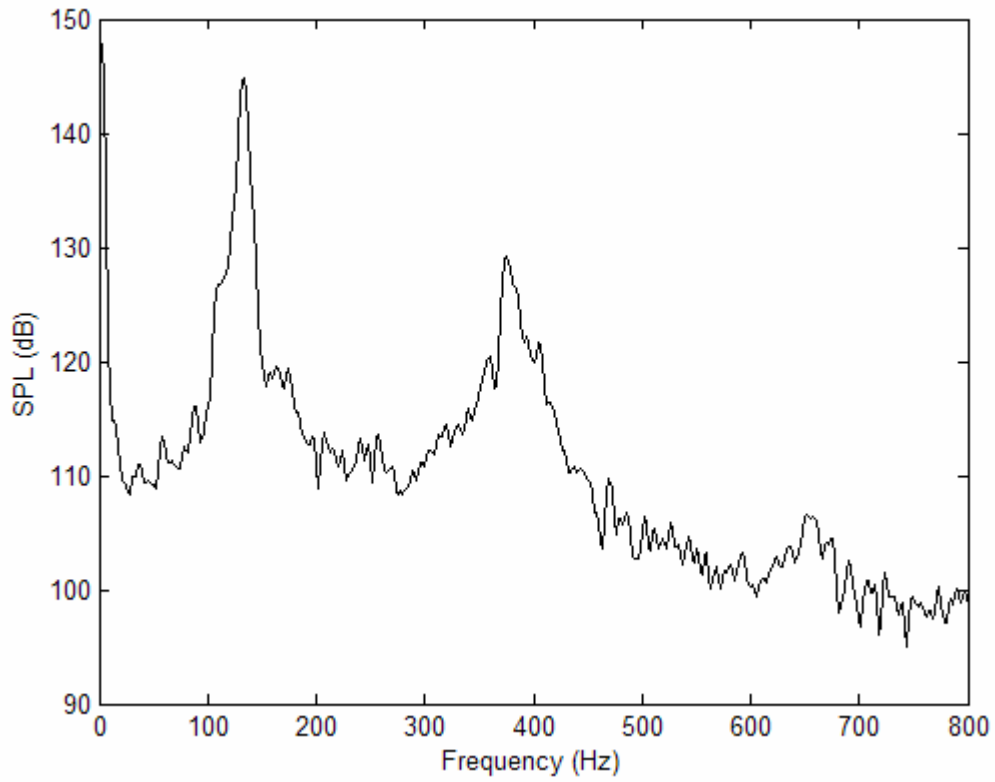


Figure E.46: GER=0.5, Controller delay=28, Gain=0.60.

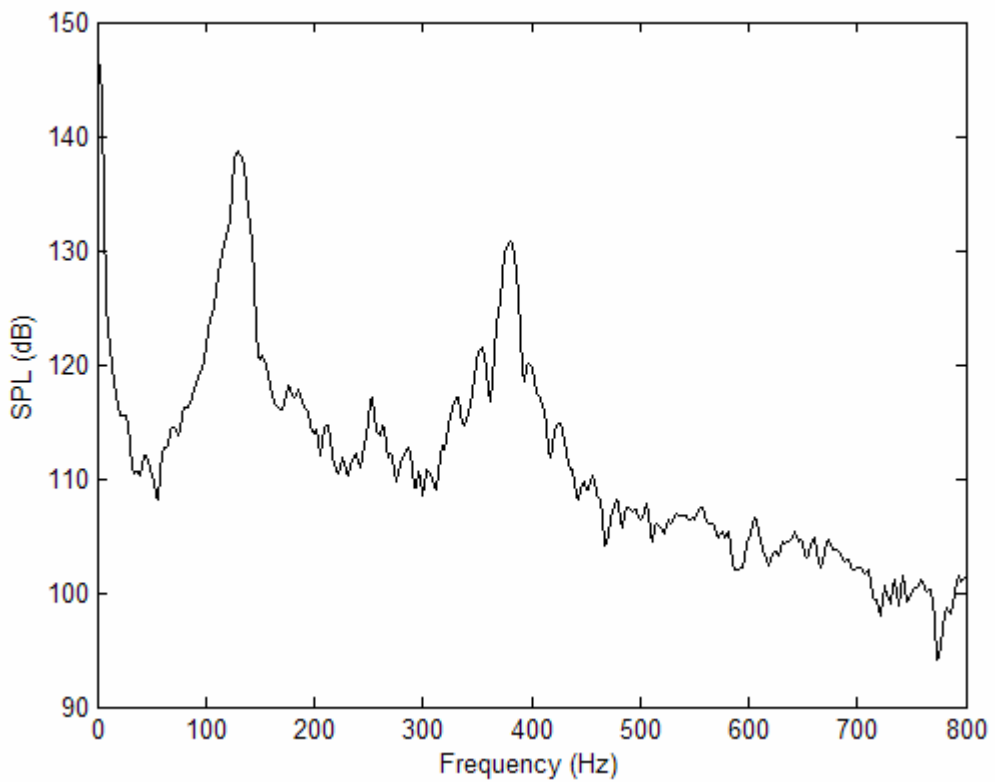


Figure E.47: GER=0.5, Controller delay=28, Gain=0.55.

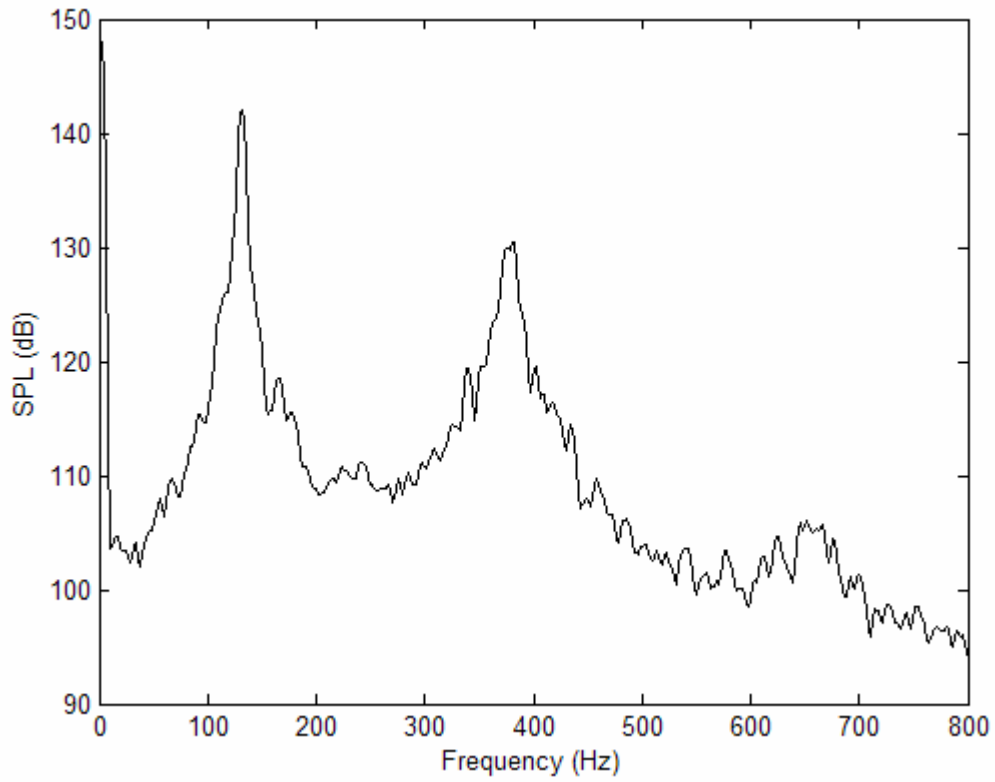


Figure E.48: GER=0.50, Controller delay=28, Gain=0.50.

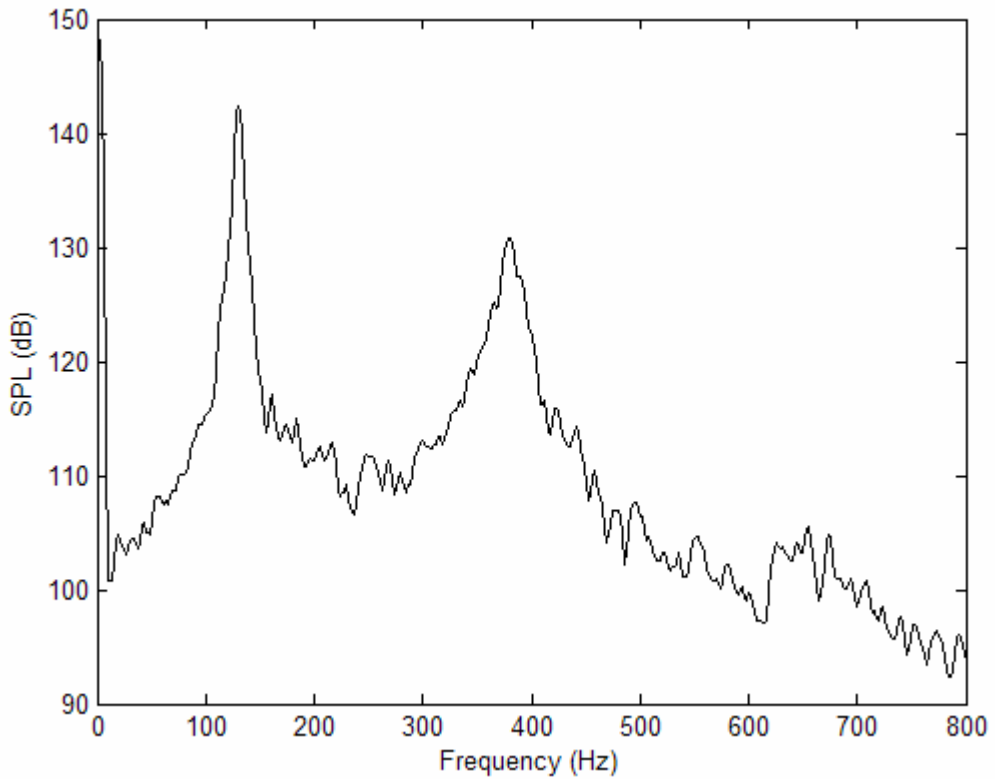


Figure E.49: GER=0.5, Controller delay=28, Gain=0.45.

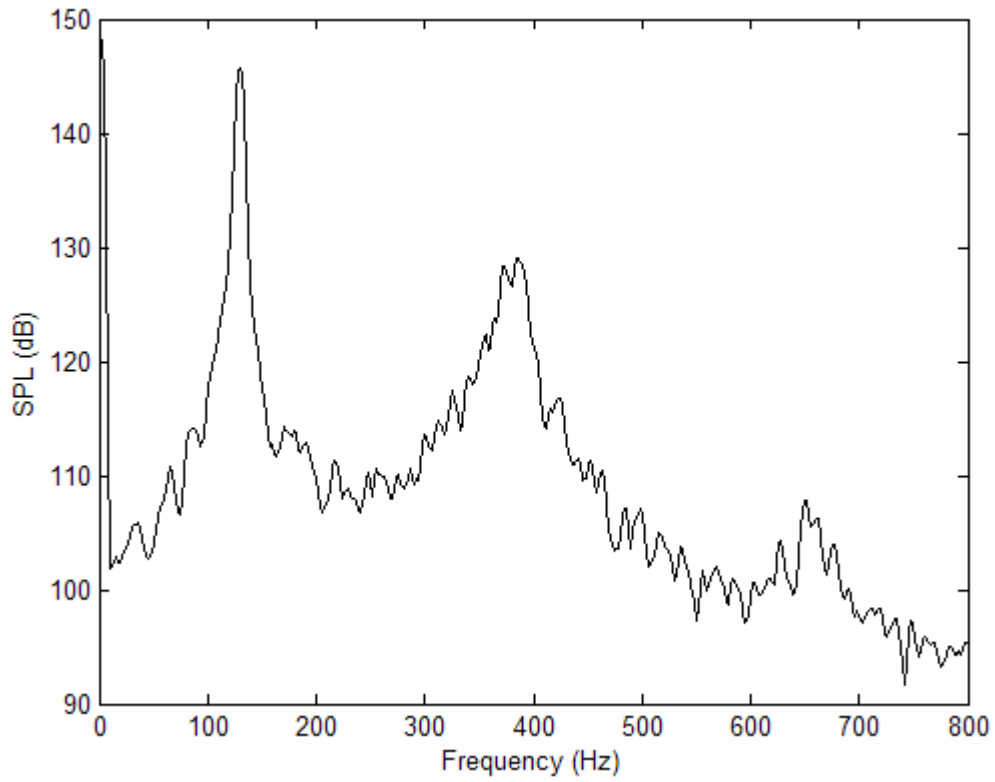


Figure E.50: GER=0.5, Controller delay=28, Gain=0.40.

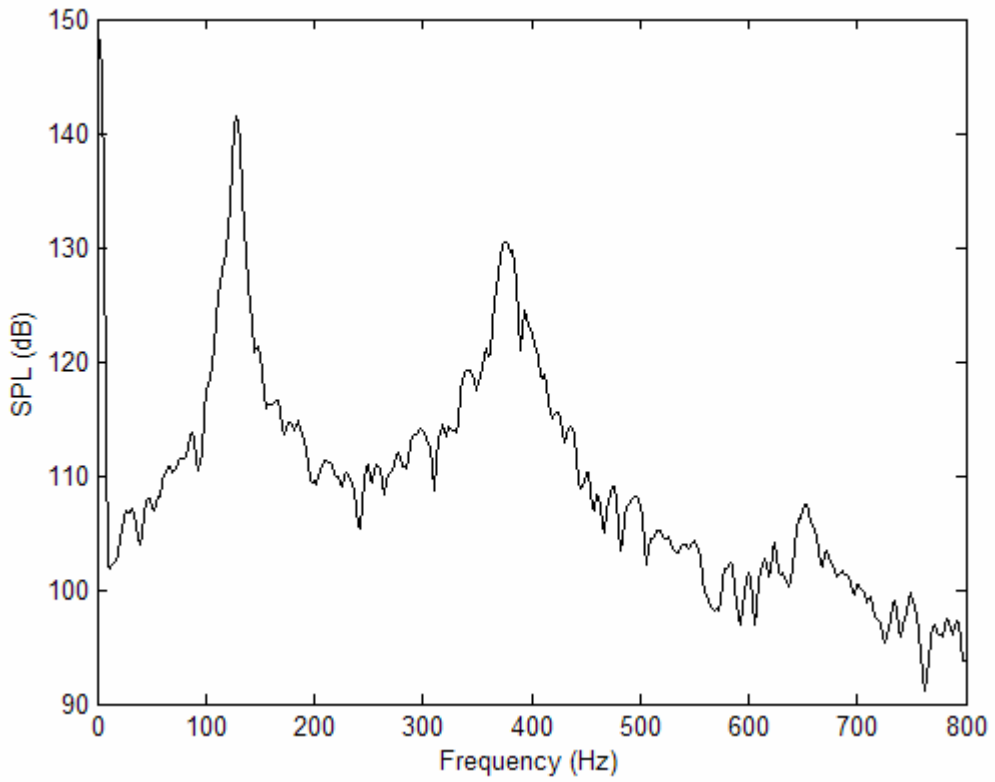


Figure E.51: GER=0.5, Controller delay=28, Gain=0.35.

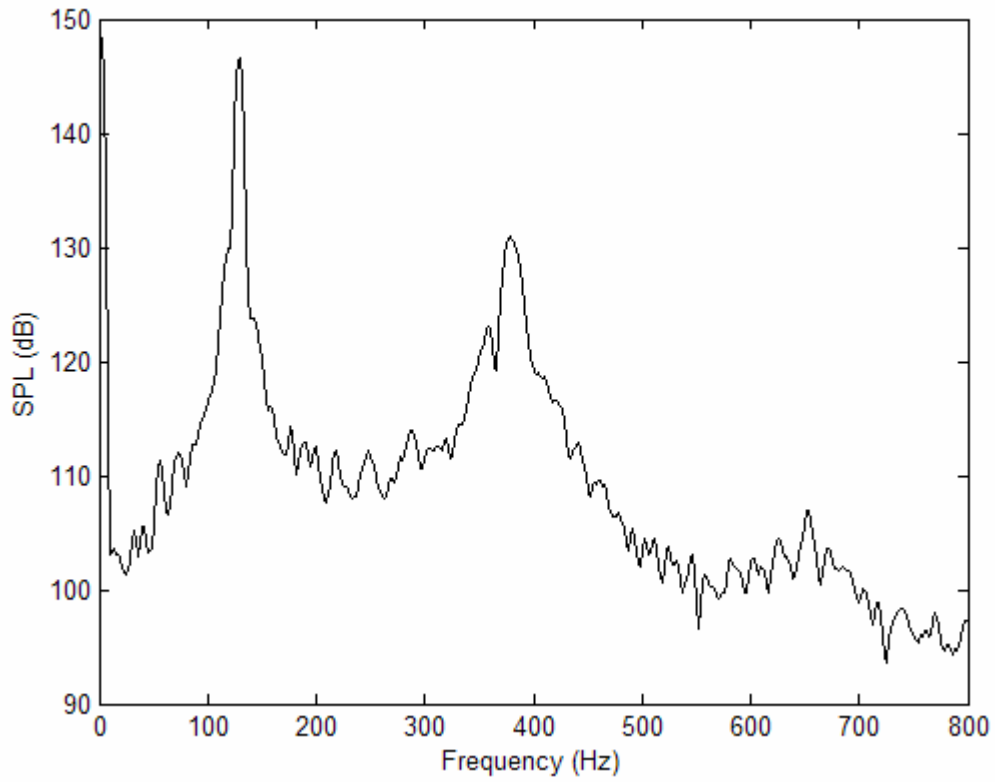


Figure E.52: GER=0.5, Controller delay=28, Gain=0.30.

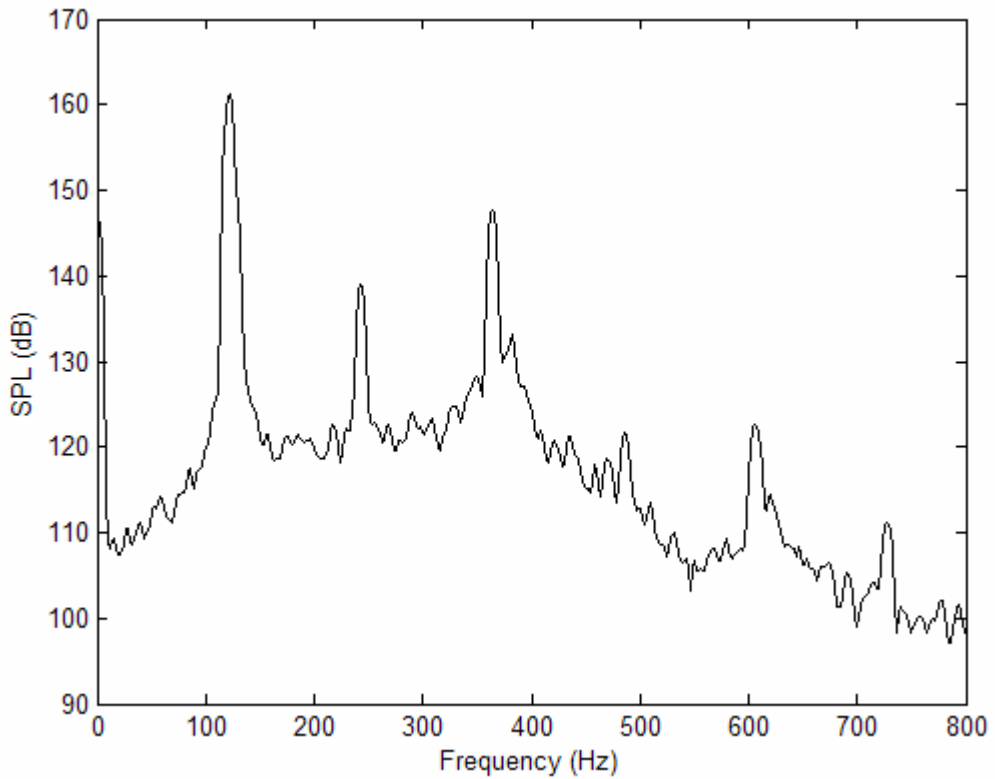


Figure E.53: GER=0.5, Controller delay=28, Gain=0.25.

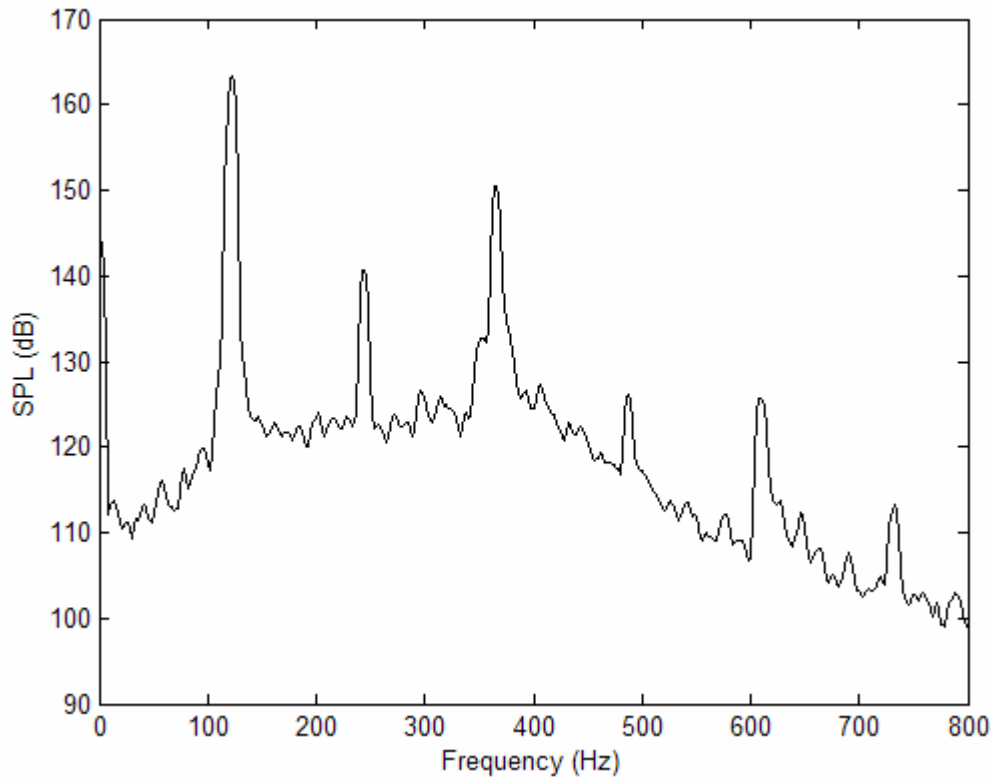


Figure E.54: GER=0.5, Controller delay=28, Gain=0.25.

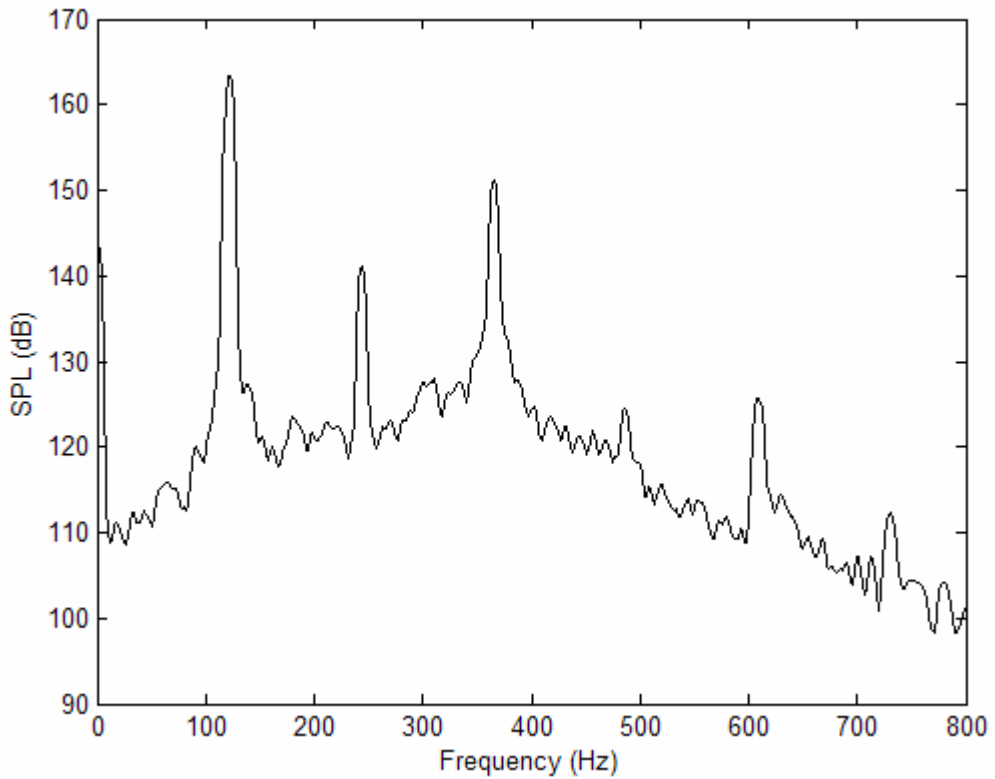


Figure E.55: GER=0.5, Controller delay=28, Gain=0.20.

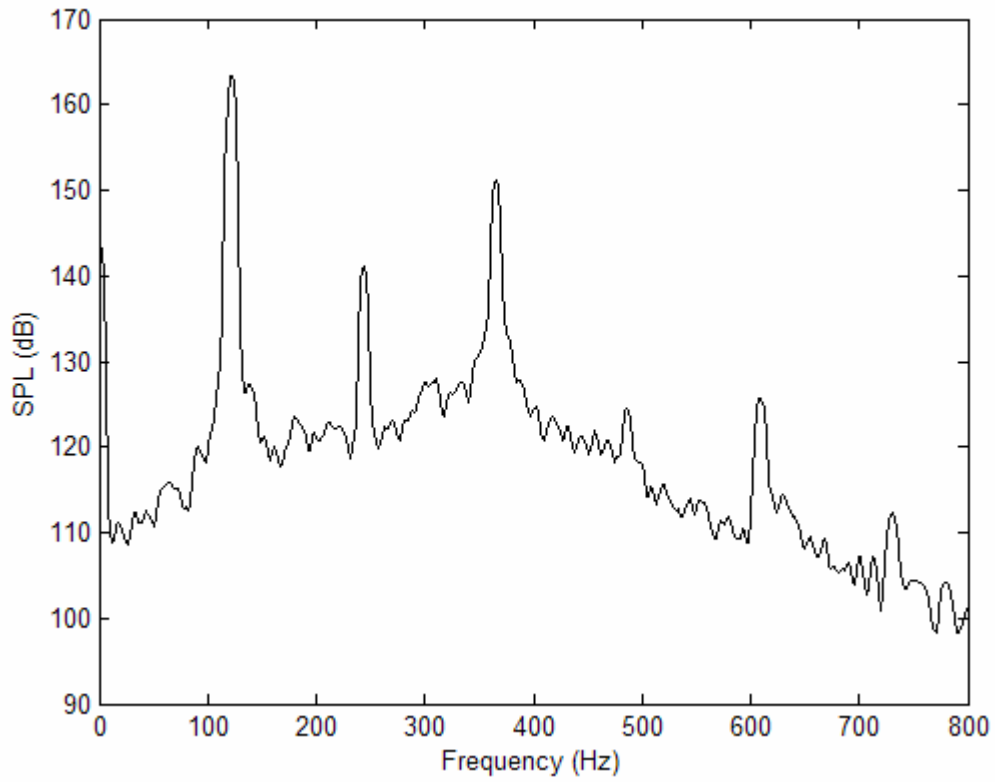


Figure E.56: GER=0.5, Controller delay=28, Gain=0.20.

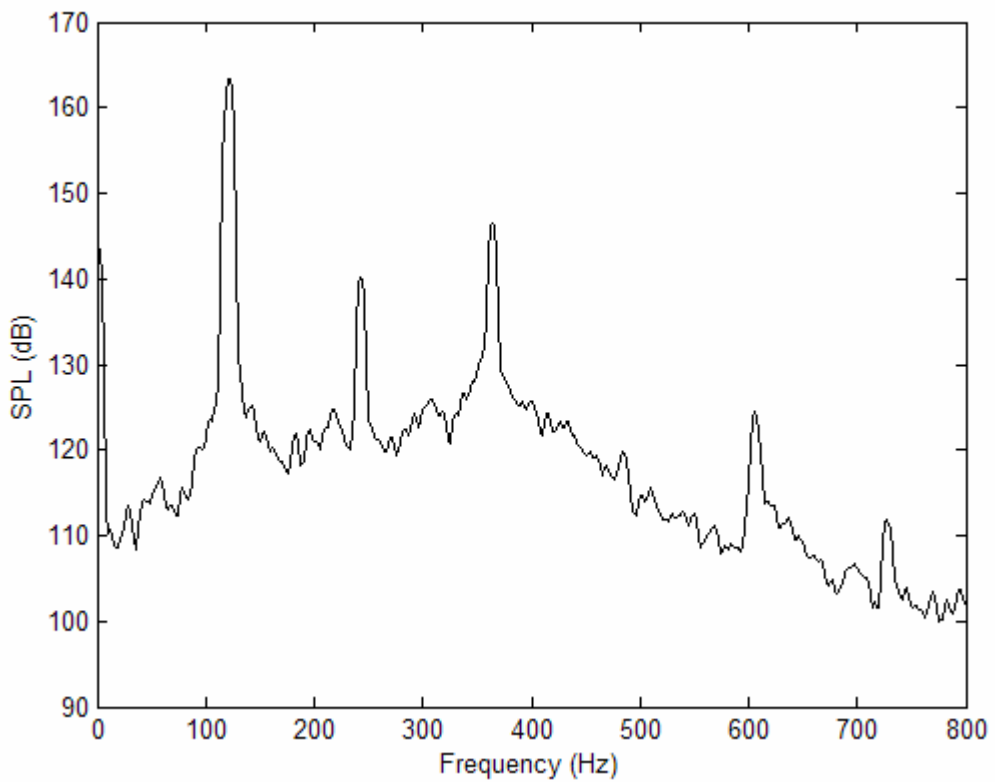


Figure E.57: GER=0.5, Controller delay=28, Gain=0.15.

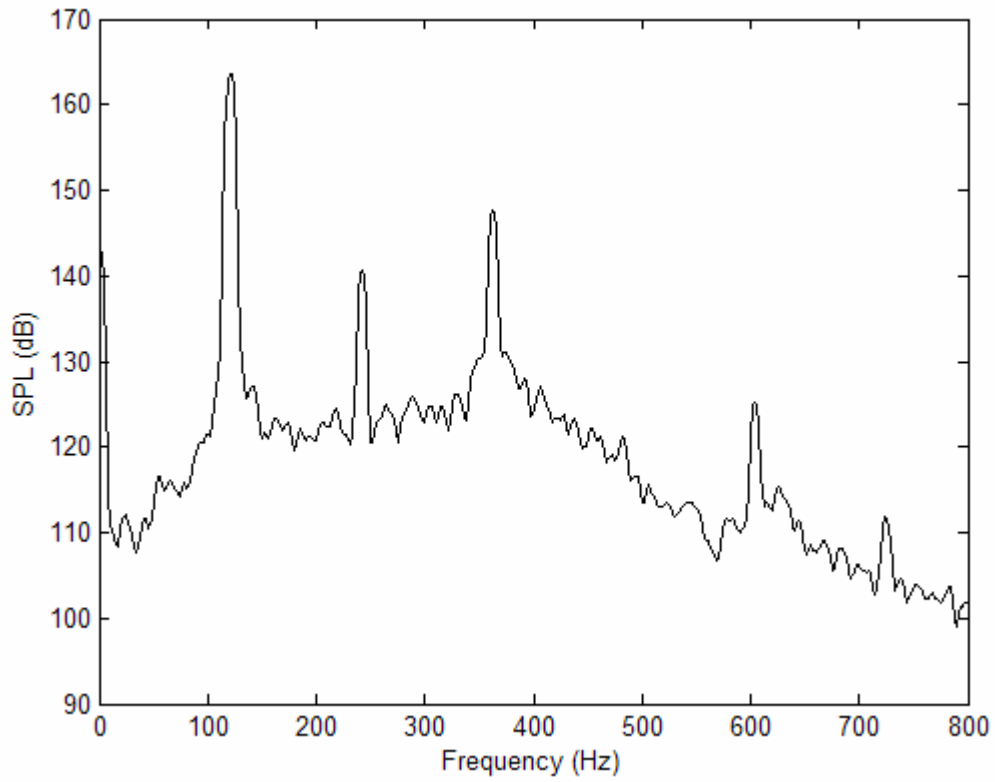


Figure E.58: GER=0.5, Controller delay=28, Gain=0.10.

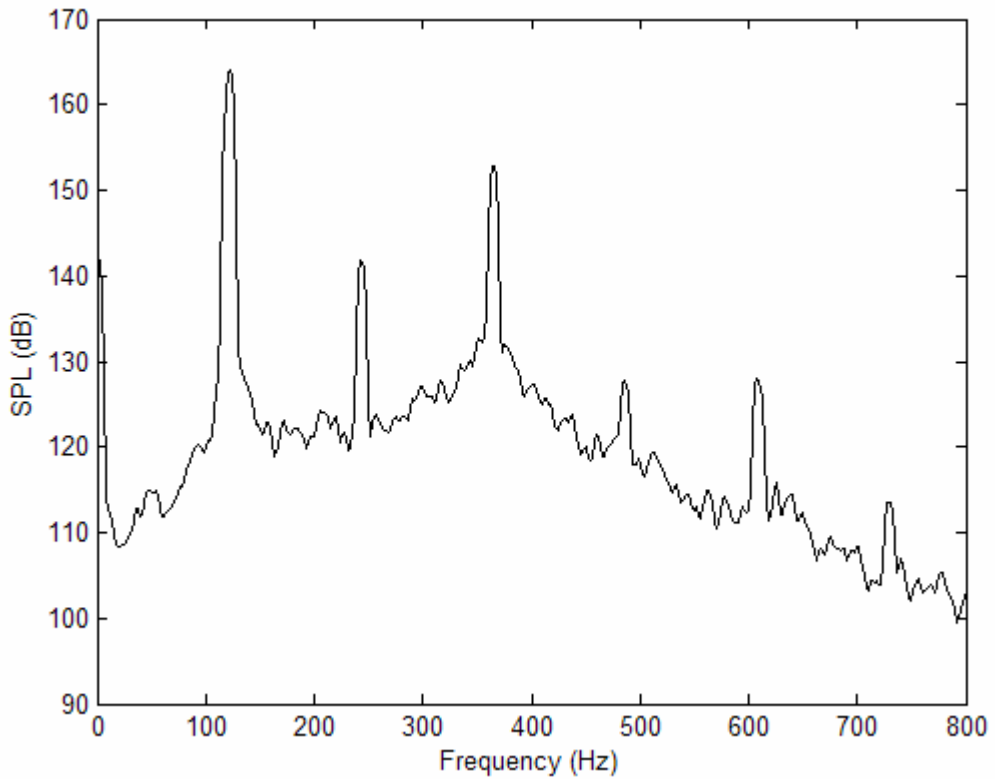


Figure E.59: GER=0.5, Controller delay=28, Gain=0.05.

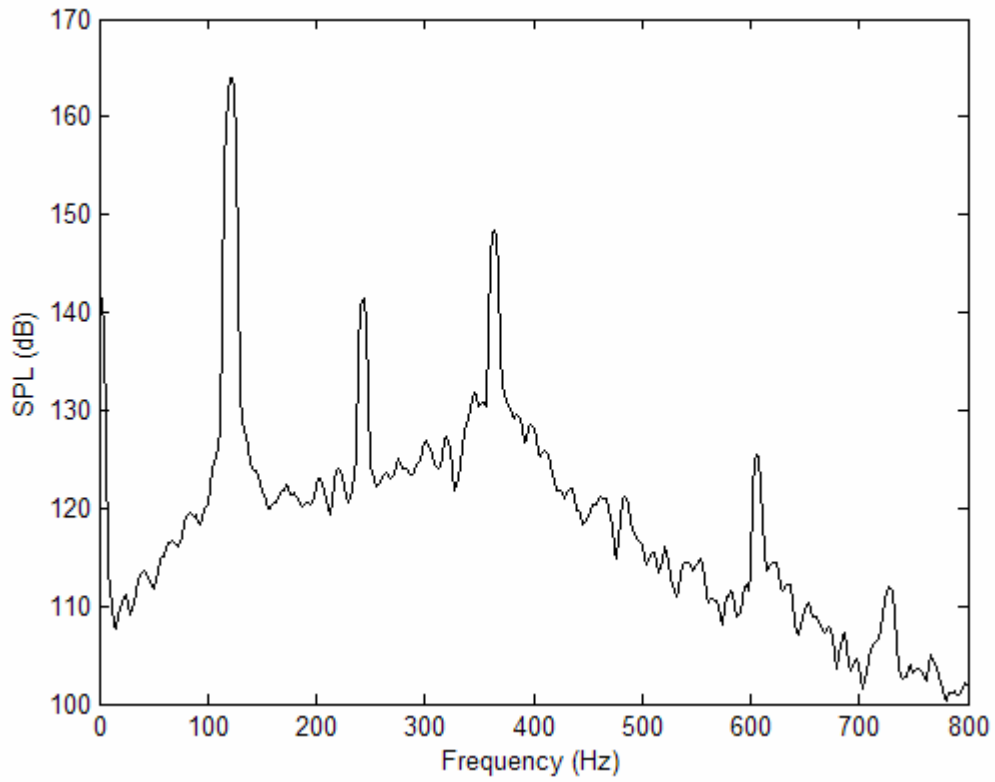


Figure E.60: GER=0.5, Uncontrolled.

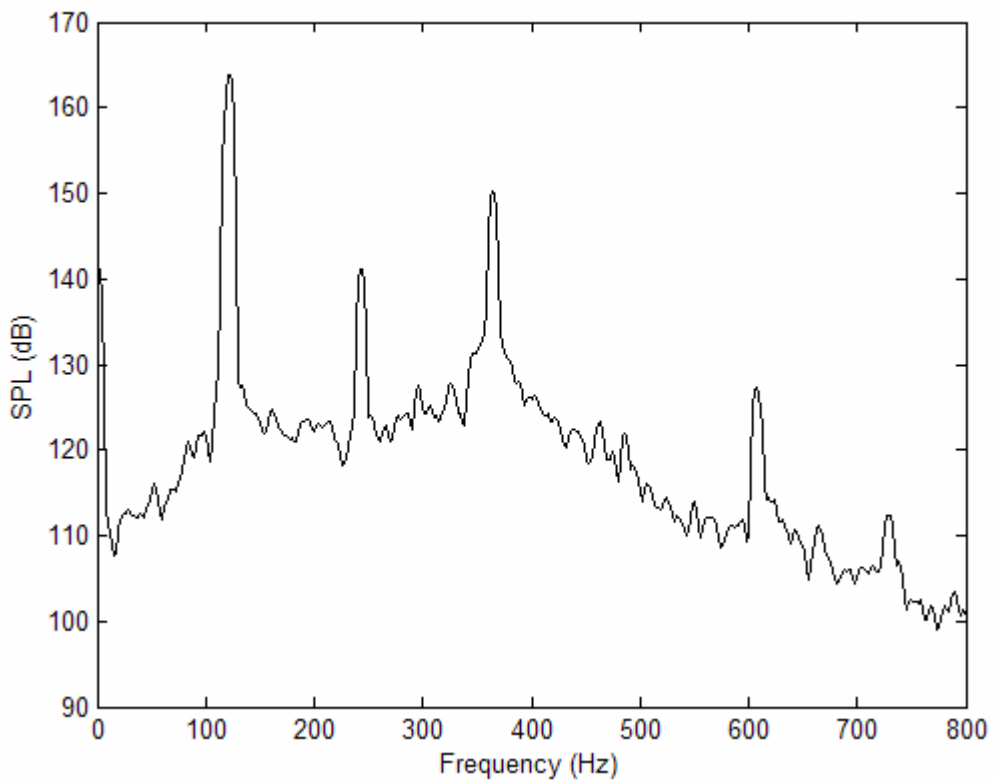


Figure E.61: GER=0.5, Controller delay=28, Gain=0.05.

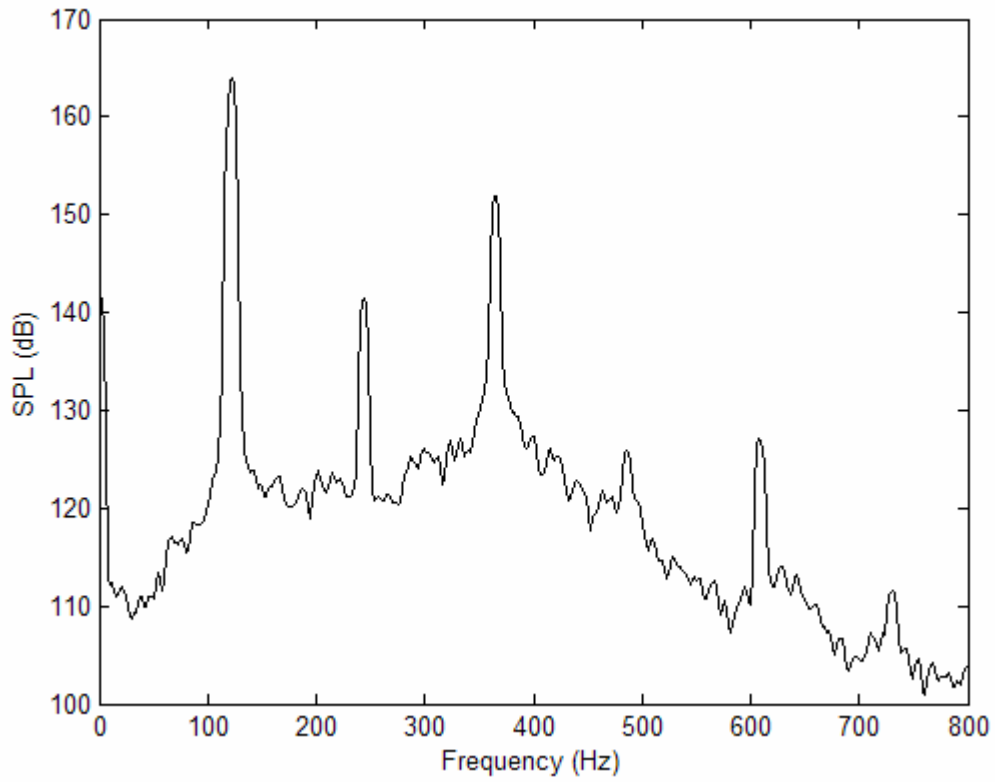


Figure E.62: GER=0.5, Controller delay=28, Gain=0.10.

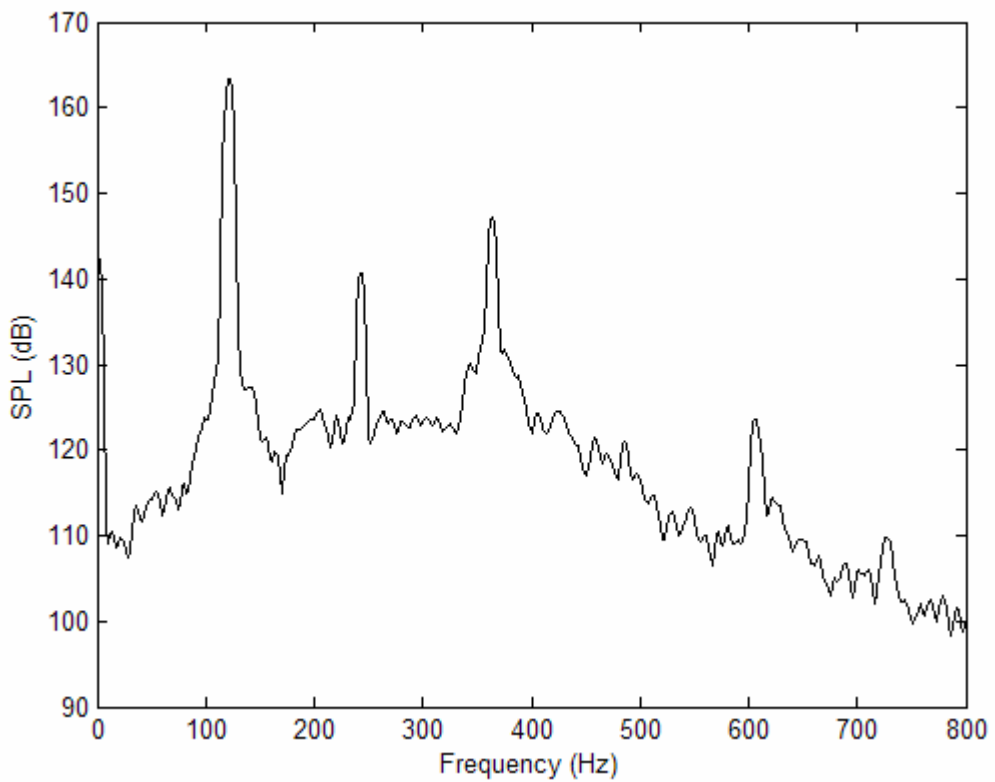


Figure E.63: GER=0.5, Controller delay=28, Gain=0.15.

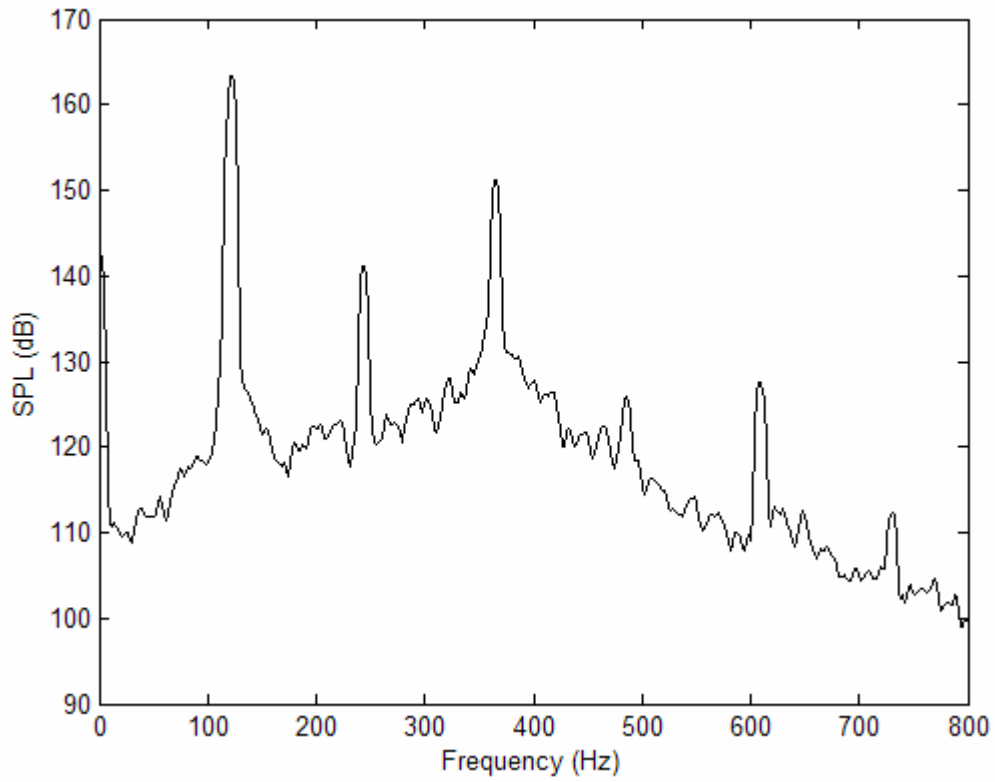


Figure E.64: GER=0.5, Controller delay=28, Gain=0.20.

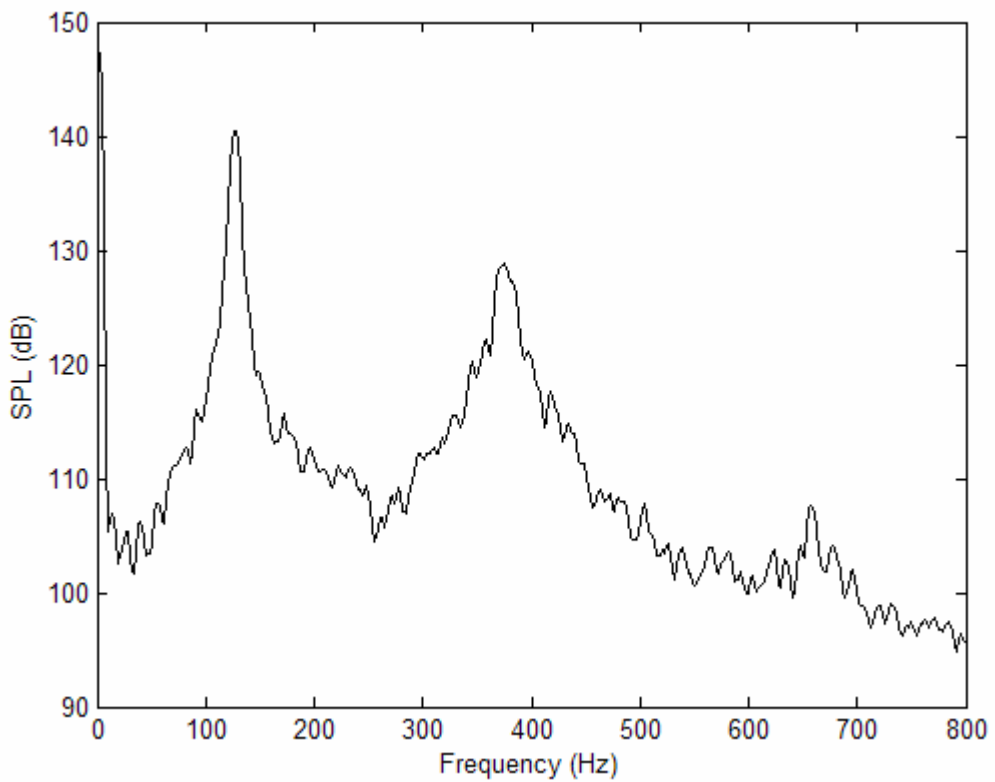


Figure E.65: GER=0.5, Controller delay=28, Gain=0.25.

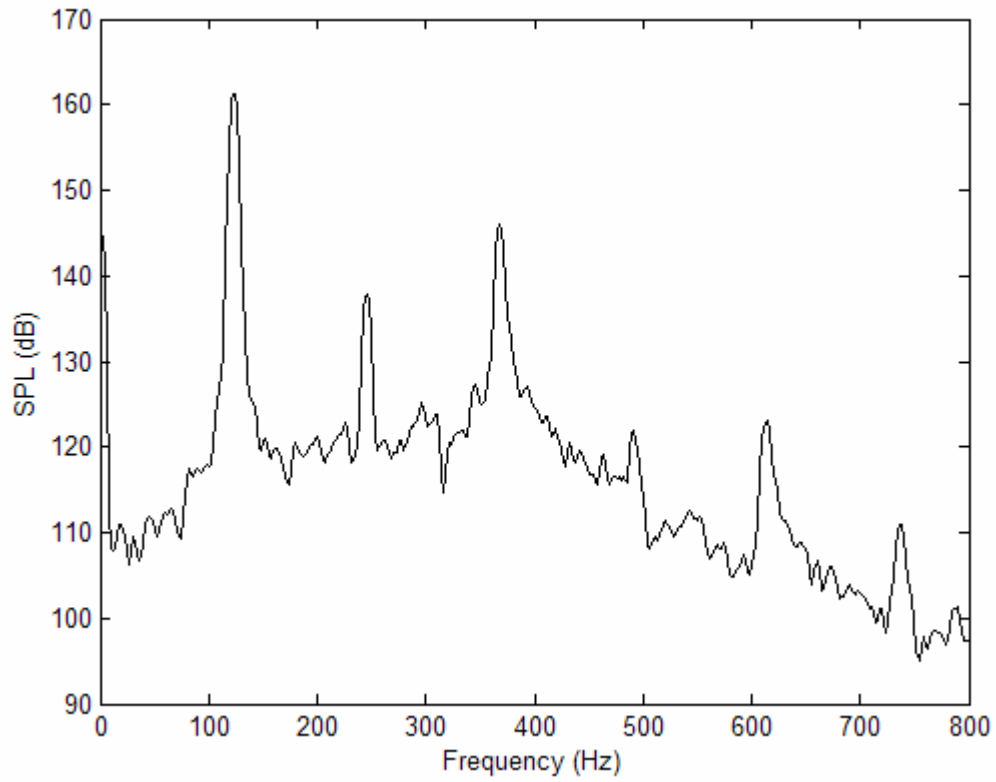


Figure E.66: GER=0.5, Controller delay=28, Gain=0.25.

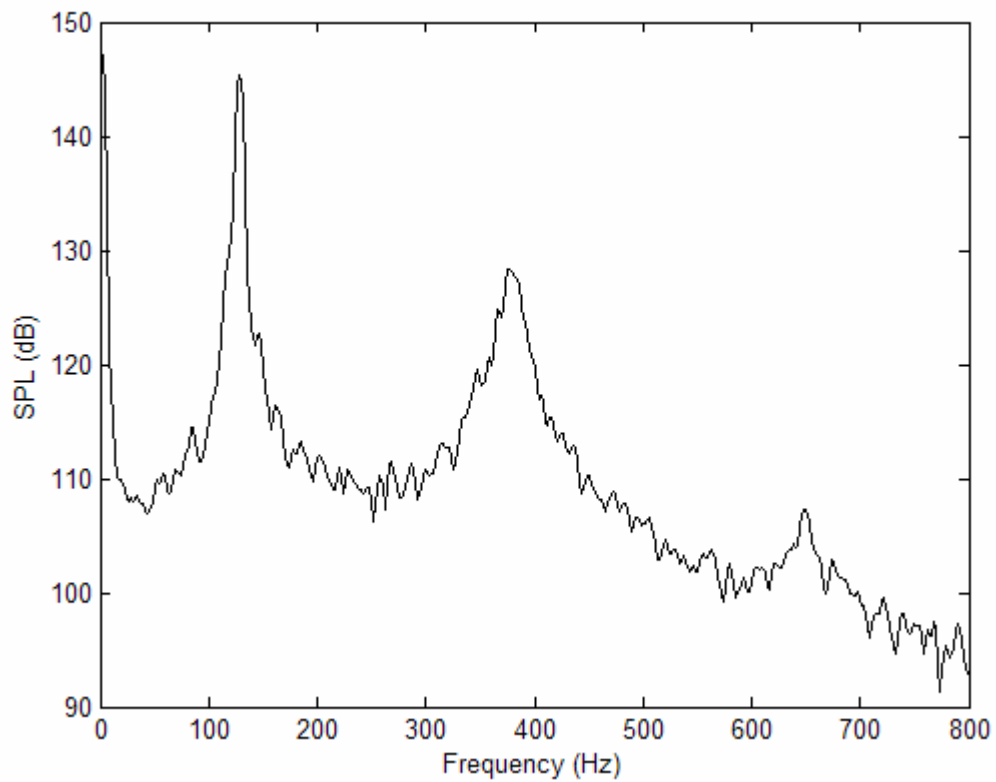


Figure E.67: GER=0.5, Controller delay=28, Gain=0.30.

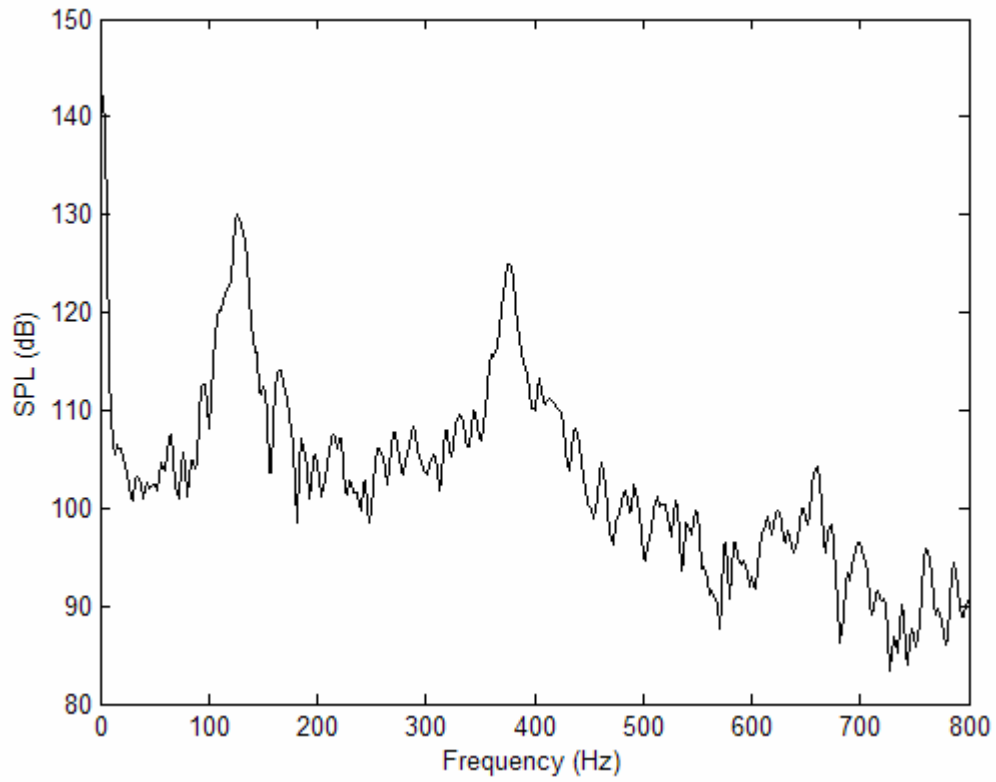


Figure E.68: GER=0.5, Controller delay=28, Gain=0.35.

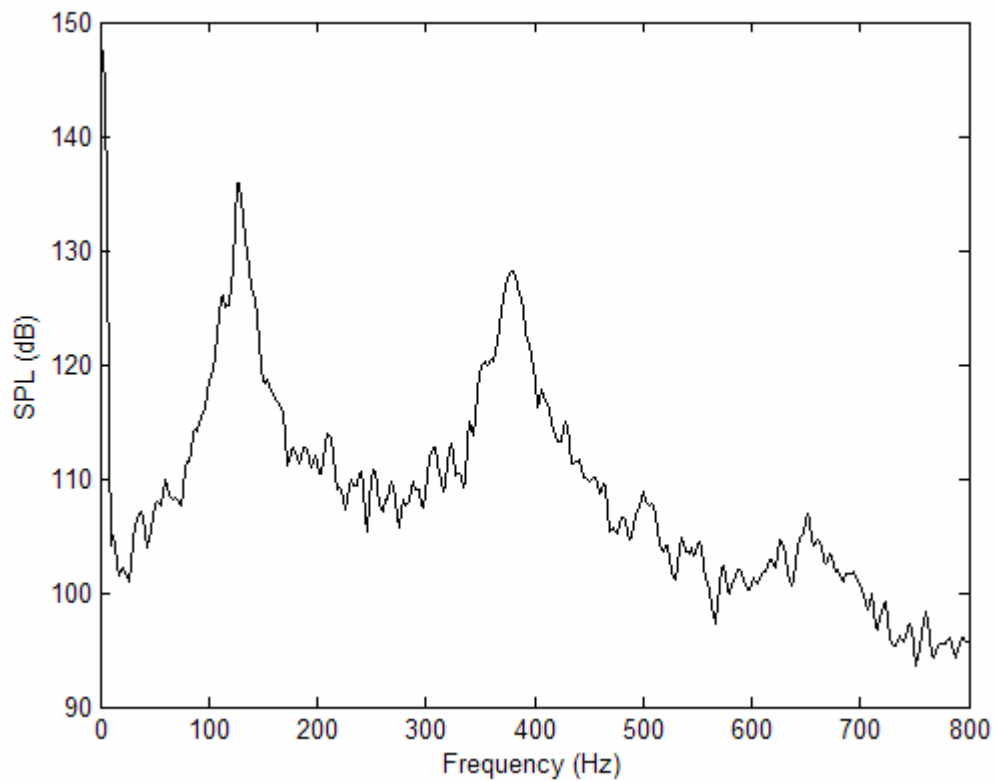


Figure E.69: GER=0.5, Controller delay=28, Gain=0.40.

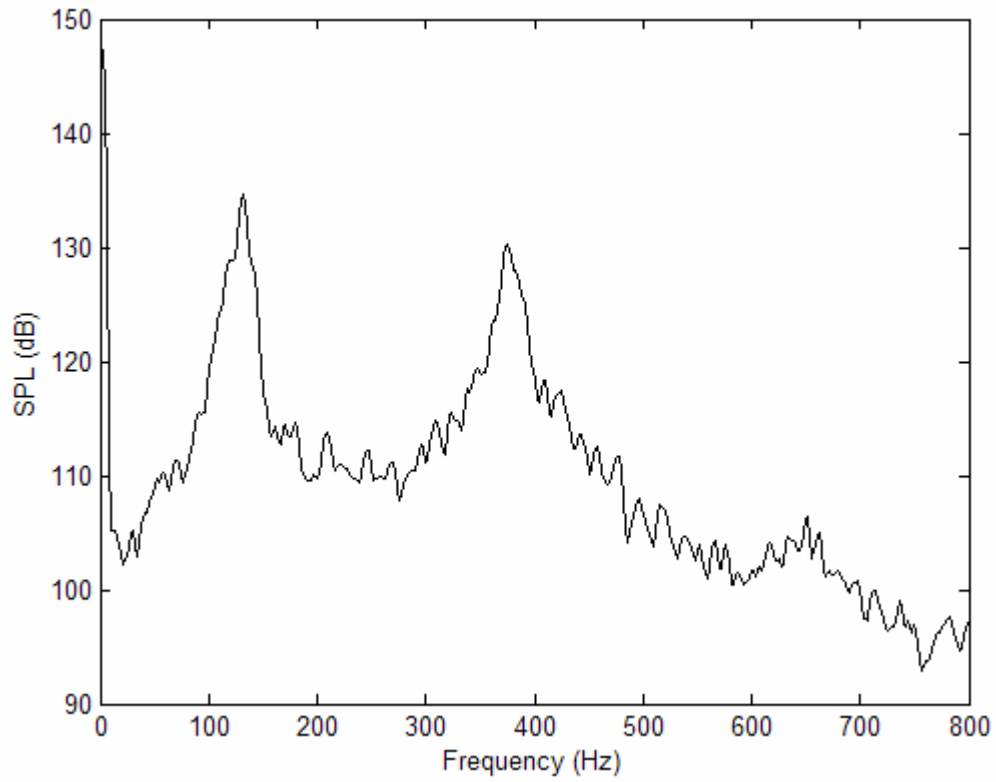


Figure E.70: GER=0.5, Controller delay=28, Gain=0.45.

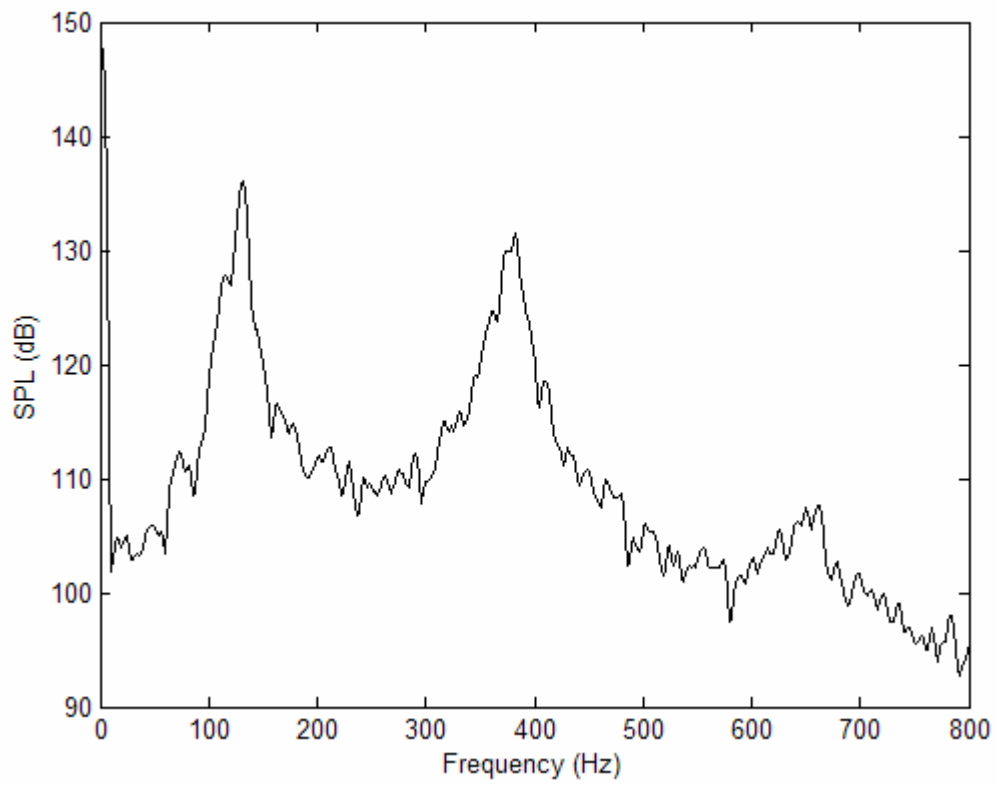


Figure E.71: GER=0.5, Controller delay=28, Gain=0.50.

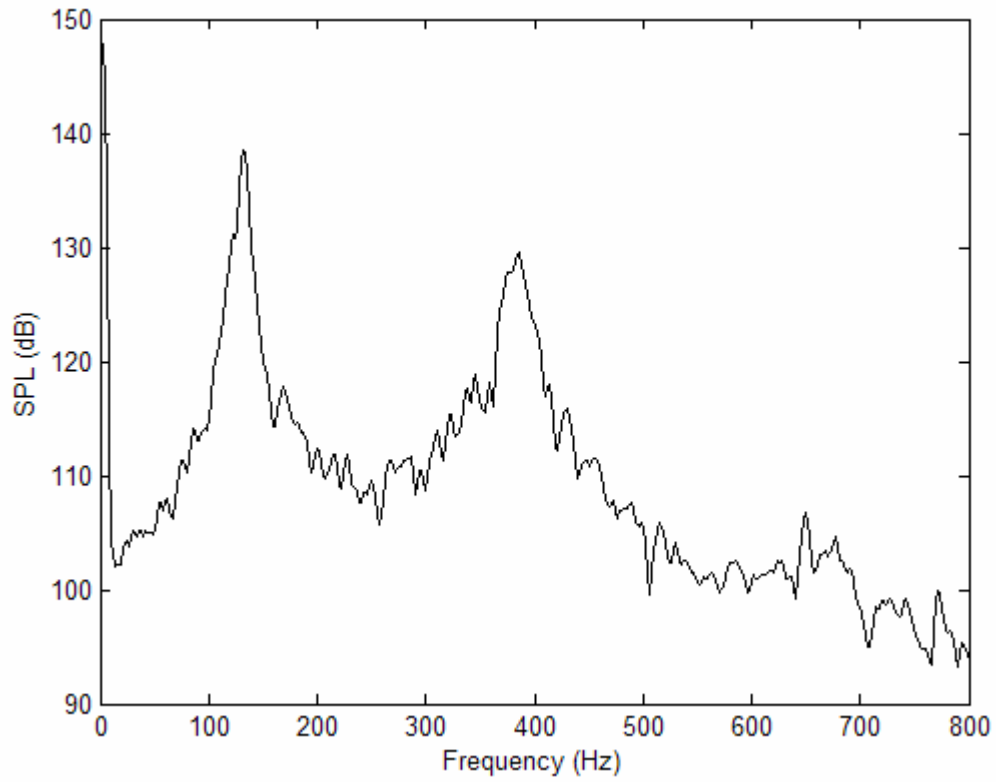


Figure E.72: GER=0.5, Controller delay=28, Gain=0.55.

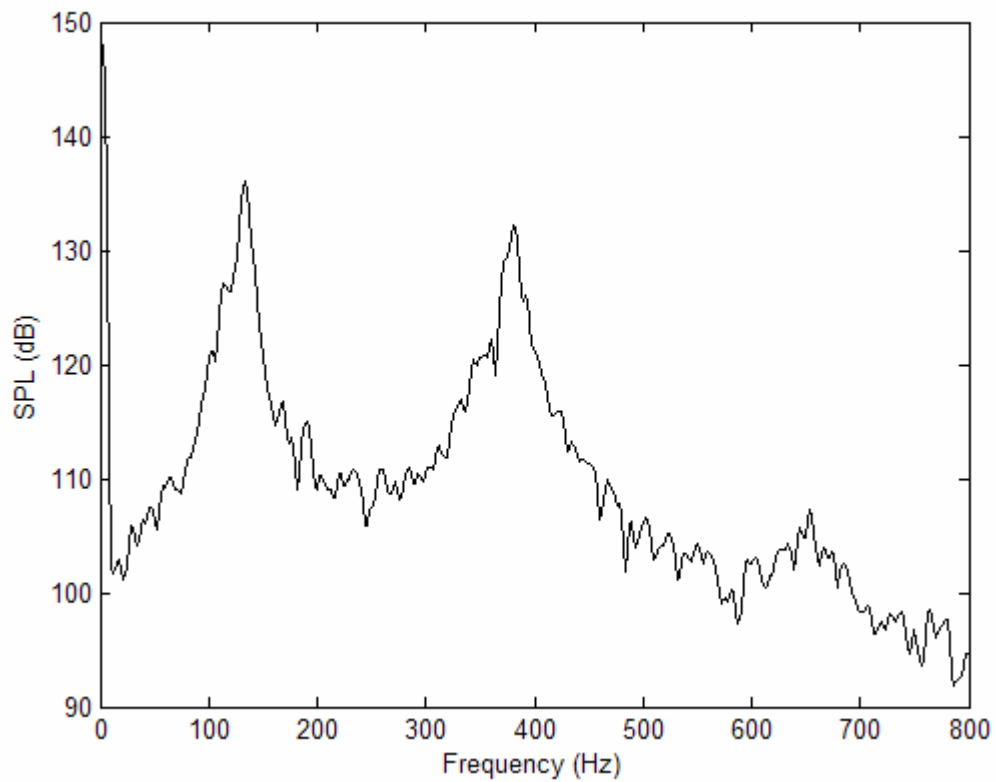


Figure E.73: GER=0.5, Controller delay=28, Gain=0.60.

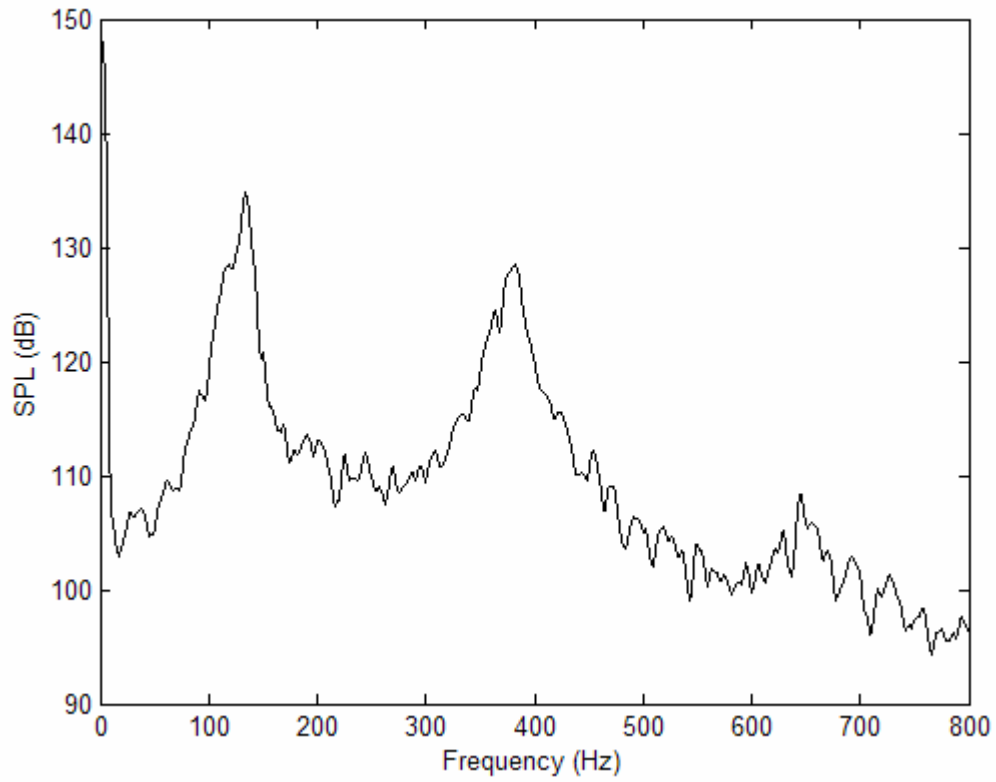


Figure E.74: GER=0.5, Controller delay=28, Gain=0.65.

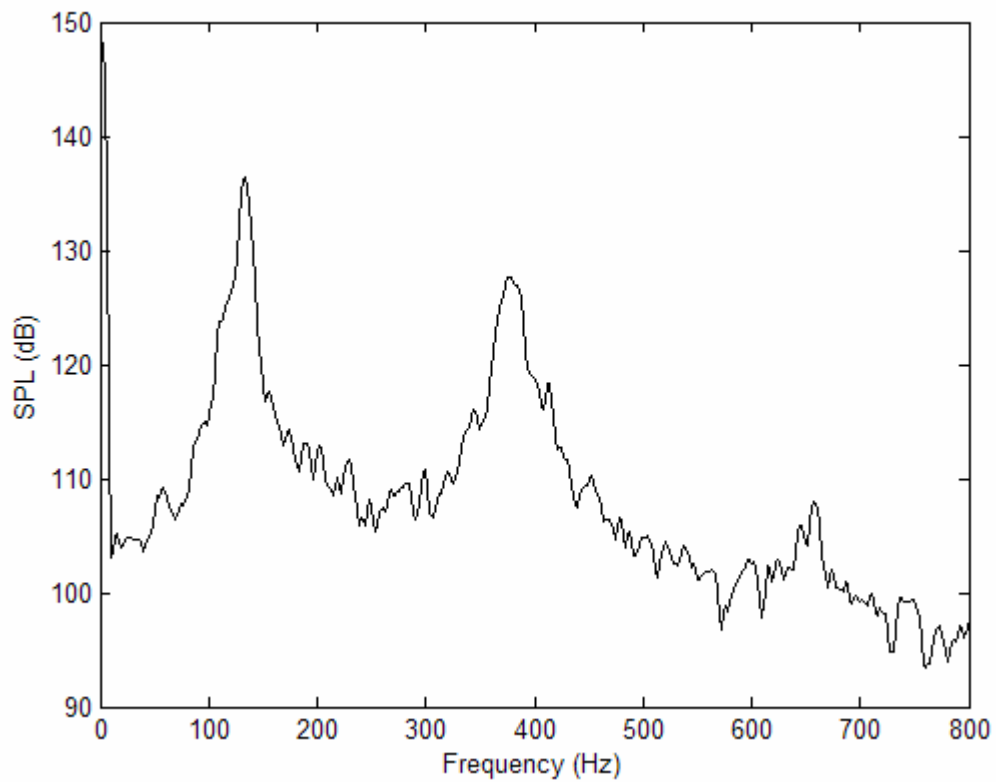


Figure E.75: GER=0.5, Controller delay=28, Gain=0.70.

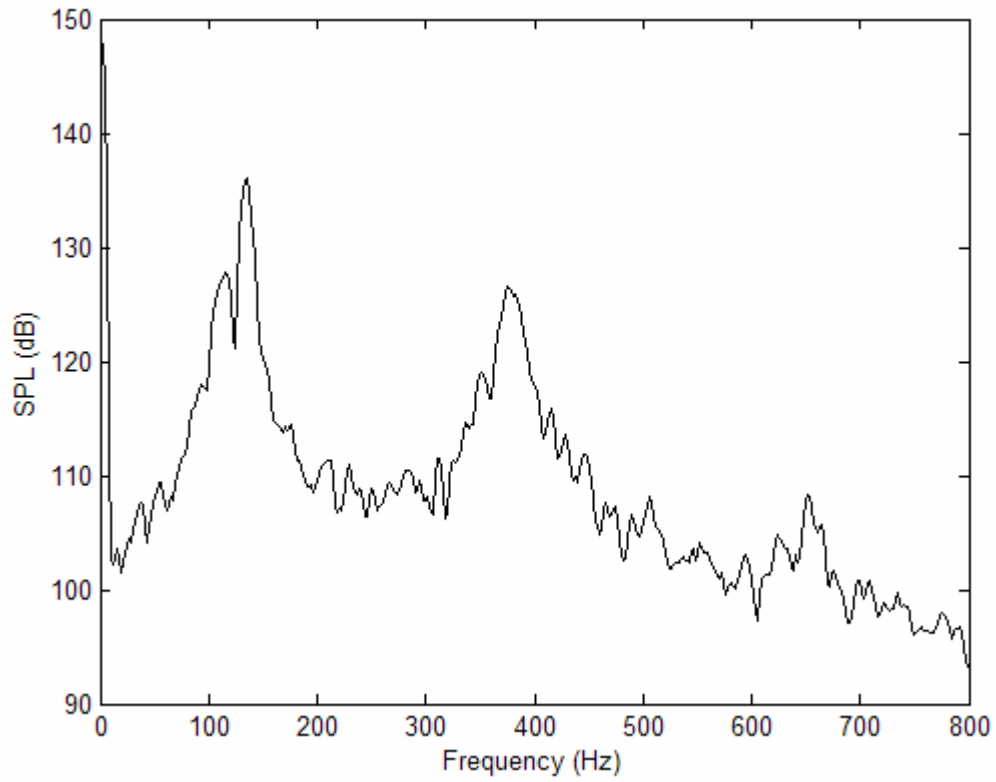


Figure E.76: GER=0.5, Controller delay=28, Gain=0.75.

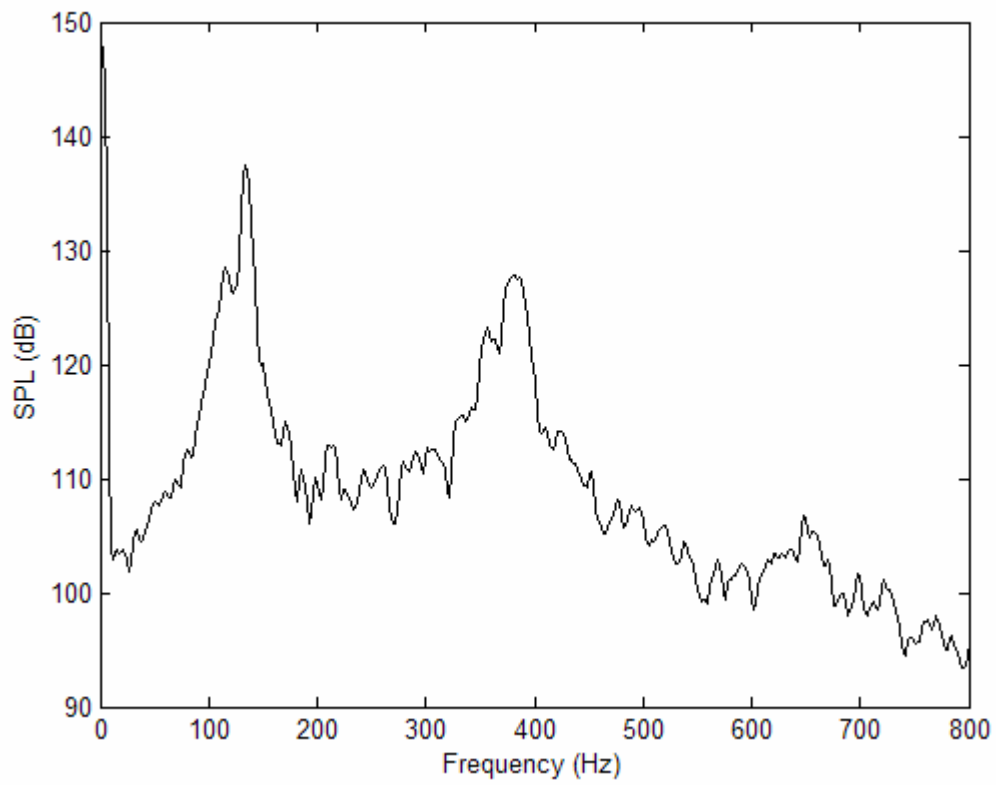


Figure E.77: GER=0.5, Controller delay=28, Gain=0.80.

Appendix F: Wiring Diagram for Nozzle Measurements

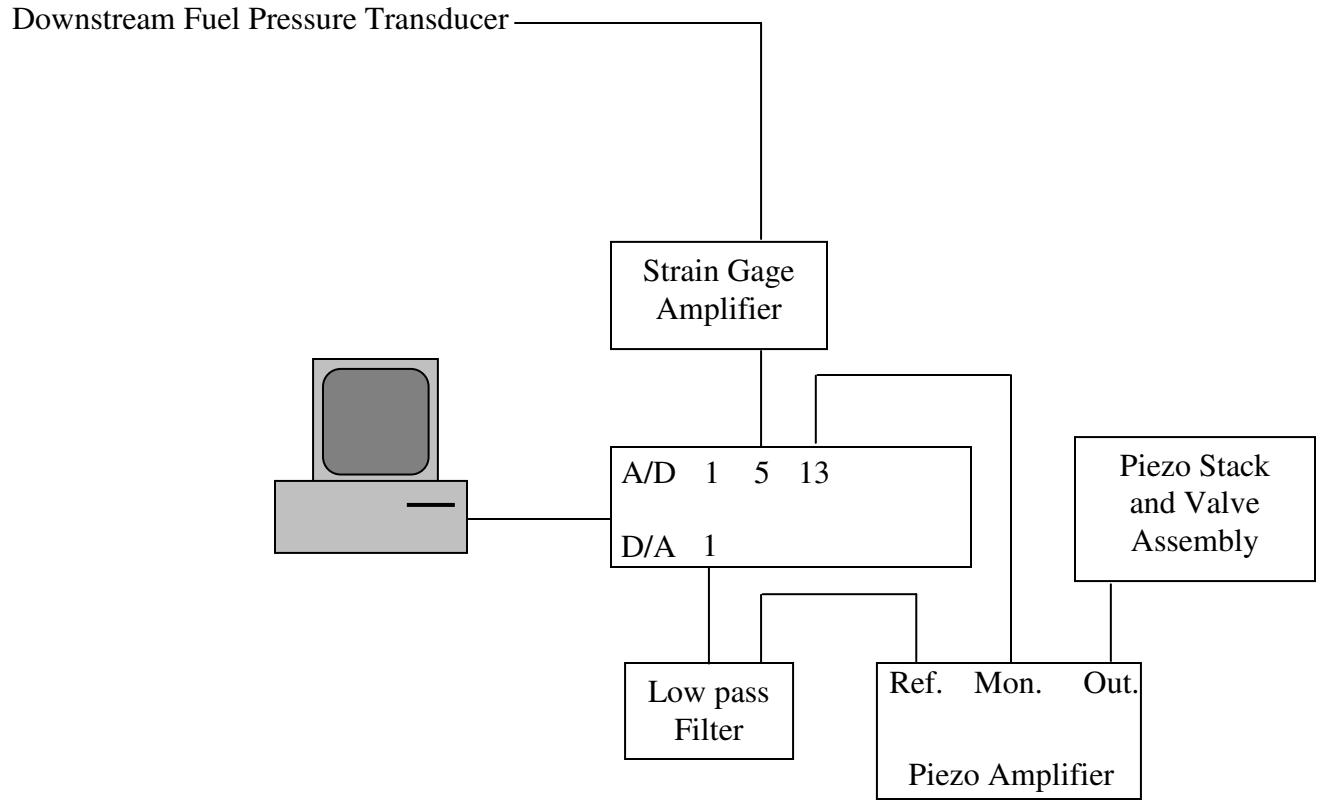


Figure F.1: Wiring diagram for nozzle measurements.

Appendix G: Error bar plots for Nozzle Measurements

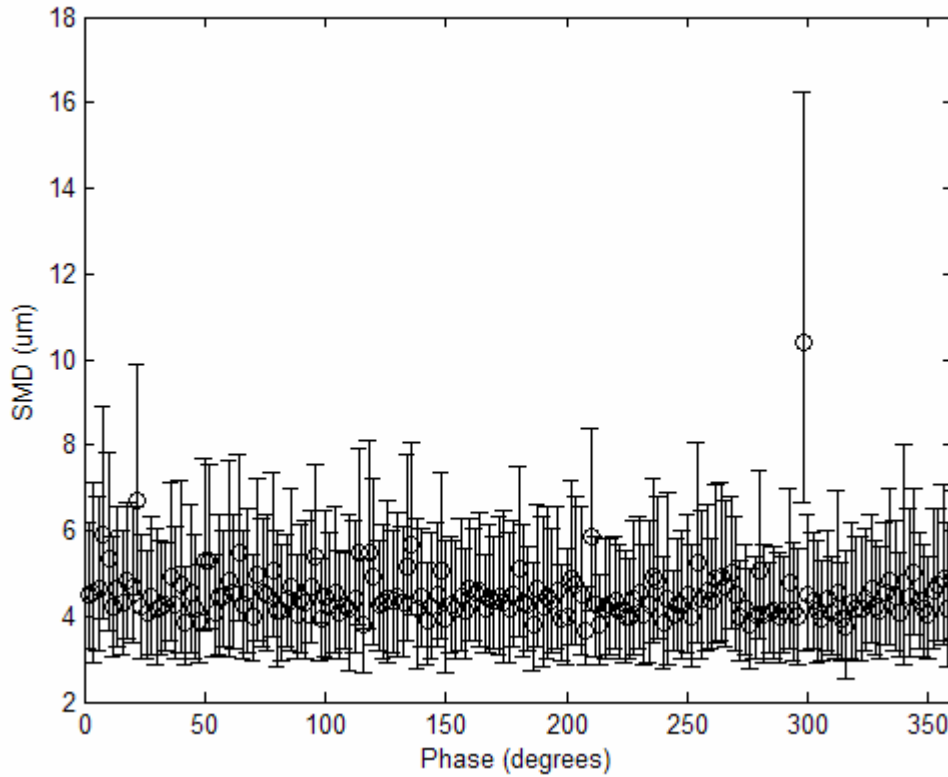


Figure G.1: Simplex nozzle, 250 psi mean pressure ± 100 , centerline.

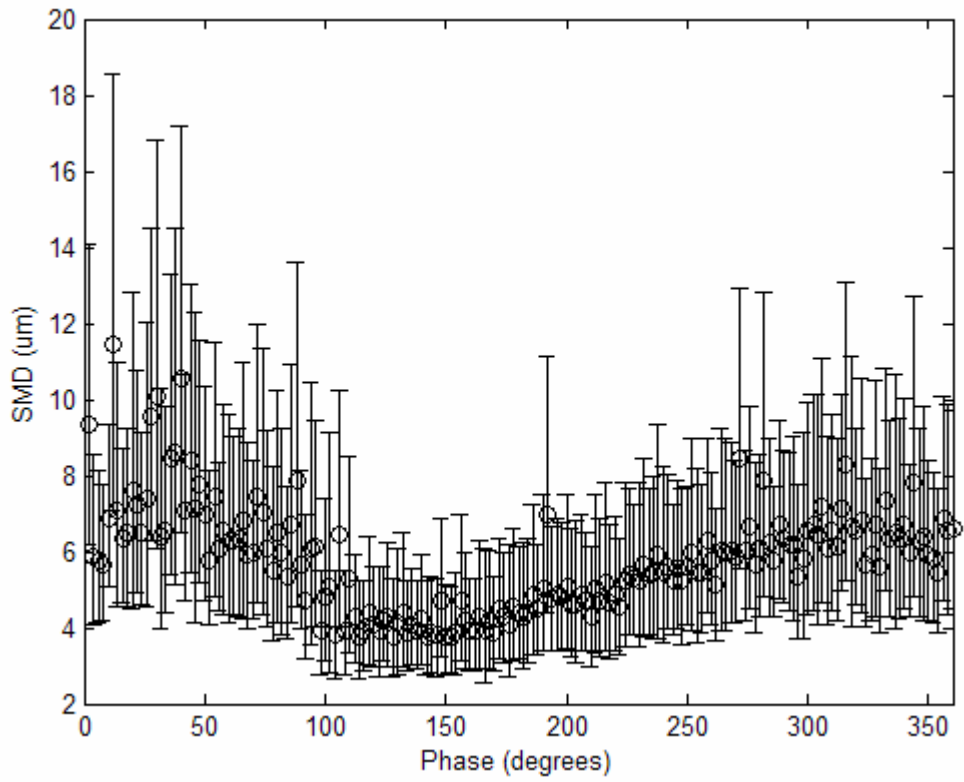


Figure G.2: Simplex nozzle, 250 psi mean pressure ± 75 , centerline.

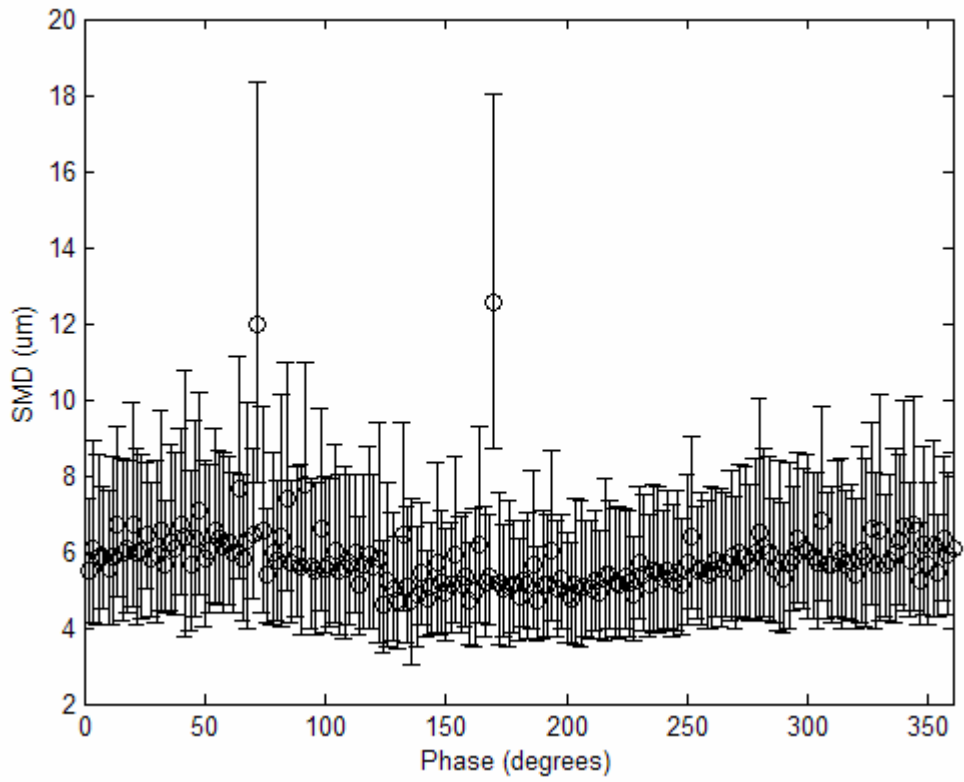


Figure G.3: Simplex nozzle, 250 psi mean pressure ± 50 , centerline.

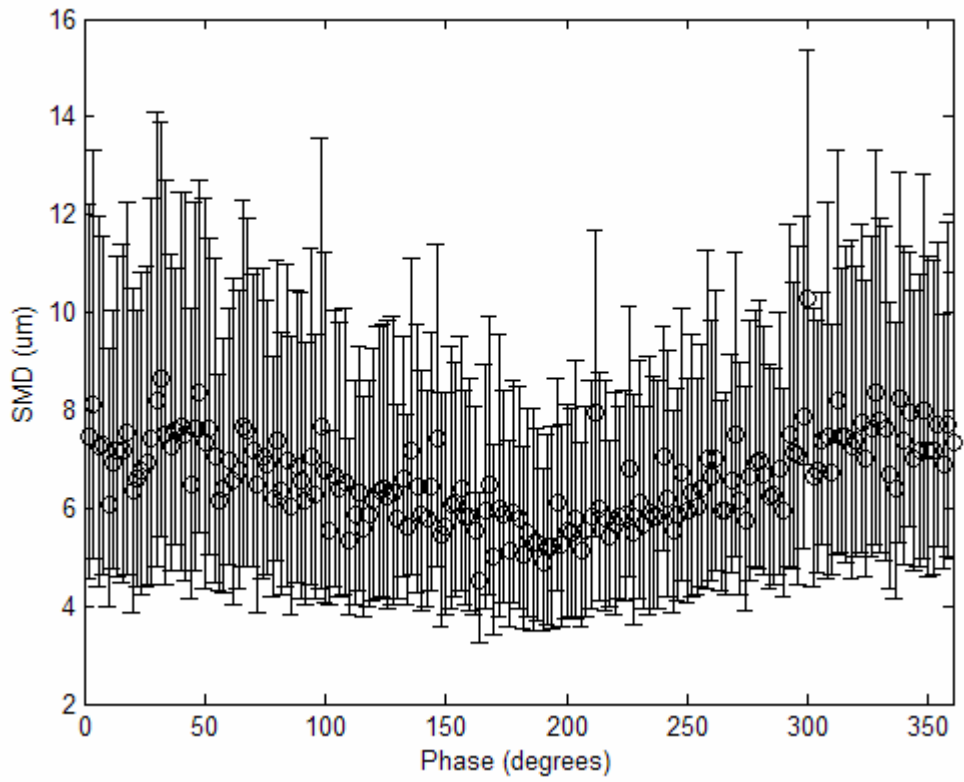


Figure G.4: Simplex nozzle, 250 psi mean pressure ± 30 , centerline.

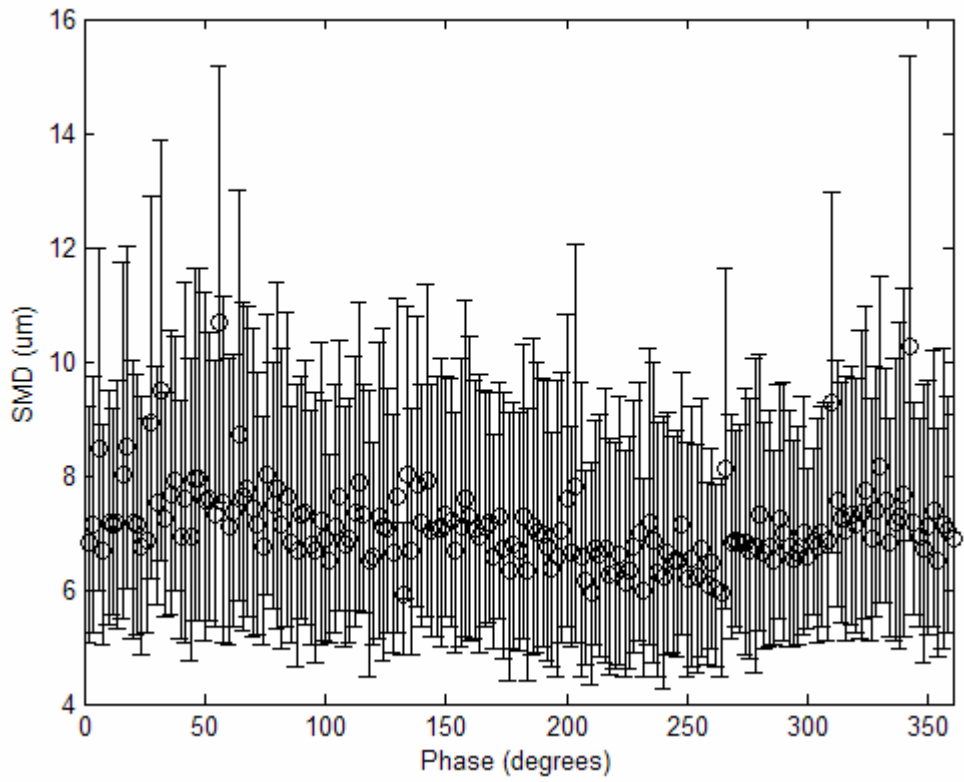


Figure G.5: Simplex nozzle, 250 psi mean pressure ± 100 , radial 0.5 cm.

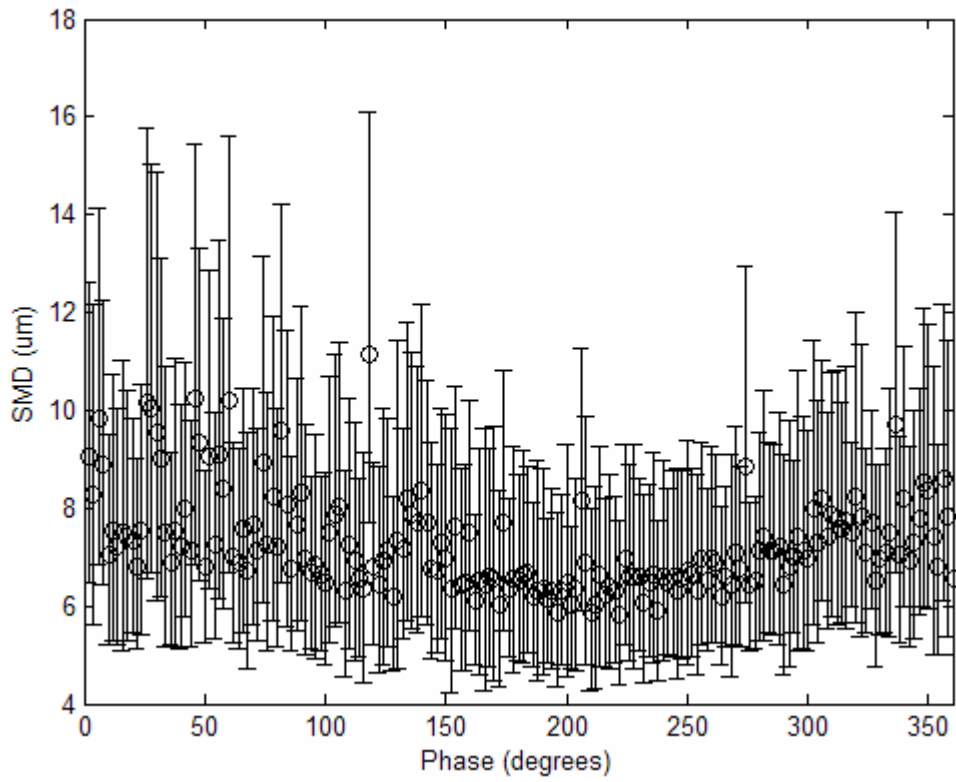


Figure G.6: Simplex nozzle, 250 psi mean pressure ± 75 , radial 0.5 cm.

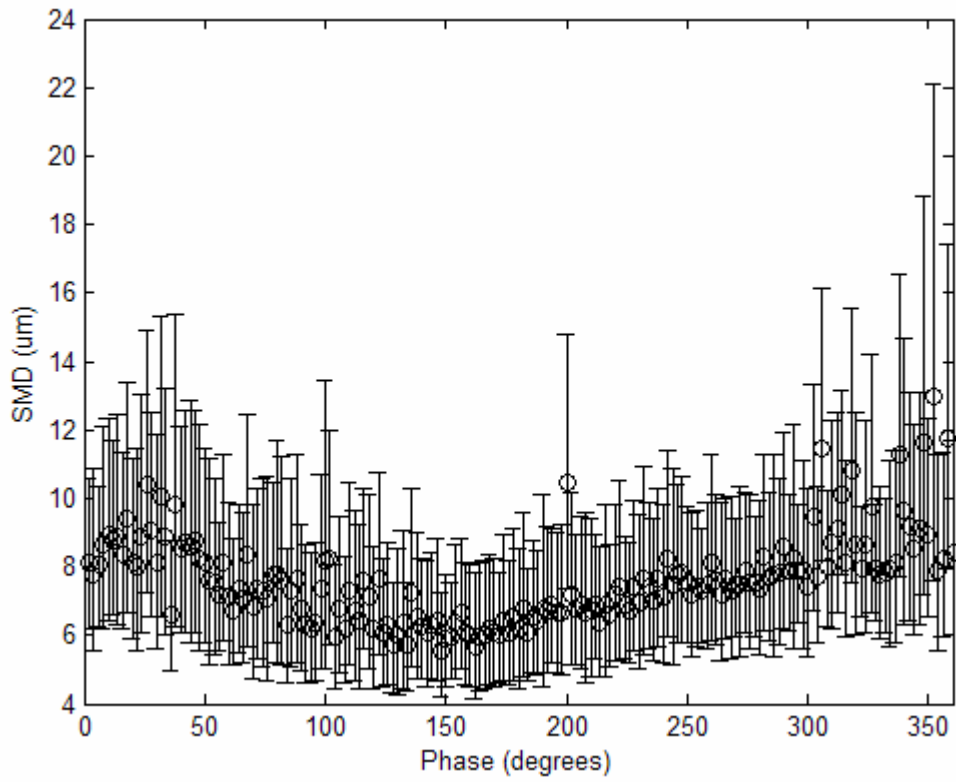


Figure G.7: Simplex nozzle, 250 psi mean pressure ± 50 psi, radial 0.5 cm.

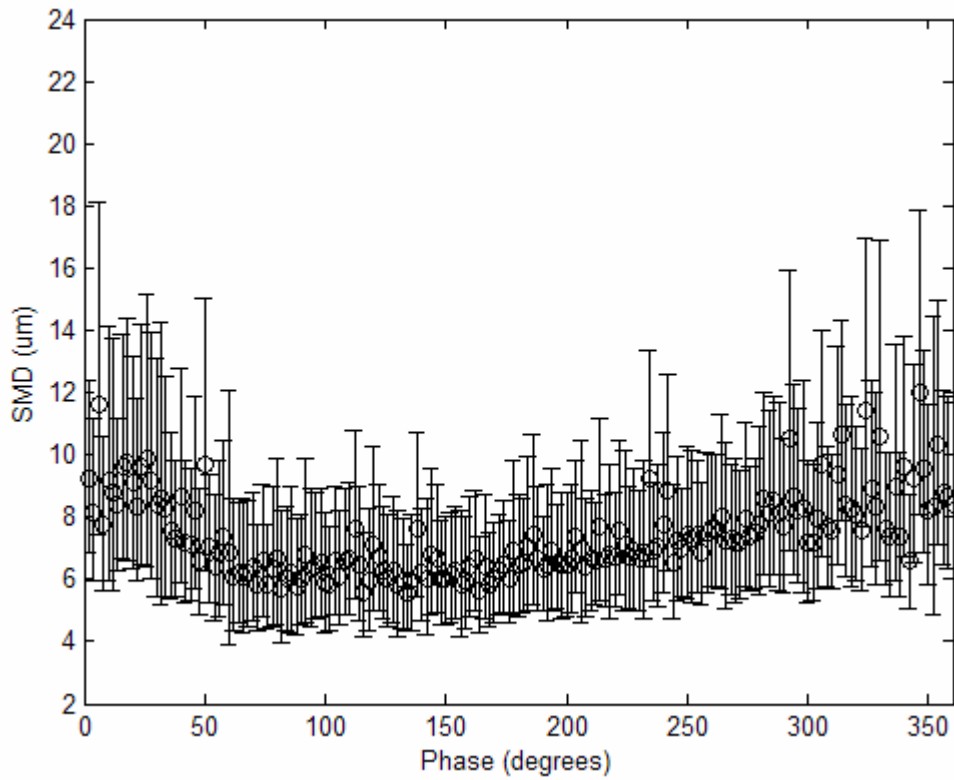


Figure G.8: Simplex nozzle, 250 psi mean pressure ± 30 , radial 0.5 cm.

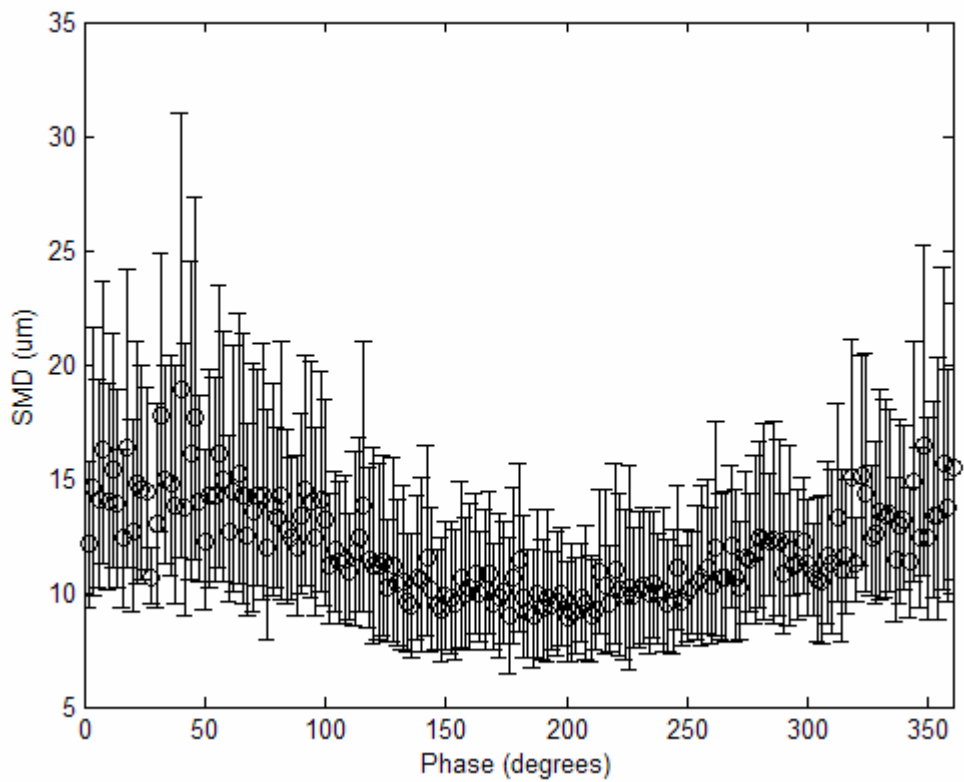


Figure G.9: Simplex nozzle, 250 psi mean pressure ± 100 psi, radial 1.0 cm.

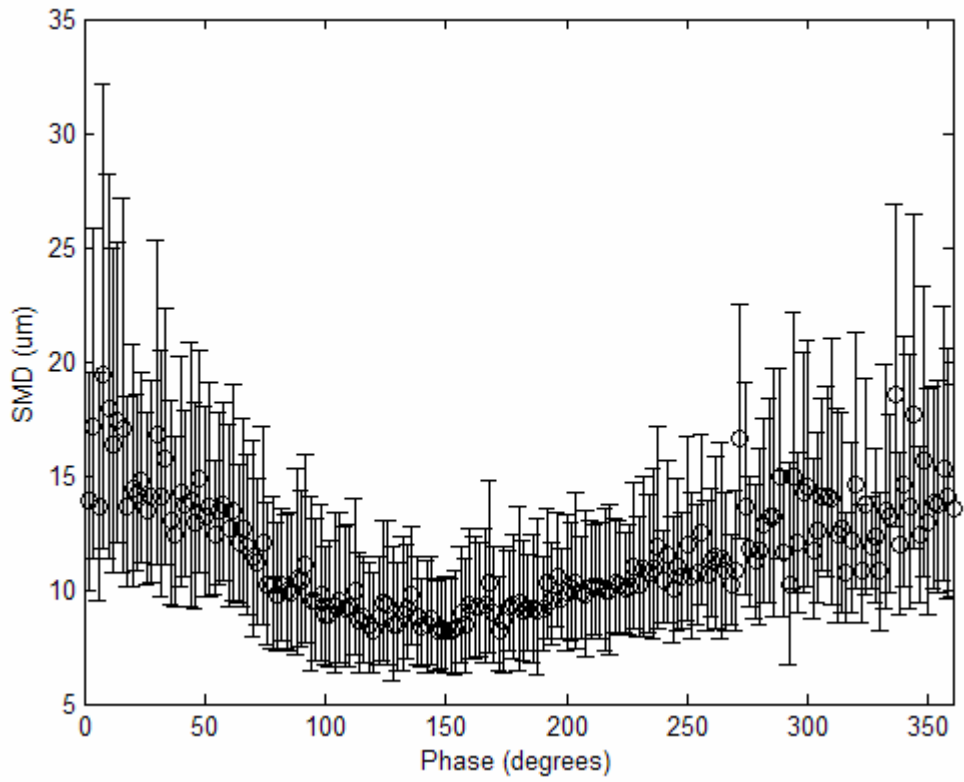


Figure G.10: Simplex nozzle, 250 psi mean pressure ± 75 , radial 1.0 cm.

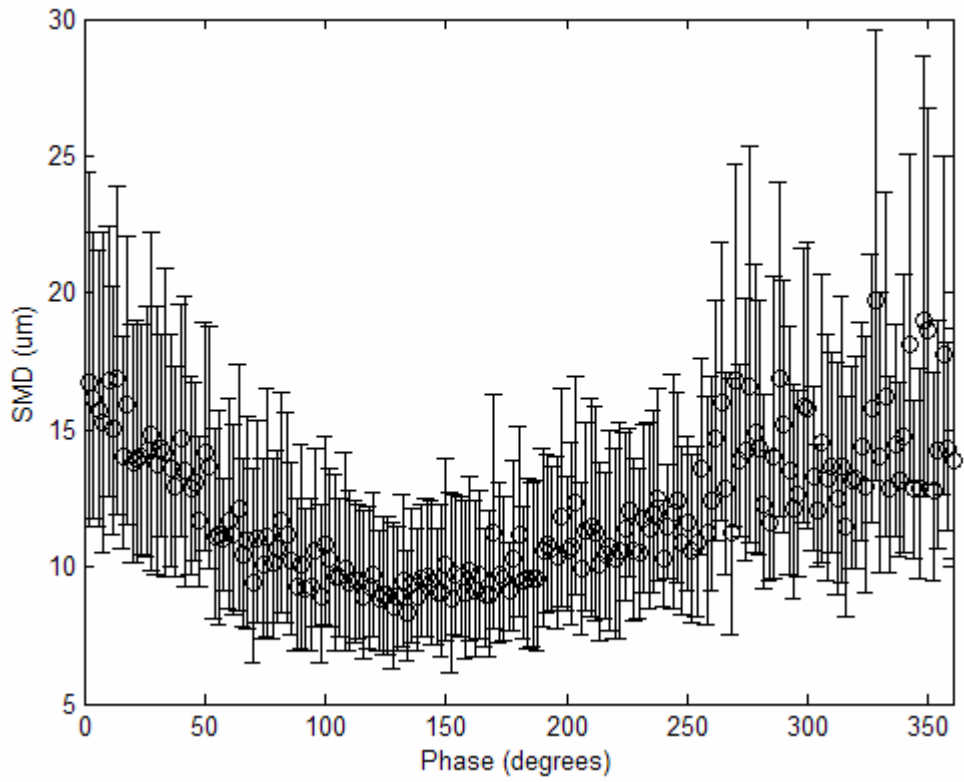


Figure G.11: Simplex nozzle, 250 psi mean pressure ± 50 , radial 1.0 cm.

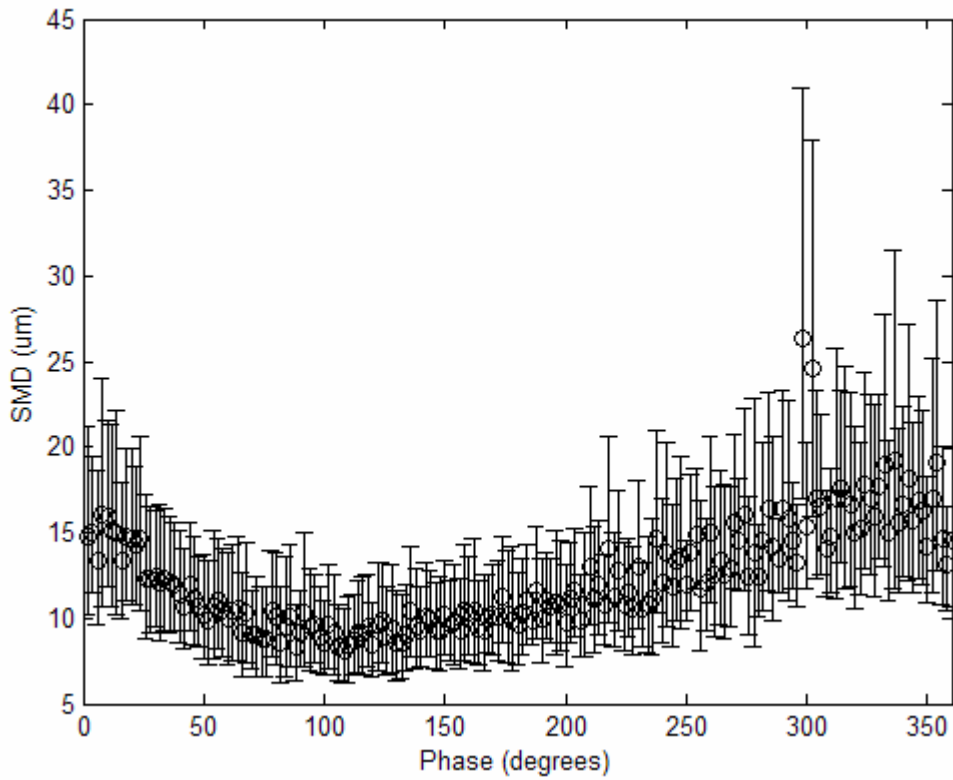


Figure G.12: Simplex nozzle, 250 psi mean pressure ± 30 , radial 1.0 cm.

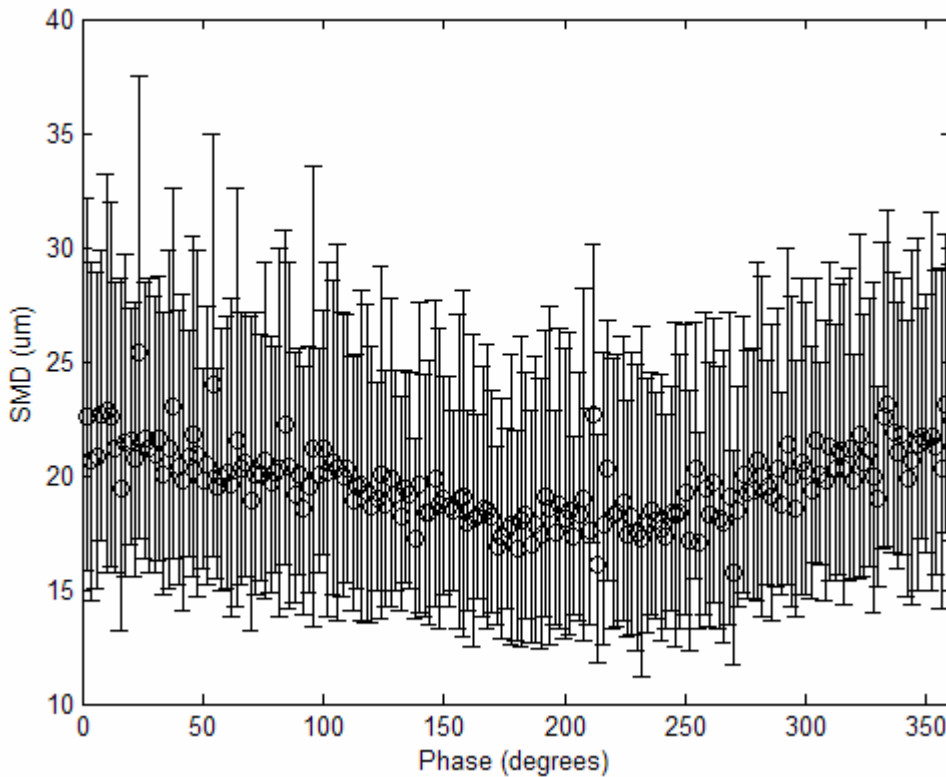


Figure G.13: Simplex nozzle, 250 psi mean pressure ± 100 , radial 1.5 cm.

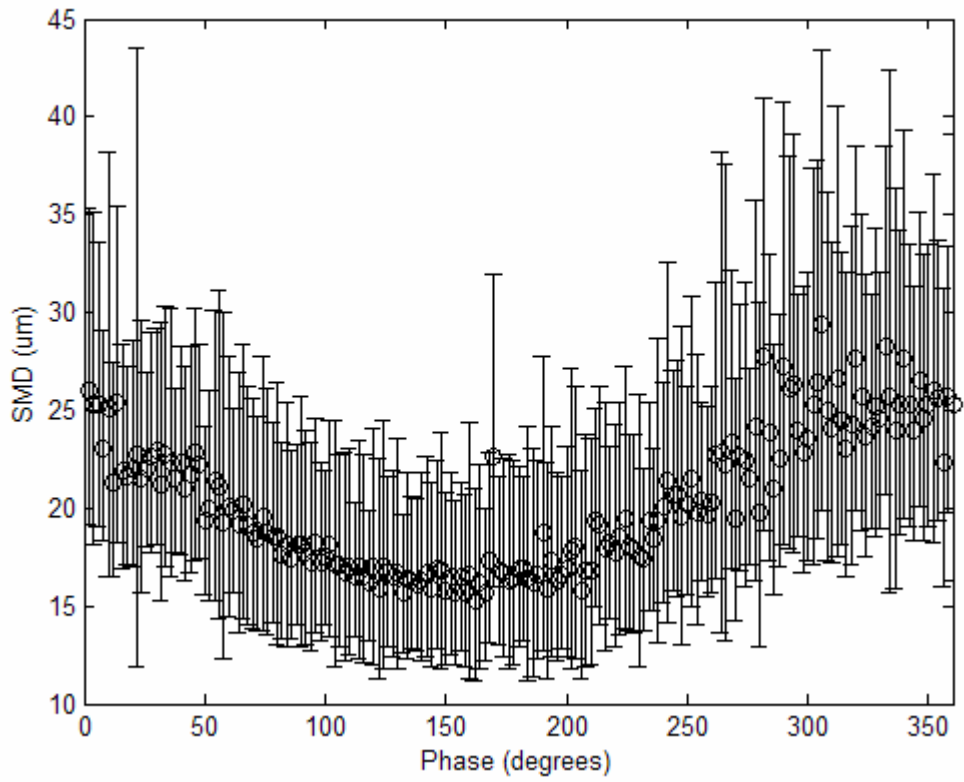


Figure G.14: Simplex nozzle, 250 psi mean pressure ± 75 , radial 1.5 cm.

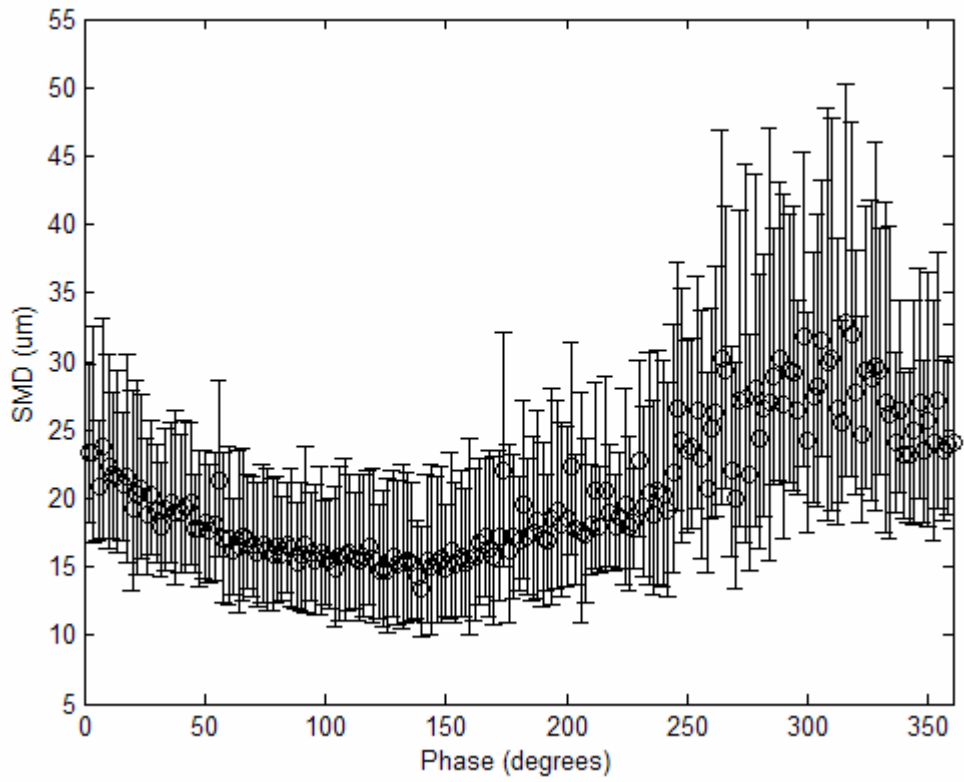


Figure G.15: Simplex nozzle, 250 psi mean pressure ± 50 , radial 1.5 cm.

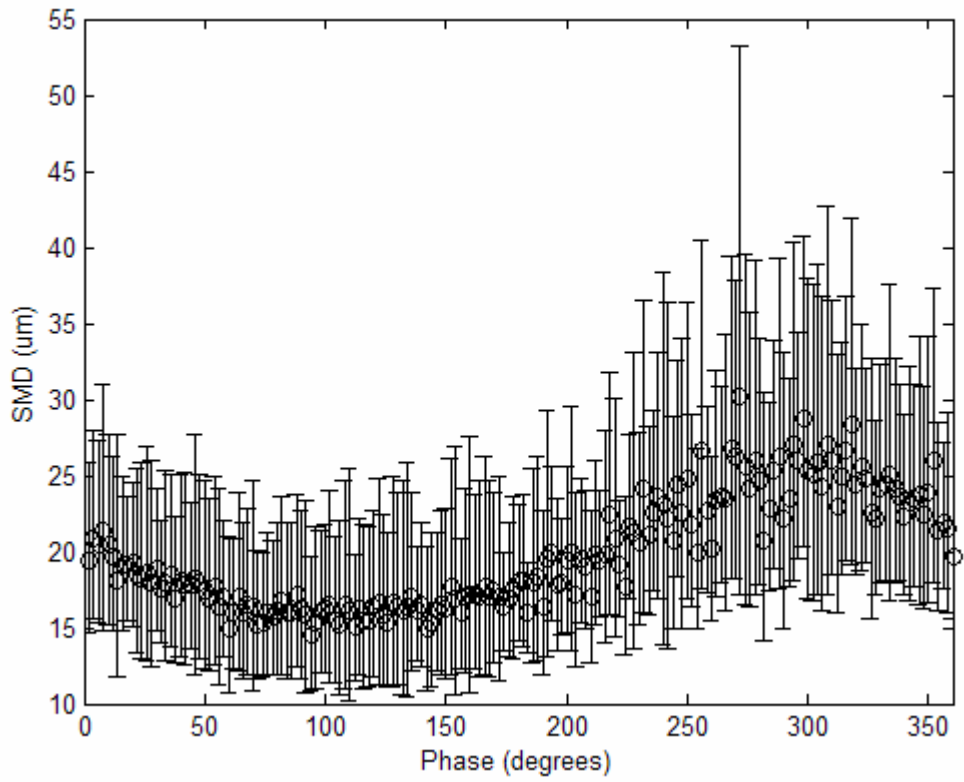


Figure G.16: Simplex nozzle, 250 psi mean pressure ± 30 , radial 1.5 cm.

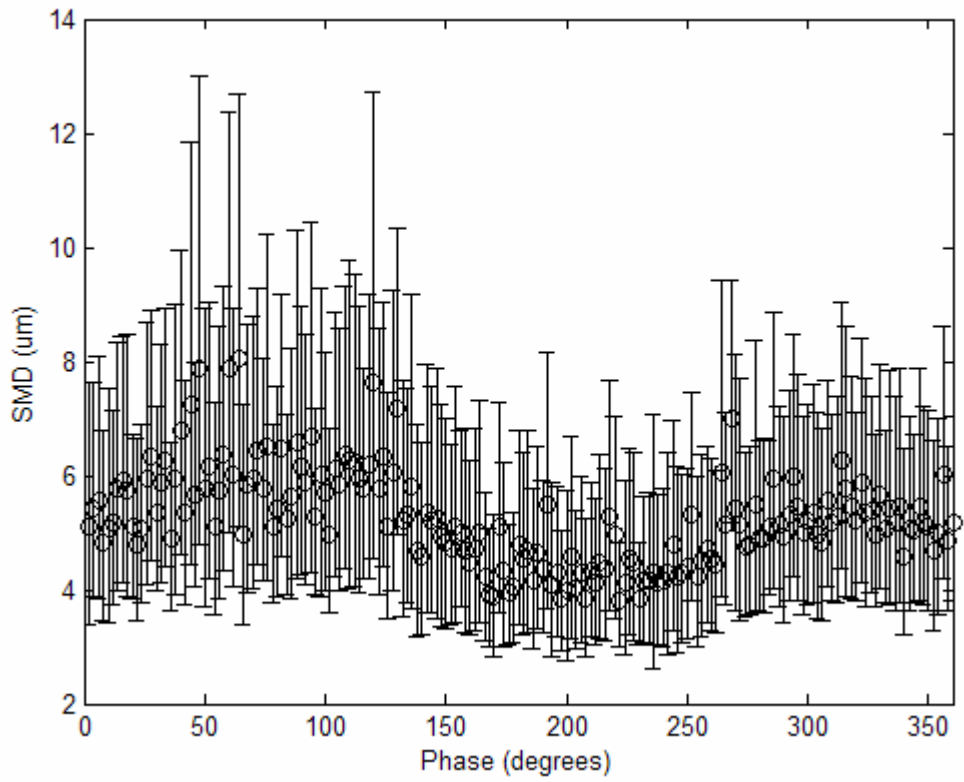


Figure G.17: Simplex nozzle, 200 psi mean pressure ± 100 , centerline.

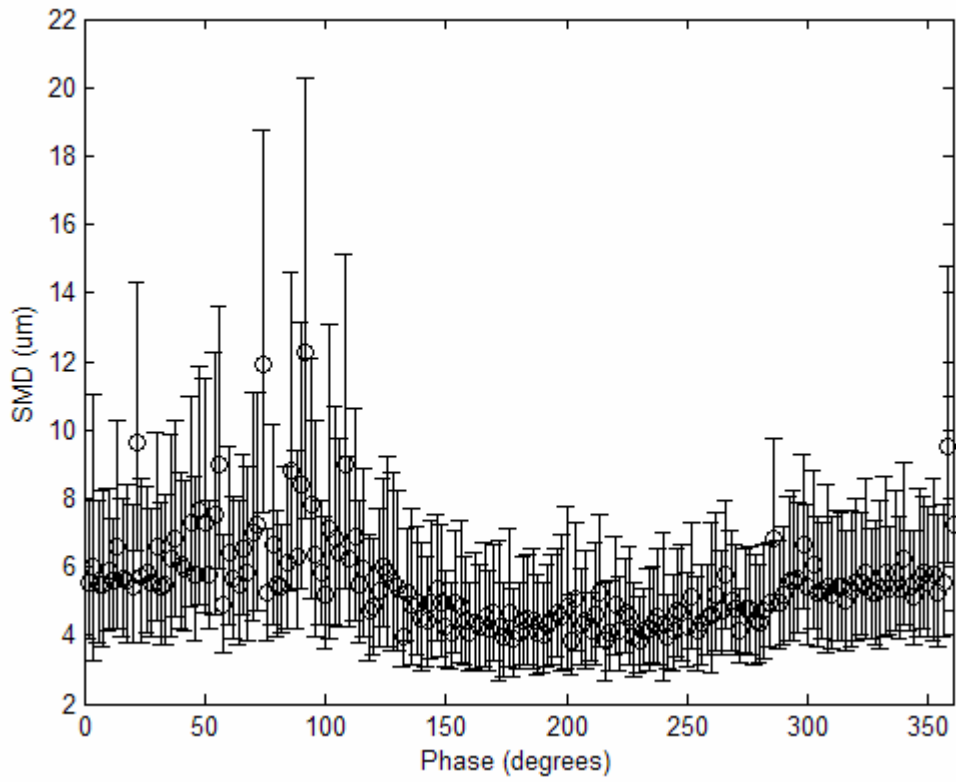


Figure G.18: Simplex nozzle, 200 psi mean pressure ± 75 , centerline.

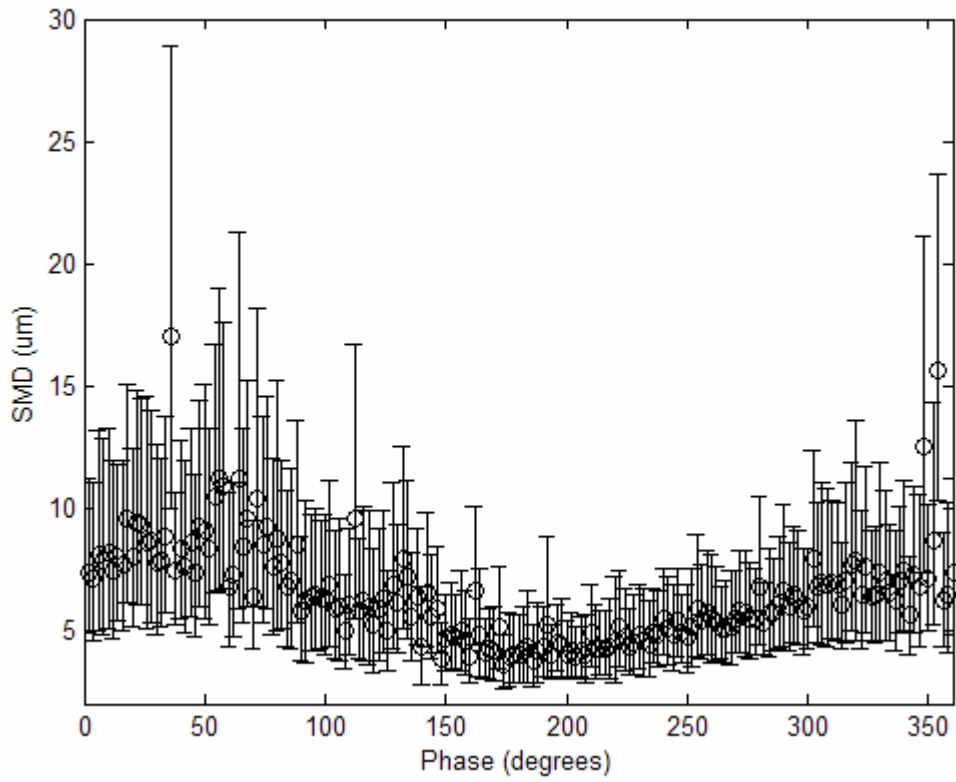


Figure G.19: Simplex nozzle, 200 psi mean pressure ± 50 , centerline.

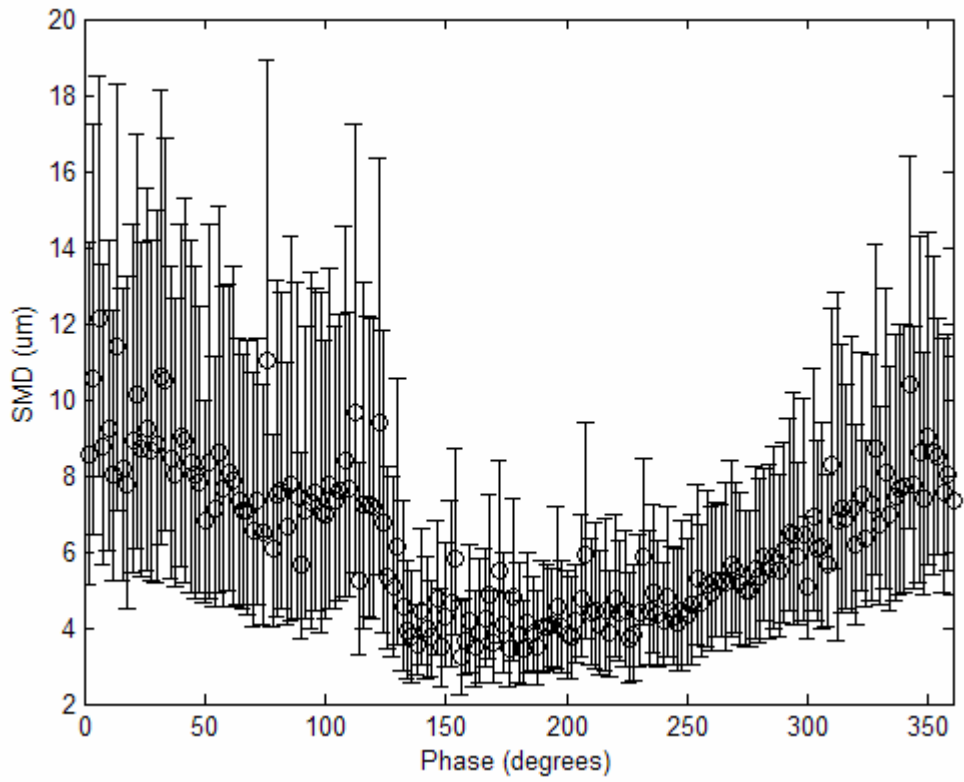


Figure G.20: Simplex nozzle, 200 psi mean pressure ± 30 , centerline.

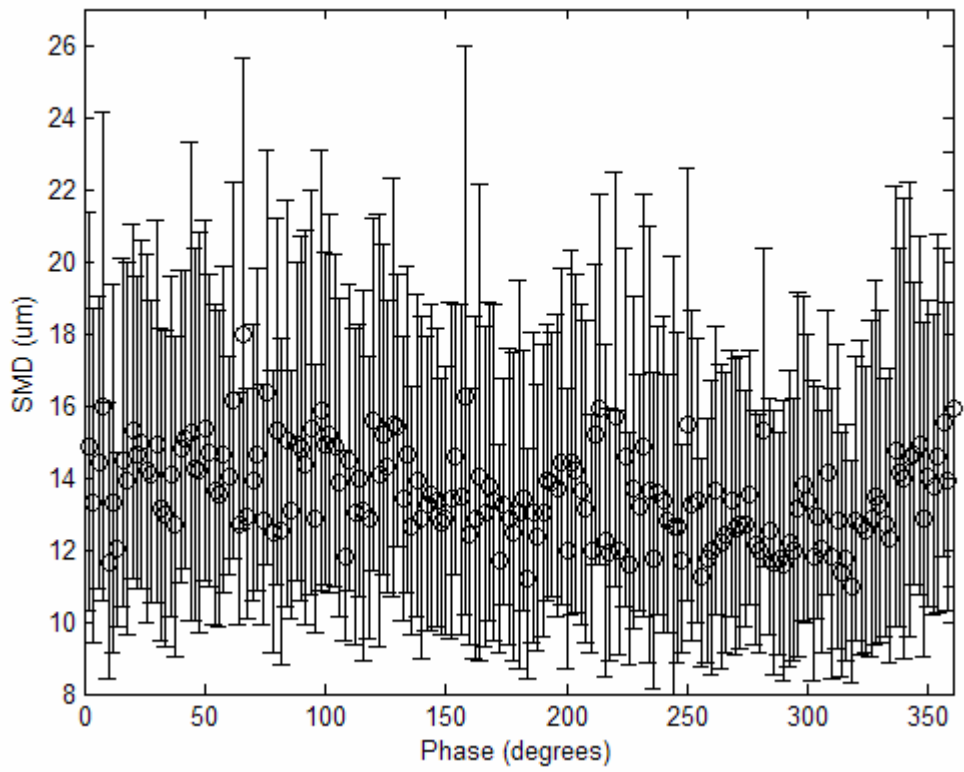


Figure G.21: Simplex nozzle, 200 psi mean pressure ± 100 psi, radial 1.0 cm.

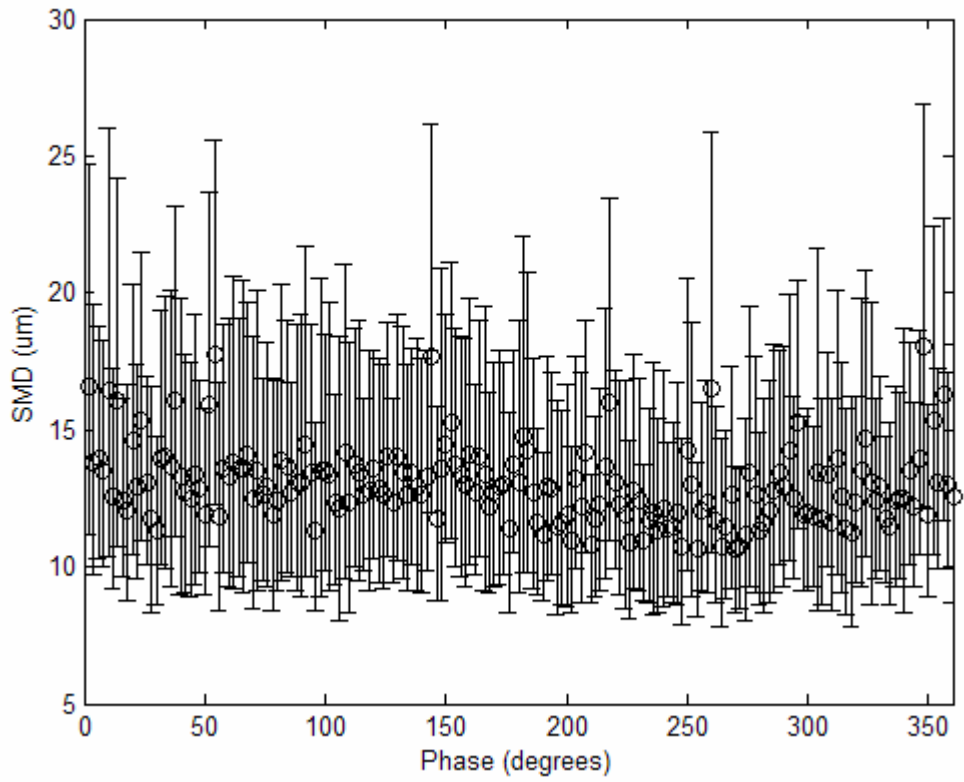


Figure G.22: Simplex nozzle, 200 psi mean pressure ± 75 , radial 1.0 cm.

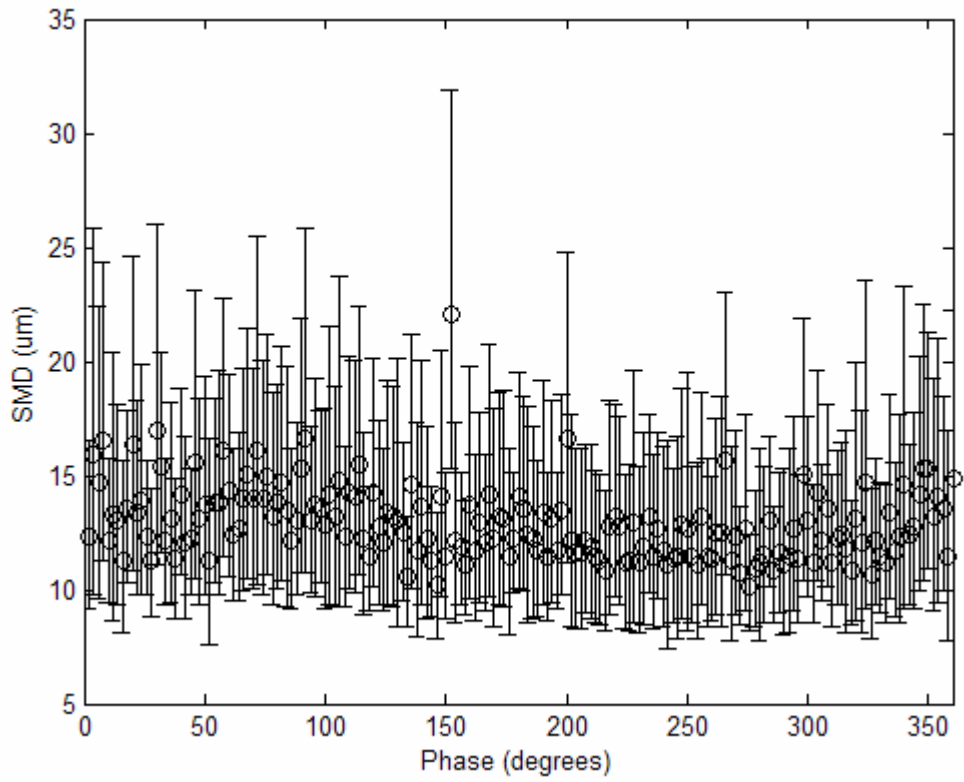


Figure G.23: Simplex nozzle, 200 psi mean pressure ± 50 , radial 1.0 cm.

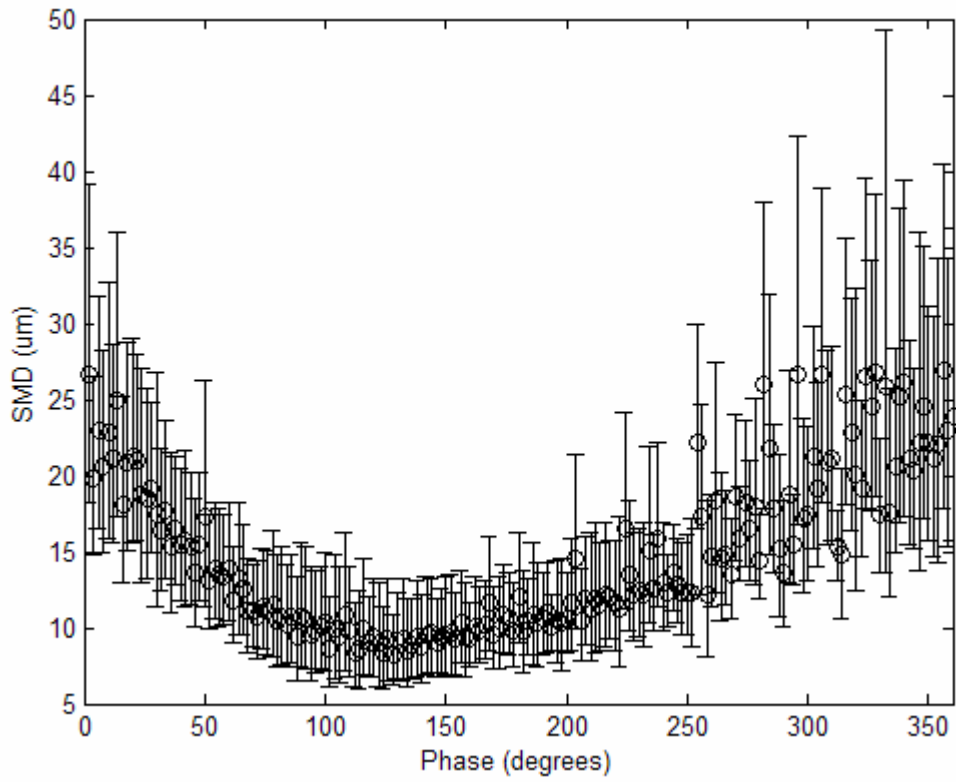


Figure G.24: Simplex nozzle, 200 psi mean pressure ± 30 , radial 1.0 cm.

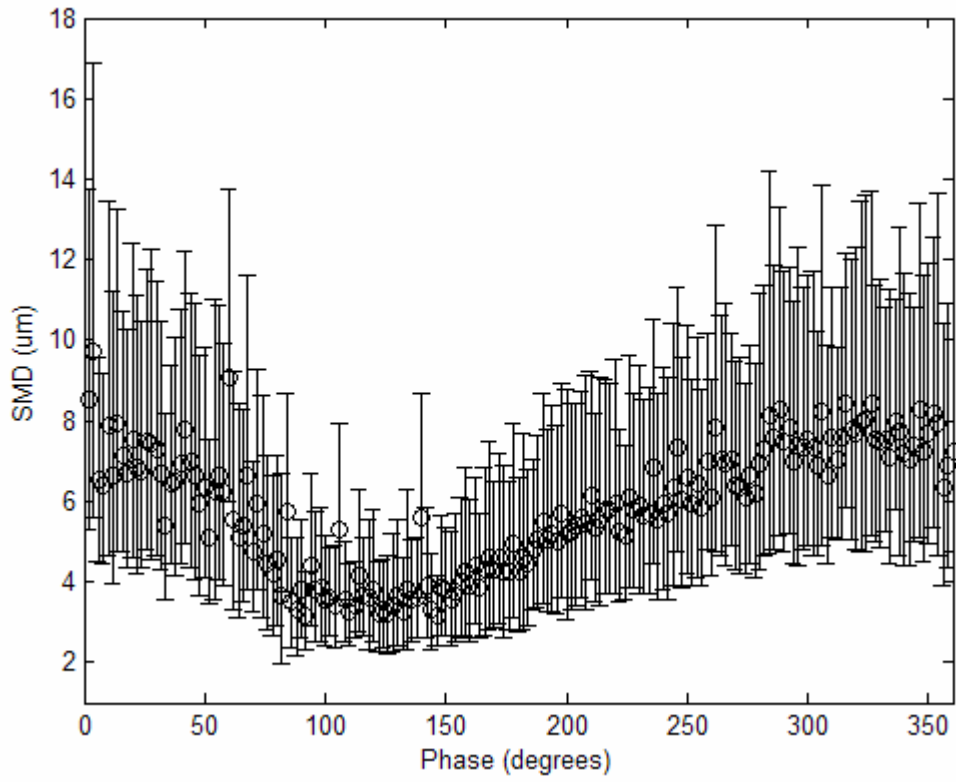


Figure G.25: Simplex nozzle, 300 psi mean pressure ± 100 , centerline.

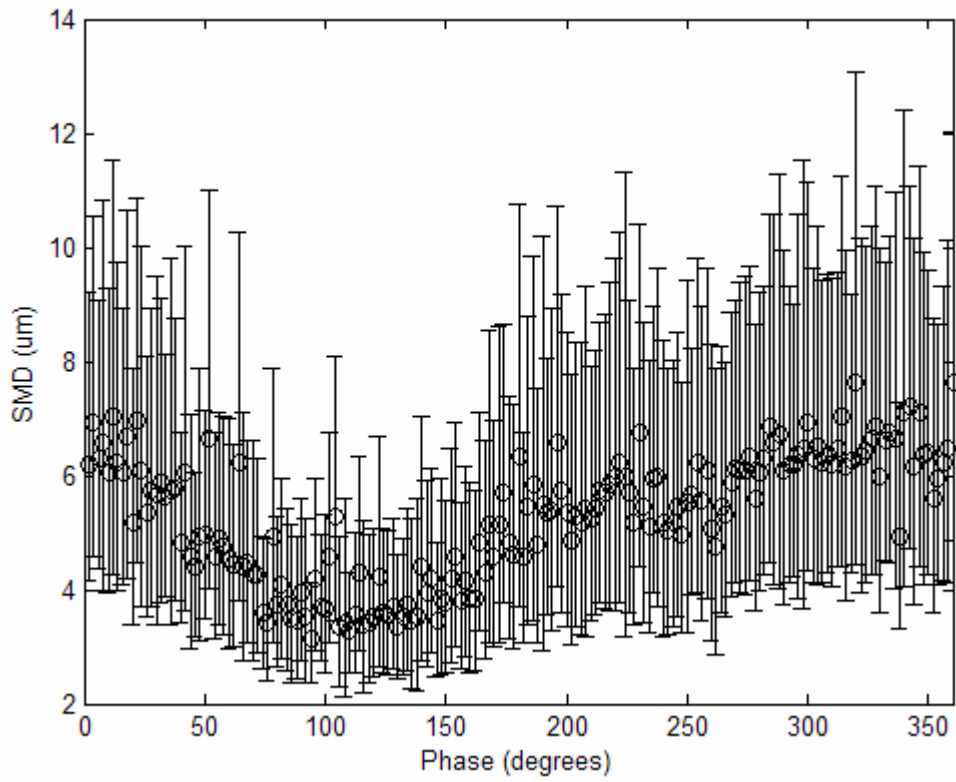


Figure G.26: Simplex nozzle, 300 psi mean pressure ± 75 , centerline.

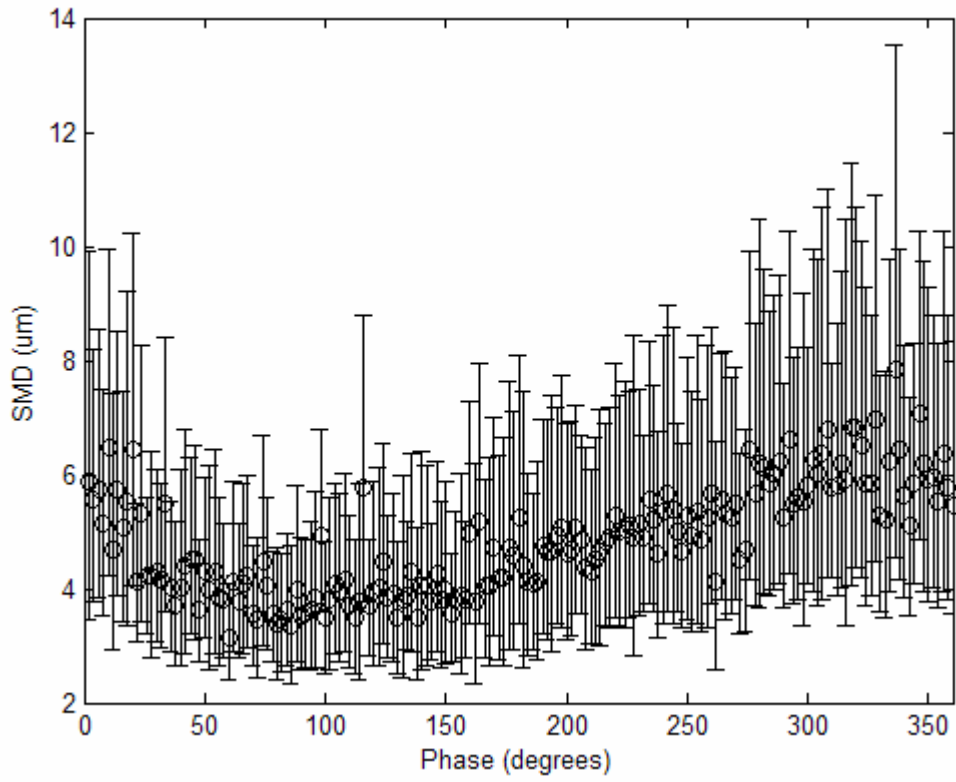


Figure G.27: Simplex nozzle, 300 psi mean pressure ± 50 , centerline.

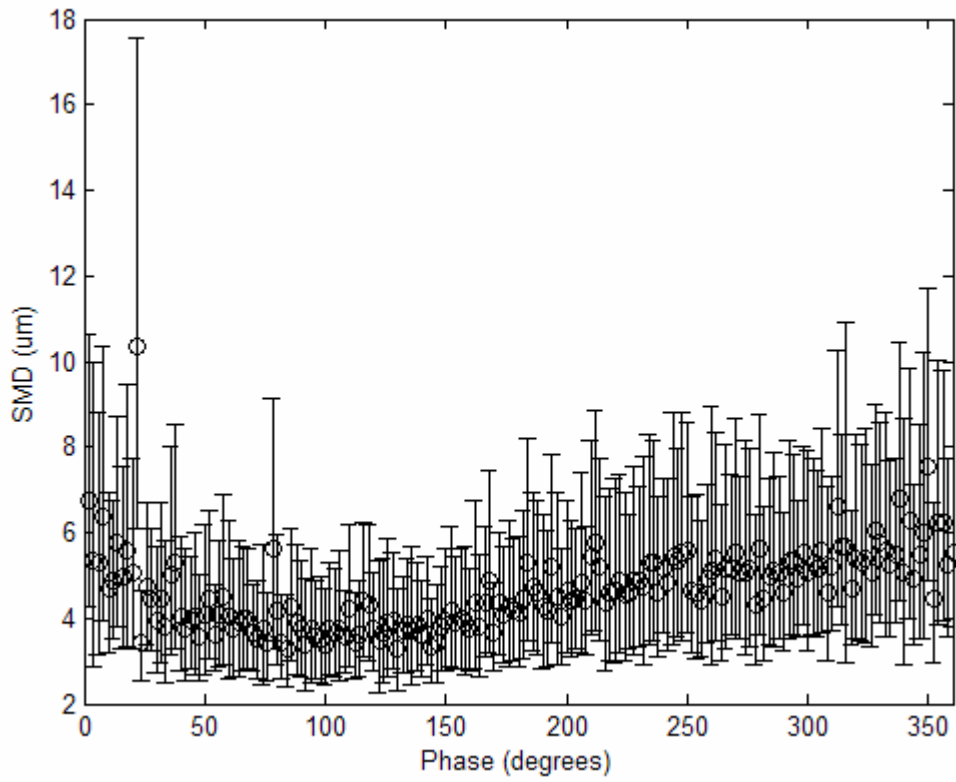


Figure G.28: Simplex nozzle, 300 psi mean pressure ± 30 , centerline.

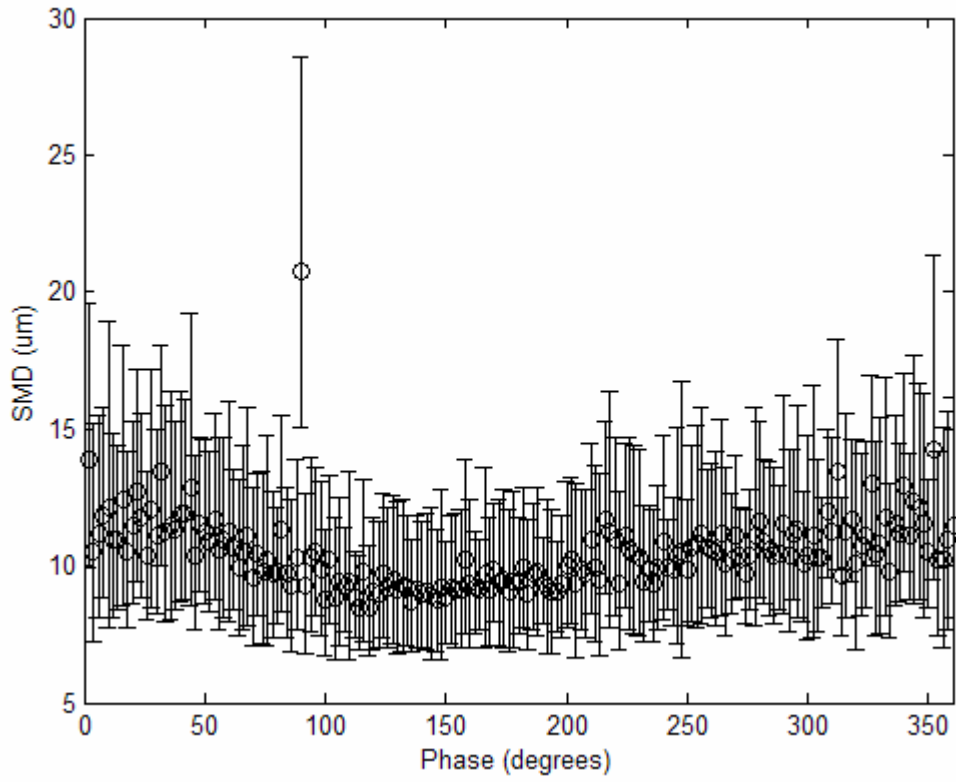


Figure G.29: Simplex nozzle, 300 psi mean pressure ± 100 , radial 1.0 cm.

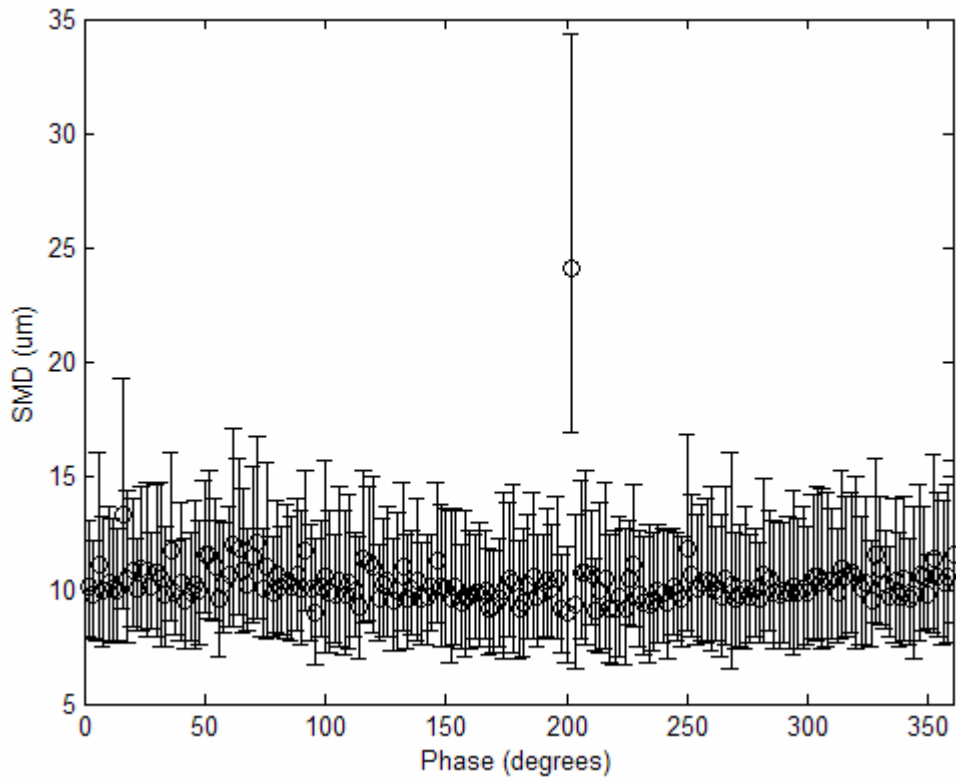


Figure G.30: Simplex nozzle, 300 psi mean pressure ± 75 , radial 1.0 cm.

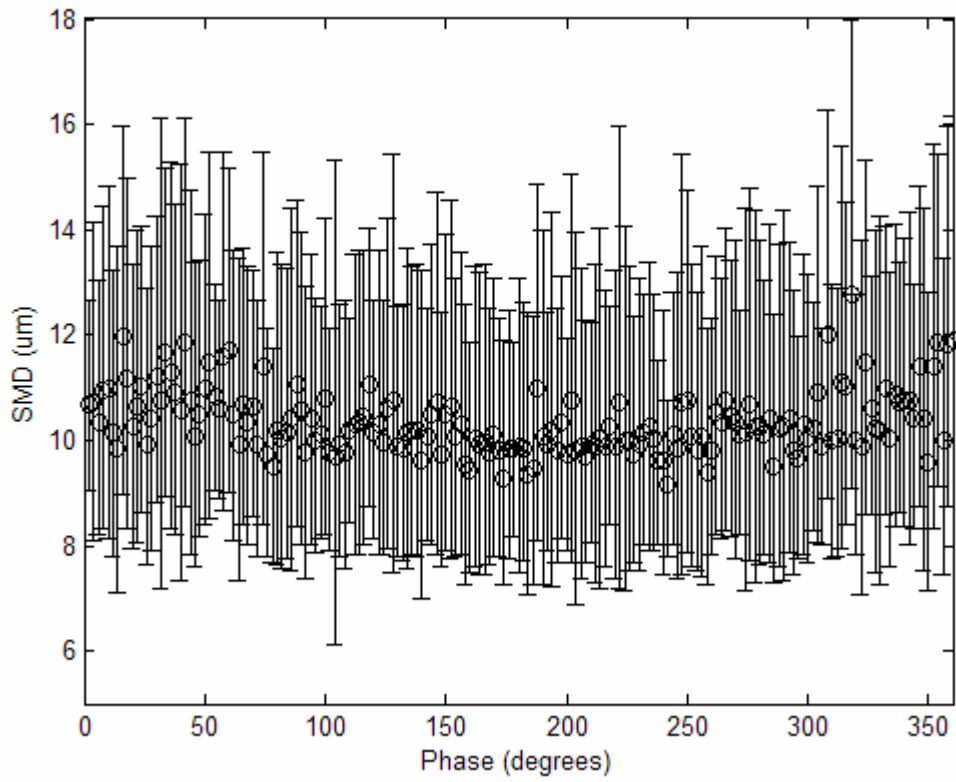


Figure G.31: Simplex nozzle, 300 psi mean pressure ± 50 , radial 1.0 cm.

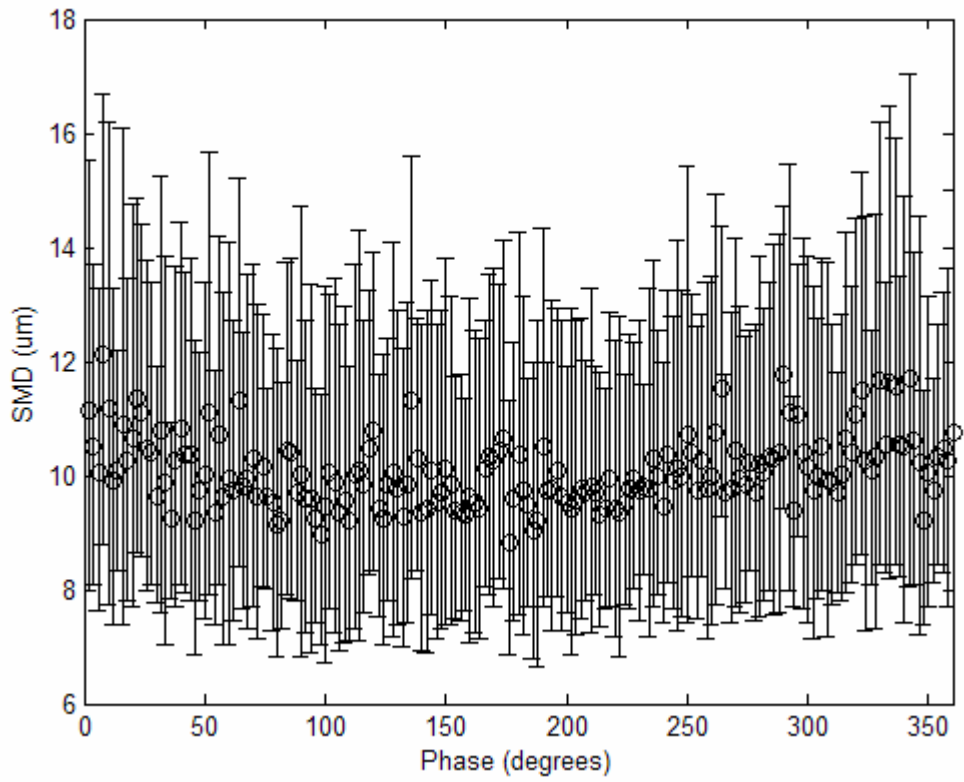


Figure G.32: Simplex nozzle, 300 psi mean pressure ± 30 , radial 1.0 cm.

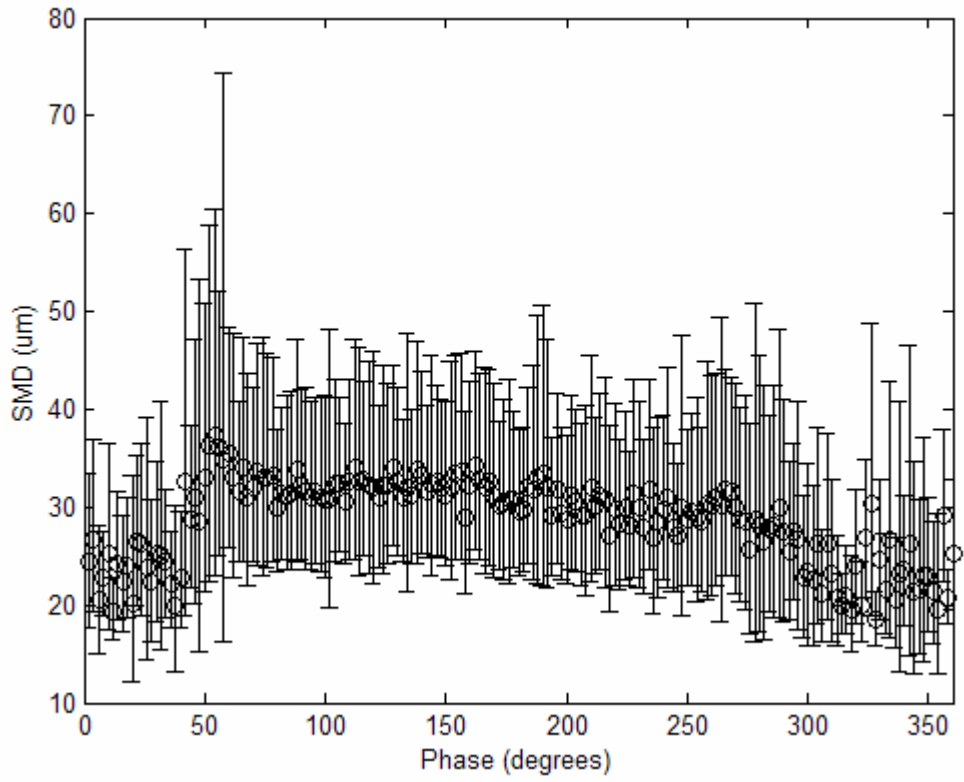


Figure G.33: Air-assist nozzle, 135 psi mean pressure ± 10 , axial 35 mm, centerline.

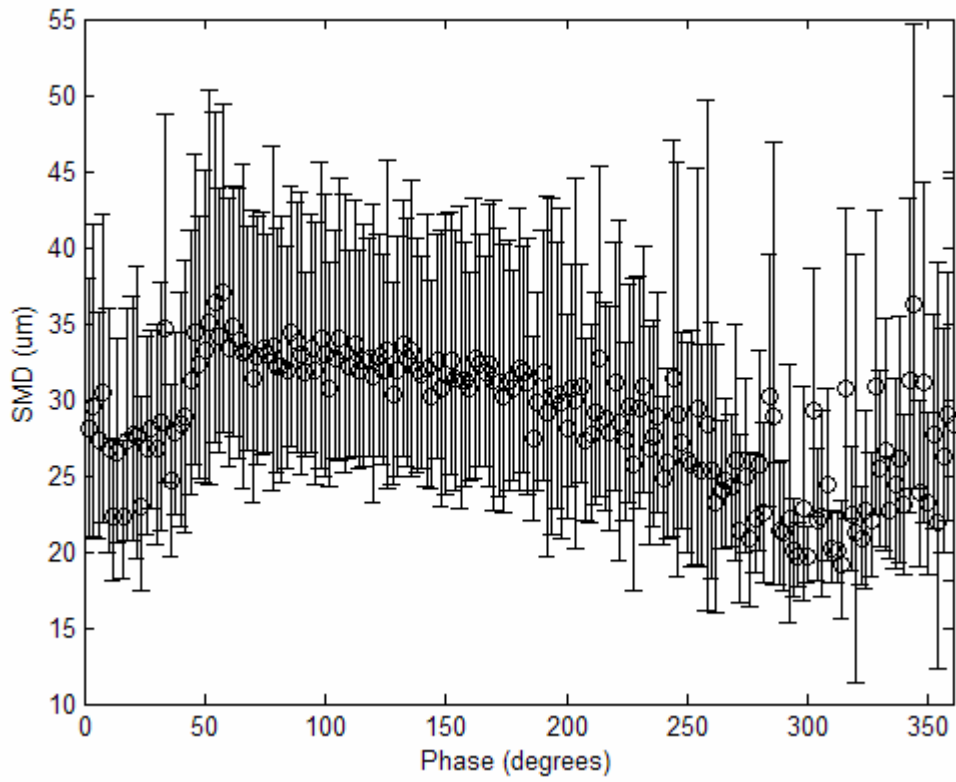


Figure G.34: Air-assist nozzle, 135 psi mean pressure ± 10 , axial 35 mm, radial 0.2 cm.

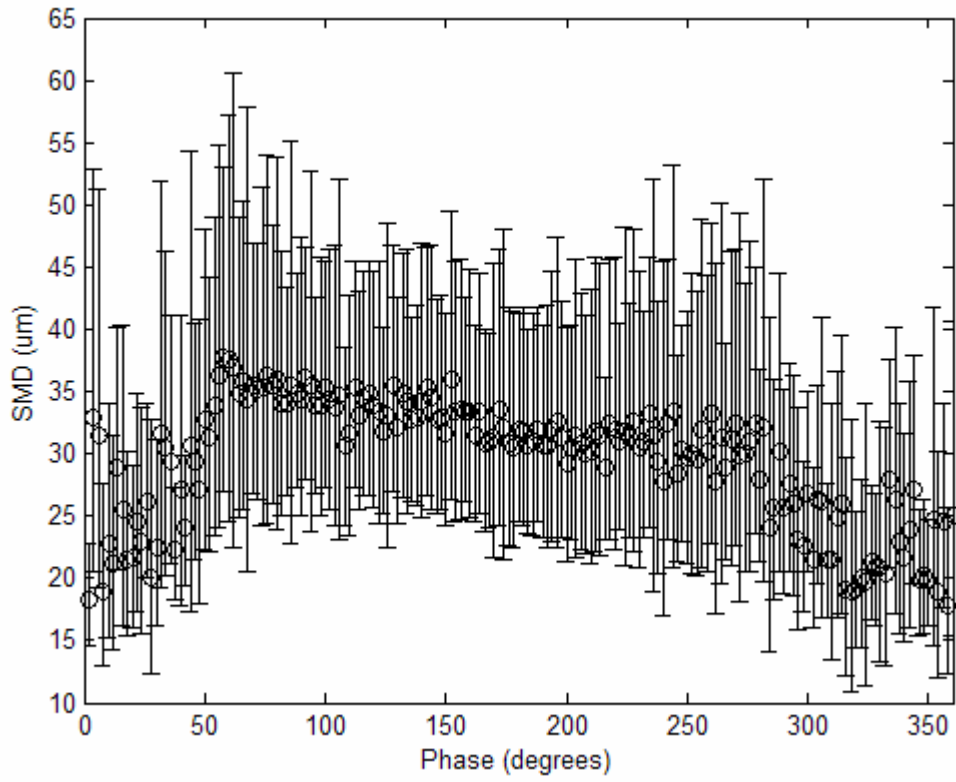


Figure G.35: Air-assist nozzle, 135 psi mean pressure ± 10 , axial 35 mm, radial 0.4 cm.

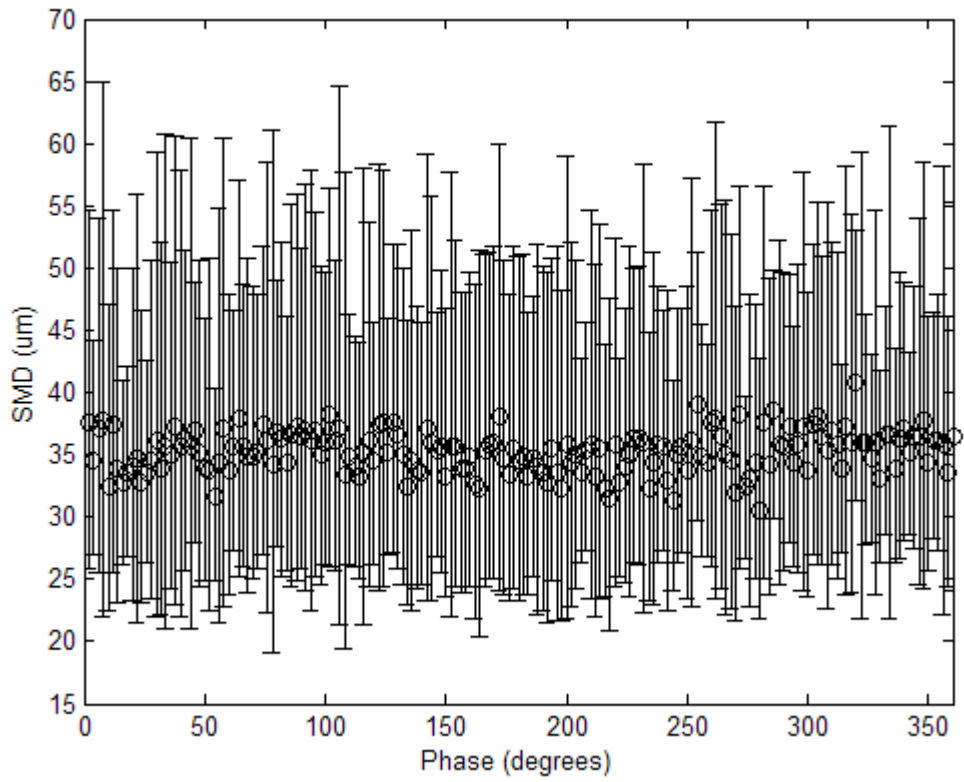


Figure G.36: Air-assist nozzle, 135 psi mean pressure ± 10 , axial 60 mm, centerline.

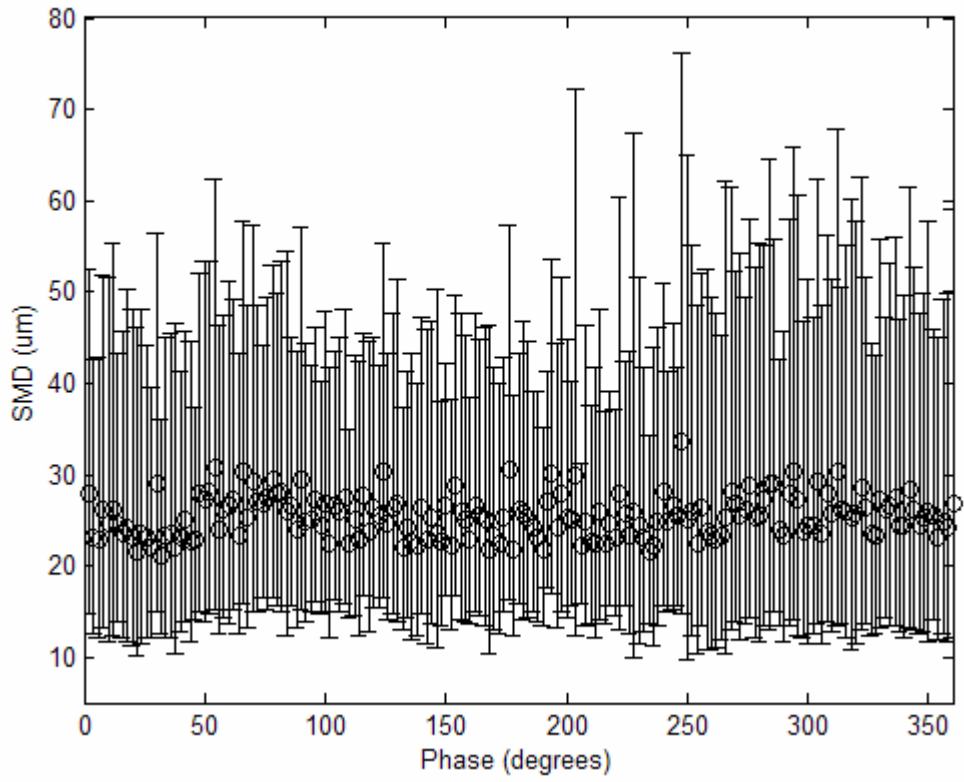


Figure G.37: Air-assist nozzle, 135 psi mean pressure ± 10 , axial 60 mm, radial 0.3 cm.

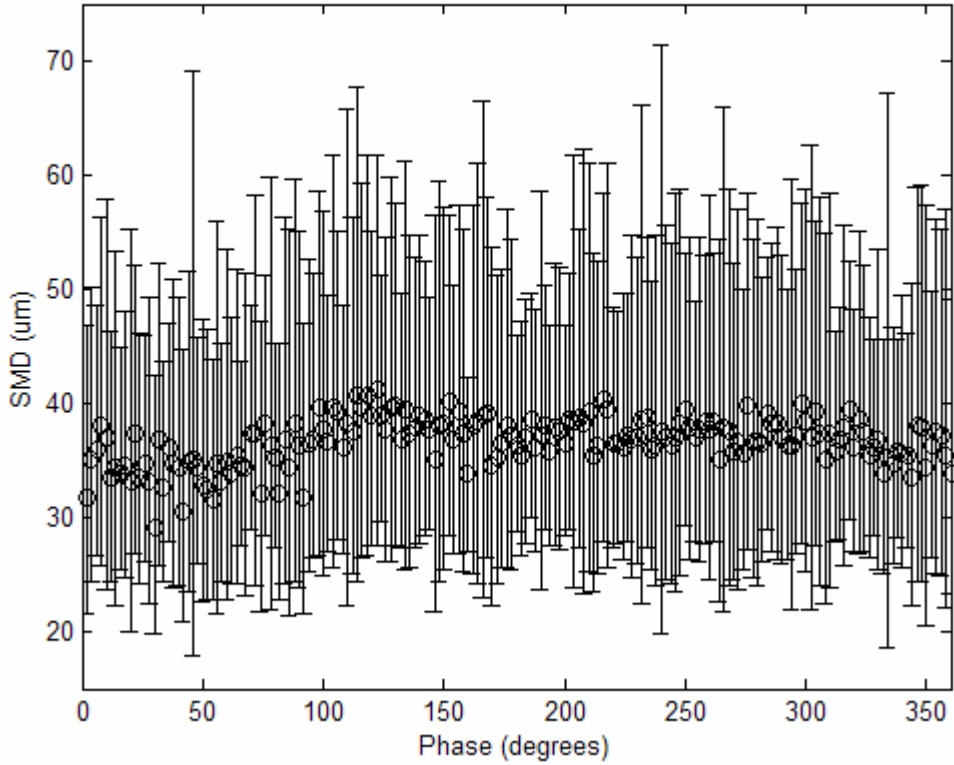


Figure G.38: Air-assist nozzle, 135 psi mean pressure ± 10 , axial 60 mm, radial 0.6 cm.

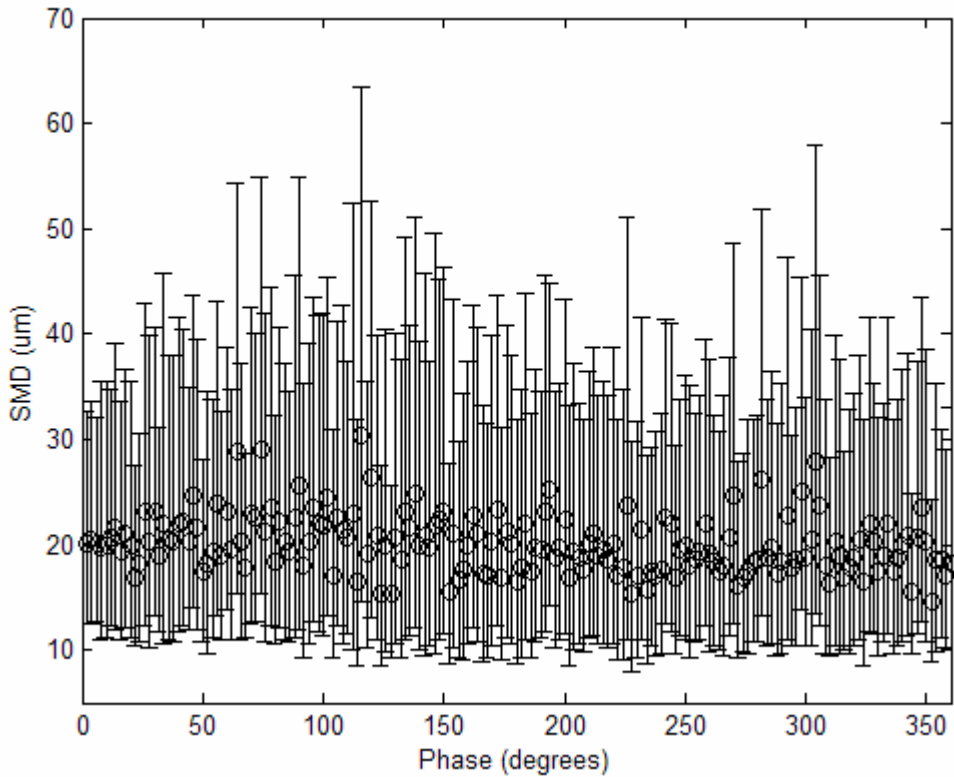


Figure G.39: Air-assist nozzle, 135 psi mean pressure ± 10 , axial 90 mm, centerline.

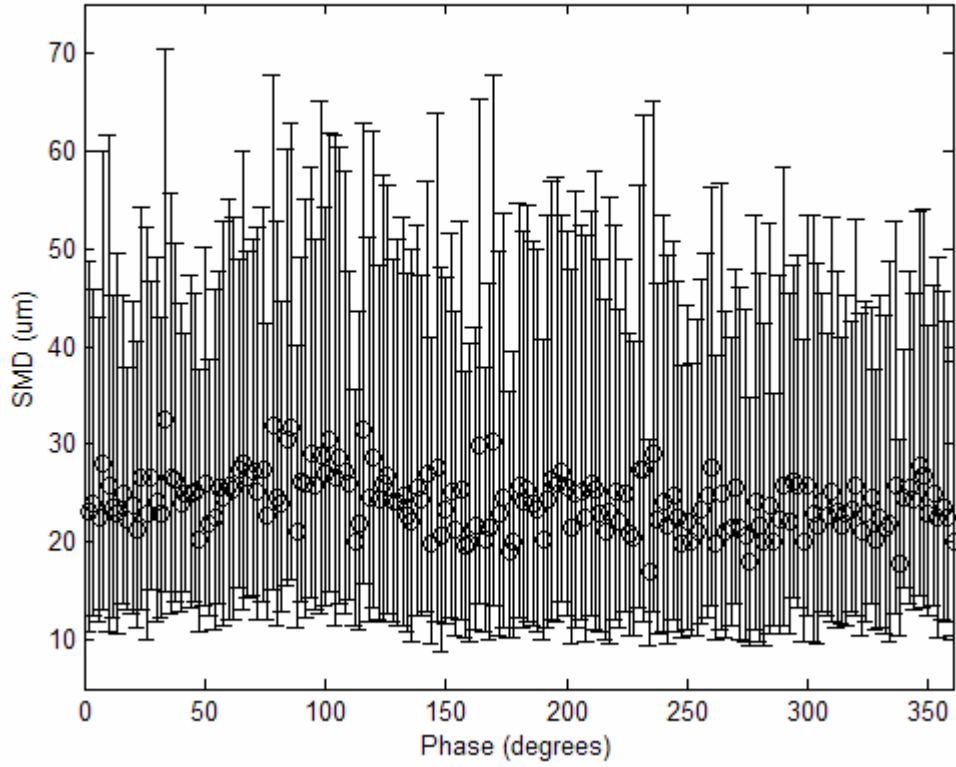


Figure G.40: Air-assist nozzle, 135 psi mean pressure ± 10 , axial 90 mm, radial 0.5 cm.

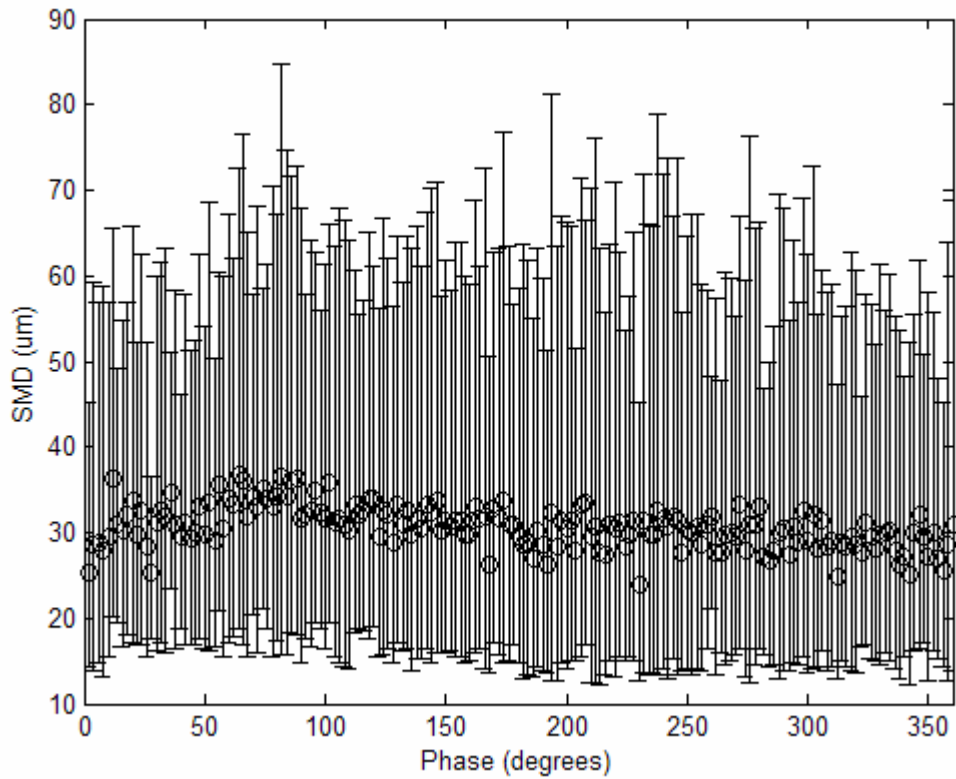


Figure G.41: Air-assist nozzle, 135 psi mean pressure ± 10 , axial 90 mm, radial 1.0 cm.

Bibliography

- [1] Banaszuk, A., Jacobson, C.A., Khibnik, A.I., Prashant, G.M., *Linear and Nonlinear Analysis of Controlled Combustion Processes. Part I: Linear Analysis*, IEEE International Conference on Control Applications, August 1999.
- [2] Banaszuk, A., Jacobson, C.A., Khibnik, A.I., Prashant, G.M., *Linear and Nonlinear Analysis of Controlled Combustion Processes. Part II: Nonlinear Analysis*, IEEE International Conference on Control Applications, August 1999.
- [3] Barooah, P., Anderson, T.J., Cohen, J.M., *Active Combustion Instability Control With Spinning Valve Actuator*, Journal of Engineering for Gas Turbines and Power, Vol. 125, 2003, pp. 925-932.
- [4] Chang, H., Nelson, D., Sipperley, C., Edwards, C., *Development of a Temporally Modulated Fuel Injector with Controlled Spray Dynamics*, Journal of Engineering for Gas Turbines and Power, Vol. 125, 2003, pp. 284-291.
- [5] Cohen, J.M., Rey, N.M., Jacobson, C.A., Anderson, T.J., *Active Control of Combustion Instability in a Liquid-Fueled Low-NO_x Combustor*, Journal of Engineering for Gas Turbines and Power, Vol. 121, 1999, pp. 281-284.
- [6] Cohen, J.M., Banaszuk, A., *Factors Affecting the Control of Unstable Combustors*, Journal of Propulsion and Power, Vol. 19, 2003, pp. 811-821.
- [7] Dantec manual: *Particle Dynamics Analyser, Installation and User's Guide*, Dantec, 1999.
- [8] Dantec Dynamics website: <http://www.dantecdynamics.com>
- [9] DeCastro, J.A., *Design and Validation of High-Bandwidth Fuel Injection Systems for Control of Combustion Instabilities*, Master's Thesis, Virginia Polytechnic Institute and State University, February 2003.
- [10] Delavan Spray Technologies: *Industrial Spray Nozzles and Accessories*, USA, 1998
- [11] Hathout, J.P., Fleifil, M., Annaswamy, A.M., Ghoniem, A.F., *Why do Secondary Peaks Occur in Experimental Active Controllers of Thermoacoustic Instability?*, AIAA Joint Propulsion Conference, July 1997, AIAA 1997-2834.
- [12] Hermann, J., Gleis, S., Vortmeyer, D., *Active Instability Control (AIC) of Spray Combustors by Modulation of the Liquid Fuel Flow Rate*, Combustion Science and Technology, Vol. 118, 1996, pp. 1-25.

- [13] Hinds, W.C., *Aerosol Technology: Properties, Behavior, and Measurement of Airborne Particles*, 2nd edition, John Wiley & Sons, INC., 1999.
- [14] Johnson, C.E., Neumeier, Y., Lubarsky, E., Lee, J.Y., Neumaier, M., Zinn, B.T., *Suppression of Combustion Instabilities in a Liquid Fuel Combustor Using a Fast Adaptive Control Algorithm*, AIAA 38th Aerospace Sciences Meeting & Exhibit, January 2000, AIAA 2000-0476.
- [15] Lagimoniere, E.E., *The Design and Construction of a High-Bandwidth Proportional Fuel Injector for Liquid Fuel Active Combustion Control*, Master's Thesis, Virginia Polytechnic Institute and State University, August 2001.
- [16] Lefebvre, A.H., *Atomization and Sprays*, Hemisphere Publishing Corporation, 1989.
- [17] Murugappan, S., Gutmark, E.J., Acharya, S., *Application of Extremum Seeking Controller for Suppression of Combustion Instabilities in Spray Combustion*, AIAA 38th Aerospace Sciences Meeting & Exhibit, January 2000, AIAA 2000-1025.
- [18] Oh, S.H., Kim, D.I., Paek, M.S., *Experiments on Air-Assist Spray and Spray Flames*, *Atomization and Sprays*, Vol. 11, 2001, pp. 775-788
- [19] Piezomechanik Gmbh website: <http://www.piezomechanik.com>
- [20] Schiller, N.H., *Design and Validation of a Proportional Throttle Valve System for Liquid-Fuel Active Combustion Control*, Master's Thesis, Virginia Polytechnic Institute and State University, October 2003.
- [21] Seume, J.R., Vortmeyer, N., Krause, W., Hermann, J., Hantschk, C.-C., Zangl, P., Gleis, S., Vortmeyer, D., Orthmann, A., *Application of Active Combustion Instability Control to Heavy Duty Gas Turbine*, *Journal of Engineering for Gas Turbines and Power*, Vol. 120, 1998, pp. 721-726.
- [22] Swagelok website: <http://www.swagelok.com>

Vita

Anne M. Hines was born August 15, 1980 in Chesterfield Missouri. She graduated from Virginia Tech in 2003 with a Bachelor of Science degree in Mechanical Engineering and a Bachelor of Arts degree in Political Science. She is a member of Pi Tau Sigma and the American Society of Mechanical Engineers. She is the recipient of the 2002 ASME Arthur L. Williston Award. In the spring of 2005 she will receive her Master of Science degree in Mechanical Engineering from Virginia Tech.